Observing Bright Stars and their Planets from the Earth and from Space

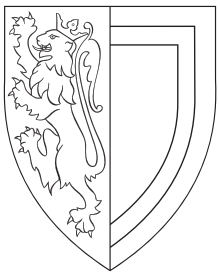

Benjamin J. S. Pope

Balliol College

University of Oxford

A thesis submitted for the degree of

Doctor of Philosophy

Trinity 2017

Abstract

The discovery and characterization of extrasolar planets is a leading frontier of science, which is limited by our ability to extract real astrophysical signals masked by systematic noise. In this Thesis I develop techniques for self-calibration in optical astronomy, in both imaging and photometry, applicable both to observations from the ground and for space telescopes, and apply these to searching for exoplanets.

Kernel phase interferometry is a method for improving high angular resolution astronomical imaging by cancelling out the effects of the turbulent atmosphere. I derive a generalization, kernel amplitude, to correct also for the effects of scintillation, or twinkling. I go on to demonstrate kernel phase for the first time from the ground using the Palomar Hale 200-Inch Telescope, as a test case for the extreme adaptive optics instruments SPHERE and GPI.

The *Kepler* satellite and its successor, the *K2* mission, have been crucial to our understanding both of exoplanets, and via asteroseismology, of stellar physics. The success of *K2* depends on correcting for its unstable pointing. Using semi-parametric Bayesian statistical models to overcome this issue, I report the discovery of 145 new transiting planet candidates in data from Campaigns 5 and 6 of the *K2* mission. Furthermore, with two novel techniques, 'smear' and 'halo' photometry, which dramatically extend the dynamic range of *Kepler* and *K2*, I recover light curves of bright stars that were previously too saturated to study, and definitively detect variability in the seven naked-eye stars in the Pleiades cluster. These new data analysis approaches enable the *K2* and TESS space missions to discover planets transiting the nearest and brightest stars, which will be ideal targets for the coming era of exoplanet characterization.

Acknowledgements

First and foremost I would like to thank Suzanne, who didn't have to take me, but did, who taught me so much and who let me explore, and who didn't have to be so kind, but was. I have learned so much from working with you; I can't have been easy to supervise, and I am deeply grateful. Thank you also to Pat, for your neverending patience, your humour, your diligence, and your hospitality, without whom this would have been a much tougher road to tread. And thank you to Niranjan for your time, and your understanding.

Very special thanks are in order for Peter, who has gone above and beyond as a mentor for the last eight years. Your unfailing support has meant so much to me. Tim, where do I even start. Working with you barely felt like work, and so much of this thesis is built on your insights. But above all that, you've been a constant friend. Thanks, mate. Hannu – I wish I could code like you and still be so cool. Roger, thanks for making me feel at home. And thanks to the other astronomers who've been so kind to me: Tim, Didier, Simon, Grant, Sasha, Rob, Faustine, Neal, Odele, Gioia, Anand, Laurent, Alex, Frantz, Guy, Will, Andrew, Dave, John, Hogg, Daniela, Ewan, and Brendon.

I've had the best office mates for these four years that anyone could wish for. Holly, Jamie, Rupert, Simon, Marisa - from coffee and conversation to commiseration, thank you. Physics buddies Alfie, Peter, Andre, Ricarda, Vinesh, Ryan and Rebecca, thank you for the balls, the pies, the pints, the laughs, and the friendship. I would also like to offer a special thank you to Ashling, the heart of the physics department.

Balliol, true to the saying, has been a kind of heaven on Earth, and I am glad beyond words to have met such wonderful Balliol people, and to have had the College's far-reaching and ever-kind support. I am especially glad for the years of warm company, cocktails, punting, walks, and wit from Josh, Elspeth, Gillian, Mirela, Ed, Sarah, Dave, Duncan, Stephane, and Jess – who are heroes, in D&D or otherwise. The other great adventure with Balliol has been on UC: with the razor-sharp Joey, Freddy and Jacob, the boy band formed in the library (of Marx & Engels). You were brilliant quizzers, and more-brilliant mates. And I've enjoyed the many lively dinners from Hall to Holywell with Laure, David, Carina, Ben, Mimi, Anupama, Helen, Francesca, Chris, and Nina. Whatever I had, Balliol gave me again – *floreat domus*.

I've never left Sydney behind, never could, and never want to. Thank you Joyce, Joe, Jess, Jane, Jason, Becky, Dom, Adam, Amasha, Amy, Clare, Hunter, Annie, Pat, Kiri, Max, Sarah, Jono, Nick, Anna-Lisa, Steph, Zara, Henry, and Sandra, for being there for me even after all these years away. I would like to acknowledge the Gadigal people of the Eora nation and the Gweagal people of the Tharawal nation on whose land I have lived and worked.

Mum, Dad, Grandad. I've been away a long time and I know it's been hard. Your love has brought me to where I am today and I'm so grateful for what you've given up. Thank you.

And Val. In every winter your kindness has been like the light of spring.

Declaration

The work in this thesis is based on research I carried out at the University of Oxford between Michaelmas Term 2013 and Hilary Term 2017.

This thesis includes work from four of my first-author, peer-reviewed publications, which form the bulk of the content of Chapters 2 to 5. I was the principal author, but in some passages comments from my coauthors have been incorporated. Some of the material from these papers has been moved to the introductory and concluding chapters (Chapters 1 and 7).

A preliminary analysis of the data in Chapter 3 was included in my Honours thesis at the University of Sydney, in which using less sophisticated code I did not achieve the same success. The reanalysis presented here is entirely new.

Chapter 4 is based on the results of an approach to systematics correction and planet discovery which was conceived by Suzanne Aigrain (following Aigrain et al., 2015) and continued in Pope et al. (2016b). The implementation of the systematics correction (K2SC; Aigrain, Parviainen & Pope, 2016) and planet search (K2PS; Parviainen, Pope & Aigrain, 2016) codes was performed jointly with Aigrain and Hannu Parviainen, who in particular was responsible for heavy computational aspects. My contributions here consisted of the application of this code to *K2* data, testing and optimization of the planet detection and vetting criteria, the identification and vetting of planet candidates, and the writing of the manuscript.

Chapter 6 is based on work led by Dr Tim White at Aarhus University, in which my major contribution was developing and testing the halo photometry code, writing introductory, methods and conclusions sections, and editing text throughout. Total Variation was White's idea, and I refactored the code, improving its precision, speed and robustness, and benchmarking and explaining the method's success. This Chapter includes a subset of the work presented in a manuscript submitted to MNRAS, 'Beyond the Kepler/K2 bright limit: variability in the seven brightest stars of the Pleiades' (White et al., submitted). In order to focus on my own original contribution, the Thesis includes the development and application of the Total Variation method. I omit much of the manuscript content on stellar physics which was principally the work of other authors, though for context and significance I include discussion of the stellar physics derived from these observations principally by White.

In addition to this, the introduction and conclusions contain content from a manuscript in preparation, of which I am the principal author, tentatively entitled 'The *Kepler* Smear Campaign I: An Asteroseismic Catalogue of Bright Red Giants'.

Benjamin Pope

(*March 2017*)

First-author Peer Reviewed Publications

4. *Kernel Phase and Kernel Amplitude in Fizeau imaging.* **Benjamin Pope**. Monthly Notices of the Royal Astronomical Society, Volume 463, Issue 4, p.3573-3581. doi: 10.1093/mnras/stw2215. This is reproduced in this Thesis as Chapter 2 and is referred to where otherwise relevant as Pope (2016).

3. *Transiting exoplanet candidates from K2 Campaigns 5 and 6.* **Benjamin Pope**, Hannu Parviainen, Suzanne Aigrain. MNRAS, Volume 461, Issue 4, p.3399-3409, 2016. This is reproduced in this Thesis as Chapter 4 and is referred to where otherwise relevant as Pope et al. (2016b).

2. *The Palomar Kernel Phase Experiment: Testing Kernel Phase Interferometry for Ground-based Astronomical Observations*, **Benjamin Pope**, Peter Tuthill, Sasha Hinkley, Michael J. Ireland, Alexandra Greenbaum, Alexey Latyshev, John D. Monnier, Frantz Martinache. MNRAS, Volume 455, Issue 2, p.1647-1653, 2015. This is reproduced in this Thesis as Chapter 3 and is referred to where otherwise relevant as Pope et al. (2016a).

1. *Photometry of Very Bright Stars with* Kepler *and K2 Smear Data*, **Benjamin Pope**, Timothy White, Daniel Huber, Simon Murphy, Tim Bedding, Douglas Caldwell, Aleksa Sarai, Suzanne Aigrain, Thomas Barclay. MNRAS Letters, Volume 455, Issue 1, p.L36-L40, 2015. This is reproduced in this Thesis as Chapter 5 and is referred to where otherwise relevant as Pope et al. (2016c).

Other Publications

1. *K2SC: Flexible systematics correction and detrending of K2 light curves using Gaussian Process regression*, Suzanne Aigrain, Hannu Parviainen, **Benjamin Pope**. MNRAS, Volume 459, Issue 3, p.2408-2419. 2016. This is referred to in this Thesis as Aigrain et al. (2016) or APP16.

Contents

1 Introduction **1**

1.1 Extrasolar Planets 4

1.1.1 Plurality of Worlds 5

1.1.2 Planet Formation 8

1.1.2.1 Migration 11

1.2 Habitability and Life 11

1.3 Methods for Exoplanet Detection 13

1.3.1 Radial Velocity - Theory 14

1.3.2 The Transit Method - Theory 14

1.3.3 Direct Imaging and Adaptive Optics 16

1.3.4 Astrometry 19

1.3.5 Microlensing 20

1.3.6 Timing Variations 21

1.4 Transmission Spectroscopy 23

1.5 A Brief History of Exoplanet Discoveries 25

1.5.1 The First Exoplanet Discoveries 27

1.5.2 First Transits 28

1.6 Space Transit Surveys 29

1.6.1 *Kepler*: Selected Scientific Results 33

1.6.2 *K2* 35

1.7 Interferometry 38
1.7.1 The van Cittert-Zernike Theorem 41
1.7.2 A Brief History of Interferometry 43
1.7.2.1 Early Optical Interferometry 43
1.7.2.2 Radio Interferometry 46
1.7.2.3 Modern Optical Interferometry 47
1.8 Asteroseismology 50

2 Kernel Phase and Kernel Amplitude **56**
2.1 Introduction 56
2.2 Matrix Theory of Phase Self-Calibration 61
2.3 Kernel Amplitudes 65
2.4 Phase Noise and Kernel Amplitudes 70
2.5 Simulation 71
2.5.1 Binaries 75
2.5.2 Phase Noise 78
2.5.3 Disks 78
2.6 Discussion 80
2.7 Conclusion 82

3 Palomar Kernel Phase Experiment **84**
3.1 Introduction 84
3.1.1 Observations 86
3.2 Processing and Results 88
3.2.1 Kernel Phase Extraction and Calibration 88
3.2.2 Bayesian Parameter Estimation 90
3.2.3 Comparison with Closure Phase 94
3.2.4 Comparison with PSF Fitting 96

3.3 Comparison between Masking and Kernel Phase 97
3.4 Discussion 99

4 *K2* Campaigns 5 and 6 Transit Candidates 101

4.1 Introduction 101
4.2 Light Curve Preparation 103
4.3 Transit Search 108
4.4 Vetting 111
4.5 Planet Candidates 115
4.5.1 Multiple Planet Systems 117
4.5.2 Spectroscopic Reconnaissance 119
4.6 Source Code and Data Products 121
4.7 Conclusions 122

5 Smear Photometry 124

5.1 Introduction 124
5.2 Method 126
5.3 Results 128
5.3.1 HD 178875 128
5.3.2 70 Aqr 129
5.3.3 HR 8500 131
5.4 Conclusions 135

6 Halo Photometry 136

6.1 Introduction 136
6.2 Halo Photometry 140
6.2.1 Data 140
6.2.2 Method 141
6.3 Photometric Precision 149

6.4 Variability in the Pleiades 152
6.4.1 Alcyone 153
6.4.2 Atlas 157
6.4.3 Electra 158
6.4.4 Maia 159
6.4.5 Merope 160
6.4.6 Taygeta 161
6.4.7 Pleione 162
6.5 Source Code 163
6.6 Discussion and Conclusions 164

7 Conclusions **167**
7.1 Conclusions 167
7.2 Future Work 169

Appendix A Tables **175**

Bibliography **I**

List of Figures

1.1 Relationships of interferometric quantities and domains. 44

2.1 Triangle of receivers 62
2.2 Relations between pupil, baseline and kernel spaces 65
2.3 Visbility bias 72
2.4 Visibility bias error 73
2.5 Example amplitude screen 76
2.6 Kernel amplitude vs. raw visibilities for binary fitting 77
2.7 Kernel amplitude vs. raw visibilities under phase noise 79
2.8 Kernel amplitude vs. raw visibilities for a disk model 81

3.1 K_s band deconvolved masking image 87
3.2 Hale Telescope medium-cross pupil model 91
3.3 Correlation diagram for α Ophiuchi kernel phases 93
3.4 Correlation diagram for α Ophiuchi bispectral phases 96

4.1 Initial BLS selection of transit candidates 109
4.2 Vetting diagrams for EPIC 212521166 112
4.3 Radius ratio versus period for vetted planet candidates 118

5.1 HR 8500 smear data 127
5.2 HD 178875 regular and smear light curves 129
5.3 70 Aqr Smear Amplitude Spectrum 130

5.4 Power spectra of red giants HR 8500 and KIC 5694720 132
5.5 Amplitude-$\nu_{\rm max}$ relation from *Kepler* 134

6.1 Pleiades image and halo example 137
6.2 K2 pixel-level systematics 142
6.3 Photometric precision as a function of magnitude 146
6.4 Photometric precision as a function of mask radius 148
6.5 Halo light curves and power spectra of the Pleiades 150
6.6 Rotational inclinations of Alcyone, Maia and Pleione 156

List of Tables

3.1 Binary Parameter Estimates for α Ophiuchi 93

A.1 Campaign 5 Planet Candidates 175

A.2 Campaign 6 Planet Candidates 177

A.3 Multiple System Planet Candidates 178

Chapter 1

Introduction

Me before all things may the Muses sweet,
Whose rites I bear with mighty passion pierced,
Receive, and show the paths and stars of heaven,
The sun's eclipses and the labouring moons,
From whence the earthquake, by what power the seas
Swell from their depths, and, every barrier burst,
Sink back upon themselves, why winter-suns
So haste to dip 'neath ocean, or what check
The lingering night retards.

Vergil, *Georgics* 2.475-8 (tr. Greenough, 1900)

Human beings of every culture have sought to understand their place in the cosmos. Their mythologies have exalted our species as the pinnacle of nature, of divine origin and unique in the universe, and many traditional societies have based their beliefs in the regularities of the motions of stars, the Sun, the Moon, and the planets (Ruggles, 2015). The modern science of astrophysics is on the cusp of answering some of the profound questions previously left to religion: what is the origin of the Earth and Solar System? Are there other worlds like it — and do they harbour life? In this Thesis, I shall present a very modest collection of research towards helping answer some of these questions, by developing and refining technology for finding extrasolar planets and for learning about their characteristics and those of the stars they orbit.

This technology will, I hope, contribute in some small way to the long-term goals of understanding stellar physics, planet formation, and searching for habitable planets and life in the universe.

I will focus on two methods for studying stars and their planets: direct imaging, in particular using interferometry and adaptive optics to try and resolve a faint planet from its parent star; and photometry, using measurements of the brightness of a star to detect the presence of planets as they pass in front and block its light (the transit method for exoplanet detection), and deduce the star's internal structure (asteroseismology). I am in particular interested in methods for obtaining measurements of bright stars in the presence of systematic noise, and self-calibrating these in post-processing. Since the first discovery in 1995 (Mayor & Queloz, 1995), the number of known exoplanets has doubled every 27.3 months ("Mamajek's Law": Mamajek, 2016), comparable to the rate of discovery of radio sources in the 1950s-1960s 'golden age' of radio astronomy (Callingham, 2017). The next stage in this field will be to go beyond surveying many faint stars to simply detect signals, as with the *Kepler* transit survey. We now want to characterize planetary systems in great detail: for this, we will want to be able to find the best possible targets, which are typically those planets transiting stars bright enough to use the best spectrographs to obtain atmospheric spectra, and to use the best adaptive optics to obtain direct images of the planets and other circumstellar material. These are in general hard to find with instruments optimized for large surveys of faint stars, but as I will show, with the right algorithms it is possible to extend the dynamic range of existing survey instruments to be able to observe even the very brightest targets.

The structure of this Thesis will be as follows. I will begin by presenting research on the 'kernel phase' approach to correcting the effects of optical aberrations on high-angular-resolution astronomical imaging, with a theoretical generalization of these ideas to account for scintillation effects (Chapter 2), together with the results of an

experiment using the Palomar Hale 200-Inch Telescope to test kernel phase for ground-based adaptive optics (Chapter 3). These ideas are applicable to other advanced adaptive optics systems, and to current and future space telescopes, and will enable better imaging of stellar systems for studying binarity, to resolving protoplanetary disks, and directly imaging young planets.

In the remainder of this Thesis, I will describe work done with the *Kepler Space Telescope* and its continuation as the *K2* mission, which uses the transit method to search for extrasolar planets. In Chapter 4, I will present a catalogue of transiting planet candidates in *K2* Campaigns 5 and 6, using Gaussian Process non-parametric models to correct for systematics. I will then demonstrate two new techniques, 'smear' and 'halo' photometry, for extracting precise light curves of stars so bright they could not ordinarily be observed due to detector saturation. Using smear photometry (Chapter 5), we are able to recover light curves of stars in *Kepler* and *K2* which were not even downloaded to Earth, instead reconstructing these from collateral 'smear' data used for calibration. With the halo method (Chapter 6), we use variations in the wide halo of diffracted and scattered light around stars as bright as the third magnitude, obtaining the first ever precise optical light curves of the naked-eye Pleiades, detecting variability in some for the first time. These new methods open the door to observing the nearest and brightest stars without imposing additional hardware requirements on existing and near-future instruments.

In a concluding chapter (Chapter 7), I will discuss the application of kernel phase to future adaptive optics and space telescopes, and explore the possibility of finding planets using the halo method around naked-eye stars using the upcoming Transiting Exoplanet Survey Satellite (TESS) and other missions.

1.1 Extrasolar Planets

To understand the formation, evolution, and composition of extrasolar planets requires a discussion of many areas of astrophysics: consideration must be given to star formation, to proto-stellar and proto-planetary disks, and stellar structure and evolution, asteroseismology, and finally to the dynamics of planetary systems. Furthermore, detecting and characterizing exoplanets is possible only at the limits of modern astronomical technology, and is currently driving massive innovation in spectroscopy, photometry, and adaptive optics and image processing. This Thesis has a broad scope, including technology development for imaging and photometry, and applying this technology to real observations both to detect planets and to characterize stars. As such, this Introduction must cover an uncommonly wide range of topics. I have endeavoured in the following to refer to relevant review articles, keeping discussion more concise than might be ideal for a review on any one topic.

Before we begin – we should define what we mean by a 'planet'. In this Thesis, I will use 'exoplanets' and 'extrasolar planets' interchangeably to refer to planets orbiting stars other than the Sun, and also simply 'planets' to refer to such objects when it is clear from context. The International Astronomical Union (IAU) defines a solar-sysetem planet as[1] 'a celestial body that

A is in orbit around the Sun,

B has sufficient mass for its self-gravity to overcome rigid body forces so that it assumes a hydrostatic equilibrium (nearly round) shape, and

C has cleared the neighbourhood around its orbit.'

Multiple definitions for 'planet' are current in the context of exoplanets (Basri & Brown, 2006), for which we cannot yet test the criteria of the IAU definition for solar-

[1]Decided at the Prague General Assembly, 2006.

system planets. I personally am sympathetic to a physics-based definition (Soter, 2006):

> A planet is an end product of disk accretion around a primary star or substar.

This distinguishes planets from objects formed by gravitational instability in a protoplanetary disk, which may be the origin of brown dwarfs, substellar objects which fuse deuterium in their early life (see Tarter, 1975, 2014, for the history of this term), and of some planetary-mass objects (Kratter & Lodato, 2016). My personal view is that the physics-based formation definition is the right way to view things in the long run, and that objects formed by gravitational instability (i.e. as the extremely low-mass tail of the binary star distribution) should not be called planets, but that in the absence of evidence the $13M_J$ deuterium fusion mass cutoff is a viable proxy.

With definitions clarified, we shall begin to think about planets themselves. We shall begin by discussing the roots of this field of study, in the history of pre-modern and early modern scientific ideas about extrasolar planets.

1.1.1 Early Ideas about the Plurality of Worlds

Pre-modern philosophical traditions have considered the possibility of other worlds like our own; this idea in its pre-modern forms is generally referred to as the 'plurality of worlds' (Dick, 1996). In the ancient Hellenic tradition, the pre-Socratic philosopher Anaxagoras, who was the first extant source in the West to explain that the Moon shines by the Sun's reflected light, suggested that the Moon might also be inhabited; Greek and Roman atomist philosophers subsequently espoused versions of the plurality of worlds idea in the sense of parallel universes, including the early Greek atomists Democritus and Epicurus, fourth-century Epicurean philosopher Metrodoros of Chios, and the late Republican Roman poet Lucretius. On the other hand, the plurality of worlds was rejected by Aristotle and his followers throughout antiquity

and into the Christian and Islamic Middle Ages, with exceptions such as Cardinal Nicholas of Cusa (1401-1464), or Muhammad al-Baqir (676–733) and Fakhr ad-Din ar-Razi (1150-1210) in the Islamic world (Shklovskii & Sagan, 1966; Dick, 1996; Weintraub, 2014). The West was not the only tradition to consider this possibility. In China, in the Xuán Yè (玄夜, 'empty space') cosmological school of thought, philosopher Dèng Mù (邓牧, 1247-1302)[2] asked "How unreasonable it would be to suppose that besides the heaven and earth which we can see there are no other heavens and no other earths?" (as quoted in Fu, 1965).

The most prominent in the early modern Western scientific tradition to suggest that not only are the stars of the night sky suns like ours, but that these might be orbited by their own planetary systems, was the Italian Copernican astronomer and occultist Giordano Bruno (1548-1600), who wrote:

> There are countless suns and countless earths all rotating around their suns in exactly the same way as the seven planets of our system... The countless worlds in the universe are no worse and no less inhabited than our Earth. (Bruno 1584b, as quoted in Kasting, 2010).

This was a subversive idea[3], and Bruno's adherence to the plurality of worlds was the tenth heresy for which he would eventually be burned at the stake in Rome's Campo de' Fiori in 1600 (Blum, 2012). Koyre (1957) argues that Bruno, by taking the Western tradition 'from a closed to an infinite universe', was as revolutionary as Copernicus to the future development of cosmology (Ayala, 2013).

[2]I have given these names in the now-standard pinyin romanization of Mandarin. These are sometimes transliterated as the Hsüan-yeh cosmology, and philosopher Teng-mu, using the dated Wade-Giles romanization.

[3]Bruno's more general Copernican ideas found no favour here in Oxford. George Abbott, later Master of University College then Archbishop of Canterbury, was a Fellow of Balliol when Bruno visited in 1583, and wrote that 'he vndertooke among very many other matters to set on foote the opinion of Copernicus, that the earth did goe round, and the heavens did stand still; wheras in truth it was his owne head which rather did run round, & his braines did not stand still' (as quoted in McNulty, 1960). Conversely, Bruno (1584a) held that Oxford was 'a constellation of most obstinate pedantry and conceit mixed with a rustic rudeness, which would try the patience of Job' (author's translation).

In the intervening four centuries, the study of exoplanets has moved (only gradually) from a subject for theology to a burgeoning field of modern astrophysics. More influential than Bruno, by virtue of not being banned, was René Descartes' 'vortex hypothesis' of the universe, under which an "indeterminate" number of star systems existed in a constant state of fluid motion (Ayala, 2013), given early and influential support by Fontenelle (1686). Descartes' vortex theory was strongly opposed by Isaac Newton and his English followers, although Newton nevertheless accepts the possibility of the plurality of worlds (Newton & Cotes, 1713). Following Newton, early modern English astronomer Thomas Wright (best known as the first to propose that the Milky Way is a locally-planar collection of stars) wrote that "Round every Star we may justly conjecture a similar system of bodies" (Wright, 1734).

The doctrine of the plurality of worlds remained influential throughout the eighteenth and nineteenth centuries (Dick, 1996). Alexander Pope referred to it in his *Essay on Man* (Pope, 1734), and Thomas Paine in his *Age of Reason* (Paine, 1794). In the scientific community, the idea retained widespread currency, referred to for instance in pioneering work on stellar spectroscopy by Huggins & Miller (1864). In contemporary popular science, the plurality of inhabited worlds was a major topic of public discourse: Flammarion (1862) and Proctor (1870) both published commercially-successful popular books arguing in its favour, while Whewell (1853) and Wallace (1903, co-originator of the theory of evolution by natural selection) argued against.

In the remainder of this Thesis, we will tend to cease to use the dated term 'plurality of worlds', in accordance with contemporary usage beginning roughly from the start of the twentieth century where rigorous astrophysical investigations first begin. While observational evidence was long lacking, theoreticians nevertheless made substantial progress in understanding the processes of planetary formation as revealed by our own Solar System.

1.1.2 Planet Formation

It is remarkable to note that in the eighteenth century, the core ideas of the modern understanding of planet formation were put forward, and that these were subsequently rejected and re-adopted over the course of the nineteenth and twentieth centuries. The modern 'nebular hypothesis' of planet formation has its roots in the the ideas of Emanuel Swedenborg (1743), Immanuel Kant (1755) and Pierre-Simon Laplace (1796), and is therefore often referred to as the Swedenborg-Kant-Laplace hypothesis[4]. Of these the work of Laplace is the most rigorous, and was considered seriously into the late nineteenth century, thoughit is not in detail correct and does not connect planet formation to star formation. Woolfson (1993) provides an excellent overview of the relevant professional-astronomical literature, which we will draw upon in this section.

Winn & Fabrycky (2015) refer to theories in which planet formation is a part of the star formation process as 'monistic' and those which require a secondary event as 'dualistic', and we shall adopt this useful terminology here. Monistic theories should make planets common in the cosmos; dualistic theories generally predict them to be rare. The most important aspect of the historical controversies has been whether planet formation is a natural by-product of star formation (as is the case with the nebular hypothesis), and planetary systems are very common in the universe, or whether planetary systems are formed as a consequence of rare events. For the first half of the twentieth century when secondary-body models were popular, it was widely believed that the Solar System was special — and therefore that life in the universe was rare. As we shall see, planets are now known to be very common, and we now know planet formation to be a monistic process.

The nebular hypothesis was challenged from the mid-1800's on for more than a century, and the most severe criticism was that while the Sun contains the vast bulk

[4]The three subjects of a *University Challenge* bonus round, in which I missed Swedenborg.

of the mass of the solar system, the angular momentum is dominated by the orbits of the planets (Winn & Fabrycky, 2015). Dualistic models were put forward proposing planet formation by cataclysmic events, typically involving additional massive bodies interacting gravitationally with the Sun, which may be a star (the 'planetesimal hypothesis'; Chamberlin, 1901; Moulton, 1905; Jeffreys, 1929; Jeans, 1942); an interstellar gas-cloud (Shmidt-Lyttleton accretion; Shmidt, 1958; Lyttleton, 1961); or a low-density protostar (the 'capture theory'; Woolfson, 1964, 1979; Dormand & Woolfson, 1989).

A monistic model of star and planet formation has resurged in the last half-century and is now universally accepted. This has been the result of a synthesis of lines of evidence (see reviews by Armitage, 2011; Hartmann et al., 2016; Williams & Cieza, 2011; Nittler & Ciesla, 2016): a theoretical understanding of accretion disks has shown that angular momentum can be effectively concentrated in planets rather than the Sun (Hoyle, 1960; Balbus & Hawley, 1991); protoplanetary disks have been observed around young stars (e.g. HL Tau; ALMA Partnership et al., 2015); isotopic evidence has shown the birth of our solar system's planets to be coeval with the birth of the Sun (Patterson, 1956; Scott, 2007; Houdek & Gough, 2011); and planetary systems have been shown to be common, vindicating monistic models of star and planet formation.

It is now believed that most or all planets form by the accretion of dusty material in a protoplanetary disk (e.g. reviews by Morbidelli et al., 2012; Kley & Nelson, 2012), which is gradually evaporating under stellar irradiation (Safronov, 1972; Wetherill, 1980; Lin & Papaloizou, 1985). Planetesimals ($\sim$ 100 km size, of which asteroids are the present remainder) are first formed in a protoplanetary disk by the agglomeration of dust particles (Bodenheimer & Pollack, 1986), and then accrete into a few planetary embryos in an 'olgarchic growth' phase (Kokubo & Ida, 1998, 2000; Chambers, 2006). Embryos which reach a high mass ($\gtrsim 1 M_\oplus$) early on, while the disk retains a large

quantity of gas, are able to have runaway gas accretion directly from the disk and become gas giants (Ida & Lin, 2004), tending to form beyond a 'snow line' or 'ice line' at which it is sufficiently cold for volatiles (e.g. CO_2, H_2O) to condense out of the disk and contribute to the stock of rocky materials to form a planetary core (Lewis, 1974; Stevenson & Lunine, 1988; Ida & Lin, 2008).

Protoplanetary disk hosts are observed as the optically-variable T Tauri stars (Joy, 1942, 1945; Ambartsumian, 1947; Herbig, 1962; Lynden-Bell & Pringle, 1974). Most relevant to this Thesis, Kraus & Ireland (2012) have observed a bright point-like source of H_α emission from the transition-disk-hosting T Tau star LkCa 15 (Lick-Calcium-15) using aperture masking interferometry, interpreting the H_α flux as evidence of a directly accreting protoplanet. The Keplerian orbit of this source, together with several other sources, has been confirmed by adaptive optics imaging (Sallum et al., 2015b). Detection and characterization of systems such as LkCa 15 using JWST and other future telescopes is a major goal of the kernel phase method developed in Chapters 2 and 3 of this Thesis.

It has also been proposed that planets could be formed from the direct gravitational collapse of regions of a gravitationally-unstable disk (Cameron, 1978). This is now believed to be the formation mechanism of at least some brown dwarfs (Stamatellos et al., 2007), and is a proposed origin for the four directly-imaged planets orbiting HR 8799 (Dodson-Robinson et al., 2009; Boss, 2011) and other long-period planets. Kratter et al. (2010) determine that such planetary-mass objects can only have formed, at least as companions to A stars (including HR 8799, F0 class notwithstanding), as the low-mass tail of the distribution of stellar companions. With direct imaging, Vigan et al. (2017) have shown giants on wide orbits consistent with forming by gravitational instability to be extremely rare. Further advances in direct imaging technology will put much more stringent constraints on the prevalence of any planets formed by this mechanism.

1.1.2.1 Migration

A major feature in shaping the architecture of planetary systems is orbital migration caused by the gravitational coupling of giant planets to the gas disk (D'Angelo & Lubow, 2008; Kley & Nelson, 2012; Triaud, 2016). Disk-coupled migration mechanisms are often classified into two types. Type I migration is a linear process whereby planets embedded in disks with a temperature gradient increasing radially experience differential torque from Lindblad resonances which causes them to spiral inwards (Ward, 1986); outer and inner wakes are raised by the planet, and the outer wake generally exerts a stronger torque under most circumstances. Type II migration is a nonlinear process whereby sufficiently-massive ($\gtrsim$ 10 $M_\oplus$) protoplanets open up gaps in their disk, and migrate inwards coupled to disk, as its viscous evolution pulls material to the star (Lin & Papaloizou, 1985). These processes acting on the largest gas giant in a system can dominate the evolution of a multi-planet system's architecture, as other planets are entrained to resonances with the giant planet and one another (Kley & Nelson, 2012). Our understanding of planetary migration and the orbital dynamics of early planetary systems is as-yet incomplete, models are not yet well-constrained through evidence in observed planetary populations. Transit surveys in the *Kepler* and *K2* missions have been important for testing models of migration, uncovering many compact systems (Hands et al., 2014; Hands & Alexander, 2016; Izidoro et al., 2017) and a hot Jupiter in a system with two other planets (Becker et al., 2015) that pose challenges to existing migration theories.

1.2 Habitability and Life

If life exists elsewhere in the Universe, its discovery would be the ultimate victory of the Copernican revolution. After showing that the Earth was not the centre of the Solar System, we know that the Sun is itself a not-very-special star in a not-very-

special place in a Galaxy not atypical among its kind, one of billions. To show that intelligent life exists elsewhere would remove the final support to traditional ideas of humanity's importance. Exoplanetary science offers the prospect of answering a hierarchy of questions surrounding life in the cosmos, both in terms of the origin of life, and illuminating possibilities for humanity's future.

In observational terms with present technology, setting aside the search for extraterrestrial intelligence through its communications (SETI, e.g. Cocconi & Morrison, 1959; Shklovskii & Sagan, 1966; Tarter, 2001) or artefacts (Dyson, 1960; Kardashev, 1964; Bracewell, 1974; Wright et al., 2014), this means trying to find 'habitable' planets. Habitability is often discussed in terms of a 'habitable zone' (a term introduced by Huang, 1959), as consisting of a range of planetary orbits in which a planet's surface temperature is suitable for life. This is generally construed to mean the zone in which the planet could support liquid water at its surface, including potential greenhouse effects, though many quantitatively different definitions have been put forward (see Lineweaver & Chopra, 2012, for a review of these possibilities). The use of this term is strongly disputed (e.g. Tasker et al., 2017; Moore et al., 2017) on the grounds that it is misleading: for example, ignoring the greenhouse effect, by its equilibrium temperature Venus might be a habitable-zone planet, even though it is certainly inhospitable. Planets orbiting M dwarfs in temperate orbits may be tidally-locked, and their atmospheres may freeze out on the night side; such magnetically-active host stars also may irradiate their planets and strip their atmospheres (Shields et al., 2016). Terrestrial planets with atmospheres may not even be the only sort of habitable planet: Sagan & Salpeter (1976) conjectured that Jupiter (or a planet like it) may be able to support buoyant life in its atmosphere. In my view, there is not yet sufficient observational evidence nor is there theoretical basis for defining a habitable zone or determining exoplanets to be habitable, and we shall prefer the term 'temperate' instead.

1.3 Methods for Exoplanet Detection

The modern methods for exoplanet detection were established theoretically decades before they were implemented in practice. In a prescient paper, Struve (1952) proposed campaigns of spectroscopic and photometric measurements to detect respectively the reflex motion of a star as it orbits its common centre-of-mass with an orbiting planet (detecting its radial velocity by the Doppler effect), and to detect dips in stars' brightness as a planet passes in front as seen by an observer[5]. These remain the two main methods (hereafter referred to as the radial velocity or RV method, and the transit method) by which planets have been detected and characterized.

Early exoplanetary science proceeded from this more or less along the lines proposed by Struve. This work was to bear fruit only after decades of research, with the RV method leading to the first exoplanets. On the other hand, today the majority of known planets have been discovered by the transit method, which is ideally suited to deep surveys of hundreds of thousands of objects in a single field of the sky. There is also the option of directly imaging the planet, which has been possible only very recently. We shall begin by discussing the main points of the RV, transit, and direct imaging methods. We shall also discuss three other methods that are only now beginning to come into their own: astrometry, gravitational microlensing, and timing. Perryman (2011) provides an excellent overview of this topic, which we shall largely follow in describing methods in this Section, but we note that since this book was published, several missions, most notably *Kepler*, have revolutionized transits, timing and microlensing as methods.

[5]Perryman (2012) notes that Lardner (1875) suggests that transits will be observable as the dimming of stars, as the cause of what we know know to be eclipses in binary stars, and implies this is suggested by other authors.

1.3.1 Radial Velocity - Theory

The RV method relies on the Doppler effect (Doppler, 1842; Einstein, 1905), where an observer will detect a change in the wavelength of radiation emitted by a source which is moving with respect to the observer's rest frame. For light, in the regime where relative velocities are much smaller than the speed of light (which in the case of exoplanets around main sequence stars is generally true), the shift $\Delta\lambda$ in wavelength λ is simply proportional to the line-of-sight velocity: $\Delta\lambda/\lambda = v/c$. This means that light from a star receding from the observer is redshifted, while if the star is approaching, its light is blueshifted. A star orbiting its centre of mass with a planet in a circular orbit, viewed from within its plane of motion, has a radial velocity with a semi-amplitude

$$K = \left(\frac{2\pi G}{P}\right)^{1/3} \frac{M_p \sin i}{(M_* + M_p)^{2/3}} \frac{1}{(1-e^2)^{1/2}} \tag{1.1}$$

We see therefore that the radial velocity signal is approximately proportional to $M_p \sin i$ and inversely with the cube root of the orbital period, and RV is therefore most sensitive to close-in massive planets, and least sensitive to planets with long periods or low masses. The RV method cannot break the degeneracy between mass and inclination, and other methods are required to uniquely determine the mass of a planet. Crucially, for a planet to transit, its orbital inclination must be close to 90°, and therefore for transiting planets, $M_p \sim (M_p \sin i)_{RV}$.

1.3.2 The Transit Method - Theory

The idea proposed by Struve of a transit photometry survey was taken up by Rosenblatt (1971), who suggested differential broadband photometry between blue and red filters would be able to distinguish a planetary transit signal from other sources of noise[6]. While Borucki & Summers (1984) showed this to be a very substantial

[6]Frank Rosenblatt was a polymath, who is best-known for the Perceptron (Rosenblatt, 1958), an early artificial neural network which can be regarded as the precursor of modern deep learning

overstatement of the achievable signal-to-noise, and recommended simple broadband photometry instead, it is nevertheless interesting that the work prefigured the use of arrays of robotically-controlled small telescopes as transit survey instruments. Rosenblatt also calculated the probability of a planet transiting its star (radius R_*) given an orbital semi-major axis a and unknown orbital inclination as [7]

$$P_t \sim \frac{R_*}{a}. \tag{1.2}$$

Given these occurrence rates, Schneider et al. (1990) proposed searching 'about one hundred [M] dwarfs', noting that for a given planetary radius these would show the deepest transit depth and the possibility of habitability in closer orbits.

The discovery of the first transiting planets in 1999-2000 stimulated a range of authors to consider computationally-efficient ways to search for and model transits in stellar light curves. The most important of these was the Mandel & Agol (2002) set of analytic transit light curves, and a series expansion taking into account limb-darkening coefficients (Giménez, 2006). Analytic partial derivatives for these models are found by Pál (2008), which are helpful for rapid optimization. A transit has a fractional depth which is given by the planet-to-star radius ratio (Perryman, 2011),

$$\Delta F = \left(\frac{R_p}{R_*}\right)^2 \tag{1.3}$$

and the transit duration

$$t_T \approx 13\left(\frac{M_*}{M_\odot}\right)^{-1/2}\left(\frac{a}{1\text{ AU}}\right)^{1/2}\left(\frac{R_*}{R_\odot}\right) \text{ hours.} \tag{1.4}$$

techniques (Mackay, 2003; LeCun et al., 2015).

[7] In Rosenblatt (1971) there is an extra factor of 3/2 which appears to be arise from a mistake in the number of steradians in a sphere. Rosenblatt (1971) also uses an arctan function which can be expanded in a small angle approximation; as Koch et al. (2010) notes, this small angle approximation is not necessary and is exact by trigonometric identity.

These parameters, together with the details of the transit shape, for a small planet with a circular orbit of radius a encode the following independent parameters about a planet-star system (Seager & Mallén-Ornelas, 2003): the planet-to-star radius ratio as above; the impact parameter

$$b \equiv \frac{a}{R_*} \cos i = \left[\frac{(1 - \sqrt{\Delta F})^2 - (\sin^2(t_F \pi / P) / \sin^2(t_T \pi / P))(1 + \sqrt{\Delta F})^2}{1 - \sin^2(t_F \pi / P) / \sin^2(t_T \pi / P)} \right]^{1/2} ; \quad (1.5)$$

where t_F is the duration of the flat part of a transit[8], and t_T the total transit duration; consequently the orbital inclination

$$\cos i = \left(b \, \frac{R_*}{a} \right) \quad (1.6)$$

and the stellar density

$$\frac{\rho_*}{\rho_\odot} \equiv \frac{M_*/\mathrm{M}_\odot}{(R_*/\mathrm{R}_\odot)^3} = \left[\frac{4\pi^2}{P^2 G} \right] \left[\frac{(1 + \sqrt{\Delta F})^2 - b^2 (1 - \sin^2 \frac{t_T \pi}{P})}{\sin^2 \frac{t_T \pi}{P}} \right]^{3/2} \quad (1.7)$$

where P is the orbital period, and G Newton's gravitational constant. These results were generalized to account for eccentric orbits by Kipping (2008).

As noted in Section 1.3.1, because transit modelling enables a determination of the orbital inclination (which for transiting planets is always close to 90°) and planetary radius, by combining transit measurements with radial velocities we can determine a planet's mass and its density.

1.3.3 Direct Imaging and Adaptive Optics

Indirect methods of detecting and characterizing exoplanets by their influence on their parent star's light can only tell us so much: in detecting planets, indirect methods

[8] If a small planet passes completely in front of a star without limb darkening, the light curve while the planet is crossing the disk is flat.

are biased, as only edge-on systems transit, and RV and transits both preferentially detect short-period planets. Furthermore, transmission spectroscopy, achievable only for that fraction of planets which transit bright stars, is subject to stellar photon noise but only a small planetary signal (Kawahara et al., 2012). It is therefore desirable to try to directly detect light from an exoplanet, whether reflected starlight or thermal emission from the planet. In this Thesis, we will be concerned with how we can observe stars through the atmosphere at high angular resolution, accounting both for blurring due to atmospheric turbulence introducing phase noise, and also for the second-order effect of scintillation.

Unfortunately, stars are bright and planets are faint: there may be factors of $10^6 - 10^{10}$ in contrast between the star and the planet (Perryman, 2011), such that directly imaging a planet is like looking for a firefly next to a search-light. In addition to this contrast problem, optical distortions due to the turbulent atmosphere impose very strong limitations on the angular resolution and contrast that can be achieved from the ground. As a result, to detect faint companions to stars it has long been necessary either to observe with space telescopes, avoiding the atmosphere altogether, or to actively (with hardware, i.e. adaptive optics or AO) or passively (with interferometric calibration, or software in post-processing) compensate for atmospheric turbulence. The turbulent atmosphere is responsible for a process called 'seeing', causing a rapidly-changing PSF which averages out into a a smooth $\sim$ arcsecond-width halo (Texereau, 1962). In this case, all information at finer angular scales than the seeing limit is washed out and irrecoverable. By 'freezing the seeing' - recording images much faster than the $\sim$ ms timescale of atmospheric changes - it is possible to beat this limit and recover information from these speckles. AO continuously measures the wavefront and controls a deformable mirror to compensate for this (Babcock, 1953; Angel, 1994; Davies & Kasper, 2012), with the presence of non-common-path errors between the sensor and the deformable mirror branches imposing a major sensitivity

limitation (Ren et al., 2012).

There are two main methods of achieving the required resolution and contrast: coronagraphy, in which starlight is blocked in a small region around the star (typically requiring adaptive optics or a space telescope); and interferometry, in which starlight is interfered with itself to enhance angular resolution or achieve other desirable optical effects.

Coronagraphs are devices for suppressing starlight in order to observe planets otherwise obsecured by the diffracted or scattered light of their host star (though they were originally developed to observe the Sun's corona without waiting for eclipses: Lyot, 1930, 1939). Technology for coronagraphy advances rapidly: the review by Oppenheimer & Hinkley (2009) is a good introduction to early results, but for more recent astronomical results I suggest the review of the field by Bowler (2016). Major ground-based telescopes have recently received coronagraphs coupled to extreme adaptive optics (ExAO) systems, including Project 1640 at the Palomar Hale 200-Inch Telescope (Hinkley et al., 2008, 2011b); Magellan AO (MagAO; Close et al., 2012); the Subaru Coronagraphic Extreme AO (SCExAO; Martinache & Guyon, 2009; Currie et al., 2013); the Gemini Planet Imager (GPI; Macintosh et al., 2008, 2014); and the Spectro-Polarimetric High-contrast Exoplanet REsearch (SPHERE) project at the European Southern Observatory's Very Large Telescope (Beuzit et al., 2008; Vigan et al., 2016). Following the HST coronagraphic instrument, space-based coronagraphs are planned for JWST (Green et al., 2005; Krist et al., 2007, 2009) and WFIRST-AFTA (Green et al., 2012; Shaklan et al., 2013; Zhao, 2014; Noecker et al., 2016).

Meanwhile optical interferometry permits measurement of visibilities and 'closure phases' which are resistant to atmospheric noise (Baldwin et al., 1986), relying on the properties of diffraction to permit self-calibration. Interferometry can be performed combining light from well-separated telescopes, or on a single telescope with an aper-

ture mask or without one (speckle interferometry). Interferometry is not necessarily an alternative to adaptive optics, and the two can be combined together (Haniff & Wilson, 1994; Rajagopal et al., 2004; Tuthill et al., 2006). In this Thesis, I will discuss the method of kernel phase interferometry, a generalization of the idea of closure phase to arbitrary telescope pupils, using a linear model of phase errors. To achieve the small-error approximation required, it is necessary to either use adaptive optics or a space telescope to obtain the full advantage of kernel phase. In Section 1.7, I will discuss some of these ideas at greater length. In Chapter 2 I will derive a generalization of kernel phase to include amplitude errors (i.e. scintillation), and in Chapter 3, I will show that kernel phase interferometry can be used to enhance adaptive optics imaging from the ground.

Before moving on, we shall review some of the other possibilities for planet detection.

1.3.4 Astrometry

The orbital reflex motion of a star due to its planetary companion is not only observable as a Doppler shift: is is also directly observable as a spatial displacement of the star's position on the sky. A star traces out an ellipse on the sky with semi-major axis (Perryman, 2011)

$$a = \left(\frac{M_p}{M_*}\right)\left(\frac{a}{1\text{ AU}}\right)\left(\frac{1\text{ pc}}{d}\right)\text{ arcsec} \tag{1.8}$$

where d is the distance to the star in parsecs and other symbols have their usual meanings, as the star follows the same Keplerian orbit as the planet, scaled by its mass. It is possible to directly determine the mass of the planet, given the mass of the star and using Kepler's laws to solve for the semi-major axis from the period of the orbit. As we can see, the signal is of order $\sim$ mas or less for typical planet

masses ($\lesssim 0.01$ $M_\odot$) even around nearby stars, making this an exceedingly difficult method for planet detection. As discussed in Section 1.5, this was the method by which the first planet detection claims were made, though these are now considered to be in error. While only a handful of claims have been made in more recent years (Muterspaugh et al., 2010; Sahlmann et al., 2014), and none with very high precision, the ESA *Gaia* astrometric mission is expected to discover $\sim (2-7)\times 10^4$ such planets in the next several years, biased towards giant planets on longer orbits (Perryman et al., 2014).

1.3.5 Microlensing

Gravitational lensing is a general-relativistic effect, whereby light is deflected by the gravitational influence of matter between source and observer (Schwarzschild, 1916; Eddington, 1919; Dyson et al., 1920; Chwolson, 1924; Einstein, 1936). The microlensing regime is a form of strong lensing, in which lensed images of the source are not resolved by the telescope, and instead we simply detect photometrically the total magnification due to the lensing (Liebes, 1964; Paczynski, 1986). This can occur if by chance alignment a nearby star passes between an observer and a more distant star, yielding a rise and fall in the brightness of the distant object by potentially many magnitudes as the observer passes through a caustic (a region of intersecting lensed rays).

While this typically occurs on a timescale of weeks, the presence of a planet orbiting the lensing star adds a very short-timescale spike to this light curve, but with similar amplitude, by modifying the shape of the pattern of caustics (Liebes, 1964). This means that high precision, high-time-resolution photometry of such an event can be used to detect extrasolar planets. Very short duration microlensing events have been detected with no long-duration component. From the statistics of ten of these, Sumi et al. (2011) have inferred a large population of planets either very distant from

or not bound to a stellar host, potentially outnumbering stars themselves, Clanton & Gaudi (2017) have shown using constraints from microlensing, RV and direct imaging that there are approximately $\sim 1.2-1.4$ free-floating planetary-mass objects per star, which may have formed around stars as planets or brown dwarfs but ejected during the dynamical evolution of the planetary system (e.g. Lissauer, 1987) or in close encounters with other stars (Laughlin & Adams, 2000).

1.3.6 Timing: Transits, Eclipses, Pulsars and Pulsating Stars

It is also possible to detect planets by timing any periodic stellar process due to the finite speed of light. As a star orbits the centre of mass with its unseen companion, it induces a light travel time effect (LTTE, also known as the Rømer delay[9]), so that events when the source is further away seem delayed relative to when the system is closer, causing deviations from a periodic ephemeris as seen by an observer. This method was first used to detect the pulsar planets, whereby extremely precise measurements of deviations in the timing of a millisecond pulsar were used to infer the presence of several planetary-mass companions (the first confirmed exoplanets; Wolszczan & Frail, 1992, see Section 1.5 for a fuller discussion).

The Rømer delay is typically the dominant effect in eclipsing binary (EB) systems, where components of a binary system pass in front of one another as seen by an observer. Eclipse timing variations (ETVs) relative to a periodic ephemeris ($O-C$ variations, **o**bserved minus **c**alculated eclipse times) can reveal the presence of a third body, from hierarchical triple systems (close binaries with a distant, lower-mass companion, e.g. Gies et al., 2012) down to planetary-mass bodies.

The mutual gravitational influence of planets on one another can also introduce transit timing variations (TTVs). Holman & Murray (2005) and Agol et al. (2005)

[9]This was the method by which Danish astronomer Ole Rømer (1644-1710) first discovered that the speed of light is finite, by observing deviations from periodicity in the orbits of the moons of Jupiter, which were late relative to a periodic ephemeris when Jupiter was at its maximum extent from Earth, and early when it was at its closest approach.

independently and contemporaneously determined that TTVs of giant planets could be used to infer the presence of Earth-mass planets in the same system. As well as the Rømer delay, three-body perturbations from Keplerian orbits are particularly relevant in this case, with TTV signals being especially strong if the planets' orbits are in a mean-motion resonance, i.e. when the ratio of their orbital periods is a ratio of small integers. Modelling TTVs can also yield the mass, relative phase and eccentricity of these objects (including proving that they are of planetary and not stellar mass), which in cases where the host star is too faint for effective RV followup may be the only effective method for this.

The TTV method has proven to be especially effective with the precise, long-duration photometry available with *Kepler*, yielding one of the first multi-planet *Kepler* systems (Holman et al., 2010), precise densities and eccentricities of multi-planet system components (Hadden & Lithwick, 2014), non-transiting planets in systems with transiting components (Nesvorný et al., 2012), and the improvement and subsequent application of these methods to a wide variety of *Kepler* planetary systems (e.g. the Transit Timing Observations from *Kepler* project: Ford et al., 2011, 2012a; Steffen et al., 2012a; Fabrycky et al., 2012; Ford et al., 2012b; Steffen et al., 2012b, 2013; Mazeh et al., 2013).

Stellar oscillations offer another clock we can use to find exoplanets by timing. Silvotti et al. (2007) used the Rømer delay method to detect a giant ($M \sin i = 3M_J$) planet orbiting V391 Pegasi, a pulsating, core-helium-burning star, with the Rømer delay manifesting as periodic phase modulations of its pulsations. Moving to the main sequence, Murphy et al. (2016) have discovered a planet in an 840-day orbit around an A star, KIC 7917485, a δ Scuti variable star whose oscillations show a phase modulation consistent with the star having a planetary companion.

1.4 Transmission Spectroscopy

Beyond simply discovering planets, we want to know about individual planets in detail: how did they form? What is their composition? Are they rocky or gaseous? Are they habitable – or indeed, inhabited? In general, these questions can only be answered in the forseeable future by obtaining spectra of their atmospheres. While direct imaging spectroscopy is an exciting prospect for the future,it is at present applicable only to a handful of planets. On the other hand, it is also possible to do exoplanet *transmission* spectroscopy, by taking a time series of spectra during a planetary transit. At wavelengths where the atmosphere is more opaque, the planetary radius will appear larger, and therefore precise differential measurements of the transit depth encode a transmission spectrum of the planet's atmosphere. Several reviews of this nascent field are already available, for example Seager & Deming (2010), Tinetti et al. (2013), and Burrows (2014a), but with such a rapidly-changing field, these are best used as reference for earlier work.

The first observation of an exoplanetary atmosphere was the detection of the sodium doublet in transmission spectroscopy of HD 209458 (Charbonneau et al., 2002), which had been predicted by Seager & Sasselov (2000, see Chapter 1.5.2). Detecting near-infrared exoplanetary atmospheres has proven a much harder task. HST and ground-based observations of exoplanet transits initially showed some featureless spectra (e.g. Bean et al., 2010), while others appeared to show molecular features (e.g., non-exhaustively, Tinetti et al., 2007; Swain et al., 2008, 2009a,b, 2010). In some of this early work, difficulties with systematic effects introduced correlated noise which could mimic spurious spectral features (as shown for instance by Gibson et al., 2011, 2012; Gibson, 2014), which can be ameliorated by using Gaussian Processes or wavelets to model these systematics. This has led to more confident detections of molecular and atomic features (Sing et al., 2013, 2015; Wakeford et al., 2016), inferring the blue optical colour of HD 189733b from the Rayleigh scattering

slope of its spectrum (Evans et al., 2013), while also finding many planets to have featureless spectra potentially indicative of clouds (e.g. Gibson et al., 2013; Evans et al., 2015). In the view of Burrows (2014b), this progression of refinements in observational technique has been valuable 'to train a new generation of scientists who, by rapid trial and error, are fast establishing a solid future foundation for a robust science of exoplanets'.

It is likely to be possible with near-future instruments such as the *James Webb Space Telescope* (JWST) and Extremely Large Telescopes (ELTs) to detect spectroscopic features unique to planets actually hosting life (we shall refer to these as 'biosignatures' in the following). Lovelock (1965) suggested that persistent chemical disequilibrium is a signature of life; this might be indicated by the simultaneous spectroscopic detection of oxygen and reduced gases such as methane or molecular hydrogen, or similar disequilibria between molecules that are not present in Earth's atmosphere but may be products of other biologies (Seager et al., 2016). It may also be possible to detect living organisms directly from the spectral effect of widespread photosynthetic vegetation analogues (Wolstencroft & Raven, 2002). Photosynthetic organisms on Earth display a 'red edge' spectroscopic feature, such that they are much more transmissive and reflective to wavelengths longer than ~ 700 nm than to shorter wavelengths, a feature which has been detected in narrowband imagery of the Earth by the *Galileo* spacecraft (Sagan et al., 1993) and in reflected Earthshine from the Moon (Seager et al., 2005).

The final years of the HST and the launch of JWST will dramatically expand this field. With a re-analysis of HST and *Spitzer* data for 10 hot Jupiters, Sing et al. (2016) and Barstow et al. (2017) have determined that there exist a continuum of atmospheric types, from featureless cloudy spectra to clear skies with detectable atmospheric components. An HST survey of 20 more exoplanets is underway with a range of masses and insolations, the Panchromatic Comparative Exoplanetary Treasury

Program, aiming to complete a catalogue of optical and near-infrared atmospheric spectra to compare to future NIR and longer-wavelength JWST observations of the same targets. Other than JWST, there are plans for dedicated transmission spectroscopy missions: TWINKLE (Tessenyi et al., 2016), a small mission proposed with a very short timeline and a spectral range from 0.5 to 5 μm, for launch in 2019; and the ESA M4 (medium-class) mission proposal ARIEL (Atmospheric Remote sensing Infrared Exoplanet Large survey; Puig et al., 2016; Tinetti et al., 2016).

It is in view of missions such as these that I am most excited about the work on bright star photometry presented in Chapters 5 and 6. The new methods used in this thesis, smear photometry and halo photometry, will enable *Kepler*, and later TESS, to explore naked-eye stars for ideal worlds for transmission spectroscopy, which has not previously been possible with nearly the same precision or completeness with existing surveys.

1.5 A Brief History of Exoplanet Discoveries

The credit for the discovery of the first exoplanet is difficult to uniquely assign. In the following, we will summarize the early history of exoplanet detections; an interested reader looking for a more detailed discussion than is available here will find Perryman (2012) enlightening.

This area of study suffered from some false starts. Early claims were made for invisible substellar companions to nearby stars from astrometric measurements, in particular 61 Cygni (Strand, 1943) and 70 Oph (Jacob, 1855; See, 1895), rejected by Heintz (1978); and a number of planets orbiting Barnard's star, the next-closest star to our Solar System after the α Centauri system [10] (van de Kamp, 1963, 1969b,a, 1975, 1982), which are rejected on their own terms and on the basis of modern obsevations

[10]Discovered by Barnard (1916) and the subject of a Starter for Ten taken by an extremely nervous Balliol Pope against Robinson College, Cambridge.

(Bartlett, 2007; Gatewood & Eichhorn, 1973; Benedict et al., 1999; Choi et al., 2013).

Despite the efforts of RV observers, the first extrasolar planetary-mass objects to be discovered were exotica quite unlike the planets found in our Solar System: the pulsar planets (Wolszczan, 2012). Wolszczan & Frail (1992) found two Earth-mass planets orbiting the millisecond pulsar PSR1257+12, and confirmed these by measuring their resonant gravitational interaction, together with an additional, lunar-mass object (Wolszczan, 1994). Other evidence for exoplanets has existed since as early as 1917, in the form of heavy-element pollution of white dwarf atmospheres (Zuckerman, 2015), in particular van Maanen 2 (van Maanen, 1917, 1919). This is now recognized as evidence for the accretion of material from tidally disrupted planets (Barstow et al., 2014), such as the *K2* disintegrating minor planet transiting WD 11451+017 (Vanderburg et al., 2015).

Setting aside these planets around stellar remnants, evidence of planetary-mass objects orbiting stars proper was still hotly contested until the late 1990's. Some we now believe to be *bona fide* exoplanets were discovered by the RV method and published in 1988-9, but were not widely accepted as planets at the time (Walker, 2012), including γ Cephei b and ϵ Eridani b (Campbell et al., 1988), and β Gem b (HD 62509; Hatzes & Cochran, 1993; Hatzes et al., 2006; Han et al., 2008). The discovery of an unseen companion to HD 114762 by Latham et al. (1989), confirmed by Cochran et al. (1991), was the first planet found via the radial velocity method to be explicitly put forward as such by the authors at the time (Latham, 2012), though its high $M \sin i$ of $\sim 11.2 M_J$ led Cochran et al. (1991) to state that 'we cannot rigorously conclude that the companion is either stellar or substellar in mass'. This degeneracy still holds, as it does not transit its host star (Robinson et al., 1990; Kane et al., 2011).

1.5.1 The First Exoplanet Discoveries

The breakthrough for RV planet searches came with the discovery of 51 Pegasi b by Mayor & Queloz (1995). With the ELODIE spectrograph at the Observatoire de Haute Provence (Baranne et al., 1996), Mayor & Queloz began a survey in April 1994 of 142 solar-type stars; an excellent review of this campaign and its consequences has been written by Mayor et al. (2014). They found a planet in a 4.2 d orbit with a minimum mass of $\sim 0.5 M_J$. Such a 'hot Jupiter' was widely unexpected, with giant planets generally thought to form beyond the 'ice line' where volatiles such as water and CO_2 freeze out. So surprising was this result that Mayor & Queloz waited a year and took further observations in the next available season, and sought additional data for confirmation from the Lick team led by Marcy. Lin et al. (1996), drawing upon earlier work by Goldreich & Tremaine (1980), showed that this hypothesis can nevertheless be supported if 51 Peg b migrated from a formation zone much further out to its present location, a paradigm for hot Jupiter formation which is still widely adhered to (Triaud, 2016).

This was to be the first of many RV planet discoveries. Subsequently, RV surveys spearheaded by the Lick Planet Search group (Fischer et al., 2014) discovered companions to 47 Ursae Majoris (Butler & Marcy, 1996), the first planet in an eccentric orbit 70 Virginis (Marcy & Butler, 1996), more hot Jupiters (Butler et al., 1997), and the first multiple system, consisting of planets around υ Andromedae (Butler et al., 1999). It soon became apparent that hot Jupiters were comparatively rare (only $\sim 1.2\%$ of stars appear to host a hot Jupiter: Wright et al., 2012), and that the majority of giant planets existed, as expected, on longer-period orbits (Marcy & Butler, 2000; Butler et al., 2006).

1.5.2 First Transits

The next major leap forward in exoplanetary science was the discovery of the transits of HD 209458, simultaneously made by Henry et al. (1999, 2000), and Charbonneau et al. (2000)[11], using an RV ephemeris to determine the expected time of transit. Charbonneau et al. (2002) subsequently detected the atmosphere of this planet, using spectroscopy during transit to show a greater transit depth around the sodium D doublet as predicted by Seager & Sasselov (2000). This was soon followed up by the detection of an extended upper atmosphere consisting of neutral hydrogen Lyman α absorption (Vidal-Madjar et al., 2003).

It would not be until 2003 that the next transiting planet would be discovered: OGLE-TR-56 was first found via OGLE (Udalski et al., 2002) as a by-product of its microlensing survey (see Section 1.3.5). This would be followed shortly by OGLE-TR-3 (Dreizler et al., 2003).

Several dedicated ground-based transit surveys were initiated in the early 2000's, including the Hungarian Automated Telescope Network (HATNet, Bakos et al., 2004), the Wide Angle Search for Planets (WASP, later SuperWASP; Pollacco et al., 2006); the University of New South Wales (UNSW) Planet Search (Hidas et al., 2005), EXPLORE (Mallén-Ornelas et al., 2003); Transiting Planets and Planetesimals Small Telescope–South (TRAPPIST, Jehin et al., 2011); MEarth (Berta et al., 2012); and the Next Generation Transit Survey (NGTS, Chazelas et al., 2012). Due to atmospheric conditions, ground-based photometry can typically achieve a photometric precision of only $\sim$ 1%, approaching 0.1% for more recent surveys such as NGTS or SuperWASP. As a consequence, Gillon et al. (2005) note that while ground-based surveys are an efficient approach for detecting giant planets across the sky, due to their low cost, deep exposures and wide accessible fields of view, 'as far as telluric planets in the Habitable Zone are concerned, space-based surveys are the only viable

[11] Remarkably, undertaken from a 10 cm telescope in a carpark!

option.'

As a shortcut to finding habitable planets, MEarth and TRAPPIST have been especially dedicated to looking for planets transiting nearby M dwarf stars. Owing to the small stellar diameters, transits of Earth-sized planets are especially deep around these stars (up to $\sim 10\%$) compared to around Solar-like stars. In addition to this, their low temperature and luminosity mean that planets in easily-observable short-period orbits ($\sim$ days) can nevertheless have Earth-like temperatures. Most notably, the TRAPPIST-1 system (Gillon et al., 2016) has been shown to host seven temperate super-Earths (Gillon et al., 2017). These are excellent targets for characterization with transit spectroscopy, for example to detect ozone (Barstow & Irwin, 2016). Nevertheless, I suggest that it is valuable to study planets across the whole main sequence, as they may differ from M dwarf planets, and while the transit depths are smaller, nearby FGK stars (for instance) are orders of magnitude brighter than similarly close M dwarfs, and therefore permit very high signal to noise measurements even though the signals themselves may be smaller.

1.6 Space Transit Surveys

The main topic of the latter half of this Thesis will be space-based transit photometry with the *Kepler Space Telescope*, and subsequent planned space missions such as TESS, CHEOPS and PLATO. I will both describe the results of a transit search in *K2* of a full two Campaigns (Chapter 4), and then two methods for obtaining very high precision photometry of saturated stars (Chapters 5 and 6). While we do not detect planets in the smll pilot study of bright stars, we do detect stellar oscillations, and achieve the precision required to detect planets in future larger studies. As such, in this Section, we will discuss the heritage of the CoRoT mission, and introduce *Kepler*, leaving ground-based missions to one side.

The first major space instrument to seacrch for planetary transits was the Convection, ROtation and Transits (CoRoT) mission, a 27 cm telescope launched in December, 2006 (Baglin, 2003). Over five years, CoRoT observed 163,664 stars for an average duration of 78 days each, discovering 530 transiting planet candidates and with an inferred false positive rate of $\sim 73\%$ (Moutou et al., 2013). One early discovery was the first brown dwarf companion to a star to have its mass and radius measured, making CoRoT-Exo-3b the 'first secure inhabitant of the brown-dwarf desert' (Deleuil et al., 2008). Most importantly, it was used to discover CoRoT-7b, the first transiting super-Earth with a measured radius (Léger et al., 2009), shown to be in a multi-planet system (Queloz et al., 2009; Faria et al., 2016). Its density has been shown to be consistent with a rocky composition over a decade of observations (Pont et al., 2011; Haywood et al., 2014; Barros et al., 2014). While on the timescales of exoplanet transits ($\sim$ hours to days) CoRoT achieves photometric precision close to its design specification (Aigrain et al., 2009), nevertheless its performance was poor compared to the subsequent *Kepler* mission (Hatzes, 2014), and the discovery of large numbers of transiting rocky planets, with longer periods, would wait until the launch of *Kepler* in 2009.

Although the discovery of transits of HD 209458 was a major breakthrough, and ground-based transit surveys achieved remarkable successes in the subsequent decade, the *Kepler* mission is undoubtedly the most significant transit survey ever conducted. It has discovered orders of magnitude more planets than any other survey (by the transit method or any other), producing a deluge of publications both in exoplanets and in astrophysics more broadly. Launched on 6 March 2009 with an 0.95 m diameter aperture and a 1.4 m diameter $f/1$ primary mirror and 42 CCD detectors, this space telescope surveyed a 115 square degree field in the constellations of Cygnus, Lyra and Draco (Borucki et al., 2010). True to its original mission concept, 'to Find Earth-Sized Planets around Solar like Stars' (Borucki et al., 1994), *Kepler* was built to

satisfy three science requirements (as stated in Koch et al., 2010):

1. A mission length of at least three years.
2. To observe at least one hundred thousand solar-like stars with ~ 5000 having $V \geq 12$.
3. To reliably detect transits of 84 ppm in 6.5 hr (half of a central transit duration for an Earth–Sun analog).

Kepler was the result of decades of planning, from before even the discovery of 51 Peg, and it is worth stepping back to examine its history prior to launch, related by Borucki et al. (2009).

Studies by Borucki & Summers (1984) and Borucki et al. (1985)[12] had built on the work of Rosenblatt (1971), suggesting that monitoring 10^4 stars with an optical fibre bundle coupled to a photometric detector array might be possible. Borucki et al. (1988, 1989) conducted unsuccessful tests of such a photometer, although Borucki & Koch (1994) still went so far as to discuss fibre options and to suggest robotically positioned detectors and multi-aperture spectrographs operated by actuator systems. The final architecture that was to be used was an array of detectors onto which a defocused image of the star field is projected.

Borucki and colleagues proposed the FRequency of Earth-Sized Inner Planets (FRESIP) mission for NASA missions in 1992, where it was rejected due to lack of confidence in its proposed silicon detectors, and again in 1994 (Borucki et al., 1994) as

[12]It is interesting to note that Borucki et al. (1985) suggested that

> The observation of nonradial oscillations which will also be a by-product of precise photometry promises to be an important method of probing the dynamics and structure of stellar interiors... With a sufficiently large number of observations, it might be possible to detect p-mode oscillations in some of the brighter stars, particularly those stars that might have amplitudes higher than those observed on the Sun.

This prediction was to be spectacularly vindicated. Of papers using *Kepler* data, as of 4 January 2017, official classifications (Barclay et al., 2016) find 980 (47%) to be primarily about exoplanets, and 1089 (53%) other areas of astrophysics, of which I determine 394 are primarily related to asteroseismology, i.e. having titles containing any one of all or part of 'oscillation', 'asteroseismology','pulsation','Blazhko','modes' or 'gravity'.

a Discovery-class mission, with CCD photometers, where it was again rejected. The FRESIP concept was *again* rejected in 1996, under the new name *Kepler* (Borucki et al., 1997), with the major change from 1994 being the proposal of an Earth-trailing Solar orbit to reduce the cost of the propulsion system, where previously it had been scheduled for a Lagrange point orbit where more regular station-keeping is required (Borucki et al., 2009). Multiplex photometry on a single CCD array had not previously been performed, and as such, a sufficient technology readiness level had to be achieved before the *Kepler* mission could be reconsidered. Using the Vulcan Photometer, Borucki et al. (1999, 2001) performed experiments at Lick Observatory, monitoring first 6000 stars simultaneously in a Cygnus field for transits, and achieving sufficient precision to detect many eclipsing binaries, and also the then-recently discovered transiting planet HD 209458. The *Kepler* Test Bed at NASA Ames (Koch et al., 1999) similarly demonstrated key components of the planned space mission, including a simulation of spacecraft jitter. Using this testbed, Jenkins et al. (2000) demonstrate algorithms for aperture photometry on a simulated starfield: in work that would foreshadow the method of halo photometry (discussed in Chapter 6 of this Thesis), Jenkins also considered on-board photometry methods using a weighted linear combination of pixels[13].

Following these successful demonstrations of key *Kepler* technologies, it was again proposed as a Discovery Mission at the NASA proposal round in 2000, and accepted in 2001 as the tenth Discovery Mission.

[13]I was unaware of this work at the time of developing the halo method, and it was brought to my attention in a very stimulating discussion with Jenkins at the TESS Asteroseismology Science Consortium (TASC) Working Group Zero (Photometry) meeting in Birmingham, 31 October–2 November 2016. Jenkins made the interesting comment that this method was demonstrated to his satisfaction in the lab, but was left out of the final *Kepler* design on Borucki's instructions over concerns that a novel photometric technique would hurt a proposal already rejected several times. I understand that elaborations beyond the static pixel scheme were also considered but not published.

1.6.1 *Kepler*: Selected Scientific Results

Kepler has discovered the majority of known exoplanet candidates, with 7056 *Kepler* Objects of Interest identified over its 47-month nominal mission, of which 1935 are validated as likely true exoplanets (Morton et al., 2016). *Kepler* has a low false positive rate of $\sim$ 10% for small planets (Morton & Johnson, 2011), and a very low (of order 2%) false positive rate for multi-planet systems (Lissauer et al., 2012, 2014b). While the majority of *Kepler* planets are too faint to efficiently follow up with spectroscopy, it is possible to photometrically validate them as likely planets rather than as false positives by modelling the shapes and prior probabilities of the transit light curve as opposed to eclipsing binary blends (Torres et al., 2011). Many of *Kepler*'s planet discoveries were the first of their kind, exploring new parameter space with *Kepler*'s exquisite precision: some of these are admirably reviewed by Lissauer et al. (2014a), though *Kepler* results have come so quickly that there have been numerous subsequent milestones. *Kepler* offered the first direct evidence of a circumbinary planet (*Kepler*-16b, Doyle et al., 2011); its first rocky planet was the smallest transiting exoplanet discovered until that point (*Kepler*-10b, Batalha et al., 2011); it found the extremely-compact six-planet system *Kepler*-11 (Lissauer et al., 2011); the first sub-Earth radius (*Kepler*-20e, Fressin et al., 2012; Gautier et al., 2012) and sub-Mercury radius planets (e.g. *Kepler*-37b, Barclay et al., 2013); the evaporating planet candidates KIC 12557548 (Rappaport et al., 2012) and KOI-2700b (Rappaport et al., 2014); the mysterious deep and irregular occultations of "Boyajian's Star" KIC 8462852 (Boyajian et al., 2016); multiple planets transiting a former red giant B subdwarf star, which would have been engulfed by the giant (Charpinet et al., 2011); and later in the mission, it detected the first rocky planet in an Earth-like orbit around a Sun-like star (the 1.6 $R_\oplus$ super-Earth *Kepler*-452b, Jenkins et al., 2015), achieving the *Kepler* mission's core science goal "to Find Earth-Sized Planets around Solar like Stars" (Borucki et al., 1994).

The planets discovered by *Kepler* begin to constrain the prevalence of Earth-like planets, most often described in terms of $\eta_\oplus$ or η_E (eta-Earth), the mean number of Earth-like planets per star. There are differing definitions of this, of which the most natural is (Lissauer et al., 2014a)

$$\eta_\oplus \equiv f(1R_\oplus, 1 \text{ year}) \tag{1.9}$$

where $f(R_p, P)d\ln R_p d\ln P$ is the probability for a star to host a planet in an infinitesimal range in $\ln R_p$ and $\ln P$ at radius and period R_p and P. Quantitatively addressing this question is of interest to the general public, for formation theory, and also helps us make decisions on future space missions, based on expected yields of planets (e.g. Léger et al., 2015).

By modelling the pipeline (including detrending and planet search), with injection tests to determine the associated false positive rate, several groups have estimated $\eta_\oplus$ with wide variation in the results (background and early work on this issue is well-summarized by Batalha, 2014, but considerable methodological advances have been made since that publication). Fressin et al. (2013) do not attempt to determine $\eta_\oplus$, but do determine frequencies of planets with a range of radii and periods, finding that $16.5 \pm 3.6\%$ of FGK stars host planets with radii between 0.8 and $1.25R_\oplus$ with periods shorter than 85 d. After some attempts based on early data without characterizing the false positive rate (Catanzarite & Shao, 2011; Traub, 2012; Dong & Zhu, 2013), Petigura et al. (2013) obtain a high estimate of $\eta_\oplus = 11 \pm 4\%$ by fitting occurrence rates in 23 bins in orbital period and planet size. Silburt et al. (2015) infer a $6.4^{+3.4}_{-1.1}$ occurrence rate of $1-2R_\oplus$, $0.99-1.7$AU planets arond solar-like stars, also reasonably high and as the authors note, consistent with the Petigura et al. (2013) analysis. On the other hand, using Gaussian Process models to constrain the distribution of occurrence rates in their grid of bins, Foreman-Mackey et al. (2014)

report a much more conservative figure for $\eta_\oplus$, of about 2% with large uncertainties. Similar population inference approaches have been taken by Dressing & Charbonneau (2015) to estimate the frequency of planets around M dwarfs, finding an occurrence rate of $0.57^{+0.06}_{-0.05}$ planets with radii $1 - 1.5R_\oplus$ and $0.51^{+0.07}_{-0.06}$ with radii $1.5 - 2R_\oplus$ per M dwarf, of which a large fraction are temperate. While estimates differ by orders of magnitude, it is nevertheless clear that planets are not at all uncommon among the stellar populations so far surveyed.

1.6.2 *K2*

It is surprising to note that wheels are essential for changing and maintaining a spacecraft's orientation. Firing thrusters costs fuel and can result in large excursions in pointing, and it is usually preferable to reorient a spacecraft by spinning internal flywheels up or down to change its main body's angular momentum. *Kepler* was launched with four such reaction wheels: one for each dimension of space, and a spare in case of failure. This redundancy was important when on July 14, 2012, one of the reaction wheels failed; the nominal *Kepler* mission was able to continue using only three wheels until May 11, 2013, when another wheel failed. Ball Aerospace engineer Doug Wiemer suggested observing in the ecliptic plane, where it was possible to orient the spacecraft such that solar radiation pressure on its solar panels would be balanced on both sides and minimally disturb its pointing (in Zastrow, 2014, we see a contemporary account of this news story, which is unfortunately not described in detail in the peer-reviewed literature). This proposal was accepted, and the *Kepler* satellite now continues as the *K2* Mission. (For clarity, *Kepler* observations in its original configuration are usually referred to as the 'nominal *Kepler* mission' to distinguish this from more general reference to the satellite and its operations).

Because this ingenious configuration is an unstable equilibrium, it is necessary to fire thrusters every $\sim$ 6 h to keep the telescope on-target, and to change fields

frequently in order to stay pointed roughly perpendicular to the Sun where it is best-balanced and where photometry is minimally contaminated by background sunlight. Accordingly, *K2*'s observing sequence consists of a succession of $\sim$ 70–80 day 'Campaigns', each targeting a field in the Ecliptic plane (Howell et al., 2014). As a result of the short Campaigns, *K2* is unable to detect planets with periods as long as were accessible with *Kepler*. On the other hand, by covering many different fields it is able to search for short-period planets around a larger number of bright stars and to probe a wider range of environments.

A consequence of the 6 hr thruster firings is that the star field moves $\sim$ 1 pixel back-and-forth across the detector with the firing sequence, which introduces severe systematics due to the stellar images moving out of the photometric aperture, and due to inter- and intra-pixel sensitivity variations in the detector (Bryson et al., 2010; Hogg et al., 2013). Nevertheless, several teams have developed software to 'detrend' *K2* light curves and remove this saw-tooth-like systematic (e.g. Vanderburg & Johnson, 2014a; Aigrain et al., 2015; Armstrong et al., 2015; Lund et al., 2015; Luger et al., 2016), including the package used in this Thesis (K2SC Aigrain, Parviainen & Pope, 2016), which uses Gaussian Processes (GPs, developed originally for mining surveys by Krige, 1951; Matheron, 1963) to non-parametrically model systematics as a function of spacecraft pointing, achieving photometric precision comparable to that of the nominal *Kepler* Mission. In Chapter 4 I will discuss this model, and present results of a planet search using the light curves obtained, finding 145 new planet candidates in *K2* Campaigns 5 and 6.

K2 has diverse science goals (see Howell et al. 2014 for a more detailed discussion). It vastly increases upon the number of bright Sun-like stars and nearby late-type stars which were included in the *Kepler* prime mission. Short-period transiting planets discovered around these stars will be particularly good targets for future atmosphere studies. *K2* is also advancing stellar astrophysics through the study of

pulsating stars, eclipsing binaries and transients, as well as observing extragalactic and Solar System targets. By surveying fields located in or close to the Ecliptic plane, *K2* observations cover several nearby, young open clusters and associations, such as ρ Ophiuchi (ρ Oph) and Upper Scorpius (Upper Sco) (Campaign 2), the Pleiades (Campaign 4), Praesepe (or the Beehive Cluster) (Campaign 5), and Taurus and the Hyades (Campaigns 4 & 13). *K2* observations of these clusters are opening a new window on young star variability, including accretion-related variability, stellar activity and rotation, and pulsations, but enable also the discovery and characterisation of young eclipsing binaries and transiting planets. The latter are particularly important systems for studying the early stages of planetary evolution.

K2 has already led to noteworthy planetary transit discoveries, some of the most notable being: disintegrating rocky planetesimals transiting a white dwarf (Vanderburg et al., 2015) and an M-dwarf (Sanchis-Ojeda et al., 2015); two unexpected additional planets in the hot Jupiter-hosting system WASP-47 (Becker et al., 2015); planetary companions to field M-dwarfs (Crossfield et al., 2015; Schlieder et al., 2016; Hirano et al., 2016a); transiting planets orbiting young stars in the Hyades and Upper Sco (Mann et al., 2016a,b); and many more individual planets. Several groups have published catalogues of *K2* planet candidates, including Foreman-Mackey et al. (2015b) (Campaign 1); Vanderburg et al. (2016) (Campaigns 0 to 3); Crossfield et al. (2016) (Campaigns 0 to 4); and Adams et al. (2016) (Campaigns 0 to 5). In addition to this, Foreman-Mackey et al. (2015a) and Osborn et al. (2016a) have presented systematic searches for single-transit events in *K2*, identifying long-period planet candidates.

A major component of this Thesis will be about the *K2* mission, including a transiting planet catalogue (Chapter 4); a method to obtain precise photometry of stars that were not conventionally observed due to saturation (Chapter 5); and another method for photometry of very bright stars, using their scattered light halo, applied

to the seven brightest members of the Pleiades (Chapter 6).

1.7 Interferometry

Some of the most precise and accurate measurements in astronomy and other sciences rely on interferometry, and I believe an interferometric perspective is the best way to understand high-resolution astronomical imaging, whether with one telescope or several. I take interferometry to mean any method explicitly using the wave nature of light to perform a measurement; because diffraction through the turbulent atmosphere imposes the main limitation on our ability to image astrophysical objects from the ground, interferometry is the natural approach to take in pushing to high resolution and high signal to noise. In particular, a main topic of this thesis is kernel phase interferometry, an approach to self-calibrating small optical aberrations to enhance imaging at and beyond the diffraction limit, applicable to arbitrary telescope apertures without any additional hardware. Kernel phase forms the subject of Chapters 2 and 3: Chapter 2 in particular is a theoretical discussion of kernel phase interferometry, while in Chapter 3 we present the first demonstration of kernel phase with ground-based adaptive optics. We will therefore introduce in the following Section some of the key ideas of Fourier optics and adaptive optics and review the history of interferometry. In general, Labeyrie et al. (2006) offers an excellent introduction to these ideas.

While light had been considered as a particle by the ancient Greeks and by Newton (1730), Huygens (1678) proposed a quantitative model of light as a wave, and a principle for calculating its effects. Huygens' Principle[14] states that the diffraction of light through an aperture can be thought of as the superposition of wavelets emitted

[14]Kirchhoff (1882) shows that this model is satisfactory in a paraxial approximation, with an additional factor $(1 - \cos\chi)$, where $\chi \equiv \pi - \mathbf{r} \cdot \mathbf{s}$, and $\mathbf{r}$ and $\mathbf{s}$ are respectively the vectors from the source to wavefront, and the wavefront to the receiver. In practice, this is not relevant to astronomical optics, where a star can be taken to be at infinity.

from every point on the incident wavefront. From this and linearity, we can construct all of the relevant optics we need for this Thesis. Consider Young's double-slit experiment (Young, 1804), where monochromatic light with wavelength λ is shone through a pair of narrow slits separated by a distance d. We want to calculate the far-field intensity distribution from such a set-up, for example on a distant screen.

In angular coordinates, for a sufficiently far field, we see that the dominant path difference between the waves emitted between the two slits is $d \sin\theta$, so that the phase difference is $d \sin\theta/\lambda$. Let us assume that the light is coherent, i.e. that it everywhere has a well-defined and stable phase. In the coherent case, the superposition of two waves is the sum of their phasors. If the apertures are equally transmissive so that the transmitted waves have amplitude A, then by taking this phase difference symmetrically between the two terms we have

$$\begin{aligned} A_{1+2} &= A_0 e^{-i2\pi d \sin\theta/2\lambda} + A_0 e^{i2\pi d \sin\theta/2\lambda} \\ A_{1+2}^2 &= 4A_0^2 \cos^2(\pi d \sin\theta/\lambda) \approx 4A_0^2 \cos^2(\pi d\theta/\lambda) \end{aligned} \tag{1.10}$$

We see that the far-field diffraction pattern of a pair of point-sources is a sinusoid, with an angular frequency proportional to the 'baseline' d/λ. If the input wavefront is tilted by an angle θ_0 (i.e. changes in phase between the two input apertures), the centre of this diffraction pattern is tilted similarly, i.e.

$$\begin{aligned} A^2 &= A_0^2 \cos^2(\pi d(\theta - \theta_0)/\lambda) \\ &= A_0^2 \cos^2(\pi d\theta/\lambda - (\theta_0 d/\lambda)) \\ &= A_0^2 \cos^2(\pi d\theta/\lambda - \phi) \end{aligned} \tag{1.11}$$

so we see that information about the incoming direction of light is translated into a phase offset in the far-field diffraction pattern.

A single baseline maps an input plane wave to a sinusoidally modulated intensity

pattern; by linearity, an arbitrary number of slits generates an interference pattern as a sum of sinusoidal patterns at the spatial frequencies determined by the baselines between the slits. A continuous aperture likewise produces a difffraction pattern which is the integral of the sinusoids generated by all baselines in the aperture: that is, the aperture's Fourier transform! We call this property Fraunhofer diffraction.

The angular coordinates of the far-field pattern can be mapped to linear spatial coordinates by placing a screen in the path of the light; but it is more convenient to use a lens or mirror to focus this light onto a a detector. We will therefore generally refer to the aperture as the *pupil plane*, and the far-field pattern it generates as the *focal plane*. The focal plane diffraction pattern induced by a pupil is called the point spread function (PSF). Unlike in radio astronomy, it is not possible at optical frequencies to measure the phase of incoming light directly; we therefore merely measure the intensity, i.e. the squared modulus of the field amplitude. It is therefore common in optical astronomy to refer to the diffraction pattern in field and intensity interchangeably as the PSF.

One very important consequence of the Fourier complementarity of pupil and image is that a smaller pupil has a proportionately larger PSF. For a circular aperture, we find that the diffraction pattern consists of a circular disk surrounded by alternating light and dark rings, as first shown by Airy (1834). The angular radius of the first dark ring or 'null' in this Airy pattern is

$$\theta = 1.22\frac{\lambda}{D} \tag{1.12}$$

where D is the diameter of the telescope aperture. It is common to choose the Rayleigh criterion for resolution, such that two objects are resolved if they are further apart than the first null (Rayleigh, 1879). An instrument which achieves this resolution is said to be diffraction-limited, which is typically only achieved from space or with AO. This means that to achieve high angular resolution, we need to either

go to shorter wavelengths or larger telescope apertures. As we shall show below, it is possible to synthesise a very wide effective aperture from combining light from multiple telescopes.

1.7.1 The van Cittert-Zernike Theorem

In a real astronomical situation, we are interested in observing more complex scenes than a simple point source! This problem is nevertheless best expressed in terms of the Fourier optics terms we have introduced. Let us consider a situation of monochromatic light from multiple sources diffracting through an aperture. We do not expect a definite phase relationship between the light from spatially well-separated emitters such as separate stars, or from thermal emission at different points on the same star; we say that sources such as this are spatially incoherent, and assume that light from such sources adds in intensity rather than in the complex phasor space of coherent light. Because the image of a point source appears at its angular position with its total flux conserved, we see by linearity that the image of a complex scene (e.g. many stars in a field of view) is then the convolution of the (intensity) PSF with the source intensity distribution.

We can use interferometry to image such systems with great precision, even though the light is not spatially coherent. There is a remarkable theorem, the van Cittert-Zernike theorem (van Cittert, 1934; Zernike, 1938) that relates the incoherent sum of interference fringes in an image to the Fourier transform of the source intensity distribution. We illustrate an outline of a derivation of this theorem in Figure 1.1; for a more detailed proof, see Labeyrie et al. (2006).

We see by the cross-correlation theorem/Wiener-Khinchin theorem (Wiener, 1930; Khinchin, 1934) that the autocorrelation of the pupil plane is the Fourier transform of the PSF intensity pattern. We can call this function the 'optical transfer function' (OTF).

Because an astronomical image is the convolution of the source and PSF intensities, we see by the convolution theorem that the Fourier transform of such an image is the product of the OTF and the Fourier transform of the source. This is the van Cittert-Zernike theorem. We usually call this space the u, v plane; measurements in this space are called visibilities, and are in general complex. If we can measure the OTF, either with a forwards model or more often by measuring the visibilities on a known point source, we can obtain $\hat{S}$ on its own by dividing the 'science' visibilities by those measured on a known point source as a calibrator. From modelling $\hat{S}$, which is usually sparsely sampled, we can then try to infer the deconvolved image S.

We can measure these visibilities in two ways. In the *Michelson configuration* (after Albert Michelson, for the Michelson & Morley (1887) experiment to detect the luminiferous aether), we measure these directly in the u, v plane by combining light from multiple telescopes without bringing it to a focus first: the interference measured by light from two points in the system pupil plane samples the autocorrelation there directly. Beams are combined on a detector, and fringes created either spatially (with for instance a tilt between the two beams) or in time (by moving a mirror or detector back and forth) and the intensity mapped out as a function of phase delay between the two beams. The magnitude of the fringe visibility V is given by

$$|V| \equiv \frac{I_{max} - I_{min}}{I_{max} + I_{min}} \tag{1.13}$$

where I is the intensity pattern of the fringes, and the phase of the complex visibility is given by the offset of the fringe from zero phase delay (as defined in Michelson, 1891b).

The second option for beam combination is the *Fizeau configuration*. Fizeau (1868) first proposed masking out the whole of a telescope aperture, except for two holes of the telescope pupil; by changing the spacing of these holes it would be possible to determine the angular diameter of a star. The fringe pattern here is simply the

image of the sky with an unusual PSF, and visibilities are extracted either by first performing a Fourier transform on the resulting image, or with a 'pixel-to-visibility matrix' (P2VM) applied directly to pixel measurements.

Because of the Hermitian symmetry of the Fourier transform, visibility moduli encode only information about the centrosymmetric component of an astronomical source, while phases encode only the point-asymmetric component. This in practice means that phase information is crucial to determining position information, especially in relation to faint companions to brighter stars.

1.7.2 A Brief History of Interferometry

In this Thesis we will deal almost exclusively with optical astronomy. Nevertheless, as we shall discuss below, while interferometry first arose in the context of optical astronomy, it led to only a small number of significant discoveries. These interferometric principles then surged to importance with the advent of modern radio astronomy after the Second World War, in the course of which interferometric technology and ideas were further developed and subsequently re-seeded into optical astronomy. In this Section we will therefore begin with some of the early work on optical interferometry, lay out the key developments in radio interferometry, before moving back to the optical domain.

1.7.2.1 Early Optical Interferometry

The first application of optical interferometry was aperture masking, and unto aperture masking it would return a century later; a good account of the surprising history of its rise, decline and recent renaissance is given by Tuthill (2012). After Fizeau (1868) first suggested determining the diameters of stars with interferometry, this measurement was first attempted by Stéphan (1874): using the 80 cm Grand Téléscope Foucault in Marseille, with an aperture mask leaving two slits separated

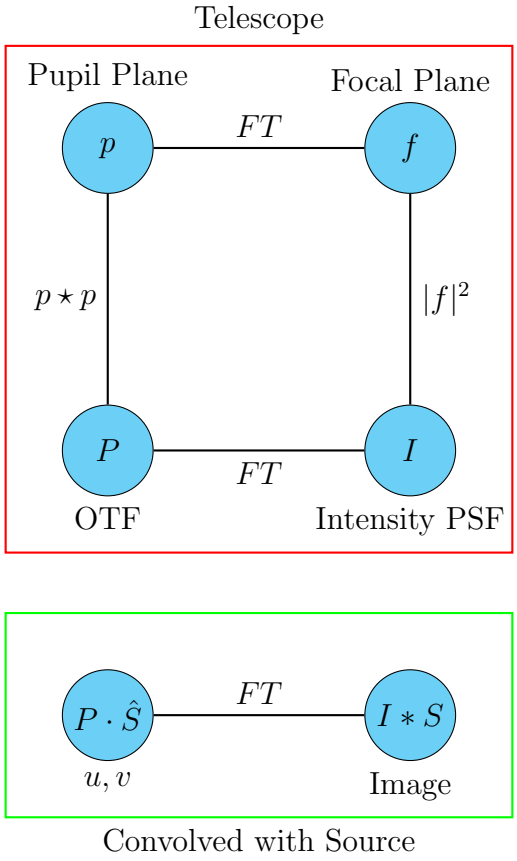

Figure 1.1: Schematic of the relationships of the various interferometric quantities and domains. In the upper section, we have the coherent diffraction of light in the pupil plane (p) to the focal plane PSF (f). These quantities are only directly measurable in the context of radio astronomy. The intensity PSF (I) is the square modulus of f, and the cross-correlation theorem implies that the autocorrelation of p, the Optical Transfer Function (OTF) P, is the Fourier transform of I. The image recorded by the telescope (if it does directly record an image) is the convolution of the source intensity distribution S with the PSF I. The convolution theorem then implies that the Fourier transform of this is the product of the OTF with the FT of S (which we label $\hat{S}$): this is the van Cittert-Zernike Theorem.

by 65 cm along their central axes, he observed all stars visible from Marseille down to the 4$^{\text{th}}$ magnitude, placing an upper limit on their angular diameters at 158 mas. Michelson (1891a) measured the angular diameters of the Galilean moons of Jupiter using an aperture mask mounted on the Lick 12-Inch Telescope[15]; Schwarzschild (1896) used the 10-inch telescope at Munich Observatory to determine the angular separations of thirteen bright binary stars, while Hamy (1899), at the Observatoire de Paris, determined the angular diameters of the moons of Jupiter, as well as that of the minor planet Vesta. Michelson repeated his masking experiments with the Hooker 100-Inch Reflector at Mount Wilson (as reported in Hale, 1919) to measure the angular separations of binary stars (Anderson, 1920a,b; Merrill, 1922).

Michelson and Pease later mounted a purpose-built interferometer on the Hooker 100-Inch, consisting of two pick-off mirrors at moveable positions along a 20' girder in front of the telescope, and used this to measure the angular diameter of Betelgeuse (the first direct measurement of a stellar angular diameter; Michelson & Pease, 1921) and a handful of other stars (Michelson & Pease, 1922).

Remarkably, in each of the cases described above, fringe visibilities were estimated by eye, with a human observer at an eyepiece determining the visibility based on their judgement. This is because phase errors from atmospheric seeing cause random delays between the interferometer subapertures, and the resulting fringes change in phase accordingly, moving side to side in the focal plane faster than technology at the time could record. After the 1920s there is therefore an extended hiatus from optical interferometry: the bright objects with angular separations that could be measured by eye had all been observed, and until new detector technology was available, no further science was possible. In this time, however, interferometry was to become more important to astronomy than ever: it would form the basis of the new field of radio astronomy, and the advances made in this area would eventually return to the

[15]Given that he used Fizeau interferometry to do so, this makes naming pupil and focal plane beam combination the Fizeau and Michelson configurations a historically unfortunate convention.

optical domain and revive interferometry there.

1.7.2.2 Radio Interferometry

Jansky (1933) first reported the detection of radio waves from the Milky Way, and in so doing started the field of radio astronomy. Following the end of the Second World War and the identification by Elizabeth Alexander of the 'Norfolk Island Effect' as radar noise from the Sun (Orchiston, 2005), Pawsey et al. (1946) determined that the solar radio flux at 1.5 m correlated with apparent total sunspot area. This led McCready, Pawsey & Payne-Scott (1947) to make the first ever radio-astronomy interferometric measurement, observing the Sun at dawn with the cliff-top antennae at Dover Heights and Collaroy, both field stations near Sydney. In this research, the radio wave received directly, and the wave reflected from the ocean, make a 'sea-cliff interferometer' a radio analogue of the Lloyd's mirror experiment in optics (Lloyd, 1834, in Titchmarsh 1941). This is equivalent to a two-element interferometer, with interference between the receiver and a virtual receiver at its position reflected in the plane of the water. They constructed a 1 D profile of solar radio flux, and showed that the flux was concentrated in the sections containing sunspot groups as determined by Mt Stromlo astrophotography. Engaging and detailed accounts of this period can be found in Goss (2012), an overview of early radio interferometry; and in Goss (2013), a biography of one of the key players in this early period, Ruby Payne-Scott. Soon Ryle & Vonberg (1948) made the next major development in radio interferometry, which would win Ryle the Nobel Prize in 1974, investigating the Sun with a two-element interferometer (the first of its kind) with 80 and 175 MHz frequencies 'separated by about ten wave-lengths, and situated on a line running east-west'.

From this point on, an explosion of research was done on radio interferometry, continuing to the present day. We shall focus on one development in particular which would be important in the optical case. Phase noise due to the ionosphere is a severe

problem in radio astronomy, and radio-domain innovations to correct for phase errors have been crucial in the optical domain. Closure phase gave rise to the family of algorithms referred to in radio astronomy as self-calibration (Pearson & Readhead, 1984), in which phase closure is used as a constraint to fit a model to, and calibrate out, phase and amplitude (i.e. complex gain) errors in a radio interferometer. Because it is not possible to directly measure the phase at each subaperture in optical interferometry, the full generic family of self-calibration algorithms cannot be exploited, but closure phase is nevertheless of vital importance in optical astronomy. A descendant of closure phase, kernel phase interferometry, is the subject of Chapters 2 and 3 of this Thesis, and as such we shall discuss in detail the history and principles of closure phase in Chapter 2. Ideas such as closure phase from radio astronomy brought back into optical astronomy, together with advanced detectors capable of recording short exposures to 'freeze the seeing', contributed to a renaissance in optical interferometry in the 1970's.

1.7.2.3 Modern Optical Interferometry

After many years of hiatus, single-telescope and multi-telescope interferometers were revived in a flurry of work beginning with the Narrabri intensity interferometer (Hanbury Brown et al., 1967), but moving quickly to coherent beam combination. Classical long-baseline interferometry in the Michelson configuration was achieved first by Labeyrie (1975), attaining fringes on Vega with a pair of small telescopes with a 12 m baseline between them at the Observatoire de Nice. This was followed by Shao & Staelin (1980) recording the first fringes with phase tracking, observing white light fringes from Polaris with a 1.5 m baseline. After decades of development, optical interferometry is now supported by common-user facilities such as the Center for High Angular Resolution Astronomy (CHARA; McAlister et al., 2005) and the Very Large Telescope Interferometer (VLTI; Glindemann et al., 2001); in this Thesis, however,

we will be mostly concerned with aperture masking and speckle interferometry.

Speckle interferometry was a breakthrough in high angular resolution imaging that shaped the future direction of the field. Recall that fringe visibilities previously had to be estimated by eye, as they danced around too much for photography and averaged out into a smooth blur without visible fringes. The advent of modern fast detectors permits this process to be done electronically for Fizeau interferometry. In speckle interferometry, instead of trying to deconvolve the difficult PSF, we simply Fourier-transform the images, which if they were added in the image plane would add to a smooth halo, and measure average squared visibilities in the u, v plane (Labeyrie, 1970).

This was generalized as speckle masking (Weigelt, 1977), where three-point correlations in the u, v plane (the bispectrum) are used instead of the raw visibilities; this is equivalent to the closure phase method. This is limited by telescope redundancy, however, and the closure phases are corrupted by phase noise. This is because in general, many pairs of points in a telescope aperture generate the same baseline. In the Fizeau configuration, we cannot separate out the contributions of redundant copies of the same baseline to the final visibility: their phasor contributions add in the complex plane, with the result that the phase of the final complex visibility is not the sum of the phases of the component vectors. In this case, closure relations will not hold exactly, and atmospheric noise will creep into closure phase measurements. As a result, to obtain closure phases in optical astronomy, it is necessary to mask out regions of the telescope leaving only a non-redundant pattern of holes, i.e. a pattern in which each pair of holes uniquely corresponds to one u, v baseline. Visibilities and closure phases are then used to constrain parametric models or non-parametric image reconstructions (e.g. Skilling & Bryan, 1984; Lawson et al., 2004). This can achieve 'super-resolution' by factors of $\sim$ a few beyond the formal Rayleigh limit provided sufficiently high signal-to-noise data are available, although with limitations on the

complexity of images at that resolution (Mawet et al., 2014).

Rogstad (1968) and Rhodes & Goodman (1973) separately proposed using the Jennison (1958) closure phase idea in optical astronomy, but it would be nearly two decades before this was achieved by Baldwin, Haniff, Mackay & Warner (1986), using a three-hole aperture mask on the University of Hawai'i 88-Inch Telescope on Mauna Kea. They narrowly beat Frater, Robertson, O'Sullivan & Norris (1987) to publication, who used the 3.9 m Anglo-Australian Telescope with a plywood aperture mask on the primary mirror, and Readhead et al. (1988) using the Palomar Hale 200-Inch Telescope. Using the Cambridge Optical Aperture Synthesis Telescope (COAST; Mackay & Baldwin, 1988; Baldwin et al., 1994), consisting of four elements and permitting baselines up to 100 m, Baldwin et al. (1996) obtained the first ever optical aperture synthesis images, of the star Capella.

Since then aperture masking has achieved some of the highest angular resolution complex optical images in astronomy. The Keck Aperture Masking Experiment (Tuthill, Monnier, Danchi, Wishnow & Haniff, 2000b), using aperture masks over the Keck I telescope primary, delivered some of the first complex optical images recovered with closure phases: the famous pinwheel nebulae around colliding-wind binaries (Monnier et al., 1999; Tuthill et al., 1999); observing the motion of hotspots in the complex structure of IRC +10216 (carbon star CW Leonis, the brightest object in the sky at mid-IR wavelengths; Tuthill et al., 2000a); and resolving the circumstellar disk around the young star LkHα 101 (Tuthill et al., 2002).

Kernel phase interferometry is a generalization of the idea of closure phase, in which sufficiently small phase errors can be corrected by closure-like relations even in the case of a redundant telescope aperture (Martinache, 2010). While kernel phase has been applied to *HST* observations to achieve super-resolution of brown dwarf binary systems (Pope, Martinache & Tuthill, 2013), it has not previously been used from ground-based telescopes, though extreme adaptive optics can achieve the required

wavefront quality. In Chapter 2 I present a further generalization to include amplitude errors (analogous to closure amplitudes first introduced by Twiss et al., 1960), while in Chapter 3 I will show that kernel phase achieves the same precision in imaging from the ground with adaptive optics as with masking.

1.8 Asteroseismology

While this thesis is primarily about exoplanets, in Chapters 5 and 6, we shall also discuss asteroseismology, the study of stellar oscillations. Asteroseismology can be used to precisely determine fundamental stellar parameters, given that different oscillation modes probe density and temperature at different depths in the stellar interior. The authoritative textbook by Aerts, Christensen-Dalsgaard & Kurtz (2010) provides a good introduction to asteroseismology in the pre-*Kepler* era, including classical pulsators (coherent variable stars) and solar-like oscillators (those with stochastically excited oscillations driven by the convective motion of material in the stellar envelope). Meanwhile Chaplin & Miglio (2013) provide an excellent review of general and subsequent work on red giants and solar-like stars.

The existence of classical pulsators has been known since the discovery of the red giant radial pulsator Mira (Hevelius & Horrocks, 1662), which varies by five magnitudes in brightness with a 333 day period. These variations in brightness are due to the expansion and contraction of the star's photosphere. There are numerous classes of classical pulsator, some of which have been very important in the history of astrophysics, for example the radially-pulsating Cepheid variables (Goodricke, 1786), whose period-luminosity relation (Leavitt, 1908; Leavitt & Pickering, 1912) formed a key rung of the cosmic distance ladder and aided the discovery of the expanding universe (Hubble, 1929). Classical pulsations such as those of the Cepheid variables are driven by the κ-mechanism (Eddington, 1917), a heat engine effect where the temper-

ature, pressure and composition of a layer in the star lie near the ionization edge of a component element, so that opacity locally increases as a function of temperature, which causes the star to become unstable to pulsation.

While the Mira and Cepheid variables have long-period radial modes, we are primarily interested in nonradial stellar oscillations in this Thesis. The theory of nonradial stellar oscillations was first put on a rigorous basis by Cowling (1941), who found that polytropic stars support three kinds of oscillation: pressure or p-modes, acoustic waves whose normal modes are asymptotically equally spaced in frequency; gravity or g-modes, whose restoring force is buoyancy and which asymptotically are equally spaced in period; and 'fundamental' surface f-modes. The asymptotic relations are especially important, in giving us the main p-mode observables the large and small frequency separations $\Delta\nu$ and $\delta\nu$, and the g-mode observable the period spacing $\Delta\Pi$. These parameters can be used to constrain bulk stellar properties and therefore a star's evolutionary state. The frequency ν_{nl} of the mode with radial order n and degree l in the asymptotic limit of high n can be shown to be to first order (Vandakurov, 1967; Tassoul, 1980; Gough, 1986)

$$\nu_{nl} \approx \Delta\nu\left(n + l/2 + \epsilon\right), \tag{1.14}$$

where the 'large separation' $\Delta\nu$ is given by

$$\Delta\nu = \left(2\int_0^R \frac{dr}{c_s}\right)^{-1} \tag{1.15}$$

where c_s is the local sound speed, R the stellar radius, and ϵ a number of order unity depending on the boundary conditions of the star. This means that frequencies of order and degree n, l and $n-1, l+2$ are degenerate to first order. These degenerate frequencies are split by higher-order terms. Usually the most important the 'small separation' $\delta\nu$, which depends on the sound-speed gradient in the core and therefore

measures stellar ages by constraining the core composition:

$$\delta\nu_{l,l+2}(n) \equiv \nu_{n,l} - \nu_{n-1,l+2} \approx -(4l+6)\frac{\Delta\nu}{4\pi^2\nu_{nl}}\int_0^R \frac{\mathrm{d}c}{\mathrm{d}r}\frac{\mathrm{d}r}{r}. \tag{1.16}$$

Modes of the same degree but different azimuthal order m are ordinarily degenerate, but deviations from spherical symmetry such as rotation can cause these to split (Cowling & Newing, 1949); modes that probe different regions of the star can be used to determine differential rotation (e.g. Beck et al., 2012a).

For g-mode pulsations, the periods are uniformly spaced

$$\Pi_{nl} = \nu_{nl}^{-1} \approx \Delta\Pi_{nl}(n + \epsilon_g) \tag{1.17}$$

where ϵ_g is again a constant of order unity. The period spacing $\Delta\Pi$ is the key observable for g-modes, given by

$$\Delta\Pi_l = \frac{2\pi^2}{\sqrt{l(l+1)}}\left(\int N\frac{\mathrm{d}r}{r}\right)^{-1} \tag{1.18}$$

where N is the Brunt-Väisälä frequency of buoyant oscillations,

$$N^2 = g\left(\frac{1}{\Gamma_1}\frac{\mathrm{d}\ln p}{\mathrm{d}r} - \frac{\mathrm{d}\ln\rho}{\mathrm{d}r}\right). \tag{1.19}$$

The condition for convection is $N^2 < 0$, such that a displaced pocket of gas continues to rise or fall rather than to oscillate. As such, g-modes are always evanescent in convective regions of a star, which is why they have not yet been observed in the Sun. Gravity mode properties are accordingly a sensitive probe of the conditions of the radiative core of solar-like and red giant stars. In red giants, these can be observed via their coupling to pressure waves: as stars evolve off the main sequence, the core contracts (bringing g-mode frequencies up) and the envelope expands (pulling p-mode frequencies down), so that these become much closer in frequency. Modes with degree

$l > 0$ are mixed modes, with p-mode character in the convective outer region and g-mode character in the core, the coupling being strongest when $l = 1$. The frequencies of these modes avoid crossing and are accordingly perturbed in frequency.

Meanwhile, in hot stars with radiative outer layers, g-modes can reach high amplitudes, giving rise to the γ Doradus variables (Kaye et al., 1999) and slowly-pulsating B stars (SPB stars; Waelkens, 1991), the latter of which are most important to this Thesis. In both types of star, g-modes are very sensitive to core properties (Miglio et al., 2008). Their $\sim$ hour (γ Dor) and $\sim$ day (SPB) pulsation timescales are amenable to very precise measurement with long photometric time series as provided by *Kepler*. In Chapter 6, we will see that several of the brightest Pleiades members are SPB stars. This class of variable pulsates in high-order g-modes excited by the κ-mechanism in which the required opacity bump is provided by iron-group elements (Dziembowski et al., 1993; Gautschy & Saio, 1993), and deviations from uniform period spacings in SPB stars constrain core rotation and mixing (e.g. Pápics et al., 2014, 2015, 2017; Triana et al., 2015; Moravveji et al., 2015, 2016). Convective overshooting, diffusive mixing, and internal differential rotation affect the mixing of nuclear fuel into a stellar core, and SPB stars are accordingly excellent laboratories for studying these processes as they affect massive stars.

Stochastically-excited oscillations are also important for astrophysics, as they tell us both about the evolution of solar-like stars and red giants, which also have convective outer layers. Obtaining precise stellar masses and ages is valuable for characterizing exoplanet host stars (Huber et al., 2013a; Silva Aguirre et al., 2015), and large samples of stellar ages (which can be classical or stochastic oscillators) also allow us to unravel the process of the Milky Way's formation and evolution through galactic archaeology (Freeman & Bland-Hawthorn, 2002; Miglio et al., 2013).

Our own Sun was the first star in which stochastically-excited oscillations were detected, and remains by far the best-characterized, with thousands of individual p-

mode frequencies identified (Reiter et al., 2015), though the detection of g-modes has remained elusive (García et al., 2007; Appourchaux et al., 2010). Solar oscillations are driven by energy from the turbulence of the Sun's convective outer region (Goldreich & Keeley, 1977; Samadi & Goupil, 2001). In general, frequencies are excited with a Gaussian envelope centred at a frequency of maximum power $\nu_{\rm max}$, which scales with the acoustic cutoff frequency (Brown et al., 1991; Belkacem et al., 2011). Meanwhile the large frequency separation $\Delta\nu$ probes the mean stellar density (Ulrich, 1986). The main scaling relations are then (e.g. Huber et al., 2011)

$$\Delta\nu \propto \sqrt{\bar{\rho}} \propto \sqrt{\frac{M}{R^3}} \tag{1.20}$$

and for solar-like oscillators,

$$\nu_{\rm max} \propto \nu_c \propto g\ {T_{\rm eff}}^{-1/2} \propto \frac{M}{R^2\sqrt{T_{\rm eff}}} \tag{1.21}$$

which given blackbody luminosity $L \propto R^2T^4$ allows us to write

$$\frac{\nu_{\rm max}}{\nu_{\rm max,\odot}} \approx \left(\frac{M}{\rm M_\odot}\right)\left(\frac{T_{\rm eff}}{T_{\rm eff,\odot}}\right)^{3.5}\left(\frac{L}{L_\odot}\right)^{-1} \tag{1.22}$$

and

$$\frac{\Delta\nu}{\Delta\nu_\odot} \approx \left(\frac{M}{\rm M_\odot}\right)^{0.5}\left(\frac{T_{\rm eff}}{T_{\rm eff\odot}}\right)^{3}\left(\frac{L}{L_\odot}\right)^{-0.75}. \tag{1.23}$$

Solar-like oscillations were first detected on another star in Procyon (Brown et al., 1991) and have since then been discovered in many solar-like stars and red giants, for example by CoRoT (Appourchaux et al., 2008; Mosser et al., 2010) and most significantly, by *Kepler*. Beyond searching for planets, *Kepler* has revolutionized the field of asteroseismology (Gilliland et al., 2010). It has yielded the first detection of gravity-mode period spacings in a red giant (Beck et al., 2011), enabling probes of interior rotation of red giants (Beck et al., 2012b) and distinguishing between

hydrogen- and helium-burning cores (Bedding et al., 2011). It has also permitted the determination of ages and fundamental parameters of main-sequence stars (Silva Aguirre et al., 2013; Chaplin et al., 2014), including planet-hosting stars (Huber et al., 2013b; Silva Aguirre et al., 2015), revealing the most ancient known planetary system, dating back to the earliest stages of the galaxy (Campante et al., 2015). By comparing asteroseismic stellar ages to stellar rotation periods, Angus et al. (2015) have shown that gyrochronology models cannot fit the data with a single relation, leading van Saders et al. (2016) to suggest a qualitative change in dynamo mechanism as stars age through the main sequence.

A legacy of the *Kepler* asteroseismology programme is a sample of benchmark stars for future work (Lund et al., 2016; Silva Aguirre et al., 2016). As well as asteroseismology, by also using optical interferometry, it has been possible to determine fundamental parameters of main-sequence and giant stars with unprecedented precision (Huber et al., 2012; White et al., 2013, 2015). Likewise by combining with spectroscopy, Hawkins et al. (2016b) produce a large sample of stars with precise elemental abundances by fitting spectroscopic data with $\log g$ and $T_{\rm eff}$ fixed to asteroseismically-determined values. It is necessary to calibrate such a study against benchmark stars with very precisely-determined parameters, which in practice requires nearby bright stars that are amenable to high resolution spectroscopy plus asteroseismology (Creevey et al., 2013); the determination of parallaxes (Hawkins et al., 2016a); diameters from interferometry (Casagrande et al., 2014; Creevey et al., 2015); or else stars which are in eclipsing binaries (Brogaard et al., 2016) or which are members of open clusters (Basu et al., 2011; Stello et al., 2011b, 2016; Corsaro et al., 2017). The methods for bright star photometry presented in Chapters 5 and 6 of this Thesis will provide a valuable sample of additional benchmark stars as a legacy of the *Kepler* and *K2* missions, and has already been used for constraining detailed individual stellar models (Hjørringgaard et al., 2017).

Chapter 2

Kernel Phase and Kernel Amplitude in Fizeau Imaging

Now I fourfold vision see
And a fourfold vision is given to me
Tis fourfold in my supreme delight
And three fold in soft Beulahs night
And twofold Always.
May God us keep From Single vision
& Newtons sleep.

William Blake

2.1 Introduction

In imaging stars and their environments from the ground, under most circumstances the chief limitation on resolution and on sensitivity to faint structure is imposed by the turbulence of the Earth's atmosphere. This 'seeing' introduces random delays in the phase of incoming light, so that when it arrives at a ground-based telescope, the wavefront is distorted and generates blurry, speckled images. Furthermore, as a higher-order effect, this wavefront distortion induces focussing and defocussing of

This Chapter has been published as Pope (2016).

the light in the Fresnel regime, so that there is also generally amplitude aberration, or scintillation, which is the reason that stars appear to twinkle. This is a major challenge in doing optical astronomy from the ground at high angular resolution, and in this Chapter I will review the history of techniques for ameliorating the effects of the atmosphere from speckle imaging; early hardware developments in non-redundant masking, where the telescope aperture is selectively masked out to facilitate optical calibration; and through to the more recent computer post-processing technique of kernel phase, where such a masking procedure is simulated purely with software. I will then present a generalization of the kernel phase idea, to kernel amplitudes, and discuss its applicability to present and future adaptive optics systems and space telescopes.

For mathematically modelling the atmospheric distortion of images, it is useful to consider any telescope, even one with a conventional filled aperture, as an interferometer, where light incident at different parts of the telescope is optically combined and caused to interfere. By measuring these interference fringes, the Van Cittert-Zernike theorem (Zernike, 1938) states that we can map out the Fourier transform of the intensity distribution of the source on the sky. This means that the Fourier plane is a natural representation for understanding optical imaging under most circumstances. Pairs of points in the telescope aperture are considered to form baselines, whose length and orientation determine the Fourier component to which the associated fringe is sensitive. Interferometers are classically considered to be either of the Michelson configuration, where the light is combined in the pupil plane, or the Fizeau configuration, where the light from all elements of the pupil is directly combined on a detector.

In radio astronomy, it has long been possible to record the electric field received at each detector, and combine these pupil-plane signals in postprocessing via a correlator. In optical astronomy, because it is not possible to directly sample the waveform

of the electric field as it is at radio frequencies, single-telescope filled-aperture imaging typically occurs in the Fizeau configuration. As a result, fringes from every pair of points in the pupil are superimposed to form the point spread function (PSF) of the telescope. This is true both of discrete sets of apertures, for example the double slit whose PSF is a sinusoidal fringe, and filled apertures, where the familiar circular telescope aperture's PSF is the Airy pattern. In the following, I will refer interchangeably to pupil elements and subapertures, and stations and antennae, using the appropriate terminology for specifically-optical applications and for historical radio applications respectively.

Sophisticated techniques for analysing images degraded by atmospheric turbulence have long been in use. By modelling the effects of the atmosphere on Fourier components of the image, speckle interferometry (Labeyrie, 1970) and speckle masking (Weigelt, 1977) have been used to resolve systems at very high angular resolution while ameliorating the effects of the atmosphere. These techniques rely on the fact that, while the PSF is degraded in potentially complicated ways, the complex visibilities in its Fourier transform can be represented simply. To achieve this, one must be able to 'freeze the seeing', i.e. to take exposures with appropriate signal-to-noise at timescales shorter than the characteristic timescale of the atmosphere's variations.

A successful solution to the problem of seeing has been the technique of aperture masking, first proposed by Fizeau (1868), where sections of the telescope aperture are deliberately blocked out to leave a non-redundant pattern of holes, i.e. a pattern of holes in which no two are separated by the same baseline, in order to make the resulting fringe pattern more resilient to aberrations and easier to calibrate. In a redundant aperture, on the other hand, multiple sets of subapertures generate the same baseline, and it is not so easy to disentangle their contributions to the resulting visibilities. Aperture masking has yielded some of the highest-resolution astronomical images obtained with a single-mirror telescope (Tuthill et al., 1999; Monnier et al.,

1999), relying on the idea of closure phase (Jennison, 1958), an interferometric self-calibration technique originating in radio astronomy. Often in interferometry, the dominant source of uncertainty is from phase aberrations in the pupil plane (i.e. for discrete interferometers, delay errors at individual stations), which are in general very large, originating from the ionosphere in the context of radio astronomy, or from atmospheric turbulence in the optical regime. These are especially important because, since the Fourier transform is Hermitian, the Fourier phases of a nonnegative real source (i.e. any astronomical image) encode only information about the asymmetric component of an image, and the moduli about its point-symmetric component (Monnier, 2007). Therefore in the absence of prior information it is crucial to have access to both; regularly in astronomy, the issue is therefore to restore phase information which is typically more-degraded by the atmosphere. In this Chapter, we will discuss the context of methods for doing this, and then show that these can be generalized to self-calibrating both phase and amplitude information.

The key idea in interferometric self-calibration is the closure phase or (bispectral phase). These are sums of measured phases around closing triangles of baselines; because errors occur locally to each station, while astrophysical signals are encoded in correlations between stations, if you add the phases measured around such a triangle of baselines, the local phase errors cancel but the astrophysical signal adds. As a result, for a simple three-element interferometer, for the price of three phase observables corrupted by aberrations, one very stable observable can be obtained, which is often a significant advantage. This idea entered optical astronomy under the guise of 'triple-correlation' speckle imaging (Labeyrie, 1970; Weigelt, 1977), which was shown by Roddier (1986) to be the exact equivalent of the closure phase idea. While aperture masking in general requires, as with speckle imaging, that exposures are taken fast enough to freeze the seeing, adaptive optics can be used to dramatically increase the timescale of phase variations and effectively remove this limitation (Tuthill et al.,

2006).

In radio astronomy, successive generations of calibration schemes have been able to use closure information in conjunction with the phases and amplitudes recorded at each antenna for self-calibration. Smirnov (2011) classifies these into first-generation schemes using closure phases but not using individual receiver phases directly, second-generation schemes which iteratively self-calibrate the phase and gain at each receiver, and third-generation schemes which use the radio interferometry measurement equation to include direction-dependent effects. Because the phases and amplitudes of individual aperture elements cannot at present be easily and directly measured, optical imaging does not yet benefit from these second- and third-generation calibration schemes. As a result, we are still limited to the classical closure relations in self-calibration, and I therefore seek to obtain the fullest and most detailed understanding of these quantities as is possible.

Kernel phase interferometry was proposed for this reason by Martinache (2010), who also coined the term itself. The key idea was a generalization of closure phase, using a matrix approach to show that a wider class of telescopes possess linearly self-calibrating quantities that can be used to improve the imaging performance of telescopes at resolutions close to the diffraction limit. Closure phases are shown to be a special case of this formalism, which in general applies to any standard Fizeau imaging system subject to only small aberrations. This technique has been used both for space telescopes such as the *Hubble Space Telescope* (Pope et al., 2013), and also for ground-based adaptive optics systems (Pope et al., 2016a).

In this Chapter, I discuss the closure and kernel quantities associated with general Fizeau interferometers and the relationship of previous methods to the more recent development of kernel phase interferometry. I propose the extension of this to kernel amplitudes, a natural generalization of the kernel phase theory which allows us to calibrate not only phase errors but also scintillation.

2.2 Matrix Theory of Phase Self-Calibration

The Jennison (1958) idea of closure phase rests on the fact that if two antennae, 1 and 2, would in the absence of noise record between them a complex visibility C_{12} having phase Φ_{12}, when they experience phase errors ϕ_1 and ϕ_2 then the recorded phase of the complex visibility between them is instead

$$\Phi'_{12} \equiv \Phi_{12} + \phi_1 - \phi_2. \tag{2.1}$$

Therefore if we add the phases around a closing triangle of baselines,

$$\Phi_{123} \equiv \Phi'_{12} + \Phi'_{23} + \Phi'_{31} \tag{2.2}$$

contains each error ϕ_i exactly once positively and once negatively, and so the errors cancel out and the closure phase Φ_{123} is invariant.

On the other hand, Lannes (1991) derives this closure phase relation in terms of a phase-transfer matrix, linearly mapping phase aberrations at discrete points in the pupil plane onto phases on the measured visibilities. This is a useful framework in which to consider generalizing the idea of closure phases to arbitrary pupils, which have kernel phases that work in the same way.

As an example, consider a three-element array, with stations at the vertices of some triangle. The matrix

$$\mathbf{A}_\phi \equiv \begin{pmatrix} 1 & -1 & 0 \\ 0 & 1 & -1 \\ -1 & 0 & 1 \end{pmatrix} \tag{2.3}$$

encodes this linear relation between the three pupil samples and the three baselines

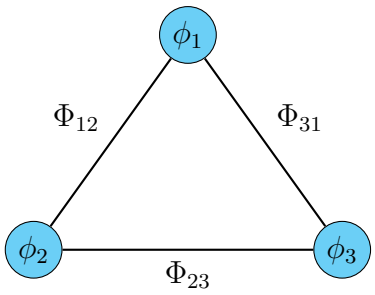

Figure 2.1: Lower-case ϕ_i are phase errors local to receiver i, while upper-case Φ_{ij} are the phases of the complex visibilities on baselines ij.

that they generate:

$$\begin{pmatrix} \Phi'_{12} \\ \Phi'_{23} \\ \Phi'_{31} \end{pmatrix} = \begin{pmatrix} 1 & -1 & 0 \\ 0 & 1 & -1 \\ -1 & 0 & 1 \end{pmatrix} \cdot \begin{pmatrix} \phi_1 \\ \phi_2 \\ \phi_3 \end{pmatrix} + \begin{pmatrix} \Phi_{12} \\ \Phi_{23} \\ \Phi_{31} \end{pmatrix} \tag{2.4}$$

where Φ'_{ij} are the phases measured on the baseline i, j; ϕ_j is the phase aberration at station j; and Φ_{ij} the true phase as would be seen on an ideal unaberrated interferometer on baseline ij. This is illustrated in Figure 2.1.

The sum of each column of this matrix is zero, so that the row-vector

$$C_\phi \equiv \begin{pmatrix} 1 & 1 & 1 \end{pmatrix} \tag{2.5}$$

must annihilate $\mathbf{A}_\phi$, i.e., $C_\phi \cdot \mathbf{A}_\phi = \mathbf{0}$. An operator C_ϕ satisfying this condition is called a 'left-kernel' operator for $\mathbf{A}_\phi$, whose rows span a 'left null space' or 'cokernel space' for $\mathbf{A}_\phi$, which motivates the use of the term 'kernel phase' for quantities of the form $C_\phi \cdot \Phi$[1], i.e. for linear combinations of baseline phases Φ that 'live in' the cokernel of $\mathbf{A}_\phi$. This will not in general be a row-vector for interferometric arrays with more elements, but a matrix whose rows consist of vectors like in Equation 2.5 which encode closure relations. A diagram illustrating the relations of these spaces is

[1]We need to choose a left-kernel as $\mathbf{A}_\phi$ and $\mathbf{A}_\phi^T$ map vectors between different spaces and multiplication is not commutative.

provided for clarity in Figure 2.2.

By summing phases around a closed triangle as above, phase aberrations do not propagate to the new closure phase observable, which accordingly is much more reliable than raw phases and can be used to anchor image reconstruction and model-fitting. In general, we will consider pupil phases as being relative to the phase at an arbitrarily chosen point, and thereby eliminate this arbitrary degree of freedom, so that pupil sample 1 is taken to have identically zero phase, and the matrix in Equation 2.3 becomes

$$\mathbf{A}_\phi \equiv \begin{pmatrix} -1 & 0 \\ 1 & -1 \\ 0 & 1 \end{pmatrix} \tag{2.6}$$

which is annihilated by C_ϕ in the same way as before.

Closure phases do not necessarily have to be taken around a triangle: Lannes (1991) identifies this cokernel of $\mathbf{A}_\phi$ as the definition of the closure operator, rather than as an alternative derivation. This operator then generates all orders of closure phase, not just the set of closing triangles, including for example loops containing four or more elements. The kernel of $\mathbf{A}_\phi$ can be found numerically by singular value decomposition (SVD), by arranging as a matrix the singular vectors whose singular values are zero. For a non-redundant aperture, this left-kernel operator's rows consist of a basis of vectors spanning the space of closure (kernel) phases.

In order for this self-calibration to be exact, closure phases must be taken around closing sets of baselines whose phases map linearly onto the measured baseline phases, which is true for non-redundant baselines, where the two stations are not separated by the same vector as any other pair of holes (or for completeness, also in the special case of phasors which have identical amplitudes on doubly-redundant baselines). The phase noise introduced to closure phases by aberrations in a circular redundant aperture scale as $\sim (D/r_{coh})$, where D is the telescope diameter and r_{coh} the atmo-

spheric coherence scale (Readhead et al., 1988). Avoiding this redundancy noise has traditionally necessitated the use of a non-redundant mask, but the advent of modern adaptive optics means that phase-based interferometric techniques can now be extended at high fidelity to filled apertures of high redundancy.

The idea of kernel phase interferometry is that, while these relations are no longer exact for redundant arrays, they approximately hold true for small phase aberrations (Martinache, 2010). This now requires that each baseline be weighted by a diagonal matrix $\mathbf{R}$, whose entries are the redundancies of each baseline (i.e. how many pairs of subapertures correspond to that baseline), such that now

$$\Phi' \approx \mathbf{R}^{-1} \cdot \mathbf{A}_\phi \cdot \phi + \Phi \tag{2.7}$$

and the kernel matrix $\mathbf{K}_\phi$ is found by SVD of $\mathbf{R}^{-1} \cdot \mathbf{A}_\phi$. As in this general case $\mathbf{A}_\phi$ never appears without $\mathbf{R}^{-1}$, it is standard to redefine the transfer matrix $\mathbf{A}_\phi$ as the originally-defined matrix of ones and zeros, rescaled by $\mathbf{R}^{-1}$. This is the redundant, weighted equivalent of the phase aberration matrix in Lannes (1991), so that the kernel phases are a generalization of the higher-order closure phases of a filled pupil. We will use this rescaling in the remainder of this text.

Such a kernel space necessarily exists for any linear imaging system with more baselines than pupil sample points, according to the fundamental theorem of linear algebra: aberrations from p pupil sample points can map onto at most a space of dimension p over the baselines, which will ordinarily have a much larger dimension than the pupil samples. This implies that we should look for further generalizations to other observables and imaging systems.

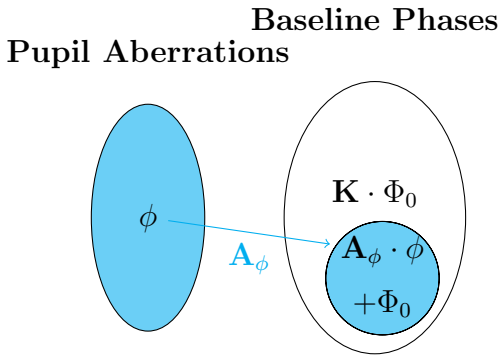

Figure 2.2: Relations between spaces of phases on pupil and baselines. The operator $\mathbf{A}_\phi$ injects phase aberrations ϕ into a subspace of baseline phases Φ. There is another subspace of baseline phases, $\mathbf{K}_\phi \cdot \Phi_0$, which are not affected by these phase aberrations, and we call these kernel phases.

2.3 Kernel Amplitudes

In this Section, we will show that there is an analogous quantity to the kernel phase in the case of amplitudes, which we will call the kernel amplitude. This allows us to self-calibrate both phase and amplitude information in arbitrary Fizeau interferometers.

Twiss et al. (1960) first introduced the concept of a four-element interferometer closure amplitude, which was subsequently systematically studied and described by Readhead et al. (1980). This quantity is an extension of the idea of closure phase to visibilities which are affected by uncertainties in the gain on individual antennae, or equivalently the throughput and reflectivity of different optical paths in optical interferometry. In the following, for ease of reference, 'visibility' is used to mean the modulus of the complex visibility unless stated otherwise, and similarly, 'gain' for the modulus of the complex gain. The derivation is similar to the Jennison (1958) idea described at the beginning of Section 2.2, except that for each visibility V_{ij} between telescopes i and j, there are gain errors g_i and g_j which multiply rather than add, so that the measured visibility is

$$V'_{ij} = V_{ij} \cdot g_i \cdot g_j \tag{2.8}$$

Therefore the quantity

$$V_{1234} \equiv \frac{V'_{12}V'_{34}}{V'_{13}V'_{24}} \tag{2.9}$$

multiplies each gain error through once on the numerator and once on the denominator; these cancel out and the closure amplitude V_{1234} is seen to be invariant with respect to this type of error.

The same matrix approach as for closure phases can be used to derive closure amplitudes. It is useful to deal with log-visibilities on each baseline, and log-gains on antennae, so that these quantities add and subtract rather than multiply and divide. Lannes (1991) notes that while the phase error on a baseline is the difference in phase between the stations, the measured log-visibility of a point source is the sum of the log-gains on each telescope. Therefore the elements of the transfer matrix $\mathbf{A}_V$ are just the absolute values of the corresponding elements of $\mathbf{A}_\phi$.

The linear gain transfer operator $\mathbf{A}_V$ for a non-redundant four-element interferometer is therefore

$$\mathbf{A}_V \equiv \begin{pmatrix} 1 & 1 & 0 & 0 \\ 0 & 1 & 1 & 0 \\ 0 & 0 & 1 & 1 \\ 1 & 0 & 0 & 1 \end{pmatrix} \tag{2.10}$$

with a transfer equation

$$\begin{pmatrix} \log(V'_{12}) \\ \log(V'_{23}) \\ \log(V'_{34}) \\ \log(V'_{41}) \end{pmatrix} = \begin{pmatrix} 1 & 1 & 0 & 0 \\ 0 & 1 & 1 & 0 \\ 0 & 0 & 1 & 1 \\ 1 & 0 & 0 & 1 \end{pmatrix} \cdot \begin{pmatrix} \log(g_1) \\ \log(g_2) \\ \log(g_3) \\ \log(g_4) \end{pmatrix} \tag{2.11}$$

$$+ \begin{pmatrix} \log(V_{12}) \\ \log(V_{23}) \\ \log(V_{34}) \\ \log(V_{41}) \end{pmatrix} \tag{2.12}$$

which we write in vector notation as

$$\mathbf{V}' = \mathbf{A}_V \cdot \log(\mathbf{g}) + \mathbf{V} \tag{2.13}$$

and we see that the operator

$$C_V \equiv \begin{pmatrix} 1 & -1 & 1 & -1 \end{pmatrix} \tag{2.14}$$

annihilates $\mathbf{A}_V$, so that

$$\log(V_{1234}) \equiv C_V \cdot \mathbf{V}' \tag{2.15}$$

$$= \log(V_{12}) + \log(V_{34}) - \log(V_{13}) - \log(V_{24}) \tag{2.16}$$

which is the standard four-element closure amplitude relation from Equation 2.9. Gains can be chosen to be relative to a fixed gain of unity as was done with phases in Section 2.2 without loss of generality, and are shown above in full unreduced form above for clarity. In software implementations, I will follow the kernel phase example and fix the gain of aperture 1 at unity.

This formalism applies to only single baselines: the visibility of a redundant baseline is the modulus of the sum of the individual phasors, so that we want to add the visibilities and not the log-visibilities. As a result, the non-redundant calculation of Lannes (1991) does not hold in the redundant case, and we must consider differential quantities in order to linearize the problem. First we note the Taylor expansion

$$\log(g) \approx \log(1 + \Delta v) \approx \Delta v \tag{2.17}$$

which means that gain perturbations away from unity map approximately linearly onto the corresponding, generally-redundant baselines. We are therefore able to consider the linear gain transfer equation

$$\Delta V' = \mathbf{R}^{-1} \cdot \mathbf{A}_V \cdot \Delta v + \Delta V \tag{2.18}$$

which can be considered as the generalization of the Martinache (2010)-style approximation to the Lannes (1991) matrix-based closure amplitudes. We therefore analogously construct $\mathbf{K}_V$ by SVD such that $\mathbf{K}_V \cdot (\mathbf{R}^{-1} \cdot \mathbf{A}_V) = 0$, and take this to be the kernel amplitude operator.

By the rank-nullity theorem, there will be at least $n_b - n_p$ kernel amplitudes, where n_b is the number of baselines and n_p the number of pupil samples. This is in general large: in the non-redundant case, n_b is combinatorically larger than n_p, and while this is lower for redundant cases, depending on the detailed pupil geometry we may recover as much as 90% of the amplitude information as is done with kernel phases (Martinache, 2013a).

The same transfer matrix formalism used to derive kernel phases can also be inverted for wavefront sensing (Martinache, 2013b; Pope et al., 2014a). In this framework, a Moore-Penrose pseudoinverse (Moore, 1920; Penrose, 1955) is generated by SVD of the transfer matrix, and used to map measured u, v phases back onto the

pupil sampling points. This requires not only that the kernel phase approximation holds, but also that the pupil itself is not inversion-symmetric; otherwise, it is only possible to sense aberration modes that are odd under inversion, and even modes are unsensed. This generalizes to the kernel amplitude formalism, although as with the case of phases, there are detailed issues surrounding matrix stability and convergence that mean that a proper examination must be left to future studies.

As the quantities we are considering in the redundant case are differential amplitudes (i.e. ΔV relative to a standard visibility), it is necessary to have some standard visibility model against which these differences can be taken. There are several possible ways to do this: most simply, an image of a fiducial point source can be used as a calibrator, such that the differential visibilities we choose when making the kernel amplitudes are the differences between the science target and the calibrator. In this approach, we calibrate pupil-dependent aberrations, but baseline-dependent aberrations are not corrected, and we expect to have potentially substantial residual systematic errors.

A sensible and self-consistent alternative to this is to use the redundancy information already encoded in the matrix $\mathbf{R}$. For a redundant pupil consisting of discrete elements, the normalized visibility of a point source is given by the magnitude of the optical transfer function (OTF) on any baseline, which is proportional to the redundancy on that baseline and normalized to unity at the origin. Thus the pupil model itself generates a starting point for calculating differential visibilities. In this case, we can then use the kernel amplitudes measured on a known point source to calibrate baseline-dependent systematics that would otherwise not be corrected.

A treatment of the full general case of phase and amplitude errors in arbitrary linear imaging systems is beyond the scope of this Chapter, but we may start to sketch out a roadmap to finding such a theory. If we write the total aberrations as a

concatenation of phase and amplitude error vectors, i.e.

$$\mathbf{a}^T \equiv [\phi^T, \mathbf{\Delta V}^T] \tag{2.19}$$

then the full transfer matrix for a linear Fizeau interferometer is the block diagonal matrix

$$\mathbf{A} \equiv \begin{pmatrix} \mathbf{A}_\phi & \mathbf{0} \\ \mathbf{0} & \mathbf{A}_V \end{pmatrix}. \tag{2.20}$$

The kernel operator for this matrix is also a block-diagonal matrix of the kernel operators of each block separately, so that at linear order the full kernel phase and amplitude problem is itself separable. For systems which mix phase and amplitude errors, the above matrix will instead have non-zero off-diagonal elements, but will have a set of kernel phase-amplitude quantities which nevertheless permit self-calibration.

2.4 Phase Noise and Kernel Amplitudes

In the above analysis, I have noted that the effects of phase errors on visibilities enter at second order. Given that phase noise generally dominates over amplitude noise in ground-based observations, it is therefore important to examine these effects at higher order, and the possibilities of linear-order phase effects, which have not been hitherto included in the kernel amplitude derivation.

The principal effect of phase aberrations on visibilities is to bias them downwards: because of the triangle inequality, the length of the sum of N vectors with any orientations is necessarily smaller than when they are all lined up. In Figure 2.3, I show the results of a simple simulation to illustrate this. We add 1000 vectors (i.e., simulate a redundancy-1000 baseline) with the same length, and phases drawn from a uniform distribution of width s, which is displayed on the horizontal axis. We see that the visibility bias is smooth, with a small uncertainty at each scale, growing stronger

and more uncertain at higher phase noise levels. Importantly, near zero phase error, the function is locally flat, and so the block-diagonal transfer matrix approximation holds.

We see that at higher levels of phase noise ($\sim$ 0.5 rad), the bias increases, as does its variance. We see this error plotted for a range of redundancies in Figure 2.4. The error is much worse for lower redundancies than higher redundancies: as we add more vectors, the central limit theorem constrains the variance of the outcome more strongly.

In cases such as these, it seems likely that the moderate phase-to-amplitude off-diagonal block may be numerically simulated for a given visibility bias, which must be measured in practice from observations and cannot be determined a priori like the standard phase and visibility transfer matrices. The singular vectors of this matrix will generate a kernel *phase and amplitude* basis, though this added layer of complexity may not be of practical utility.

2.5 Simulation

In the following, I present the results of a number of simulations to determine the performance of kernel amplitudes relative to raw visibilities. As diffraction simulations to generate PSFs are much more computationally expensive than subsequently convolving these PSFs with binary or disk templates, I adopt the approach of using a single ensemble of PSFs and introducing successively fainter versions of a binary or disk, with all other parameters held fixed. As a result, the simulations in this section are intended to display the relative performance of the two techniques under identical conditions, rather than to forecast actual contrasts achievable in real observations. In Section 2.5.1 we search for a single point-like companion; in Section 2.5.2, we do the same as before, but testing for the effects of phase noise on kernel amplitudes; and in

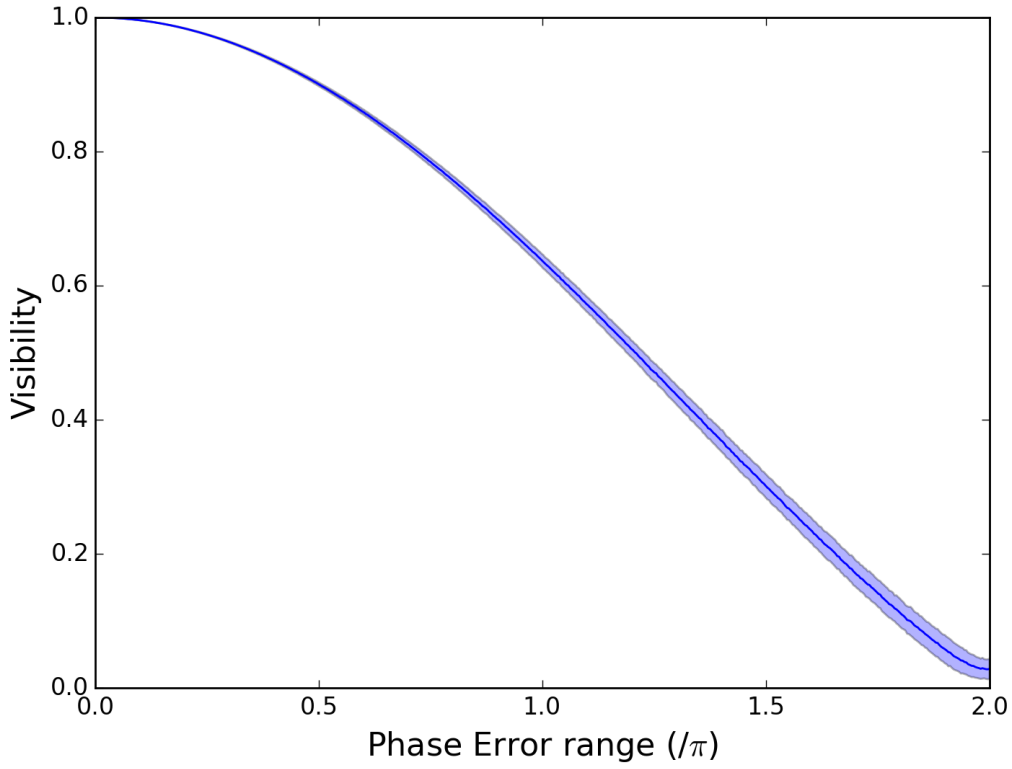

Figure 2.3: Visibility bias, with uncertainties (1σ), for a 1000-redundancy baseline, with equal visibilities and phases drawn from a uniform distribution of width s on the horizontal axis.

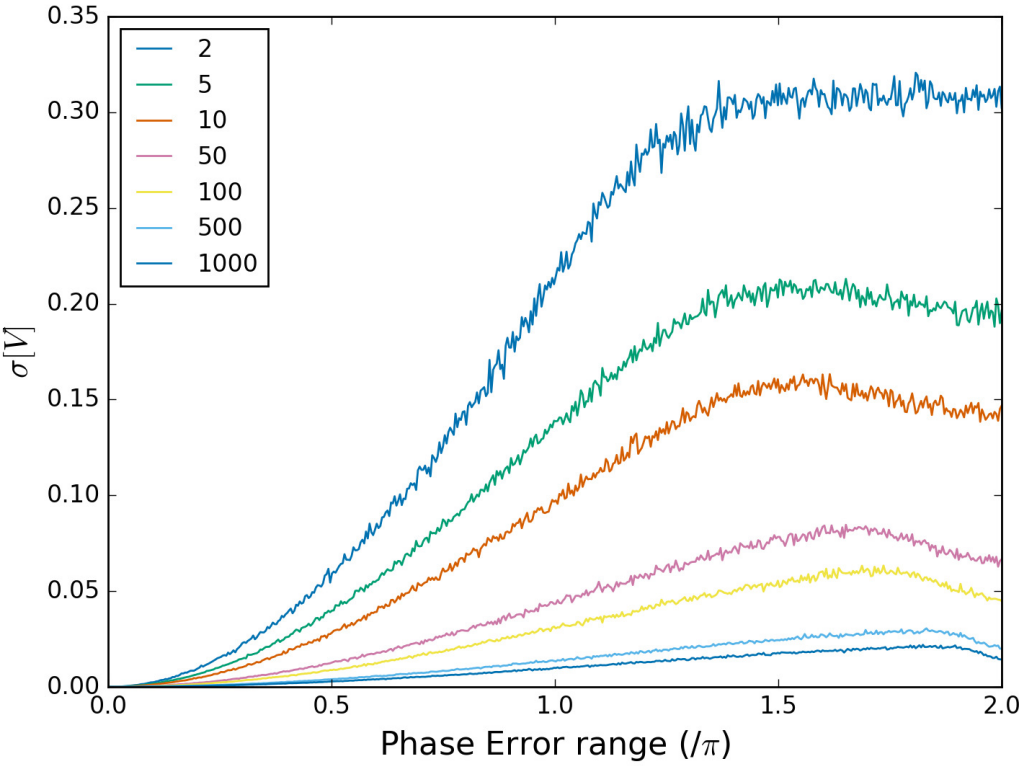

Figure 2.4: Visibility bias error: standard deviations of visibilities across 5000 simulations on a single baseline, for a range of baseline redundancies (listed in legend).

Section 2.5.3, we illustrate how kernel amplitudes are sensitive to a symmetric target (which kernel phases alone are necessarily insensitive to), in this case a circumstellar debris disk. In many but not al cases the kernel amplitude approach produces a less biased estimate, with more conservative errorbars, and typically extends comparable sensitivity to fainter contrasts than using raw visibilities alone.

In Sections 2.5.1 to 2.5.3, I have generated a sample of 100 amplitude screens, calculated using the analytic Rufenach (1975) power spectrum for Fresnel diffraction from a single layer of turbulence,

$$P_S = 4P_\phi \sin^2(\kappa_r^2/\kappa_F^2) \tag{2.21}$$

where P_ϕ is drawn from a Kolmogorov spectrum with $r_0 = 1$mm, κ_r is an isotropic spatial frequency and κ_F the Fresnel wavenumber $\kappa_F = \sqrt(4\pi/\lambda z)$, and z is the height of the turbulent layer, which we choose to be 30 km. This is simulated across a pupil of the same dimensions as the Palomar Hale 200-Inch Telescope (outer diameter 5.093 m, secondary diameter 1.829 m), and then scaled so that the amplitude is positive-definite with variations of a specified scale. These parameters are generous but not unreasonable, but specifically chosen to guarantee sufficiently low spatial frequency pupil plane speckles that these are computationally efficient to sample. A more detailed simulation would require a much denser discrete pupil model and correspondingly larger interferometric field of view. I also note that while these speckles are rather large for the fiducial Hale 200-Inch telescope model used here, a smaller telescope will more often experience scintillation speckles of a similar scale relative to the telescope diameter. An example of such an amplitude screen is shown in Figure 2.5.

These screens then multiply the pupil binary mask function to generate the input pupil plane. This is Fourier transformed to generate PSFs, which are then convolved

with source functions to generate images. No shot or detector readout noise is added. I then use MultiNest (Feroz et al., 2009, 2013) to conduct a Bayesian fit of an analytic parametric models to the ensemble mean of the squared visibilities or kernel amplitudes extracted from these.

2.5.1 Binaries

To test the stability of kernel amplitudes, we first simulate binary systems without any phase aberrations, from Kolmogorov spectrum scintillation screens of peak-to-trough variation 10% relative to the unaberrated image, to explore the effect of scintillation directly. (This is a high but not very high value, with typical scintillation ranging up to $\sim 1\%$ in RMS photometric amplitude with a more complicated spatial distribution). In the following, PSFs generated as above are shifted and added to simulate a binary at a varying contrast and a separation of 150 mas ($\sim 1.4\lambda/D$). I then fit an analytic binary model to the ensemble mean of kernel amplitudes or squared visibilities from these, taking a uniform prior in contrast (the ratio of primary to secondary flux) between $c/2$ and $2c$ for each input contrast c. The results are displayed in Figure 2.6.

I note that the fits from mean kernel amplitudes have smaller errorbars than those from raw visibilities, and that in all cases these overlap with the true value. This is not the case for visibilities: these fits are perturbed by systematics that are not well-accounted for and retrieve larger errorbars in position and a downward bias in contrast increasing as we push to the fainter end.

I expect that this effect is more pronounced at lower contrasts for higher-amplitude scintillations, and vice versa, and illustrates that while under good observing conditions visibilities behave well, that kernel amplitudes allow us to push to greater precision and sensitivity at a given level of scintillation.

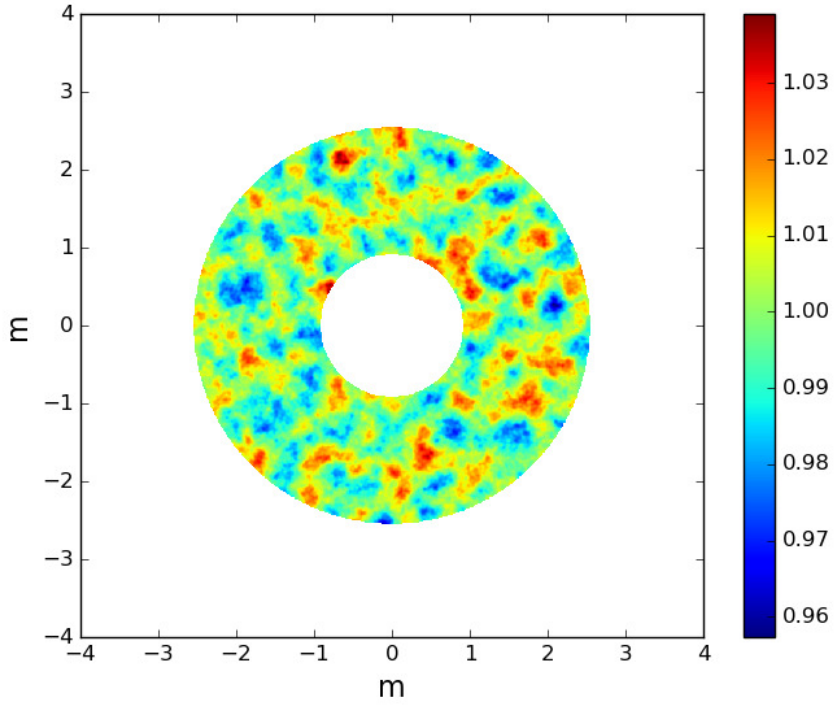

Figure 2.5: Example amplitude screen. Colourmap in dimensionless units of relative amplitude.

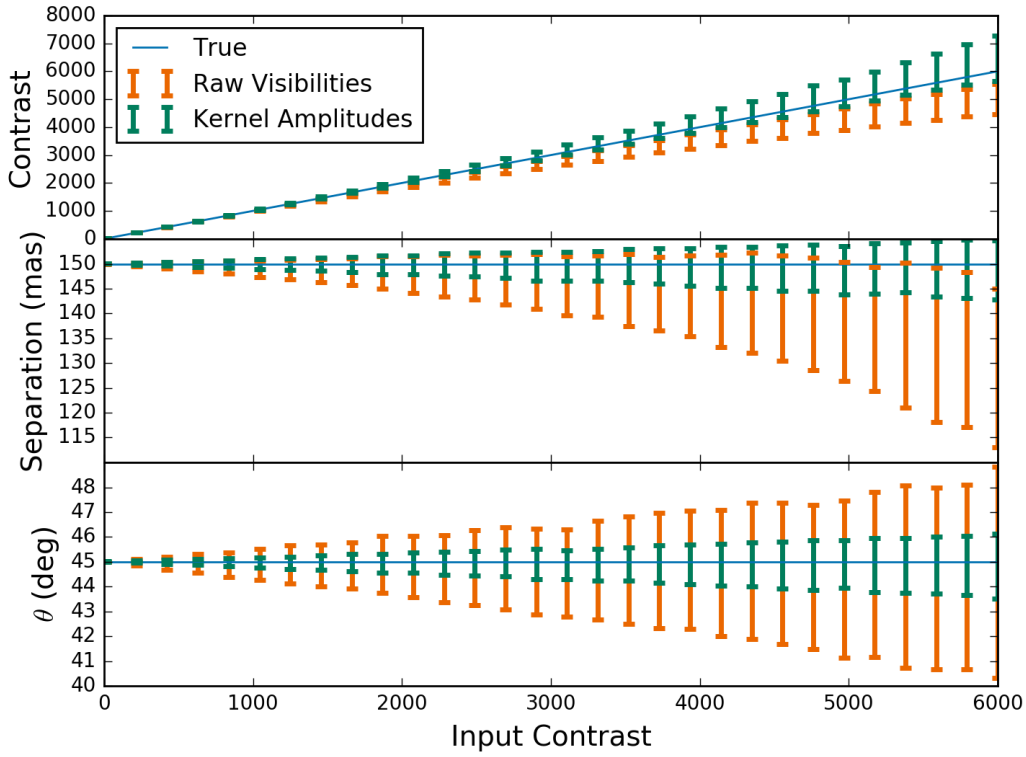

Figure 2.6: Kernel amplitude (dark teal) and raw visibility (bright orange) best fits to the ensemble mean of 50 sets as a function of input binary contrast, under conditions of 10% scintillation and no phase noise. Both methods obtain precise estimates at low contrasts, but at higher contrasts the estimate from fitting to raw visibilities is increasingly biased, while the kernel amplitudes maintain a close 1:1 correlation.

2.5.2 Phase Noise

To determine the effect of phase noise on the practical use of kernel amplitudes, I re-did the binary simulations in Section 2.5.1 with the same parameters, except with the pupil screen changed to a 1.5 rad peak-to-peak variation, where these are drawn from the same Gaussian random fields as in Section 2.5.1 scaled by a square root factor for consistency (as atmospheric scintillation ordinarily enters at second and higher order in the phase variation). These simulations include no amplitude noise. Binary models are then fitted as above, using the same kernel amplitude operator.

As seen in Figure 2.7, posterior parameter uncertainties are successively degraded to higher contrasts for both raw visibilities and kernel amplitudes, with no obvious indication of severe failure on either part out to high contrast and with neither obviously performing better or worse than the other in either contrast or angle, although visibilities perform better at reconstructing the separation. From these results, I take that the kernel amplitude is not much more adversely affected than the raw visibility, which is in line with our expectations that it should have no special self-calibrating property in this regard.

2.5.3 Disks

In addition to simulating binaries, which are inherently point-asymmetric images, I also simulate elliptical annuli as an example of centrosymmetric circumstellar disks. PSFs are generated as in Section 2.5.1, and convolved with a top-hat-like model which takes the value unity between two similar ellipses, and zero everywhere else. These are scaled by the desired contrast (taken as the ratio of total unresolved flux to disk flux) and added to the original PSF. An elliptical annulus has the analytic visibility function of the normalized difference between two ellipses, with five parameters: semi-major axis, eccentricity, position angle of the major axis, contrast ratio, and thickness (ratio of the difference in semi-major axes of the inner and outer ellipse, normalized

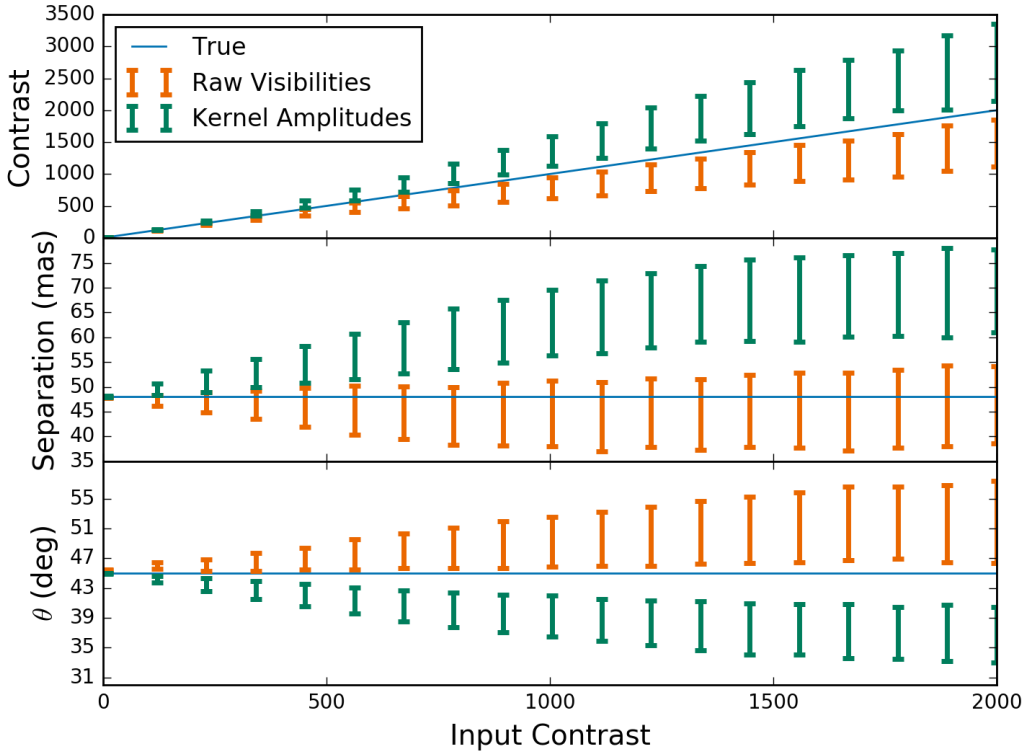

Figure 2.7: Ensemble mean kernel amplitude (dark teal) and raw visibility (bright orange) best fits as a function of input binary contrast, under conditions of phase noise with no amplitude aberrations.

to the outer).

We fit these in the same way as with the binaries in Section 2.5.1, except that with five parameters it is no longer feasible to fit each realization separately, so I only fit to the mean signal at each contrast. As seen in Figure 2.8, both kernel amplitudes and raw visibilities perform well at low contrasts, and then gradually lose effectiveness at higher contrasts. We see that raw visibility fits are biased low in contrast, with many-σ systematic discrepancies from the true contrasts, while for kernel amplitudes, error bars get larger but always include the true value. The two methods seem to perform similarly well as a function of contrast for $\Delta a/a$, with visibilities biased a little high and kernel amplitudes low, while for position angle θ, eccentricity e, and semi-major axis a (except at high contrast), kernel amplitudes offer more precise and accurate measurements out to high contrast.

As with the binary case in Section 2.5.1, the amplitude errors introduced are in practice very large in an observational context, and have been chosen to illustrate the difference between kernel amplitudes and visibilities. Higher contrasts will be reachable with lower amplitude noise. It is not apparent from Figure 2.8 that kernel amplitudes reach a dramatically better performance than raw visibilities for disks, but they nevertheless appear to be somewhat more accurate, and often more precise, than using raw visibilities.

2.6 Discussion

Kernel amplitudes have promise for improving observations in optical regimes where small-to-moderate amplitude aberrations are a limiting noise source. While phase aberrations are under normal circumstances a much more severe problem, correcting amplitudes is useful under several circumstances:

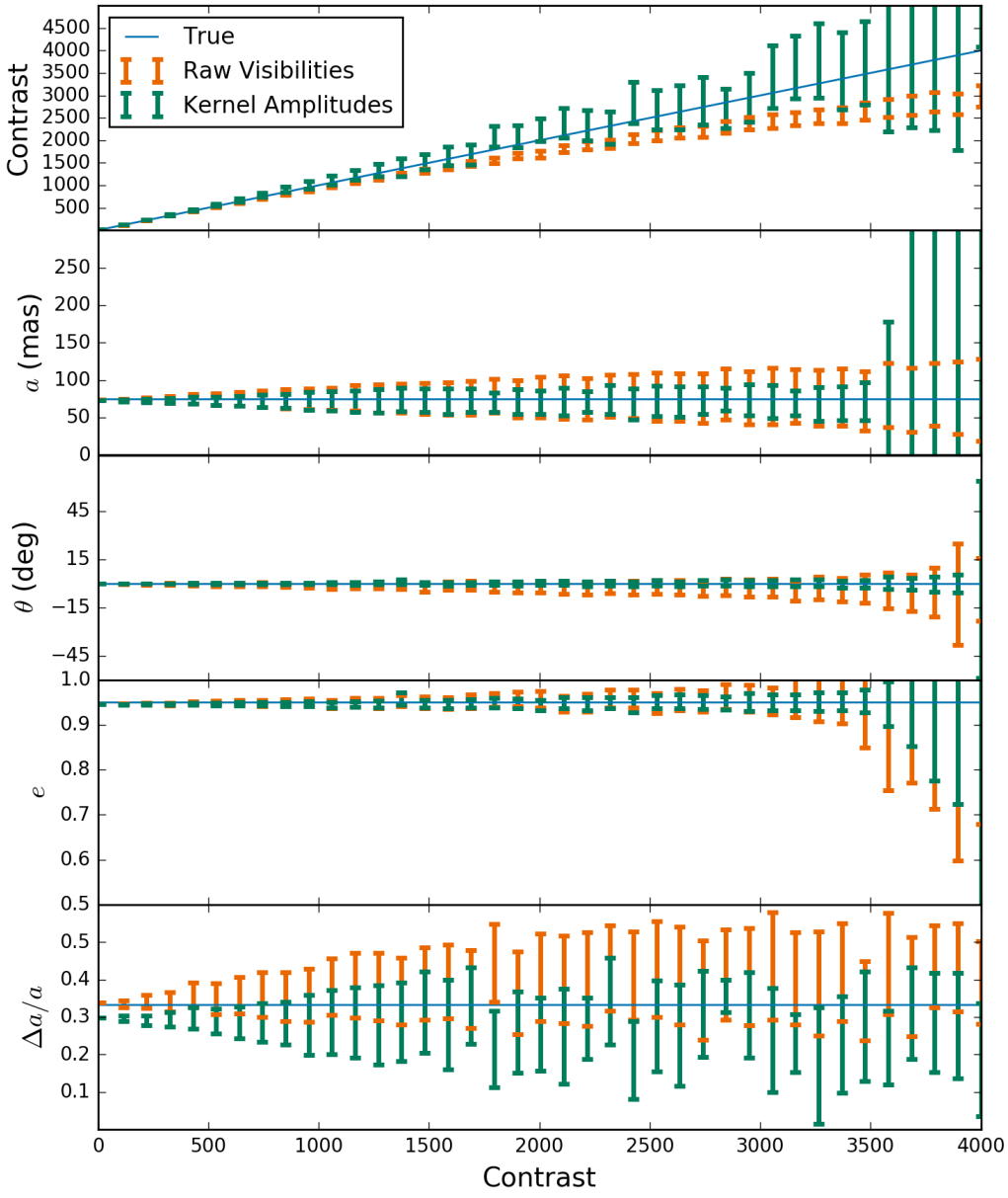

Figure 2.8: Ensemble mean kernel amplitude (dark teal) and raw visibility (bright orange) best fits for a disk model as a function of input binary contrast.

a) Amplitude errors arising from plane-wave atmospheric scintillation impose limitations on the performance of adaptive optics (Angel, 1994; Lee et al., 2006). In cases where these cannot be otherwise corrected, imaging performance may be enhanced by anchoring models or image reconstructions with kernel phases and amplitudes.

b) In certain cases it is important to establish with great precision the optical visibilities of an astrophysical object whose angular size is close to the diffraction limit of available telescopes. For instance, in studying dusty circumstellar environments with aperture masking, it is useful to consider differential visibilities between two polarization channels (Norris et al., 2012, 2015). In such situations, uncertainties in the throughput of each optical channel contribute significantly to the error budget. While future instruments may be able to directly measure this with pupil remapping (Perrin et al., 2006), for the present and near-term a software solution may be preferable. Differential (polarimetric) kernel amplitudes permit the extension of the experiments described above to, for example, the SPHERE-ZIMPOL extreme-AO polarimetric imager (Langlois et al., 2014). By using a filled pupil and extreme adaptive optics, kernel phases already enable us to push towards fainter objects than are accessible with the large throughput losses from aperture masking on comparable instruments. We have shown kernel amplitudes have the potential to enhance this effect in situations where scintillation is also a problem.

2.7 Conclusion

With kernel amplitudes and kernel phases, we now have a full formalism to describe all self-calibrating observables in a direct Fizeau imaging system, such as most full-aperture telescopes. This means that both even and odd symmetry components of an image reconstruction can now be directly based upon self-calibrating observations.

By including both even and odd image components, we will be able to improve existing methods of imaging stars, circumstellar and protoplanetary disks, and other astrophysical sources with both extended symmetric structure and embedded inhomogeneities. This may be of limited use in standard imaging, but in specialist cases where scintillation is the limiting factor (such as in Section 2.6) this may be a step forward. I hope that this will prove useful in forthcoming imaging campaigns with adaptive optics and space telescopes.

The fundamental theorem of linear algebra also implies that similar self-calibrating observables may be discoverable for other linear imaging systems, whenever the relevant measurement basis (e.g. baselines) is of substantially higher dimension than the pupil samples which generate it. It will be of compelling future interest to establish the extent to which this is true of coronagraphic systems, whose sensitivity to small phase and amplitude aberrations is a key limiting factor in the search for exoplanets.

In the interests of open science, IPython Notebooks and Python scripts implementing the simulations used in this Chapter are available at `https://github.com/benjaminpope/pysco`, under a GNU General Public License (v3).

Chapter 3

The Palomar Kernel Phase Experiment: Testing Kernel Phase Interferometry for Ground-based Astronomical Observations

Light is the left hand of darkness
and darkness the right hand of light.

Ursula K. Le Guin
The Left Hand of Darkness

3.1 Introduction

Kernel phase interferometry has not previously been used to resolve a close system with ground-based full-aperture extreme adaptive optics observations, and a detailed discussion of kernel phase reduction compared to other competing techniques has not been published. The method was first demonstrated for space-based observations: Pope et al. (2013) first applied kernel phase interferometry to a sample of brown

This Chapter has been published as Pope et al. (2016a).

dwarf systems imaged by Reid et al. (2006) and Reid et al. (2008) using the *HST*-NICMOS NIC1 camera, finding five additional binary systems. Martinache (2011) reported the extraction of kernel phases from a Keck II NIRC ground-based adaptive optics image, but did not report the detection of any companion, while Ireland & Kraus (2014) have presented a kernel-phase image reconstruction of the LkCa15 system in an M filter. In this Chapter, we discuss kernel phase and non-redundant masking (NRM) observations of the close binary system α Ophiuchi (α Oph, or Rasalhague) under identical observing conditions on the same night, with a view to using this as a benchmark for comparing the two methods. This is the first time such a simultaneous comparison has been made. A preliminary analysis of these observations was presented in conference proceedings by Martinache (2013a); Hinkley et al. (2015).

Hinkley et al. (2011a) carried out an adaptive optics NRM study of this system, a nearby binary with an A5 III primary, in order to characterise its orbital parameters. Hinkley et al. (2011a) find a contrast ratio of 27.9 ± 8.3 in the K band from resolved Palomar-PHARO (Hayward et al., 2001) imaging. The primary is known to be rotating at $\sim 89\%$ of its predicted breakup velocity (Zhao et al., 2009). It is a δ Scuti star, and asterosesimic analysis with MOST shows rotationally-modulated g-modes that probe the conditions of the interior (Monnier et al., 2010). Establishing its mass with precision is therefore valuable for constraining models of its rotational dynamics. Hinkley et al. (2011a) predicted the companion would pass periastron at $\sim$ 19 April 2012, and for this reason there was an observing campaign in 2012 to track its orbit at its apparent closest point, which is particularly critical in delivering a fully-constrained dynamical orbit. While α Oph is ordinarily a well-separated binary, at periastron the companion is buried within the PSF of the primary.

3.1.1 Observations

Observations were made on 26 June 2012, two months after periastron, using the PHARO camera on the 5.1 m Hale Telescope at Mt. Palomar Observatory. Data were obtained using a 9-hole aperture mask, an 18-hole aperture mask and with the full aperture (with no mask) in CH_4 and K_s bands, whose filters are centred at 1.57 μm and 2.145 μm respectively with bandpasses of 0.1 and 0.310 μm. The 9-hole mask contained projected baselines ranging from 0.75 to 4.15 m with a projected hole diameter of 0.5 m, while for the 18-hole mask the projected baselines ranged from 0.37 to 4.81 m with a projected hole diameter of 0.25 m.

In addition to α Oph, PSF reference stars ϵ Oph and ϵ Her were observed as calibrators. These data were then reduced to a standard FITS cube form using existing masking code. Regrettably, the full aperture observations in the CH_4 band suffered from poor AO performance and detector saturation and were excluded from the present study. The seeing varied between 1.5 and 2 arcseconds during the observations. By modelling the PSF, we determined the median Strehl across the exposures to have been ~ 0.51 in the K_s band.

In the full-pupil imaging, a neutral-density filter was used to diminish the brightness of the star, as is necessary to avoid saturating the science camera. This introduces a 'ghost' (a reflection artefact), which severely limits the maximum size of the window that can be used in kernel phase analysis, as discussed in Section 3.3. In future, it would be beneficial to choose filters in such a way as to avoid ghosts wherever possible, or to avoid using such filters altogether, for example by using very short exposure times or simply observing fainter targets.

Non-redundant 18-hole aperture masking observations with a Brγ filter were processed to obtain the arguments of the mean bispectrum, i.e. bispectral-amplitude-weighted average closure phases. We used a Markov Chain Monte Carlo (MCMC) method to fit a binary model to these closure phases, recovering a companion at

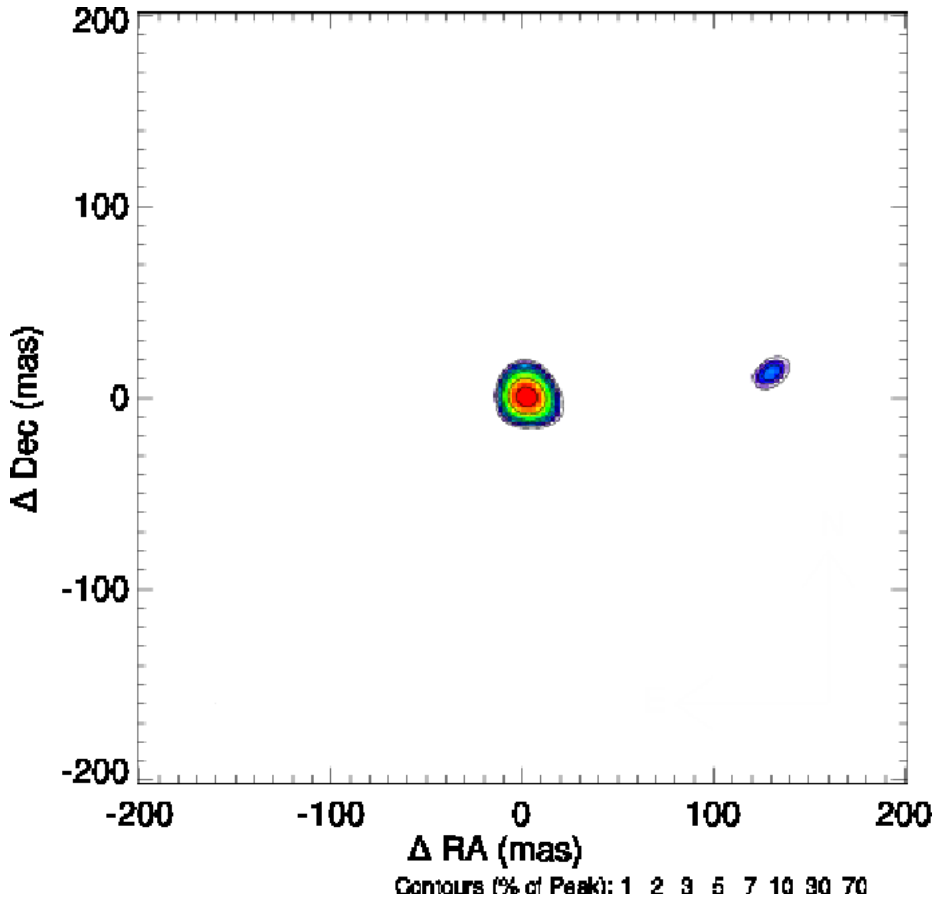

Figure 3.1: Maximum Entropy model-independent image reconstruction using BSMEM for K_s band non-redundant masking data.

131.2 ± 1.4 mas separation, position angle $82.8 \pm 0.7°$ and 27.6 ± 1.2 contrast. As we were not able to obtain Brγ observations with a filled aperture, these are useful only for comparison with the kernel phase data. Non-redundant 9-hole observations with a K_s filter found the same companion at 129.6 ± 2.2 mas separation, $83.5 \pm 1.1°$ position angle and 28.7 ± 2.3 contrast. This contrast ratio is consistent with the 27.9 ± 8.3 in the K band reported in (Hayward et al., 2001). In addition to this, we performed a maximum entropy model-independent image reconstruction using BSMEM (Figure 3.1), in which it is apparent that the parametric model accurately captures the information about the source intensity distribution. These aperture masking observations set the standard with which the kernel phase-based analyses must be compared.

3.2 Processing and Results

In Sections 3.2.1 and 3.2.2 we discuss the methods used to analyse data in this Chapter. In the interests of reproducibility and open science, we have made public our code and data: .FITS files for our raw data are stored on Figshare [1], together with the IPython notebook which was used to analyse these observations; and the PYSCO PYthon Self-Calibrating Observables package, a Python module for extracting and analyse kernel phase data, is available in a public GitHub repository [2]. All other packages used in this analysis are publicly distributed elsewhere. We welcome efforts by other researchers to apply this body of analysis software to these or other data, with appropriate citation.

In all full-frame images, the peak of the PSF pushed the detector into its nonlinear response regime. Kernel phase requires strict linearity, being a Fourier technique, and so each frame therefore had to be calibrated with a nonlinear gain curve map in order to restore linearity. The core of ϵ Oph was fully saturated in K_s band, and therefore ϵ Her was used as the sole calibrator.

3.2.1 Kernel Phase Extraction and Calibration

As discussed in Section 2.1, kernel phases are self-calibrating linear combinations of phases, which are robust with respect to small residual wavefront errors. We calculate a matrix to generate these *a priori* based on an assumed discrete model of the pupil.

We obtained direct images of the PHARO 'medium cross' pupil, and found the ratio of the outer radius to the central obscuration, and of this radius to the thickness of the spiders, to differ to a small extent from the nominal values reported in Hayward et al. (2001). This is very important to establish carefully, as information from longer baselines than exist in the telescope consists purely of noise and will corrupt any

[1] `http://figshare.com/s/4e69f7b2b30411e4bf4a06ec4bbcf141`
[2] `https://github.com/benjaminpope/pysco`

kernel phases obtained. In order to establish a precise pupil model as is necessary for kernel phase, we used the visibility amplitudes extracted from the point-source calibrator, ϵ Her, to constrain the overall scale of the pupil. This may differ from the published values because of an error in the measured projected pupil size, or an offset in the effective filter bandpass, which we model as the nominal K_s band centre of 2.145 μm, but may differ from this nominal value due for example to a slope in the stellar spectrum.

The absolute magnitude of the Fourier transform of the image of a point source, in the case of a flat wavefront, is a map of the optical modulation transfer function. This is itself found as the autocorrelation of the pupil, whose magnitude is approximately given by the redundancy of each baseline in a discrete pupil model. We therefore varied this overall outer scale in the vicinity of the value reported in Hayward et al. (2001), which lists a projected radius of 2.32 m. In order to be as sensitive as possible to the outer radius, we perform a least-squares fit by brute force between the logarithms of the redundancy matrix elements and the magnitude of the stacked Fourier transforms of all 100 observed frames. The fit is best-conditioned by the low visibilities, at the edge of the pupil, and there is some discrepancy at intermediate visibilities (low spatial frequencies), where we are sensitive to the faint binary-like signal of the ND filter ghost and residual low-order aberrations. Ideally, we would model this pupil cojointly with the binary model, and marginalize over uncertainties, which in the present circumstances we are unable to do due to the prohibitively long computational times. The best fit is found with an outer projected radius of 2.392 m, which we therefore adopt as fixed in the following analysis. The discretized pupil generated with this model is shown in Figure 3.2, containing 1128 elements, and generating 3256 baselines.

Using a singular value decomposition (SVD), we find this model to generate 2692 kernel phases. We centre each image in real space and recentre it to sub-pixel precision

by subtracting a phase slope in its Fourier transform, and apply this matrix to phases extracted from the corresponding 3256 baselines in this Fourier transform in order to obtain the kernel phases.

There are several differences between the application of kernel phase to this dataset and to the previously-published *HST* sample in Pope et al. (2013). In particular, each observation consists of a datacube of 100 frames, yielding excellent experimental diversity so that the statistics on each kernel phase can be readily recovered, as opposed to the case with the *HST* snapshot data where an ensemble average over many different targets was required. Kernel phases are therefore extracted separately from each frame of data, and then combined such that in the following Sections we take as our data the ensemble mean of each kernel phase over the set of frames, and the statistical uncertainties are taken to be the standard errors of the mean (SEM).

As is standard practice in NRM interferometry, the PSF reference stars ϵ Oph and ϵ Her were processed in the same way. By subtracting the kernel phases measured on these point sources, it is therefore possible to calibrate systematic offsets in the instrumental kernel phase measurements. The uncertainties on each of the calibrator's kernel phases, again taken to be the standard error of the mean, are added in quadrature to the uncertainties on the science target's kernel phases.

In addition to this, we also add in quadrature a second error term of 1.35° to account for uncalibrated systematic errors. We fit a parametric binary model to the data as described in Section 3.2.2, and iteratively adjust the magnitude of this additional error term so that the reduced χ^2 of the best-fitting parameters is approximately unity.

3.2.2 Bayesian Parameter Estimation

The next step is to fit a parametric model to these kernel phase data, defined by the binary parameters separation (mas), position angle (deg) and contrast, proceeding

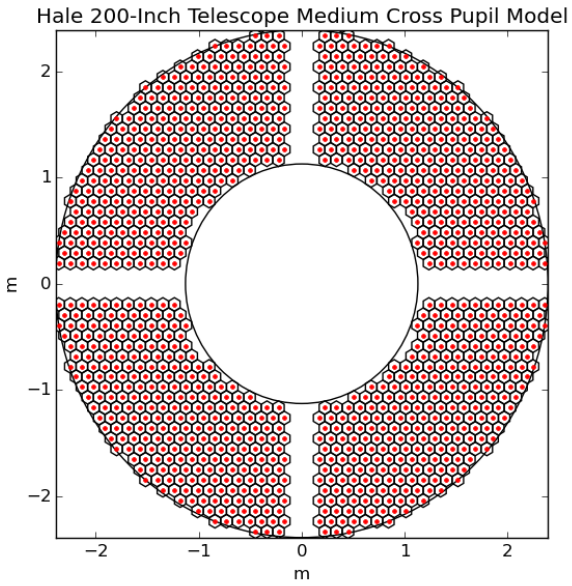

Figure 3.2: Hale Telescope medium-cross pupil model. Red dots represent pupil sampling points; note that they avoid the spiders, which on the Hale Telescope are vertical and horizontal with respect to the detector axes.

in a similar fashion to Pope et al. (2013). We estimate these parameters using two Bayesian inference algorithms, namely MultiNest (Feroz et al., 2009), an implementation of multi-modal nested sampling, and emcee (Foreman-Mackey et al., 2013), an affine-invariant ensemble Markov Chain Monte Carlo sampler. We used both approaches firstly as a check for consistency, but also because they have complementary strengths (Allison & Dunkley, 2014): on the one hand, MultiNest efficiently and reliably converges on the global peak of a posterior distribution without significant sensitivity to an initial guess and avoids being trapped in local likelihood maxima. On the other hand, emcee is more effective at exploring and characterizing potentially non-Gaussian, curving degeneracies in the shape of the posterior mode; as noted in Pope et al. (2013), there is typically significant degeneracy between separation and contrast in kernel phase fits to systems at close to the diffraction limit, and it is important to explore the shape of this curve.

We began by running MultiNest, obtaining the parameter estimates listed in

Table 3.1. The corresponding correlation diagram is displayed in Figure 3.3. After our first attempt with no additional uncertainty added in quadrature, we iteratively re-ran the MCMC adding an additional error term in quadrature until the fit of the posterior mean achieved a reduced χ^2 of approximately unity. This term was found to be $\sim 1.35°$ in the kernel phase case, and $7.0°$ in the case of the bispectral phases.

As discussed above, interferometric determinations of binary parameters at close to the diffraction limit often suffer from degeneracy between contrast and separation. As a result, we used the MultiNest output to initialize an emcee run with 100 walkers and 200 burn-in steps and recorded 1000 subsequent steps to sample from the posterior. From this, it is apparent that there is only a small degree of covariance between these parameters, and we find good agreement between the MultiNest and emcee estimates of the posterior mean and standard deviation.

In order to test whether the kernel phase processing itself introduces a bias into the contrast and separation estimates, we simulated binaries with the same parameters each as the best fit to the kernel phase full aperture observations and to the non-redundant 9 hole closure phase measurements. These simulations use no atmosphere, but include a realistic Palomar 'medium cross' pupil model identical to that used to derive the kernel phase relations. Model fitting is performed with MultiNest as in Section 3.2.2, with uncertainties on each kernel phase taken to be the same as from the real observations. For an input model with the parameters of the kernel phase model (129 mas, 83.6 degrees, 34.2 contrast) we retrieve 129.4 ± 1.2 mas separation, 83.5 ± 0.3 deg position angle and contrast 34.3 ± 1.0; and for the aperture masking parameters (129.6 mas, 83.5, 28.7 contrast), we retrieve 129.7 ± 1.0 mas, 83.5 ± 0.3 deg and 28.8 ± 0.8 contrast. It is evident from these fits that kernel phase fitting itself introduces no bias towards lower contrasts.

Table 3.1: Binary Parameter Estimates for α Ophiuchi at JD 2456104.847025.

Mode	Separation (mas)	Position Angle (deg)	Contrast (K_s)
Kernel Phase	129.3 ± 1.2	83.6 ± 0.3	34.2 ± 1.1
PSF Fitting	131.9 ± 0.5	84.3 ± 0.4	19 ± 2.4
Aperture Masking	129.6 ± 2.2	83.5 ± 1.1	28.7 ± 2.3
Bispectral Phase	140.9 ± 1.0	86.7 ± 0.7	15.4 ± 0.7

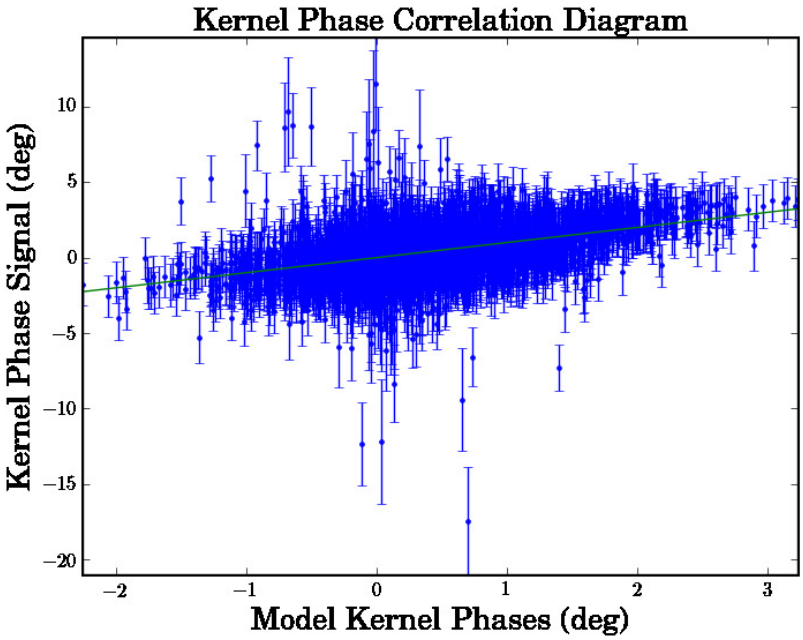

Figure 3.3: Correlation diagram for α Ophiuchi kernel phases in K_s band. We plot model kernel phases on the x-axis and the observed signal on the y-axis, such that for a good fit we expect the data to lie on a straight line of gradient unity (overplotted green line).

3.2.3 Comparison with Filled-Aperture Bispectral (Closure) Phase Analysis

Using the same full-aperture observations analysed with kernel phase in Section 3.2.2, we also performed an identical analysis using the arguments of the bispectrum, i.e. closure phases. The closure phases are the arguments of the bispectrum or 'triple product' of three complex visibilities around a closing triangle, and we therefore call these closure phases or bispectral phases interchangeably. Roddier (1986) recognized bispectral analysis as being equivalent to the existing triple-correlation method of speckle masking (Labeyrie, 1970; Weigelt, 1977), and it provides a more robust observable than raw phases even on partially redundant pupils (Haniff & Buscher, 1992).

For a redundant pupil, there are a combinatorically large number of baselines, and for reasons of hardware memory we are not able to use a pupil model as dense as in the above kernel phase analysis. We instead use a pupil model with the same dimensions but only 508 pupil samples. Using this coarser model we conduct a kernel phase fit, finding good agreement with the denser model, with a separation of 127 ± 1.8 mas, a position angle of 83.2 ± 0.4 degrees, and a contrast ratio of 32.2 ± 1.4. We see that this is in reasonable agreement with the denser model and aperture masking observations.

We then find all possible combinations of triangles and test for closure, finding 378662 closing triangles in our redundant pupil model. As there are only 1456 independent u, v baselines, the information in the raw bispectrum is extremely redundant, and unless we model our data in a reduced-dimensionality representation, we will both encounter unnecessary computational cost, and underestimate our uncertainties. We therefore first construct the 378662×1456 matrix containing the full set of closure relations, and find a rank-reduced operator with the same range using a sparse SVD. Using this, we find that the space of closure phases is spanned by the expected $N_{baseline} - 2 = 1454$ orthonormal vectors, and use these as our bispectral observables. These are therefore linearly-independent closure phases (Sallum et al., 2015a), but

we do not have a sufficiently large number of observations to re-diagonalize these as statistically-independent closure phases as in Kraus & Ireland (2012); Ireland (2013). It is important to note that in the general non-redundant cases these orthonormal closure phases do not span the same space as kernel phases, and that only in the case of a non-redundant pupil are these two spaces of observables expected to be the same. Ideally, we would for each triangle average the complex bispectrum across all frames, extract the phase of the resulting mean complex bispectrum, and then project these onto the minimal spanning set of orthonormal closure phases. Due to the combinatorically large number of triangles this is not possible, and we instead average the orthonormal closure phases themselves.

Data are processed as for the kernel phases in Section 3.2.1, except using this orthonormalized matrix of closure phase relations instead of the kernel phase matrix. We recover the binary at a separation of 140.9 $\pm$ 1.0 mas, 86.7 $\pm$ 0.7 degree position angle and a contrast of 15.4 $\pm$ 0.7. The very small uncertainty quoted on this fit is statistical, and clearly the dominant error here is systematic. The position angle and separation are roughly similar to that determined in Section 3.2.2 with kernel phase, but offset by $\sim$ 10 mas in separation, and the best-fitting contrast is much lower, at 15.4 $\pm$ 0.7, which is $\sim$ 2 times lower than the best kernel phase or masking estimate and similar to that from PSF fitting. This is consistent with the effects of a speckle introduced by a phase aberration perturbing all the full-frame images, while kernel phase and aperture masking are by construction resilient against this form of aberration.

While the difference in sampling density means that we do not compare the kernel phase and bispectral methods on a level playing field, we note that finding the full set of triangles generated by the denser model was not possible due to memory constraints, and therefore the bispectral method is inherently more limited than kernel phase in its applicability to very dense, redundant pupils. We are therefore restricting

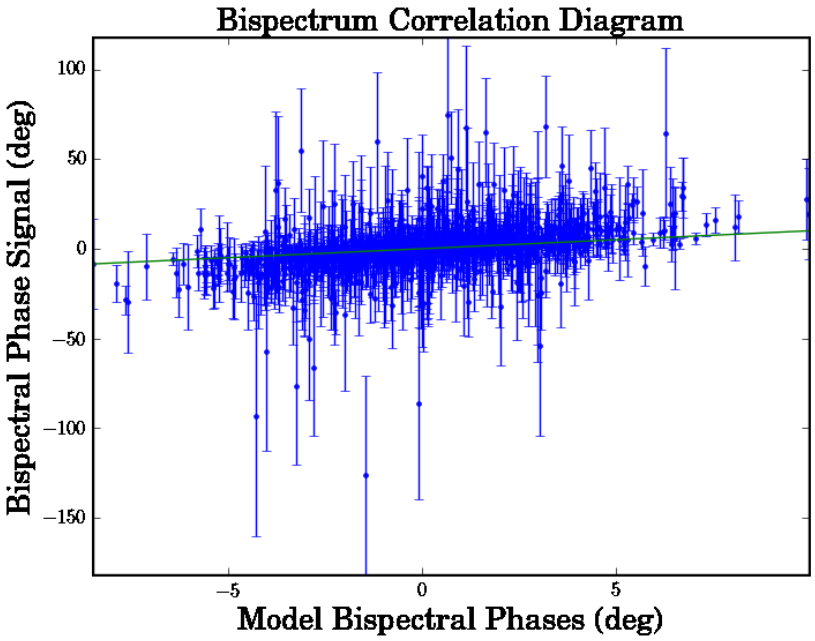

Figure 3.4: Correlation diagram for bispectral phases for α Ophiuchi in K_s band. We plot model phases on the x-axis and the observed signal on the y-axis, such that for a good fit we expect the data to lie on a straight line of gradient unity.

our comparison to methods of equivalent computational resource usage.

3.2.4 Comparison with PSF Fitting

In this situation we lack the diversity of calibration images to use the most advanced PSF analysis techniques, such as LOCI (Lafrenière et al., 2007) or KLIP (Soummer et al., 2012), but the 100 frames of our single calibrator are sufficiently diverse to permit PSF fitting. We adopt a maximum-likelihood approach, finding the best-fitting incoherent sum of two shifted calibrator PSFs that minimize a χ^2 objective function for each individual frame of α Oph. The offset and scaling between these two calibrator PSFs is then taken to be the model parameters of the binary system. In Table 3.1 we report the mean and standard error of the mean of all such fits with a χ^2 within a factor of 2 of the median χ^2 across all frames, to allow for the possibility of failing to retrieve the binary in some frames.

We note the low contrast found in the results of PSF fitting, not found in the kernel

phase analysis. We suggest that a quasi-static speckle very close to the position of the binary companion, or a variable incoherent second ghost at the same location, could cause this effect, which is corrected in the kernel phase approach. This good kernel phase correction is consistent with this being a phase-aberration induced speckle; in the case of an amplitude-induced speckle, it would be desirable to find an equivalent 'kernel amplitude' which would be self-calibrating with respect to such an aberration, but such a quantity is not presently known.

We note that this PSF fitting approach is enabled by the diversity over both many calibrators and many frames on each calibrator, whereas in principle any single image can be analysed with kernel phase given appropriate single images of calibrators. This is an advantage for kernel phase in campaigns where many short exposures are not feasible, or in space telescope snapshot campaigns, where PSF diversity may otherwise be lacking.

3.3 Comparison between Masking and Kernel Phase

For our benchmark α Oph dataset, the kernel phase analysis strongly favours a binary model over a point source, and successfully obtains the same system configuration as found with aperture masking. The results are displayed in Table 3.1. The spatial astrometric components agree remarkably well, to much better than 1σ, and in contrast the kernel phase is slightly higher, at 34.2 vs 28.7. As the uncertainties on each are ~ 1.1 and ~ 2.3 respectively, we see these estimates do not entirely agree, though the higher contrast value derived from kernel phase may represent a systematic error which may require further improvements to the method. As noted below, the uncertainties on the kernel phase-derived contrast are probably underestimated here, though with present software implementations and the limited number of frames available in these observations, this cannot be resolved at present. Nevertheless, it is

clear that kernel phase presents a realistic alternative to aperture masking for telescopes with extreme AO, with the potential for significant advantages in throughput and Fourier coverage.

The science target was observed in the middle of the detector, near the corner of the four CMOS chips which tile the focal plane. This leads to lines of noise running through the sides of the PSF. On the other hand, the calibrators were observed in the middle of each chip ('dithered'), as is standard practice. The subtraction of systematic errors from the science data was therefore imperfect, and in future it will be important to dither the science source and calibrators identically.

The binary astrometry from kernel phase is reasonably close ($\sim 1.5-2\sigma_{masking}$) to that obtained by aperture masking; this is remarkably good agreement given that the observations were performed under far from ideal conditions: as noted in Section 3.1.1, on the night these observations were made, the seeing was $1.5-2$ arcseconds, which is substantially worse than median for Palomar. This translated to the relatively low Strehl of 0.5 in K_s, somewhat low for extreme-AO and toward the lower end of the kernel phase regime. We therefore note that we may expect improved performance under better AO conditions in future.

The retrieved binary parameters are remarkably insensitive to the size of the super-Gaussian window used in preprocessing. By the convolution theorem, windowing an image is equivalent to convolving its Fourier transform with a kernel whose dimension is inversely proportional to that of the window. A narrower window therefore has a wider convolution kernel, which blurs Fourier phase information. This results in both a blurring in the Fourier plane, which is especially significant at high spatial frequencies where this mixes real signals from inside the support of the modulation transfer function with noise from outside its support.

In addition to the above instrumental errors, we noted in Section 3.2.4 that systematic optical aberrations are likely to remain even after calibration. By using an ensem-

ble of calibrators as described in Kraus & Ireland (2012), it is possible to substantially improve the correction of systematic errors. Residual uncalibrated systematics enter at first order in phase, and third order in kernel phase, and can introduce statistical correlations between kernel phase relations which are algebraically orthogonal. It is possible to diagonalize kernel phases and closure phases in a Karhunen-Loève basis which properly takes into account their statistical covariance (Ireland, 2013); such a calibration is improved significantly with greater calibrator diversity than is available in this work. In future, it will be valuable to include more calibrator sources, and observe these and the science target with a range of pupil orientations to maximize the calibration diversity. We expect that this may reduce systematic effects, and also increase the parameter uncertainties somewhat, given that presently we assume data to be independent which are in fact correlated.

The issue of pupil modelling remains an outstanding problem for kernel phase, in that at present it is not feasible to marginalize over uncertainties in pupil scale, or to model the pupil as densely as may be preferred for high-performance applications. There are therefore systematic errors associated with any mismatch between the discrete pupil model and the real effective model of the telescope, as well as any amplitude aberrations or spatial variations in transmission. Resolving this difficulty is beyond the scope of this Chapter, but will be important for future work.

3.4 Discussion

The recovery of the α Oph binary system illustrates both the potential of kernel phase in conjunction with extreme AO, and the potential for improvements in future observations. It is clear that kernel phase recovers the binary parameters with remarkable precision, and it will be a valuable tool in probing systems than cannot be observed with aperture masking. In this test case, under ideal conditions for aperture masking

and more challenging conditions for kernel phase, nevertheless kernel phase delivers comparable results. The performance of kernel phase in this low to moderate Strehl, single calibrator regime is not expected to be representative of higher Strehls and multiple calibrators - an analysis of which would be important future work.

We have also demonstrated the benefits of using kernel phases over more standard PSF fitting and bispectrum (closure phase) approaches in parameter estimation. Deconvolving structure from an AO-corrected PSF is significantly enhanced by the use of kernel phase, and we expect this will enable new science to be done at and near the diffraction limit.

As noted in Pope et al. (2013), wavelength diversity across several filters can help alleviate the degeneracy between separation and contrast, by jointly fitting to kernel phases extracted in several bands and enforcing the condition that the position of a companion must be fixed, while its flux can vary. This is a promising option for future kernel phase work, as the extreme AO systems SPHERE and GPI are equipped with integral field spectrographs which can obtain images in many wavelength channels simultaneously.

Given these encouraging results, we see that the best current adaptive optics systems are already able to make use of kernel phase for high contrast imaging. In particular, we have shown that in the extreme-AO regime, kernel phase obtains comparable results to those using non-redundant masking. Where for hardware reasons or due to throughput considerations it is not possible to use a mask, or where very dense Fourier coverage is desired for imaging, the kernel phase approach may be much more effective than standard alternatives, opening up new parameter space for high-resolution imaging of faint companions and circumstellar environments. We have also discussed observing strategies, and in particular the importance of calibrator sources and wavelength diversity, which will be of use in planning future kernel phase work from the ground.

Chapter 4

Transiting exoplanet candidates from *K2* Campaigns 5 and 6

He, who through vast immensity can pierce,
See worlds on worlds compose one universe,
Observe how system into system runs,
What other planets circle other suns,
What varied being peoples ev'ry star,
May tell why Heav'n has made us as we are.

Alexander Pope, *Essay on Man*

4.1 Introduction

In this Chapter we present a new pipeline to correct *K2* light curves for instrumental systematics and stellar variability, search them for planetary transit candidates, and perform a series of diagnostic tests to weed out false positives. We apply this pipeline to Campaigns 5 & 6 (hereafter C5 and C6), identifying 77 and 71 single-planet candidates among the 25139 and 28291 targets surveyed in each Campaign, as well as 5 systems showing multiple sets of transits. While our method is applicable to any *K2* light curve, and indeed readily adaptable to data from other instruments, a par-

The material in this Chapter has been published as Pope et al. (2016b).

ticular focus of its design has been to ensure good performance for young, variable stars, which represent a larger fraction of the most interesting targets for *K2* than for previous transit search missions.

The different pipelines used on *K2* data to date differ in subtle ways from each other, and from ours, at every stage of the light curve detrending, transit search and vetting process, but particularly important differences are found in the light curve extraction and detrending step. This is because of the importance of instrumental systematics (and, to a lesser extent, stellar variability) in *K2* data. In the *K2* mission, the *Kepler* satellite is balanced at an unstable equilibrium, using two reaction wheels and with solar radiation pressure keeping the third axis approximately steady. The third axis orientation must be maintained, however, by small thruster firings every $\sim$ 6 hours, moving a typical star by of order $\sim$ 1 pixel across the detector, with the result that *K2* data contain significant pointing-related systematic photometric trends that make robust inference about the presence of planets more difficult than in the nominal *Kepler* mission. Several data-reduction pipelines have been developed by different groups to compensate for this effect (Vanderburg & Johnson, 2014a; Aigrain et al., 2015; Armstrong et al., 2015; Foreman-Mackey et al., 2015b; Lund et al., 2015; Luger et al., 2016, 2017), including our detrending pipeline (which we use in this Chapter) (Aigrain et al., 2016, hereafter APP16). A unique feature of our approach is that systematics and stellar variability are modelled simultaneously rather than sequentially, which significantly improves the results when both effects are significant, especially on similar timescales. The methods used in the remainder of our pipeline for transit search and vetting are relatively standard, but were implemented with particular attention to scalability and computational efficiency, and in such a way as to enable easy, uniform human vetting at the present time, as well as – in the future – progression towards a fully probabilistic asssessment of the likelihood that individual candidates are *bona fide* planets.

The remainder of this Chapter is structured as follows. Sections 4.2, 4.3 and 4.4 describe our light curve preparation, transit search and vetting methodology, respectively. Our catalog of transiting planet candidates from C5 and C6 is given in Section 4.5, together with the results of preliminary spectroscopic reconnaissance. Section 4.6 gives links to the code used in our pipeline, all of which is publicly available, and we give our conclusions and discuss plans for future improvements in Section 4.7.

4.2 Light Curve Preparation

K2 photometric time series are typically affected by sawtooth-like variations in measured flux, due to the drift and subsequent thruster reset of the spacecraft boresight roll angle. This effect, needed to maintain spacecraft pointing near the unstable equilibrium induced by solar radiation pressure, causes each star to move by of order ~ 1 pixel over the course of each thruster-reset period of ~ 6 hours. This is translated into variations in flux by the differential sensitivity between pixels (inter-pixel variations) and across the surface of each pixel (intra-pixel variations), and by the loss of light outside the photometric aperture as it imperfectly matches and tracks the point spread function (aperture losses). Other systematic effects are also present (as they were in the light curves from the original *Kepler* mission), but the pointing-related variations are by far the most prominent. In addition to these instrumental systematics, the light curves also contain intrinsic stellar variability, most commonly due to the rotational modulation of star spots. Both systematics and variability can severely hinder the detection of planetary transits, and must be filtered or modelled before the transit search can proceed.

The standard approach until now has been to do this sequentially, first modelling the systematics while ignoring the variability, then using some variation on a high-pass

filter to remove most of the variability while preserving any planetary transits (the latter step exploits the fact that transits occur on shorter timescales than most forms of stellar variability). However, this approach breaks down when both systematics and variability are of comparable amplitude, and occur on similar timescales. While the typical rotation periods of *K2* target stars (days to weeks) are significantly longer than the ~ 6 hour characteristic timescale of the pointing variations, there is nonetheless significant power in the variability of many stars on 6 to 12-hour timescales. This is particularly problematic for *K2*, which observes a larger fraction of young, rapidly rotating, active stars than earlier transit-search missions. In such cases, modelling the systematics and variability simultaneously tends to be more effective, particularly if – as in the case of *K2* – the systematics can be constrained to depend primarily on the star's position on the detector, which should have no impact on its intrinsic brightness. This is the approach implemented in the K2SC pipeline (APP16), which uses a Gaussian process to model the systematics and variability simultaneously.

Gaussian Processes (GP) are a family of non-parametric models for data analysis (pioneered in the context of mining by Krige, 1951; Matheron, 1963), whose early history is reviewed by Cressie (1990) and whose recent applications in time-series modelling are described by Rasmussen & Williams (2005) and Roberts et al. (2012), the notation of the latter of which we will use here. A GP defines a probability distribution over functions, such that any finite set of discrete samples from these functions are jointly Gaussian-distributed, with a likelihood function for data $\mathbf{y}(\mathbf{x})$

$$p(\mathbf{y}(\mathbf{x})) = \mathcal{N}(\mu(\mathbf{x}), \mathbf{K}(\mathbf{x})) \tag{4.1}$$

$$= \frac{1}{\sqrt{(2\pi)^N \det \mathbf{K}}} \exp\left(-\frac{1}{2}\mathbf{y}^T \mathbf{K}^{-1} \mathbf{y}\right) \tag{4.2}$$

where μ is a mean function, and $\mathbf{K}$ is a covariance matrix whose entries are $K_{ij} = k(x_i, x_j)$, where x_i is the i^{th} sample of a discrete vector. The covariance function

$k(x_1, x_2)$ is used to describe the overall structure of the the function for regression. Ordinary least-squares fitting or χ^2 minimization is a special case of a GP where the covariance matrix is diagonal and with N data points:

$$p(\mathbf{y}(\mathbf{x}))\frac{1}{\sqrt{(2\pi)^N\sigma^{2N}}}\exp(-\frac{1}{2}\chi^2) \tag{4.3}$$

The difference here is that the more general GP allows for *correlated* noise as opposed to the white noise in standard least squares fitting, although white noise can be included easily in $\mathbf{K}$. While the input $\mathbf{x}$ may simply be time, it can represent arbitrary quantities and include more than one dimension, for example in the K2SC pipeline where it includes the $2D$ position on the detector. This is easily implemented, because if multiple input variables such as time $\mathbf{t}$ and $2D$ position $(\mathbf{x}, \mathbf{y})$ are independent, then the GP probabilities multiply and therefore their exponents add, so that the sum of separate GP covariances depending on different variables is also a valid GP covariance taking a multidimensional argument. Therefore in the following equations, the argument written $\mathbf{x}$ of $\mathbf{K}$ is potentially multi-dimensional, e.g. $(\mathbf{x}, \mathbf{y}, \mathbf{t})$, and we use $\mathbf{x}$ and $\mathbf{y}$ as placeholders for the input and output for simplicity.

If we condition our GP on some observed data $\mathbf{y}(\mathbf{x})$, then we can predict the distribution for observations $\mathbf{y}_*(\mathbf{x}_*)$, which is also normally-distributed:

$$p(\mathbf{y}_*(\mathbf{x}_*)) = \mathcal{N}(\mathbf{m}(\mathbf{x}_*), \mathbf{C}(\mathbf{x}_*)) \tag{4.4}$$

From the standard Gaussian conditional and marginal identities, the posterior mean $\mathbf{m}(\mathbf{x}_*)$ and covariance $\mathbf{C}(\mathbf{x}_*)$ are given by

$$\mathbf{m}_* = \mu(\mathbf{x}_*) + \mathbf{K}(\mathbf{x}_*, \mathbf{x})\mathbf{K}(\mathbf{x}, \mathbf{x})^{-1}(\mathbf{y}(\mathbf{x}) - \mu(\mathbf{x})) \tag{4.5}$$

$$\mathbf{C}_* = \mathbf{K}(\mathbf{x}_*, \mathbf{x}_*) - \mathbf{K}(\mathbf{x}_*, \mathbf{x})\mathbf{K}(\mathbf{x}, \mathbf{x})^{-1}\mathbf{K}(\mathbf{x}_*, \mathbf{x})^T \tag{4.6}$$

The prior mean μ represents a deterministic component to the model, while the covariance kernel k represents a stochastic component incorporating both astrophysical variability and instrumental systematics. k and μ are in general parametrized by *hyperparameters*. In the model used in K2SC we have a mean normalized flux of unity with no free parameters, while the stochastic model contains two distinct components: the first depends on time only, and represents the variability (plus any residual systematics not related to position), and the second depends on position only and represents the pointing-related systematics. We model the stellar variability one of two ways, either with the quasi-periodic exponential sine squared kernel in time (Rasmussen & Williams, 2005)

$$k(t_i, t_j) = A_t \exp\left(-\Gamma \sin^2\left(\frac{\pi}{P}|t_i - t_j|\right)\right) \tag{4.7}$$

where Γ is a correlation scale, P the period of oscillations. and A_t is the amplitude of the time variations, or with a squared exponential kernel

$$k(t_i, t_j) = A_t \exp\left(\frac{-|t_i - t_j|^2}{2\tau^2}\right) \tag{4.8}$$

where τ is a timescale for correlations. We decide between the two by calculating a Lomb-Scargle periodogram (Lomb, 1976) of the input lightcurve; if this shows a strong periodicity, we choose the quasi-periodic kernel. Otherwise, we represent stellar variability with a slowly-varying squared exponential kernel. In either case, the covariance kernel for position is squared-exponential with a separate length scale for each dimension:

$$k(x_i, x_j, y_i, y_j) = A_{xy} \exp\left(-\frac{1}{2}\frac{|x_i - x_j|^2}{l_x^2} - \frac{1}{2}\frac{|y_i - y_j|^2}{l_y^2}\right) \tag{4.9}$$

Because the sum of two GPs is also a GP, we are free to use the sum of these models

as a joint model for the systematics and stellar variability. We therefore have the final covariance kernel

$$\mathbf{K}_{tot} = \mathbf{K}_t + \mathbf{K}_{xy} + \sigma^2 \mathbf{I} \tag{4.10}$$

incorporating a diagonal matrix with entries σ^2 to represent white noise.

A sophisticated outlier rejection scheme is used to ensure that flares, eclipses and transits do not adversely affect the modelling, but are nonetheless preserved. We optimize the hyperparameters of the covariance function k_{tot} (namely σ, (l_t, l_x, l_y) or (Γ, P, l_x, l_y), A_t and A_{xy}) in order to obtain the best fit to a given dataset, taking the posterior means with optimized parameters as our final model. The corrected flux is then the raw flux minus the predictive mean for the x, y component, with time held constant, and the inferred astrophysical variability is the predictive mean for time with x, y held constant. This systematics correction scheme is described in further detail in APP16.

We begin with the *K2* light curves available at the Mikulski Archive for Space Telescopes (MAST), which we process with K2SC to remove both systematics and variability. We exclude EPICs 200008644 – 200009280 in C5, which correspond to cluster superstamps (large contiguous regions of active pixels that cover star clusters) and to trans-Neptunian objects, and 200041889 – 200061149 in C6, which track Trojan asteroids. While cluster science is a key science goal of *K2*, standard MAST-pipeline aperture photometry is not reliable in the extremely crowded fields of the cores of clusters, as are treated with superstamps. Many more widely distributed cluster members and probable cluster members outside the superstamp have MAST lightcurves; we exclude from the analysis presented here stars with very high cluster membership probability, in particular Praesepe stars (C5), as the subject of a separate study, in which we report a Neptune-sized planet transiting an M dwarf (Pepper et al., 2017).

In APP16, we tested K2SC on both the Simple Aperture Photometry (SAP) light

curves, and light curves corrected for common-mode systematic trends by the *Kepler* Presearch Data Conditioning (PDC) pipeline (Twicken et al., 2010; Stumpe et al., 2012; Smith et al., 2012). We found that the latter typically result in slightly improved photometric precision on transit timescales (as measured using our proxy estimate of the 6.5-h combined differential photometric precision, or CDPP). This is most likely due to the fact that some of the common-mode trends removed by the PDC pipeline are related to variations in (e.g.) telescope focus and the temperature of various components, and not directly to the pointing, and are thus not modelled by K2SC. On the other hand, K2SC significantly improves the precision of PDC light curves, and enhances our ability to detect planetary transits (as demonstrated by APP16 using transit injection tests). We therefore use the K2SC-processed PDC light curves as our starting point for the transit search. The interested reader is referred to APP16 for more details on K2SC and its application to *K2* light curves.

4.3 Transit Search

Candidates are initially identified by a Box-Least-Squares (BLS) algorithm (Kovács et al., 2002) which evaluates a signal-to-noise statistic, the signal detection efficiency (SDE), for a simple box-shaped transit for a grid of zero epochs spanning the Campaign and for periods ranging from 0.7 d to 98% of the total duration of the Campaign, using our own version of the algorithm (Parviainen, 2016). We apply this search to a GP-detrended light curve, which has been prewhitened, where we subtract the GP time component to model smooth out of transit variations (Carpano et al., 2003). We record the SDE, and best-fitting period, epoch and duration for each target.

Using this preliminary fit, we then fit a transit model using the PyTransit package (Parviainen, 2015), a fast implementation of the Mandel & Agol (2002) analytic transit light curves.

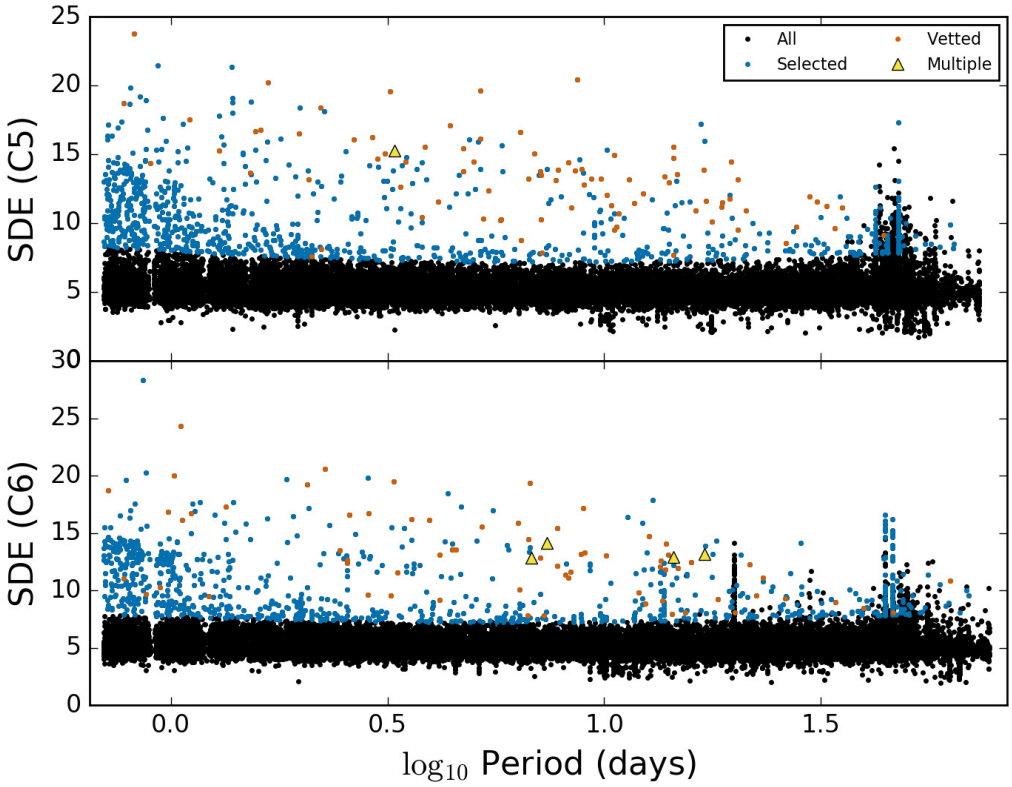

Figure 4.1: Initial selection of transit candidates based on the BLS detection statistic and period. We display SDE versus period for all objects in black, for C5 (top) and C6 (bottom). EPICs selected for visual examination (as described in Section 4.3) are shown in blue, and targets which pass the vetting process (described in Section 4.4) in orange. Yellow triangles display the first detected planet for the multiple-planet systems described in Section 4.5.1.

We use the BLS SDE to identify promising candidates for more detailed study. Using the injection test results from APP16 (Figure 10), we expect non-planet-hosts to be distributed around a mean SDE of ~ 6, roughly uniformly in log-period. In APP16 we therefore recommended a cut in SDE of ~ 8 as a simple and effective way of selecting transit candidates. As is apparent in Fig. 4.1, in our real data, there is in fact some slope to this distribution, as well as a larger number of candidates at short periods.

In order to deal with this, we define an SDE threshold as a function of period. First, we discard single transit candidates as beyond the scope of this study, and examine the remaining objects. In preliminary inspection, we note that ~ 65 long-period candidates in C6 result from systematics associated with particular pairs of bad epochs, leading to a pileup of candidates with poorly-corrected lightcurves with zero epochs in two ~ 0.5 d windows. We therefore identify these from a histogram of fitted BLS zero epochs, and remove these candidates before proceeding. We also discard candidates for which the log-likelihood of a sinusoidal fit is greater than that of a transit, as a way of removing the most obvious variable sources. We then split the objects into 50 bins in period space, each containing an equal number of objects (469 for C5 and 457 for C6), thus using a variable bin size. In each bin we find the median SDE, and the median absolute deviation-estimated standard deviation. Since there is a trend in the median as a function of period, we fit a second-order polynomial to the distribution of period as a function of median SDE, subtract this from each, and find the standard deviation of the residuals. We then select for further analysis all candidates that lie more than 3 σ above this value in each bin. We illustrate this in Figure 4.1, displaying a plot of SDE versus period for both Campaigns, including all objects, selected objects, and vetted objects.

4.4 Vetting

The procedure described in the previous section leads to a preliminary candidate list for each Campaign, which still contains both false detections caused by light curve artefacts or other abnormalities, and astrophysical false positives, i.e. transit-like events which are not caused by a planet. To identify these and produce a cleaner candidate list, we visually inspect the light curves, along with a set of diagnostic plots based on transit model fits, broadly following the approach outlined in Batalha et al. (2010).

Some light curves are affected by poorly-corrected systematics. These show residual ~ 6 hour variability which can lead to a spuriously large BLS detection statistic. We therefore systematically discard detections at the characteristic thruster firing period, and multiples thereof. Furthermore, the time component of the K2SC GP model does not always model very short-period or high-amplitude stellar variability well. This is especially true for classical pulsators such as RR Lyr and Cepheid variables: while the overall variability pattern is modelled adequately, the extrema are not, leaving periodic dips in the residuals, which can lead to a high BLS statistic. Finally, while planetary transits and short-duration stellar eclipses are typically flagged as outliers by the K2SC model (so that they are left unchanged by the detrending process), the outlier flagging procedure is less successful for high-amplitude eclipsing binaries (EBs) where the eclipse duration exceeds a few percent of the period. In those cases, the time component of the GP model partially reproduces the eclipses, leaving in the residuals shallow, periodic eclipse-like events which can superficially resemble planetary transits. All of these categories of false positive are readily identified by visually comparing the raw light curve, the systematics and time-dependent components of the K2SC GP model, and the detrended light curve.

Eclipsing binaries (EBs) are the major source of false positives remaining after this step. The different types of EBs that can mimic a transit signal are discussed

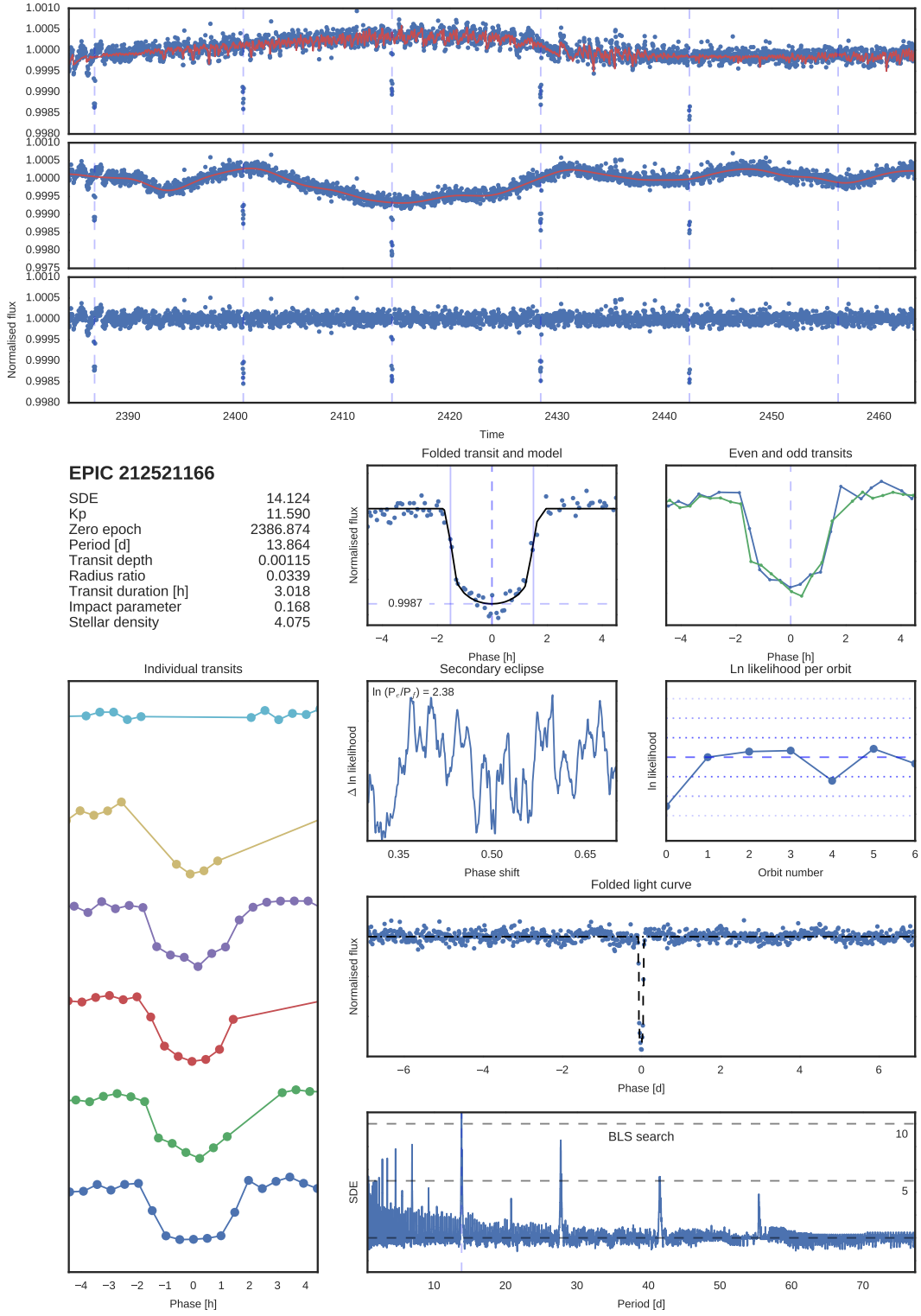

Figure 4.2: Example of a single-page vetting report for one of our candidates, EPIC 212521166. See text for details of the individual panels.

extensively in the literature (see e.g. Charbonneau et al. 2004 for an overview); we merely list them here: grazing EBs, EBs containing a large primary or small secondary star, and blended EBs (EBs whose eclipses are diluted by the light of a third star enclosed in the photometry aperture). To aid in the identification of such systems, we systematically produce, for all our candidates, a single-page report displaying key diagnostics in graphical and numerical form, as listed below. An example of such a report is shown in Figure 4.2, the reports for all the candidates listed in Section 4.5 are provided online as supplementary material. The report shows, from top left to bottom right:

- *Unfolded light curve plots* showing the raw light curve, the systematics and time-component of the K2SC GP model, and the detrended light curve used in the BLS transit search. The location of the transits is indicated by vertical dashed lines (if the light curve contains > 20 transits, only the first 20 are marked);
- *Main BLS and transit fit parameters* giving the BLS SDE detection statistic, the *Kp* magnitude of the target (magnitude in the *Kepler* bandpass), and the best-fitting parameters of a transit fit to the phase-folded detrended light curve;
- *Folded transit plot* showing the best-fit model overlaid on the phase-folded light curve;
- *Even and odd transit plots* showing, in different colours, the binned phase-folded light curves for even- and odd-numbered transits (helpful in identifying near-equal mass EBs where the BLS-detected period is half the true orbital period);
- *Individual transit plots* showing each transit (or the first 20 if the total number exceeds 20) separately (helpful in identifying false detections caused by light curve artefacts);
- *Secondary eclipse detection plots* showing the log-likelihood of a secondary eclipse

with the same parameters as the best-fit transit model, but variable depth, as a function of phase from 0.3 to 0.7 (EBs with low to moderate eccentricities but detectable secondary eclipses cause a clear peak in such a diagram);

- *Per-orbit transit likelihood plot* showing the log-likelihood of the best-fit transit model for each transit event separately (strong variations from one transit to the next indicate that the detection may be caused by or affected by light curve artefacts);

- *Full folded light curve plot*: this can reveal secondary eclipses occurring outside the 0.3–0.7 phase range, or additional transit events

- *BLS periodogram* providing an additional means of assessing the significance of the detection (subsidiary peaks can also reveal additional sets of transits in the light curve).

All the transit model fits are performed using the PyTransit package, which implements the analytic model of Mandel & Agol (2002). The parameters of the transit fits are epoch, period, planet-to-star radius ratio, impact parameter and stellar density. We also report the transit depth and duration, which are computed from the best-fit transit model. Note that the transit models are evaluated with 3 min time-sampling and binned up by a factor of 10 to account for the smearing of the ingress and egress caused by the relatively sparse sampling of *K2* long cadence observations. The vetting process for transit candidates identified during the *Kepler* prime mission (see e.g. Batalha et al. 2010) also relies on the use of so-called "rain diagrams": plots of flux versus x- and y-position of the target centroid. Such diagrams are highly effective at identifying blended EBs, where the target centroid can change significantly during eclipses (except for hierarchical triple system where the EB and contaminant are essentially co-located). In the case of *K2*, one must use the difference between the star's predicted position (based on the overall pointing variations of the satellite)

and its measured centroid. We systematically produce such plots and use them in the vetting process, but they have not yet been incorporated into the single-page reports.

Any candidates which show clear signs of being false detections, or being caused by EBs, on the basis of the diagnostics described above, are discarded from the final candidate lists. Rather than define quantitative criteria for rejecting or keeping a candidate, at least two individuals vet all the candidates independently, and only those considered passable by all the vetters are retained. This clearly leaves scope for considerable improvement: ideally we would like to perform a systematic, quantitative assessment of the probability that each candidate is indeed a planet, based on all the available information. One way to do this automatically is to use machine learning tools, such as the random forest algorithm recently implemented for *Kepler* (McCauliff et al., 2015), trained on transit candidate lists vetted by humans. However, this is beyond the scope of the present Chapter.

4.5 Planet Candidates

In Tables A.1 and A.2 we list the planet candidates that pass the tests described in Section 4.4, for C5 and C6, respectively. The last two columns give the number of reconnaissance spectra obtained for each candidate, where applicable, and the status of the candidate based on the spectra plus any other available information (see Section 4.5.2 for more details). The period and radius ratio of these candidates is displayed in Figure 4.3. Out of 996 and 981 objects pre-selected for visual inspection in C5 and C6 respectively, we select 87 & 77 as *bona fide* candidates after vetting. A vetting diagnostic diagram similar to Figure 4.2 is provided for each candidate in the supplementary online material.

Our C5 candidate list includes the hot Jupiter EPIC 212110888b, which has been independently discovered (from its *K2* light curve) and spectroscopically confirmed

by Lillo-Box et al. (2016) and Hirano et al. (2016b). With an 0.8% transit around an F9 star, the two publications agree on a mass of $M_p \sim 1.7 \pm 0.1\ M_J$ and a radius of $1.4 \pm 0.1 R_J$, differing within uncertainty according to the different stellar models. In addition to this, Osborn et al. (2016b) have obtained RV spectroscopy of EPIC212521166 b, first reported by Aigrain et al. (2016), finding it to be a massive mini-Neptune with similar photometric parameters to those reported here.

Several long-period candidates were found around stars whose light curves display stochastic oscillations on timescales of a few hours, and are hence likely to be red giants (EPIC 212411479, 212438212, 211996053, and 212481820). Although they did not explicitly fail any of the vetting tests, we did not include them in the final candidate lists, as it is difficult to distinguish a real transit from residuals from imperfectly modelled, stochastic stellar variability on the same timescale. We note however that these events are in principle detectable, and might warrant more detailed study.

Our target sample partly overlaps with that of Adams et al. (2016), who searched for ultra-short-period planets (up to 1 day only) in Campaigns 0–5. They report list four candidates in C5: of these, we do not pre-select EPIC 211357309 or 211995325 for followup based on the BLS SDE, while we do preselect 211685045 and 212150006. Both of the planets we miss have periods shorter than the 0.7 d cutoff we impose on our initial search. We did not include shorter periods in our search because both very short period pulsating stars and residual pointing systematics at $4c/d$ cause many false positives in that regime. EPIC 212150006 is listed in Table A.1 as a *bona fide* planet candidate. Our light curve for 211685045 appears to show residual variability consistent with a false positive, so it was rejected at the vetting stage.

We have also compared our list candidate list for both Campaigns to those kindly provided by A. Vanderburg (priv. comm.). As we were co-ordinating our spectroscopic reconnaissance efforts, we shared our targets lists for magnitudes $K_p < 13$. Within that range, there is a very substantial overlap between our lists, with only a small

number of objects found by one group but not by the other. In several cases, we have rejected candidates found by Vanderburg as having evidence for a secondary eclipse; in other cases, Vanderburg finds evidence of a secondary eclipse where we do not (see Comments in Tables A.1 and A.2). A few of our candidates were not detected by Vanderburg, these correspond to active stars whose variability and systematics are better-modelled by the K2SC GP model than by piecewise polynomial detrending. Finally, we failed to detect a few of Vanderburg's candidates. In those cases, we see no evidence for a transit in our light curve, but the signal is clear in the K2SFF light curves. These are all bright stars, for which we suspect that the K2SFF photometric apertures are better suited to the point spread function than those used by MAST (Vanderburg & Johnson, 2014a).

This comparison shows that the different light curve detrending, transit search and vetting processes are complementary, and that a more complete candidate list may be obtained by combining the results of several pipelines than by any single pipeline. We also note that the overall transit detection potential of *K2* may be best exploited by combining K2SFF aperture photometry (or similar) with K2SC detrending.

4.5.1 Multiple Planet Systems

We also checked for additional transiting planets in the systems identified in Section 4.4. At the vetting stage, we made note of systems for which there was visual evidence of more than one set of transits. For each such system, we then subtracted the best-fit model for the first set of transits and repeated the transit search and fitting on the residuals. The process was iterated until no further sets of transits were found.

We detect two sets of transits around each of EPIC 212012119 (C5); and 212393193, 212703473, and 212779596 (C6), and three sets of transits around 212768333 (C6). The parameters of these systems are presented in Table A.3. For each of these sys-

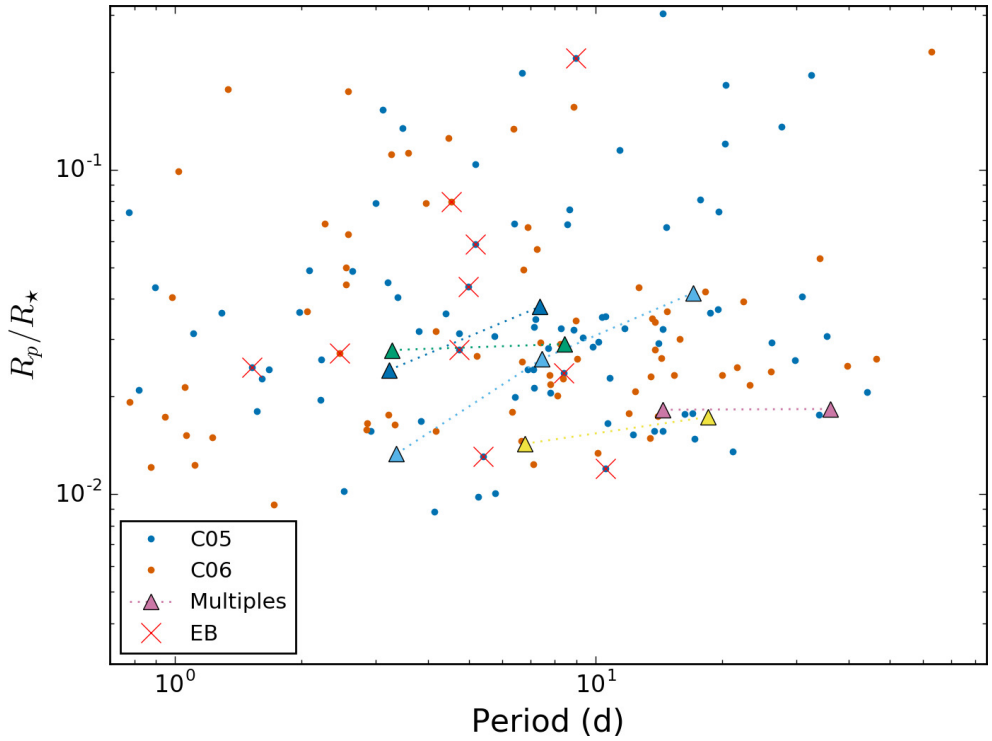

Figure 4.3: Radius ratio versus period for all vetted planet candidates from C5 (blue) and C6 (orange). Multiple systems are shown as triangles, with planets in each individual system sharing the same colour and joined by dotted lines. Objects which were found to be binaries following reconnaissance spectroscopy (see Section 4.5.2) are displayed with red crosses superimposed.

tems, we provide a vetting diagnostic diagram similar to Figure 4.2 for each set of transits separately in the supplementary online material.

EPIC 212651213 and 212651234 show two identical sets of transits which pass our initial vetting procedure, indicating a photometric blend. EPIC 212651213 was later found to be triple-lined (see Section 4.5.2), while 212651234 shows no RV variation over 3 epochs. We therefore conclude that EPIC 212651213 is an eclipsing SB3 system, and the apparent transits on 212651234 are the result of a photometric blend. These two systems are therefore not included in Table A.3.

In addition to these, we detect three transit-like events with $\sim$ 3 to 5% depth around EPIC 212656205, which do not have a periodic relation and have different depths. These may represent a planar hierarchical multiple stellar system, or multiple close-in giant planets.

4.5.2 Spectroscopic Reconnaissance

For most of the objects in the EPIC catalogue, spectra have not previously been obtained and only photometric information is available. A single, moderate to high resolution spectrum can be used to determine the host star's spectral type and evolutionary stage, and to check for obvious signs of binarity (double- or triple-lined spectra). For single-lined, main-sequence cool stars, additional spectra can reveal km/s radial velocity variations, indicative of a stellar or substellar companion. All our candidates which passed the vetting stage and were bright enough for efficient spectroscopic follow-up ($Kp \leq 13$) were observed at least once with the Tillinghast Reflector Echelle Spectrograph (TRES), at the 1.5-meter Tillinghast Telescope on Mt Hopkins, Arizona. TRES has three spectroscopic resolving power settings available: 41,000 (high), 30,000 (medium), and 20,000 (low); reconnaissance is typically conducted in the medium resolution mode. In most cases, the radial velocity (RV) precision achievable with TRES ($\sim$ 0.1km/s or somewhat better) is not sufficient to

detect the signal of a planetary-mass companion to a main sequence star, except for hot Jupiters under favourable conditions.

Where possible, the systems were observed at or near quadrature in order to maximise the chances of resolving multiple sets of stellar lines. Any systems identified as giants, double- or triple-lined binaries based on the first observation were not observed any further. These are noted as "GIANT", "SB2" or "SB3" in the final column of Tables A.2 and A.2. Additional spectra were taken near the opposite quadrature for some of the remaining single-lined candidates, if the planet-to-star radius ratio indicated that an orbital solution might be feasible with TRES. If the resulting radial velocity change was too large for a planetary companion, the system was classified as a single-lined stellar binary (labelled "SB1" in the tables). In the case of EPIC 212110888, which contains a hot Jupiter, further additional spectra were obtained in order to obtain a full orbital solution, which is consistent with the parameters published by Lillo-Box et al. (2016) and Hirano et al. (2016b), with TRES spectra best fit by a 166 ± 21 ms^{-1} RV semi-amplitude planet, with a mass of $1.18^{+0.15}_{-0.15}$ M_J. One system (EPIC 212808289) may host a warm Jupiter, but additional spectra, ideally with better radial velocity precision, are needed to confirm this. The inner planet in EPIC 212703473 is also a likely hot Jupiter. For EPIC 212066407 and 212803289 we list RV semi-amplitude K as determined by TRES, while for 211733267 and 211818569, with 2 epochs showing little variation we list upper limits on K. The remaining systems included in the TRES reconaissance spectroscopy program which were not found to show any evidence of binarity are simply noted as "OK" in Tables A.2 and A.2. For the brightest among them, a full orbital solution might be feasible with dedicated high-precision radial velocity instrument, otherwise a statistical evaluation of the likelihood that the companion(s) is/are indeed planetary ("validation") could be performed based on all the information available to date plus high spatial resolution imaging.

Overall, the TRES reconaissance program enabled us to rule out 8 out of the 86 single-planet candidates from C5, and 2 out of the 71 from C6, as giants or spectroscopic binaries, for a final total of surviving 147 single-planet candidates across both Campaigns.

4.6 Source Code and Data Products

In the interests of open science, we have our code implementing the methods described in Sections 4.2, 4.3 and 4.4 publicly available. It consists of several open source packages distributed under a GPL license. We invite interested readers to use, modify and contribute to this code as an evolving resource for the astronomical community. The K2SC systematics correction code (Aigrain et al., 2016) is available on GitHub at

`https://github.com/OxES/k2sc`,

the transit modelling code PyTransit (Parviainen, 2015) at

`https://github.com/hpparvi/PyTransit`,

and the code used to carry out the BLS transit search and produce the candidate reports, K2PS (Parviainen, Pope & Aigrain, 2016), is available at

`https://github.com/hpparvi/k2ps`.

The data used and produced in the course of this Chapter are also publicly available. The full set of K2SC-processed *K2* lightcurves is available at MAST

`https://archive.stsci.edu/prepds/k2sc/`,

and the candidate reports used in the vetting process are provided with the published version of the work in this Chapter (for surviving candidates only) as supplementary online material (Pope, Parviainen & Aigrain, 2016b), and the TRES spectra of our candidates have been uploaded to the 'ExoFOP–K2' website

`https://exofop.ipac.caltech.edu/k2/`.

4.7 Conclusions

We have presented a new pipeline to search for transiting planet candidates in *K2* data, and reported the results of applying this pipeline to Campaigns 5 & 6, together with reconnaissance spectroscopy of the brightest of our candidates. We recover known planets and identify false positives due to stellar-mass companions. We have made our code, light curves, and diagnostic data products publicly available to facilitate confirmation and comparison, and look forward to comparing our results with future work using other methods.

We have compared our results to those by Adams et al. (2016), the only published catalog which covers one of the Campaigns we have analysed (C5), as well as with the unpublished candidate list produced by A. Vanderburg for both C5 and C6. In both cases, our results are generally consistent. The two candidates identified by Adams et al. (2016) and not by ourselves lie outside our chosen period search range. In several cases, we identified candidates found by Vanderburg, but discarded them at the vetting stage. On the other hand, we also failed to detect a few of his candidates altogether, and these correspond to cases where the photometric precision of our light curves is not as good as that of the K2SFF light curves used by Vanderburg for the same object.

We also identify a small number of candidates, which were not reported by other teams. These are predominantly orbiting variable stars, which is consistent with our stated intention to write a pipeline that is particularly robust to astrophysical variability. More detailed comparison to other methods will become possible once more groups have published candidate lists for C5 and C6, and once we have processed earlier Campaigns, for which published candidate lists are already available.

Our results are broadly compatible with the K2SC injection tests presented in APP16, but a direct comparison is not feasible, as we have made some small but significant changes to our transit search methodology since. We will repeat the injection tests at a later date, after processing more Campaigns, to provide a quantitative assessment of the sensitivity of our final pipeline. There are a number of possible modifications to our pipeline that may yield improvements in sensitivity or reliability in the future. First, as noted above, for some bright stars our light curves are not as precise as those used by some other teams. We use the PDC-MAP light curves as our starting point; these are extracted using fixed, pixelized photometric aperture masks. For some types of stars (particularly bright stars, as noted in Vanderburg & Johnson 2014a and Lund et al. 2015), these apertures may not be optimal. Better sensitivity to shallow transits might be achieved by applying K2SC to light curves extracted using more optimized apertures. Another area where we hope to make progress in the near future is in making the vetting process more automatic, perhaps by implementing and training machine learning algorithms to distinguish between planetary transits and false positives.

Beyond the discovery of individual interesting systems, a significant element of the long-term legacy of the *K2* mission will be improved estimates of short-period planet incidence rates around types of stars which were relatively under-represented in the *Kepler* prime mission (such as M-dwarfs), as well as the ability to check for if the incidence of short-period planets depends in a measurable way on direction within the Ecliptic plane. By making all our code publicly available, we hope to facilitate the evaluation of such incidence rates, by providing all the tools needed for complete end-to-end simulations of the detection process.

Chapter 5

Photometry of Very Bright Stars with *Kepler* and *K2* Smear Data

Consider first, that great
Or bright infers not excellence.

Milton, *Paradise Lost*, VIII 90-91.

5.1 Introduction

The *Kepler* and *K2* missions have been used to discover thousands of new exoplanets, in a statistical sample made possible by the telescope's ability to observe many faint stars simultaneously at high fidelity. Unfortunately, with some notable exceptions (e.g. θ Cyg, $V = 4.48$: Guzik et al., 2016), *Kepler* has not observed many bright stars with the same precision. In this Chapter, we will demonstrate one method for recovering light curves of such stars from new or archival data.

Because of limitations on communications bandwidth with the *Kepler* spacecraft, not all targets 'on silicon' (i.e. in the spacecraft field of view) are downloaded. Instead, 'postage stamps' of active pixels are downloaded around predetermined targets of

This content of this Chapter has been published as Pope et al. (2016c).

interest, and data from other pixels are discarded. The situation is particularly difficult for the brightest stars: when these sources saturate the detector, electrons bleed along the saturated columns, with the result that very large apertures are required to capture all of the stellar flux. Therefore these brightest stars are very expensive in terms of the limited number of pixels that can be downloaded, and many were omitted from the target lists. The situation is even more difficult in *K2* because the 'postage stamps' must be larger in order to account for the apparent motion of the sources as the roll angle varies, and also because the ecliptic target fields contain a much higher density of nearby bright stars.

Beginning with the *K2* Campaign 3 data release, engineering data were made publicly available on the Mikulski Archive for Space Telescopes (MAST). These included collateral data for both long and short cadence, which consist of measurements of photometric 'smear' for each column in the CCD. Since the *Kepler* camera lacks a shutter, light falling on the detector during the read-out stage causes photometric smear that must be calibrated. The short cadences (SC) consist of the sum of nine 6.02 s exposures for a total integration of 54.2 s, and the long cadences (LC) are the sum of 30 times these, for a total of 1626 s. The light landing during read-out is added column-by-column and stored as 'collateral' smear data at each cadence of both the *Kepler* and *K2* Missions. Kolodziejczak & Caldwell (2011) suggested using these smear pixels data to obtain photometry of otherwise unobserved *Kepler* stars. They outlined a method for extracting light curves from these data and presented several examples, but to our knowledge this has not been followed up in subsequent work. The goal of this Chapter is to demonstrate that smear pixels can be used to extract scientifically useful photometry for very bright stars in both *Kepler* and *K2* fields.

The upcoming Transiting Exoplanet Survey Satellite (TESS) (Ricker et al., 2015) aims to study such nearby, bright stars to identify promising candidates for further

study, but many *K2* targets will be out of its reach. TESS will observe polar regions most frequently and devote significantly less time to equatorial fields, with the result that the ecliptic objects studied by *K2* are excluded from most of the nominal TESS Mission. Therefore, for these targets, *K2* smear data provide the only space-based photometry likely to be available in the near future.

5.2 Method

The smear data consist of FITS tables containing 'virtual' and 'masked' smear flux. These contain, respectively, smear information from 12 masked rows at the start of each read-out and 12 over-clocked rows after each frame is read out. The 12 smear rows are co-added for each region and stored as 1D arrays listing the sum for each column of the CCD. An example for the case of HR 8500 is shown in Fig. 5.1. For 70 Aqr and HD 178875, we took the sum of the virtual and masked flux as our raw smear observable. For a target star that falls near the upper or lower edge of the detector, one of these smear arrays can be affected by saturated flux bleeding along the column. As a result, for HR 8500, only the masked flux was suitable, as discussed in Section 5.3.3.

Two factors restrict the usefulness of the smear data to the brightest stars. One is the fact that the data are summed across all 1024 rows of the detector, so that targets in the same column are confused. The other is that, as noted by Kolodziejczak & Caldwell (2011), the effective exposure time for smear data is much less than for ordinary target pixels. This is because we have 12 rows each of masked and virtual smear, which measure the incident flux during the 0.52 second readout, so that the effective exposure time is only $12/1070 \times 0.52/6.02 \sim 1/1034$ of the true pixel exposures for each of the virtual and masked smear, or $\sim 1/517$ if both can be used. Hence, the photometric precision for bright stars is expected to be equivalent

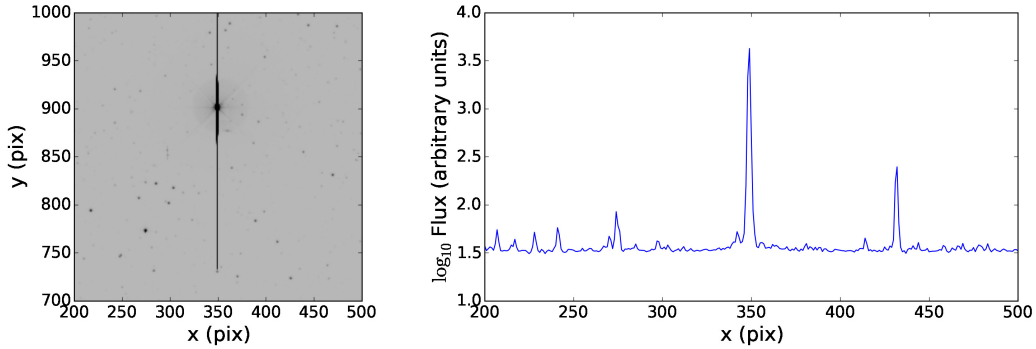

Figure 5.1: Smear data from *K2* Campaign 3 for the bright star HR 8500. Left: Part of the full-frame image, including HR 8500 as the saturated star with a long bleed column extending above and below. Right: 1D masked smear profile, with HR 8500 clearly visible as the highest peak.

to that of a star ~ 6.7 mags fainter observed in the standard way, but for stars fainter than a *Kepler* magnitude (Kp) of ~ 9 (as defined in Koch et al., 2010), detector read noise dominates and the smear precision falls off faster than the square root of the number of photons.

For a more detailed description of the smear data we recommend to the reader Caldwell et al. (2010), Quintana et al. (2010), the *Kepler* Data Processing Handbook (KSCI-19081-001; Fanelli et al., 2011), and the *Kepler* Instrument Handbook (KSCI-19033; Van Cleve & Caldwell, 2009).

For each target star, we visually inspected the full-frame images (FFIs) taken at the beginning of each Quarter (*Kepler*) (hereafter Q) or Campaign (*K2*) and located the relevant columns in the corresponding smear data. An example for *K2* C3 is shown in Fig. 5.1. We see that the columns containing the bright saturated star HR 8500 (Section 5.3.3) correspond to a very strong peak in the smear data. Having identified the target in the smear data, we selected an appropriate range of columns, taking care to avoid confusion with nearby sources, and extracted a time series for each column. In the case of HD 178875 (Section 5.3.1) in the original *Kepler* field, we took the sum of these time series as the light curve for the star.

For stars observed in *K2*, pointing corrections introduce potentially large systematics. The photometric precision of *K2* is lower than in the nominal Mission because the roll-axis equilibrium is unstable and must be corrected by thruster firings every ~ 6 hours, with momentum dumps on the other two axes every 2 days. We corrected for these by tracking the 1D centroid of the smear peak, and extracting photometry using an aperture with a 3-pixel flat top and 2-pixel cosine bell (Hanning) taper on either side of this. We then applied the method of Aigrain et al. (2015), using a Gaussian process (GP) systematic model, using a 1D squared exponential kernel for continuum variations as a function of time. We model the pointing variations with a 2D squared exponential kernel taking as inputs the predicted x and y position of a nearby star: for HR 8500, this was EPIC 206249807, and for 70 Aqr it was EPIC 206164235.

While in Sections 5.3.3 and 5.3.2 we present an analysis of systematics-corrected lightcurves, the corrections are minor and the raw lightcurves support the same qualitative conclusions. Other detrending methods may also achieve similar results.

5.3 Results

5.3.1 HD 178875

HD 178875 (KIC 3429637) is one of the brightest δ Scuti stars in the original *Kepler* field, with a Kp mag of 7.711. Over the first 2 yr of the *Kepler* Mission it showed a growth in pulsation amplitude that was attributed to its advanced evolutionary state, near the terminal-age main sequence (Murphy et al., 2012).

We have extracted the six strongest oscillation frequencies present in the smear data of this star, and they agree with those published by Murphy et al. (2012) to within the 1-σ uncertainties. A light-curve segment with a six-frequency fit is shown in Fig. 5.2. The msMAP (Stumpe et al., 2014) and smear light curves resemble each

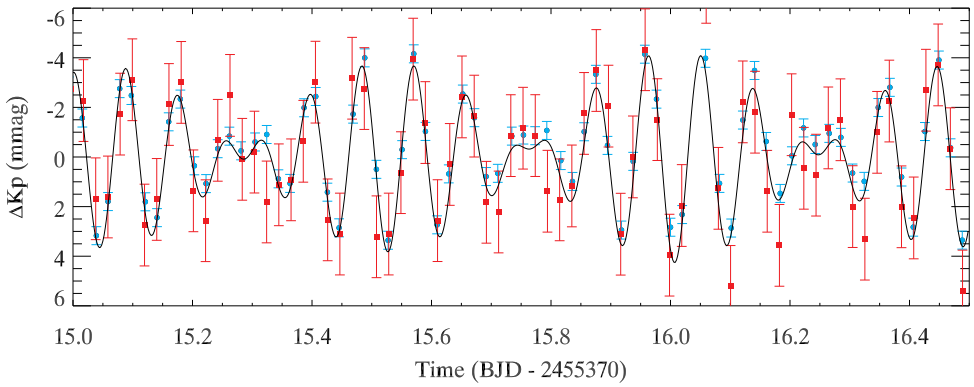

Figure 5.2: Light-curve segment from Q6 for HD 178875 from the msMAP data (blue circles) and the smear data (red squares). The black line shows a six-frequency fit.

other closely, although the latter has a higher noise level because of the much lower effective exposure time. The error bars drawn in Fig. 5.2 are proportional to the per-point residuals after the non-linear least-squares fit.

Stellar oscillation frequencies are the fundamental data of asteroseismology. Their recovery to 1-σ precision in smear data against published values that used aperture photometry is a good demonstration of the utility of these data.

5.3.2 70 Aqr

Some stars are so bright on the *Kepler* CCD that it is impractical to assign sufficient pixels to perform aperture photometry. An example in the *K2* field for C3 is 70 Aqr (HR 8676; HD 215874), which has a magnitude of $V = 6.2$. It is in some ways a typical δ Scuti star – its effective temperature (7300 K; Paunzen et al. 2002) puts it in the middle of the δ Scuti instability strip, its rotational velocity (100 km s^{-1}; *ibid.*) lies at the mode of the distribution for stars of its spectral type (Royer et al., 2007), and the Fourier transform of its *Kepler* smear light curve (Fig. 5.3) is typical in that it contains a few tens of statistically significant peaks. However, its Fourier transform is unusual in other ways – its highest oscillation peak puts it in the top percentile of *Kepler* δ Scuti stars by peak amplitude (see, e.g. Murphy 2014), and the frequency

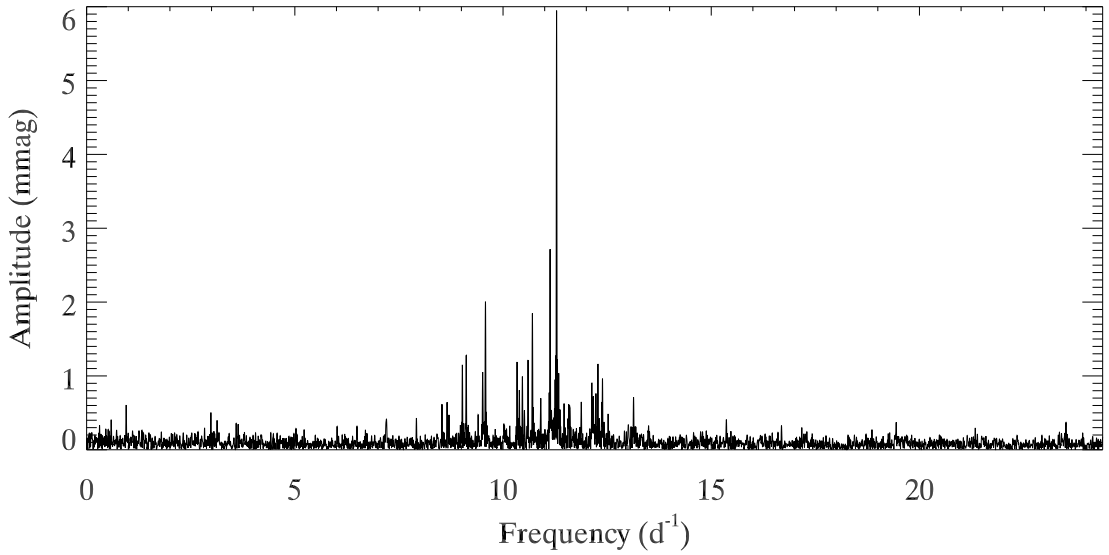

Figure 5.3: Amplitude spectrum of the *K2* C3 smear data for the δ Scuti star 70 Aqr.

distribution is rather narrow.

The *K2* photometry provided here offer another epoch of observations for this star. Literature data suggest 70 Aqr undergoes amplitude variability, as is common in δ Scuti stars (see Bowman & Kurtz 2014 for a recent discussion). For instance, the catalogue of δ Scuti stars by Rodríguez et al. (2000) lists an amplitude of 20 mmag in V, whereas the *Kepler* smear data for the two peaks at 11.2859 and 11.1298 d^{-1} have amplitudes of 6.1 and 2.9 mmag, respectively. The older literature has amplitudes ranging from 8.5 to 25 mmag, each for different oscillation periods (Weiss, 1977; Hildebrandt, 1992), suggesting the dominant mode is not always the same. In all cases, these ground-based observations cannot match the excellent duty cycle of *Kepler*.

One of the greatest problems in the study of δ Scuti stars is mode identification. This is usually performed with multi-colour photometry or time-series spectroscopy. *Kepler*/*K2* observes in white light only, and so ground-based observations are still very valuable for mode identification. Although 70 Aqr is unremarkable as a δ Scuti star, it is bright enough for successful ground-based observing campaigns, and now

thanks to the smear data we can produce a high-precision light curve despite the gross saturation on the *Kepler* CCD.

5.3.3 HR 8500

Red giants exhibit radial and non-radial oscillations that are stochastically excited and damped by convection (De Ridder et al., 2009). The amplitudes of these oscillations are significantly smaller than those in δ Scuti stars (Kjeldsen & Bedding, 1995), so detection of red giant oscillations provides a more stringent test of the precision of smear data photometry.

HR 8500 (EPIC 206246606) is one the brightest red giants within the *K2* C3 field of view, with a visual magnitude of 5.8. As for 70 Aqr, HR 8500 was not targeted due to the large number of pixels that would be required. As HR 8500 lies near the edge of the detector, its bleed column intersects with the virtual smear rows, so that the virtual smear data are affected strongly by the pointing cycle. Where the charge piles up like this, the measured smear flux is not expected to be linear with the incident flux. The associated systematics are, in the case of HR 8500's virtual smear column, of the same order as the raw flux and are not well-corrected with Gaussian process systematics models. Under these circumstances, it is preferable to use only the masked smear array. In doing so, we lose a factor of two in flux, but have a substantially reduced contribution from pointing systematics.

Using $B - V = 1.165$ from the EPIC catalog (Huber & Bryson, 2015) with the colour-$T_{\rm eff}$ relations by Ramírez & Meléndez (2005) we estimate $T_{\rm eff} = 4570$ K, which combined with the Hipparcos parallax (van Leeuwen, 2007) and a bolometric correction $BC_V = -0.45$ (Alonso et al., 1999) yields a radius of $\sim 13.6 R_\odot$. Assuming a typical mass range for red giants of $1 - 2 M_\odot$, we expect HR 8500 to oscillate with a frequency of maximum power $\nu_{\rm max} \sim 20 - 40 \mu$Hz.

The top panel of Fig. 5.4 shows the power spectrum of HR 8500 obtained from

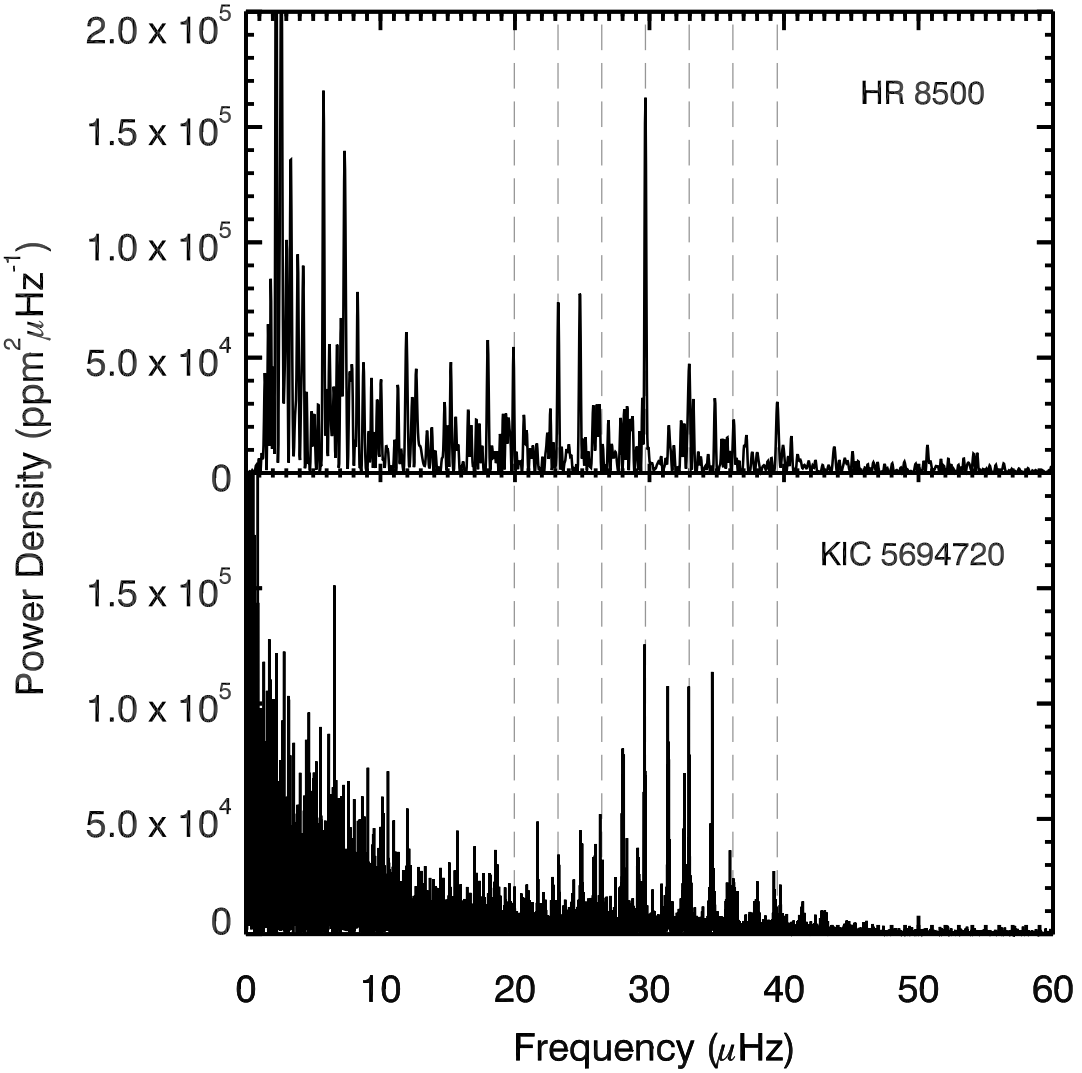

Figure 5.4: Top panel: Power spectrum of HR 8500 *K2* C3 smear data after outlier rejection and high-pass filtering with a boxcar width of 10 days. Dashed lines indicate the locations of radial oscillation modes. Bottom panel: Power spectrum of the red giant star KIC 5694720, with frequencies scaled to match those measured in HR 8500 (the scaling factor was 0.98).

the smear data. The spectrum shows a power excess around $\sim 30\mu$Hz, consistent with the expected $\nu_{\rm max}$ value from colours and the Hipparcos parallax. Using the method of Huber et al. (2009) we measured $\nu_{\rm max} = 29.2 \pm 2.5\mu$Hz and an amplitude per radial mode of $A = 99 \pm 20$ ppm. To further test whether the detection is compatible with solar-like oscillations, we compared our measurements to over 1000 red giants observed in the original *Kepler* Mission, which follow a well-established relation between $\nu_{\rm max}$ and oscillation amplitudes (Hekker et al., 2009; Baudin et al., 2011; Stello et al., 2011a). As shown in Fig. 5.5 the amplitude measured in HR 8500 is fully consistent with the *Kepler* sample.

For comparison, the power spectrum of a similar red giant, observed throughout the *Kepler* Mission, is shown in the bottom panel of Fig. 5.4. The frequency axis has been scaled by a factor of 0.98 in order to align peaks in both power spectra. From this we are able to identify the radial oscillation modes in HR 8500, and determine the characteristic frequency spacing, $\Delta\nu$, between modes of consecutive radial orders to be 3.25 ± 0.02 μHz.

Oscillating red giants are plentiful in the *Kepler* and *K2* fields (e.g. Stello et al., 2013). Through the use of asteroseismic scaling relations (Ulrich, 1986; Brown et al., 1991; Kjeldsen & Bedding, 1995), stellar properties including mass and radius can be determined from $\Delta\nu$ and $\nu_{\rm max}$, which is invaluable for population studies of the Milky Way galaxy (Miglio et al., 2013). However, these scaling relations require calibration to avoid systematic biases. Bright stars such as HR 8500 may be well characterised through complementary methods such as long-baseline optical interferometry, providing the means to test and calibrate these relations (e.g. Huber et al., 2012; White et al., 2013).

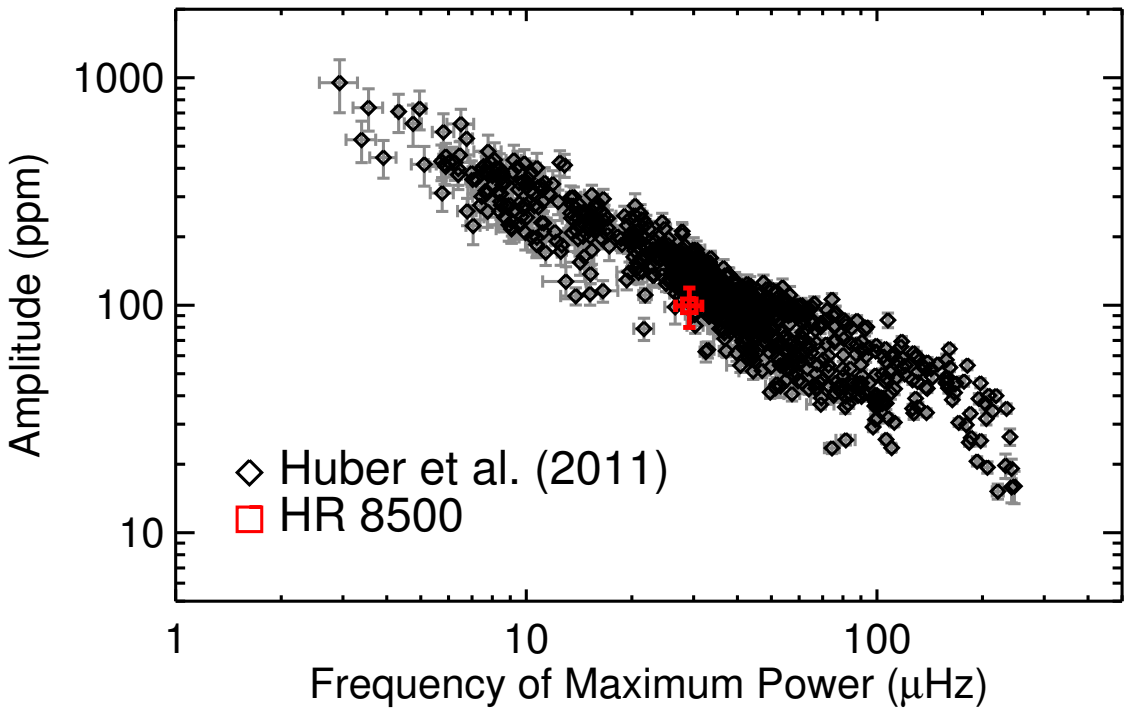

Figure 5.5: Oscillation amplitude versus frequency of maximum power for over 1000 red giants observed by the *Kepler* Mission taken from (Huber et al., 2011). The red square shows the measured values for HR 8500 from the *K2* C3 smear data.

5.4 Conclusions

As we have shown with the examples above, collateral smear data dramatically expand the possibilities for bright star science with *Kepler* and *K2*. These ecliptic targets will not be observed by TESS, or will only be observed briefly, and this is therefore the only opportunity in the immediate future for space-based photometry of these bright stars.

The collateral archive already contains observations of many stars which can now be revisited. There are 29 stars with Kp$<$ 7 mag that were not observed by the nominal *Kepler* Mission, and a further 18 stars that were only observed in a few quarters. There are 17 stars in each of *K2* C3 and C4 brighter than Kp = 7 mag that were not targeted. Furthermore, collateral data for s 0, 1, and 2 have not yet been made available, but there are 142 unobserved targets with Kp$<$ 7 mag. Given the encouraging results of the analysis of C3 targets presented here, we believe they will also present valuable opportunities for advancing stellar astrophysics.

In allocating active pixels for future *K2* campaigns, it will be valuable to consider allocating short cadence pixels to columns containing targets of interest, as the smear data for these columns will then be available at short-cadence time resolution, a less-bandwidth-intensive method to obtain information about these stars on short time scales. We also note that custom apertures for bright stars, which are expensive in terms of pixels, may be unnecessary in many cases, easing the overall competition for bandwidth and permitting future Campaigns to observe a larger number of faint targets.

Chapter 6

Halo Photometry

The sire and builder of the Trojan town
was Dardanus; but he, Electra's child,
came over sea to Teucria; the sire
of fair Electra was great Atlas, he
whose shoulder carries the vast orb of heaven.
But thy progenitor was Mercury,
and him conceiving, Maia, that white maid,
on hoar Cyllene's frosty summit bore.
But Maia's sire, if aught of truth be told,
was Atlas also, Atlas who sustains
the weight of starry skies. Thus both our tribes
are one divided stem.

Aeneas to Evander, Vergil, *Aeneid* VIII.137-148
(tr. Williams, 1910)

6.1 Introduction

The *Kepler* mission (Borucki et al., 2010), which had the primary purpose of detecting Earth-like planets via the transit method, has also been a boon for stellar astrophysics by providing precise photometric light curves for studying stellar variability across the Hertzsprung-Russell (H-R) diagram.

This Chapter is an extract from a manuscript submitted to MNRAS, White et al. (submitted).

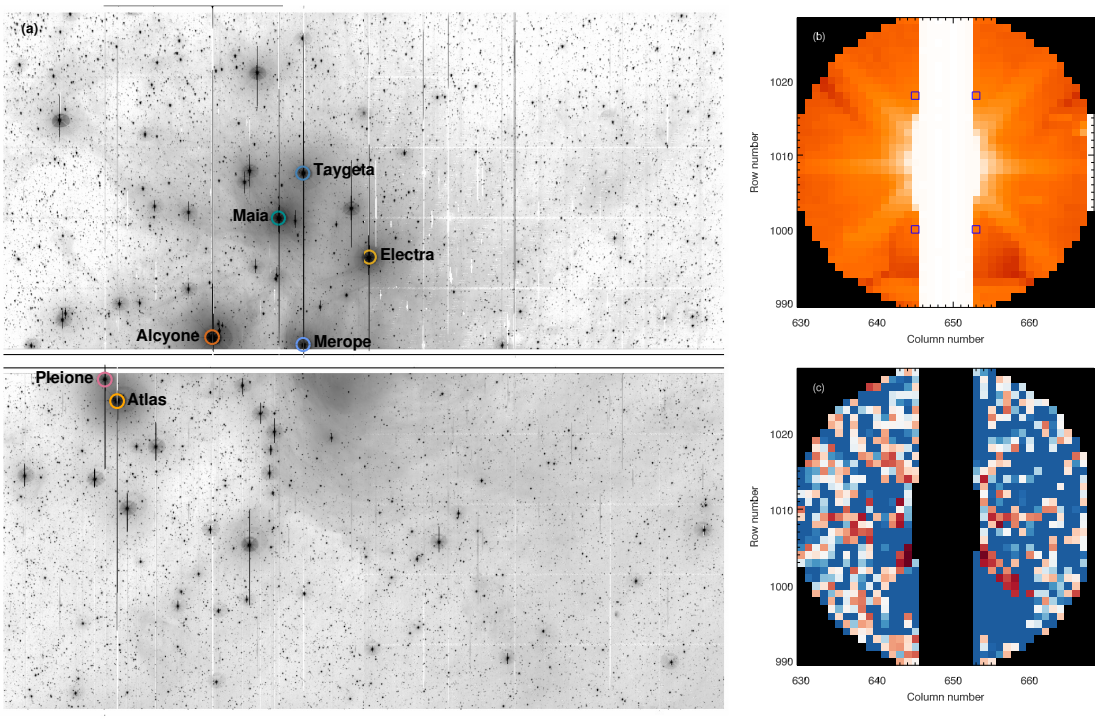

Figure 6.1: (a) Full frame image of Module 15 at the beginning of K2 Campaign 4. The target pixel masks around the seven brightest stars in the Pleiades are indicated: Alcyone (red), Atlas (orange), Electra (yellow), Maia (green), Merope (light blue), Taygeta (dark blue), and Pleione (pink). (b) Target pixel mask and *Kepler* image of Alcyone. Segments of the light curves of the four highlighted pixels are shown in Fig. 6.2. (c) Optimal weights for the Alcyone light curve. Red pixels have been up-weighted, while blue pixels have been down-weighted.

In particular, *Kepler* has advanced our understanding of B-type stars building on earlier work with the MOST (e.g. Walker et al., 2005; Aerts et al., 2006; Saio et al., 2006) and CoRoT (e.g. Huat et al., 2009; Neiner et al., 2009; Degroote et al., 2009, 2010) space telescopes. While *Kepler* has revealed variability in dozens of B stars (Debosscher et al., 2011; Balona et al., 2011; McNamara et al., 2012), the greatest impact has stemmed not from the quantity of observed stars, but from the high quality of the long, nearly-uninterrupted time series.

The brightest stars ($V \lesssim 6.0\,\mathrm{mag}$) in the K2 fields are particularly desirable targets because these stars are the most amenable to complementary observations, including polarimetry and interferometry. The combination of asteroseismology with

other modes of observation places strong constraints on stellar properties, by lifting degeneracies, and dependencies on stellar models (e.g. Cunha et al., 2007). These well-characterized stars therefore provide the most stringent tests of stellar models, and can be used to examine internal processes (e.g. Hjørringgaard et al., 2017).

These bright stars also offer unique opportunities to not merely detect, but to characterize, transiting exoplanets, as has been done with the well-studied 55 Cancri e (discovered to transit by Winn et al., 2011; Demory et al., 2011), which orbits a $V = 5.95$ mag star. Demory et al. (2016a) have shown the planet to have an extremely large temperature gradient and Demory et al. (2016b) have shown it displays variability in thermal emission form its dayside atmosphere. Only two known planets transit a brighter star, HD 219134 ($V = 5.57$; Motalebi et al., 2015; Gillon et al., 2017), and adding even one new candidate to this list would be a significant breakthrough for exoplanetary science.

However, observations of bright stars present unique challenges. Most significantly, telemetric bandwidth limitations restrict the amount of data that can be downloaded from the *Kepler* spacecraft. Pixels are only downloaded from 'postage stamps' around pre-selected targets. The *Kepler* CCDs saturate for stars with $Kp \lesssim 11$–12 mag, with excess flux bleeding along CCD columns. To recover the entirety of the stellar flux, the postage stamps for bright stars must include long bleed columns, thereby requiring a very large number of pixels. Consequently, data from few of the brightest stars are ordinarily selected to be downloaded. For the nominal *Kepler* mission, the field was even chosen to avoid as many bright stars as possible to minimize the impact they would have on the primary, planet-finding mission (Koch et al., 2010). Of the 14 stars on active silicon brighter than $Kp = 6$ mag, only θ Cyg (Guzik et al., 2016), V380 Cyg (Tkachenko et al., 2012), and 16 Cyg A (Metcalfe et al., 2012) were targeted over multiple observing quarters, HD 185351 (Johnson et al., 2014), and HR 7322 (Stokholm et al. in preparation) were only observed for a single quarter in

short cadence mode (58.85 s sampling), and nine stars were completely unobserved.

The desire to observe the brightest possible targets therefore calls for novel methods to recover light curves from an economically feasible number of pixels. In Chapter 5, we have shown that light curves of bright stars can be recovered from *Kepler* calibration 'smear' data, allowing for the observation of stars that were not specifically targeted. While a very valuable method and going a long way to solving this problem, it has a few drawbacks that lead us to continue to pursue other methods. One such drawback is the much shorter integration time and small number of pixels used for smear measurements, which leads to lower photometric precision with a photon noise equivalent to a star ~ 6.7 mag fainter. Another is that smear measurements are made along CCD columns, so targets falling on the same columns are confused. This is a particular concern in clusters, such as the Pleiades, and in the crowded K2 fields in the galactic plane. Finally, the bleed columns of bright stars, particularly those near the edge of the CCD, can also saturate the smear pixels in those columns, rendering them useless.

Another method has been developed by Aerts et al. (2017) to observe the O9.5Iab star HD 188209 with *Kepler*. This $V = 5.63$ mag supergiant was intentionally placed between CCDs during the nominal *Kepler* mission. Nevertheless, scattered light from this bright star 'contaminated' two nearby targets on active silicon, allowing for the variability in the supergiant to be successfully recovered.

We have developed this idea further with a new method that uses the flux recorded by non-saturated pixels in the halo surrounding a bright star. In this Chapter, we show that stellar variability may be successfully observed with this limited aperture, despite losing much of the stellar flux. While this method is susceptible to aperture losses, compounded by systematics inherent in the K2 mission, namely pointing drifts and inter- and intra-pixel sensitivity variation, we show that appropriate weighting of the contributions from each pixel can effectively neutralize these effects. To illustrate

this method, we have applied it to the seven brightest stars in the Pleiades, all of which are late B-type stars, and were observed during K2 Campaign 4.

6.2 Halo Photometry

6.2.1 Data

K2 Campaign 4 observed a field in the direction of the constellation Taurus from 2015 February 8 to 2015 April 20. Fig. 6.1(a) shows the full-frame image of the Pleiades open cluster (M 45) on the two CCDs of Module 15 of the *Kepler* spacecraft. The seven brightest stars, ranging from $Kp = 2.99$ to 5.19 mag, were each targeted with a circular aperture with a radius of 20 pixels, and observed in long cadence mode (29.4 min sampling). Each aperture consists of 1245 pixels, an allocation equivalent to approximately six to twelve $Kp = 12$ mag stars. Electra and Merope were near the edge of the CCD, and their target apertures were truncated along one side by several columns. Fainter cluster members were targeted with regular apertures. A detailed investigation of the rotation of these stars using K2 data has been recently reported (Rebull et al., 2016a,b; Stauffer et al., 2016).

Fig. 6.1(b) shows the image of Alcyone within the aperture. The central columns are saturated. Additionally, pixels in column 668 are saturated by the bleed column of the nearby star 24 Tau. We construct each light curve from the unsaturated pixels in the halo. Three-day segments of the light curves of the four pixels highlighted in Fig. 6.1(b) are shown in Fig. 6.2. The light curve of each pixel clearly shows the change in flux caused by the pointing drift, with corrections made by thruster firings at $\sim$6 h intervals.

Several pipelines have been developed to process K2 data and remove these pointing-drift systematics, such as K2SFF (Vanderburg & Johnson, 2014b), K2P2 (Lund et al., 2015), K2SC (Aigrain et al., 2015, 2016), K2VARCAT (Armstrong et al., 2015) and

EVEREST (Luger et al., 2016, 2017). While these methods have been highly-successful for fainter stars, even approaching the photometric precision of the nominal *Kepler* mission, they have substantial difficulties when dealing with the large aperture loses that arise with these target pixel masks, necessitating an alternate photometric method.

6.2.2 Method

Each circular aperture is dominated by the light of the bright central star it contains. The first major feature is saturation, where each of the core pixels bleeds flux in both directions along its column. Even for very saturated targets, this process is conservative, with the consequence that extremely elongated apertures have been used to perform photometry at the cost of many pixels (Kolenberg et al., 2011). Other than this, there is a complex, position-dependent point spread function (PSF), resulting from both the usual diffraction through the limited telescope aperture and from multiple orders of reflection in the telescope optics, which makes a significant contribution for these bright stars. To first order, this resembles an image of the telescope pupil; higher orders of reflection impose structure related to the focal plane CCD array, and multiple distorted images of both the array and the pupil. It is therefore not straightforward to model the PSF to perform photometry, as is common in other contexts (Schechter et al., 1993) and has been previously done with *Kepler* (Libralato et al., 2016). Instead, we adopt a different approach to optimally extract a light curve from this complex 'halo' of scattered light.

As seen in Fig. 6.2, the pointing drift signal is anti-correlated on either side of the roll motion, while the stellar signal will be correlated across the aperture. This means we can separate the spatially-dependent pointing drift signal from the stellar signal and other instrumental signals that may be correlated across the aperture, such as focus drift. On this basis, we propose a new method to construct a light curve

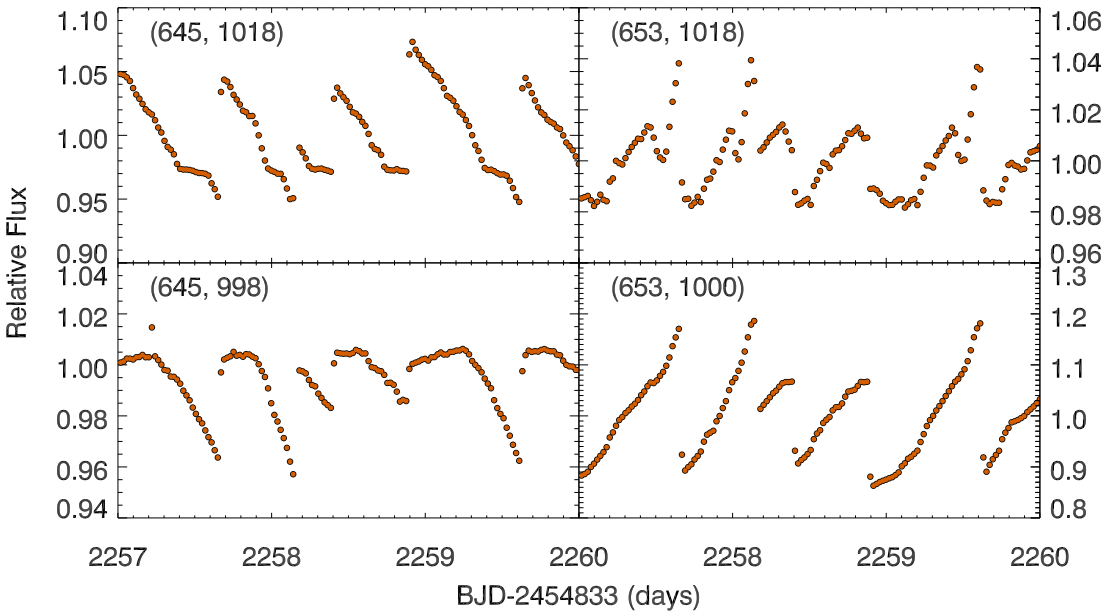

Figure 6.2: Three day segments of the four pixels highlighted in Fig. 6.1(b). The pixel coordinates are labelled. The drift signal clearly dominates, but is anti-correlated on either side of the roll motion, which is primarily from left-to-right in this figure.

from a weighted sum of the non-saturated pixels, with the weights chosen to minimize pointing systematics and aperture losses. This is therefore a simultaneous method for aperture photometry and systematics correction, which are ordinarily done in separate stages. We refer to this method as halo photometry.

The flux f_i of the final light curve at each observation i is chosen to be

$$f_i = \sum_{j=1}^{M} w_j p_{ij}, \tag{6.1}$$

where w_j is the weight of pixel j, p_{ij} is the flux in pixel j at observation i, and M is the number of pixels. The weights w_j are all defined to be positive and their sum is constrained to be unity. If the weights were all constant, this would reduce to simple aperture photometry. Instead, we have a soft aperture, and a suitable objective function must then be defined in order to find the optimal weights, of which several choices are possible. While a band-limited PSF would allow for negative weights in principle, we constrain these to be strictly positive in order to avoid signal

self-subtraction.

Noting that the jumps caused by the thruster firings in K2 are large and sudden, whereas stellar variability is generally more gradual, we are inspired to consider minimizing the differences between consecutive observations across the time series, that is, we minimize the normalized first-order total variation (TV) of fluxes given by

$$\mathrm{TV} = \frac{\sum_{i=1}^{N} |f_i - f_{i-1}|}{\sum_{i=1}^{N} f_i}, \tag{6.2}$$

where N is the total number of observations. Because the jumps occur in opposite directions on either side of the roll motion, and the wide diversity in pixels can compensate for inter- and intra-pixel sensitivity variation, the right combination of weights can effectively remove jumps. Furthermore, because stellar variability is present in all pixels and the weights are constrained to be positive, it is hard to spuriously suppress real stellar variability, even in cases where this variability is sudden such as a flare or transit event. We also consider second-order TV, where centred second finite differences replace first differences as above. Higher orders can likewise be defined, but in practice, we find that first or second order differences are sufficient for our present purpose. We note that TV need not be normalized by the mean flux term we include in the denominator, but we introduce this normalization to avoid finding the trivial solution where dark pixels are chosen to minimize total flux and therefore spuriously minimize absolute TV. We apply a sequential least squares programming algorithm implemented in SciPy (Jones et al., 2001) to find the weights that minimize equation (6.2), and the algorithm converges quickly on a modern laptop.

An alternative objective function would be to use the normalized quadratic variation (QV), that is, the sum of the square of differences between consecutive observations,

$$\mathrm{QV} = \frac{\sum_{i=1}^{N} (f_i - f_{i-1})^2}{\sum_{i=1}^{N} f_i}. \tag{6.3}$$

We have investigated the use of QV for this application, and found it achieved visibly poorer results on real and simulated data compared to TV.

To understand why TV may be preferable to QV, it is worth noting that TV has been very widely applied as a regularizing term in many domains of signal processing, especially for image data and for de-noising step-wise constant functions with high frequency noise (Rudin et al., 1992; Strong & Chan, 2003). These signal processing applications have their foundation in compressed sensing theory. For a continuous function, the TV is the arc length between two points; in the discrete case, this becomes the sum of absolute values of finite differences. In the language of Minkowski metrics in linear algebra, the sum of absolute values of a vector's elements is called the $\ell 1$ norm, also known as the taxicab or Manhattan metric: this is the distance between two points subject to the restriction that you can only move parallel to the axes, as on a grid of streets (Menger & Sutton, 1952). Other metrics include the sum of least squares of the components of a vector, which is the $\ell 2$ or Euclidean norm, while the number the nonzero elements of a vector in some basis, a measure of sparsity, is called the $\ell 0$ norm. So TV is the $\ell 1$ norm on the derivative of a function, whereas QV is the $\ell 2$ norm. From compressed sensing theory, it can be shown that by minimizing $\ell 1$ norms under certain general conditions (which is computationally easy) it is also possible to minimize the $\ell 0$ norm (which is otherwise computationally hard), and therefore that TV is the appropriate objective function for enforcing sparsity in the gradient of a time series or image (Candes et al., 2006). Therefore, if we assume that a true signal has a small gradient with respect to time nearly everywhere, it is often effective to minimize TV to constrain a reconstruction from noisy data. We do not see a clear reason why the gradient of stellar variability should be sparse, and employ the method *ad hoc*, rather than explicitly as a case of compressed sensing.

Pixel-level decorrelation (PLD) in K2 has been explored by Luger et al. (2016), extending earlier work by Deming et al. (2015), using least-squares ($\ell 2$) methods to

project light curve residuals onto principal components of normalized pixel time series. In their approach, simple aperture photometry is first used to obtain a raw light curve, which is then used to normalize the raw pixel time series. In Luger et al. (2016), the further step is taken of generating second- or third-order polynomials in these time series, to obtain a large basis set spanning nonlinear components of the aperture losses. We note that $\ell 2$ approaches to weighted-pixel soft aperture photometry were proposed by Jenkins et al. (2000), and independently investigated by Hogg, Foreman-Mackey & Goodman (unpublished), but we do not know of any previous TV-based method.

Fig. 6.1(c) shows the final weights for the light curve of Alcyone, with up-weighted pixels shown by red shades, while down-weighted pixels are indicated by blue shades. Comparison with the image in Fig. 6.1(b) reveals that the diagonal halo features, consisting of the diffraction spikes and the higher-order reflection artefacts of the telescope spiders, are heavily up-weighted.

Halo light curves obtained as above typically contain small residual roll systematics and more substantial long-term drifts. We correct residual roll systematics using κ2sc, a Gaussian Process-based K2 detrending pipeline which jointly models stellar variations and instrumental systematics (Aigrain et al., 2016). For the longer-term systematic drifts, we fit and subtract a polynomial of variable order, typically eight or nine, to remove these trends. The trend removal affects frequencies lower than $0.2\,\mathrm{d}^{-1}$. The lightcurve of Maia exhibits a long-period signal that is intrinsic to the star, as well as the longer-term systematic drifts. To avoid overfitting in this case, we use the polynomial fit of nearby Taygeta to set the high-order coefficients, while allowing coefficients up to the quartic term to vary. While it would be preferable to fit a linear combination of cotrending basis vectors (CBVs; Smith et al., 2012; Stumpe et al., 2012), those available for K2 unfortunately are dominated by thruster firing systematics and are unsuitable to fit to otherwise-clean light curves possessing only

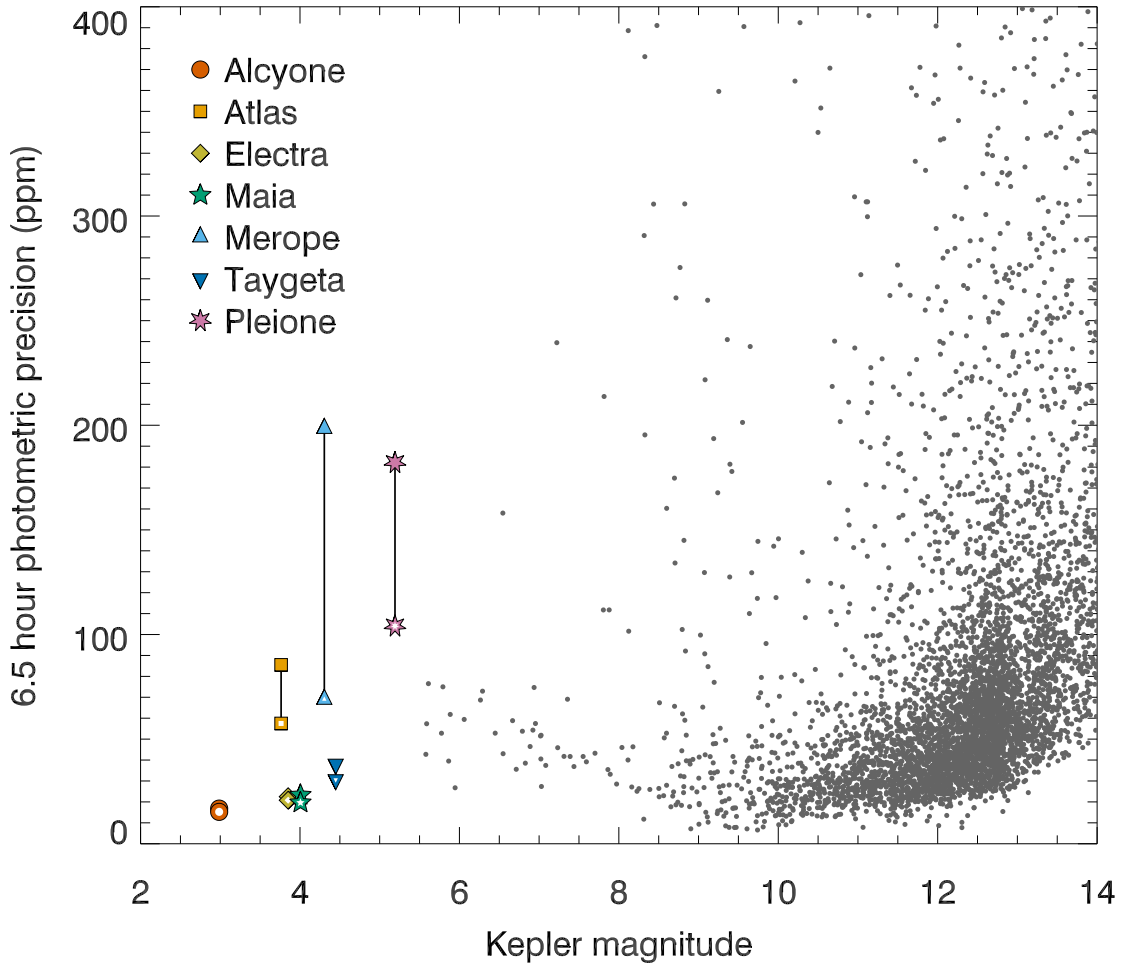

Figure 6.3: Photometric precision as a function of *Kepler* magnitude. The solid symbols indicate light curves prepared with the halo method alone, while open symbols are for those with further corrections using K2SC; these two measurements are connected by solid lines for each star. For comparison, the grey dots indicate CDPP for K2 C4 dwarfs ($\log g > 4$) using K2SC.

long-timescale trends. Furthermore, the long-timescale common-mode systematics in halo photometry are not yet well-quantified, and it is not clear whether the CBV approach is well-suited to these light curves. We leave this as the subject for future work.

With the large diversity of available pixels there is the potential for over-fitting. Spurious signals might be introduced, or real astrophysical variability removed, either by the TV objective function suppressing time variability, or by inappropriately weighting noisy pixels. To account for the former, it would be ideal to divide up the light curve into separate chunks, and use these separately for training and validation. For instance, one might train weights on the first half of the light curve, and use these to extract photometry from the second, and vice versa. This is a computationally-expensive approach that we have not adopted.

We considered it important to address the problem of pixel-level abnormalities by checking whether the same light curve could be reproduced from independent subsets of pixels. To select independent sets of pixels with similar overall distribution, we unravel the array coordinates, and select eight ensembles taking every eighth pixel time series. We then applied the method on these subsampled pixel arrays and produced light curves for each. We find that the long-term trend behaviour of all of these light curves differs, but that after filtering, subsampled light curves reproduce the same overall behaviour as the globally-optimized light curve. A consensus light curve, consisting of the means of the subsampled light curves, is very similar to the globally-optimized light curve, again except for an overall trend. Finding no reason to prefer one or the other, we use globally-optimized light curves for the scientific analysis in the remainder of this Chapter.

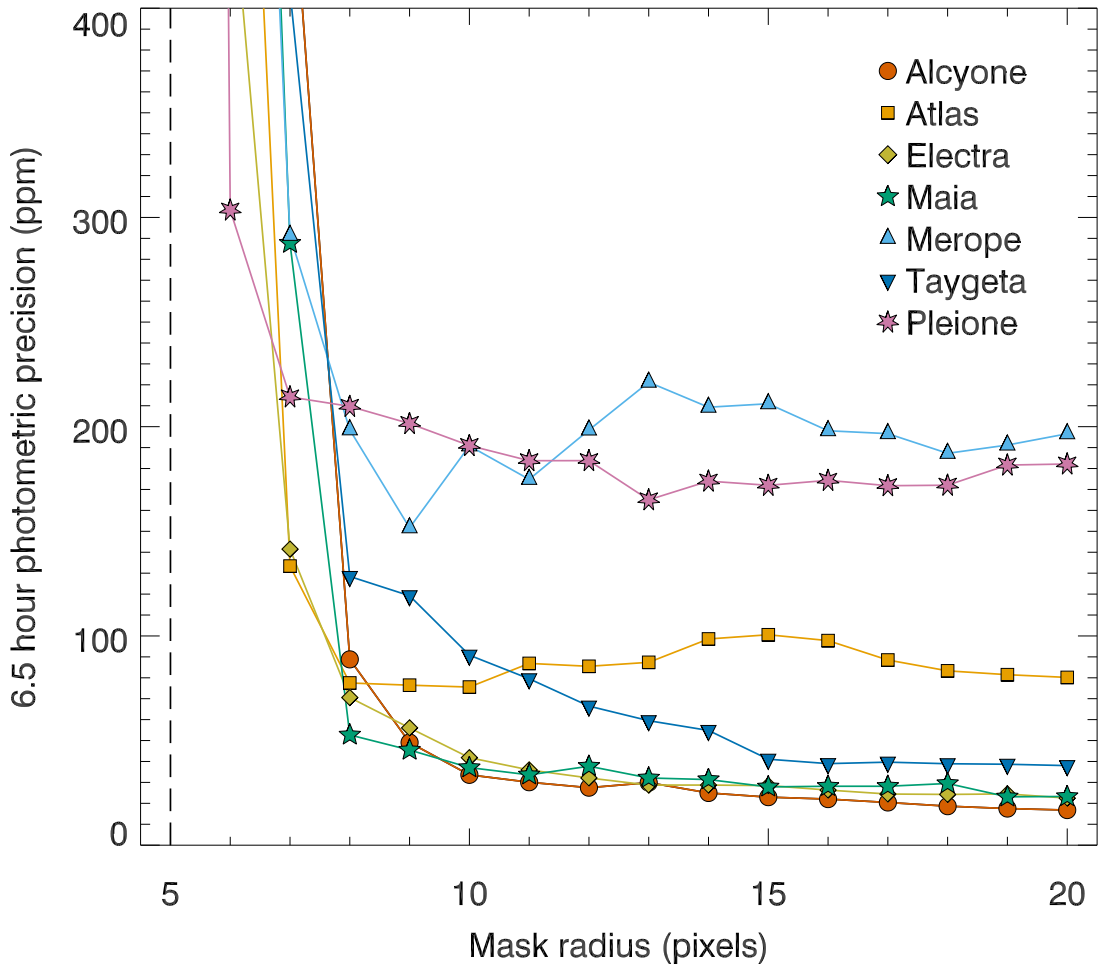

Figure 6.4: Photometric precision as a function of mask radius for each star. The dashed line at a mask radius of five pixels indicates the region below which almost all pixels are saturated.

6.3 Photometric Precision

The efficacy of K2 data processing pipelines has commonly been determined by measuring the 6.5 h Combined Differential Photometric Precision (CDPP; Christiansen et al., 2012). This measurement, however, is strongly influenced by the presence of stellar variability in a time series, so a straight application of CDPP is not informative in such a situation. When benchmarking K2 pipelines, CDPP values are therefore usually reported for dwarf stars for which stellar variability is minimal.

We do not have any bright and photometrically-quiet dwarf stars to test the halo photometry method on, so an alternative approach is required. We clean the light curves of the stellar signal by iterative sine-wave fitting (also called prewhitening) using the program Period04 (Lenz & Breger, 2005), and then measure the CDPP of the residual light curves. We use the Aigrain et al. (2016) CDPP-equivalent, which first removes long-term trends with a Savitzky-Golay filter, then takes the mean of the standard deviations of all consecutive 13-sample (6.5 h) segments of the light curve, ignoring outliers more than 5σ away from the mean.

The CDPP for each star is shown in Fig 6.3, both for light curves processed using our halo photometry method alone (solid symbols) and with further processing with the k2sc pipeline to remove any remaining systematics results (open symbols). We find that k2sc typically reduces the CDPP of halo light curves by $\sim$ 10 per cent, although in the cases of Atlas, Merope, and Pleione, the CDPP is reduced by k2sc by 32, 65, and 42 per cent, respectively.

Comparison of the CDPP of the halo targets with the CDPP of fainter dwarf stars processed with the k2sc pipeline (grey dots in Fig. 6.3) shows that the precision from halo photometry is generally as good as that obtained for regular targets. For three of the halo targets, however, the CDPP is significantly higher than expected. We note that these three stars – Atlas, Merope and Pleione – have the highest amplitude stellar variability (see Section 6.4), and are significantly improved by further processing using

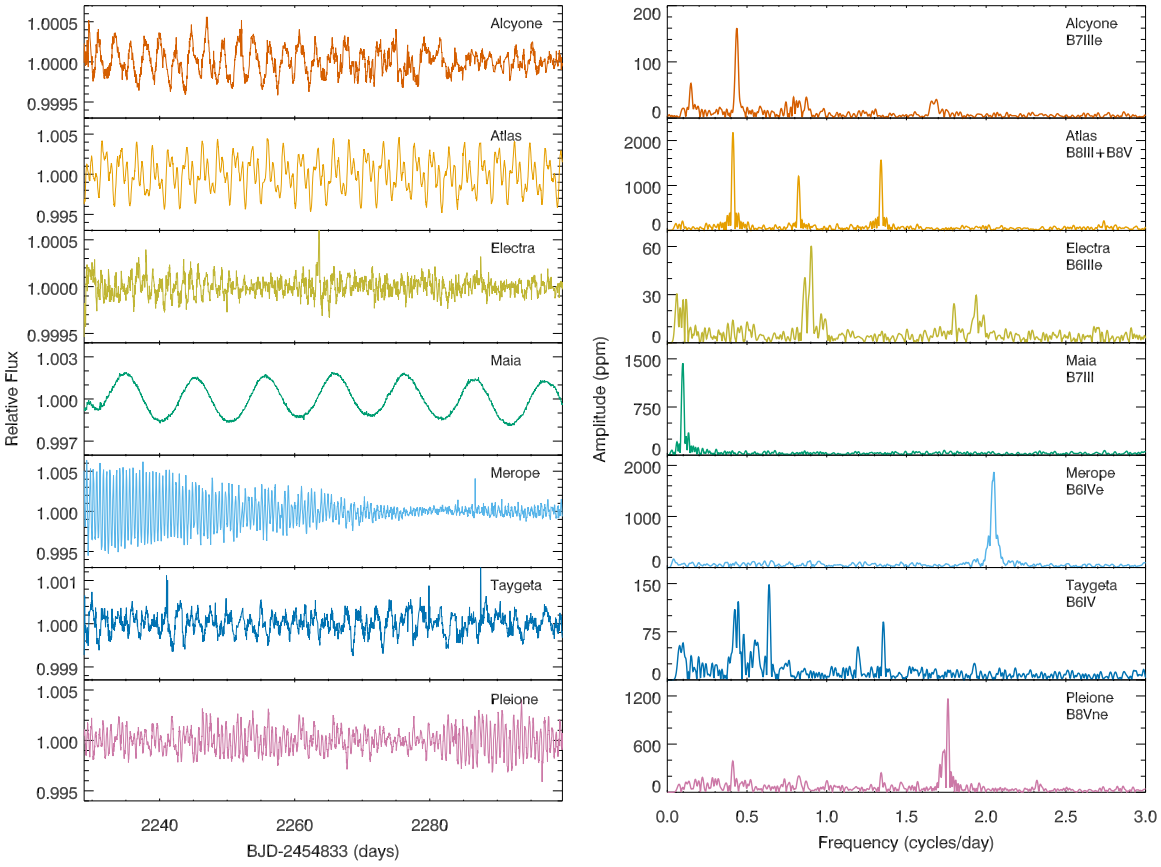

Figure 6.5: Time series (left) and amplitude spectra (right) of the brightest stars in the Pleiades. Brightest to faintest objects are listed top to bottom. Note the changes in scale on the y-axes.

K2SC. We attribute the increased CDPP to the halo photometry algorithm being less effective at suppressing jumps in the light curve in the presence of high-amplitude stellar variability.

The fact that the CDPP is comparable to that of fainter stars, and even as good in some cases as the best CDPPs of the fainter stars, is indicative that this method delivers photometry of the quality required in principle to detect exoplanet transits. It is nevertheless important to establish in future work whether the TV minimization removes planetary transit signals as sharp, short-duration events: we suspect that because TV preserves $\sim$ hour-scale stellar oscillations, as shown in Section 6.4, that this is not likely to be a problem for transit events on this timescale.

As halo photometry is intended as a solution to the problem of pixel allocation for very bright objects, it is important to determine how its precision varies with the size of the allocated pixel mask. Furthermore, it may be important to avoid contamination from other nearby bright sources to reduce the mask size beyond the requirements imposed by bandwidth constraints. The raw K2 data were obtained with 20 pixel radius circular masks; we run the algorithm separately on masks with radii from 6 to the full 20 pixels and measure the 6.5 h CDPP as a function of mask radius. At 5 pixels and below, almost all pixels are saturated. The results are shown for all seven stars in Fig. 6.4. The precision follows an L shaped curve: radii much less than 8 or 9 pixels give very poor photometric precision, and there is some improvement, albeit limited, for radii much larger than this. The bump around $\sim$ 15 pixels for Atlas corresponds to the position of the nearby background star 2MASS J03491192+2403507, and we interpret this as the result of contamination. We note that, except for the columns lost due to saturation, these curves resemble the photometric signal as a function of radius for normal CCD images of a star (Howell, 1989), supporting the conclusion that we are seeing a true stellar profile in the PSF wings of these bright stars. From these tests we conclude that further reductions in the required number of pixels are possible.

A mask with a 12 pixel radius is generally sufficient to achieve good precision, which is equivalent in terms of pixel allocation cost to the requirements for approximately two to four $Kp = 12$ mag stars.

6.4 Variability in the Pleiades

The naked-eye Pleiades were the first collection of stars to be recognized as a cluster (Michell, 1767), and together with many fainter members they remain one of the most prominent and well-studied open clusters. While the cluster contains over 1000 members (e.g. Bouy et al., 2015), with an age of ∼125 Myr (Stauffer et al., 1998) it is visually dominated by several hot, massive stars. The seven brightest stars in the Pleiades, which we study here – Alcyone, Atlas, Electra, Maia, Merope, Taygeta, and Pleione – are all late B-type stars. Their time series and amplitude spectra are shown in Fig. 6.5. We search all seven halo light curves using the K2PS planet-search package (Parviainen et al., 2016; Pope et al., 2016b), but do not find any evidence of transiting planet candidates or eclipses.

It is remarkable to note that, although these stars are from the same cluster, and therefore have a similar age and initial composition, and they span a narrow range in mass and effective temperature, they display a diverse range of variability, both in terms of amplitude and frequency content. Such diversity would not be able to be seen from the ground; periods in the range 0.5–3 d are difficult enough, but amplitudes below a mmag are impossible with single-site data (see e.g. De Cat & Aerts, 2002). It has only been with the dawn of space-based photometric missions, such as MOST, CoRoT and *Kepler* that such low amplitude variability could be detected reliably (e.g. Aerts et al., 2006; Degroote et al., 2009; Balona et al., 2011).

Variability may arise from a number of phenomena, including various pulsation mechanisms and rotational modulation. These types of variability may appear similar,

and further knowledge of the star's properties can be useful to make the distinction.

Four of the stars are known Be stars (Alcyone, Electra, Merope, and Pleione), meaning they have shown emission lines in their spectra associated with a circumstellar 'decretion' disc (for a recent review of Be stars, see Rivinius et al., 2013). Pleione is known to transition between a Be phase and a shell phase – the difference between such phases is understood to be the orientation of the disc, with shells occurring when it obscures the central star (Struve, 1931). Spectra contemporaneous with the K2 observations available at the Be Star Spectra (BeSS) database[1] (Neiner et al., 2011) show all four stars presently show emission features, and Pleione is in a shell phase. These circumstellar discs can also be a potential source of variability in the time series. Many Be stars are known to pulsate (Baade, 1982; Bolton, 1982; Rivinius et al., 2003; Walker et al., 2005; Saio et al., 2007; Neiner et al., 2009). Aerts (2006) concluded that the pulsating Be stars are not a separate class of variable stars, but rapidly-rotating and complex examples of the SPB star class. There is evidence to suggest that these pulsations are responsible for mass-loss episodes that launch stellar material into the decretion disc (Rivinius et al., 1998, 2003; Huat et al., 2009; Baade et al., 2016), and a model has been developed to explain how pulsations, coupled to rapid, sub-critical rotation can achieve this (Kee et al., 2014).

In the remainder of this Section, we discuss the variability of each star in turn, in conjunction with observations recorded in the literature, to deduce the likely nature of each target.

6.4.1 Alcyone

Alcyone (η Tauri, 25 Tauri, HR 1165, HD 23630) is a blue giant of spectral type B7IIIe, and is the brightest star in the Pleiades ($V = 2.87$ mag).

The K2 time series and amplitude spectrum of Alcyone are shown in the top row of

[1] `http://basebe.obspm.fr`

Fig. 6.5. The spectrum is dominated by a frequency at $0.4360\pm0.0004\,\mathrm{d}^{-1}$, although power is present at other frequencies as well, including at one-third of this primary frequency. There are low amplitude groupings of frequencies around 0.8 and $1.6\,\mathrm{d}^{-1}$. Such frequency groupings have been seen before in Be and regular B stars (Walker et al., 2005; Cameron et al., 2008; Diago et al., 2009; Huat et al., 2009; Neiner et al., 2009; Balona et al., 2011; McNamara et al., 2012). Balona et al. (2011) speculated that these groupings were caused by rotational modulation, however Kurtz et al. (2015), using the excellent frequency resolution of the full *Kepler* mission, were able to show that all peaks could be explained as simple combinations of a few modes. Such combination frequencies are indicative of non-linear coupling between pulsation modes. We therefore conclude that these low-amplitude peaks are caused by SPB oscillations.

The highest-amplitude frequency in the Alcyone amplitude spectrum may also be due to SPB pulsations. It occurs at a frequency close to half that of the frequency grouping at $0.8\,\mathrm{d}^{-1}$, and is somewhat broadened, suggesting that it is an unresolved peak of several frequencies. The peak at $0.15\,\mathrm{d}^{-1}$ can also be explained as a combination frequency.

Another possibility is that the highest-amplitude frequency arises from rotational modulation, or even from variability of the circumstellar disc. We can consider if this frequency occurs at an appropriate timescale to be caused by rotation. We calculate the critical velocity from the mass and radius given in Frémat et al. (2005), using this radius as an estimate of the equatorial radius. Rotation at the critical velocity would have a frequency of $0.61\pm0.07\,\mathrm{d}^{-1}$. The $v \sin i$ was found to be $140\,\mathrm{km\,s}^{-1}$ by Abt et al. (2002); the minimum possible rotational frequency is $0.30\,\mathrm{d}^{-1}$. The peak at a frequency at $0.4362\pm0.0016\,\mathrm{d}^{-1}$ is therefore consistent with being caused by near-critical rotation.

If this is the rotational frequency, then with an estimate of the stellar radii and the

known $v \sin i$, the inclination of the star can be estimated. In order to account properly for the prior distribution of i and propagate uncertainties correctly, we implement a Markov Chain Monte Carlo (MCMC) model in PySTAN[2]. We choose an isotropic prior for the inclination such that $\cos i \sim \text{Uniform}(0, 1)$, $i \in [0°, 90°]$. The rotational frequency f and radius R are taken to be normally distributed. Finally, we model our projected velocities as $v \sin i \sim \text{Normal}(2\pi Rf \cdot \sin i, \sigma_{v \sin i})$, and we assume a 10 per cent uncertainty on $v \sin i$ in the value given by Abt et al. (2002). We burn-in this model for 5000 MCMC steps, discard these, and generate a further 5000 samples from the posterior distribution. We find an inclination angle of $48 \pm 6°$ and display a normalized histogram of these samples in Fig. 6.6 as a marginal posterior probability density function, together with those of the other stars we shall discuss in turn. The inclination found is consistent with the orientations implied by the interferometric measurements of the circumstellar disc (Quirrenbach et al., 1997; Tycner et al., 2005).

The highest-amplitude frequency can therefore be explained as either an unresolved group of frequencies arising from SPB pulsation, or as the rotation frequency. We favour the pulsation explanation due to its ability to account for all the variability in the time series at all frequencies. Nevertheless, it is possible that the fundamental pulsation time scale is commensurate with the rotational time scale.

[2] `http://mc-stan.org/interfaces/pystan`

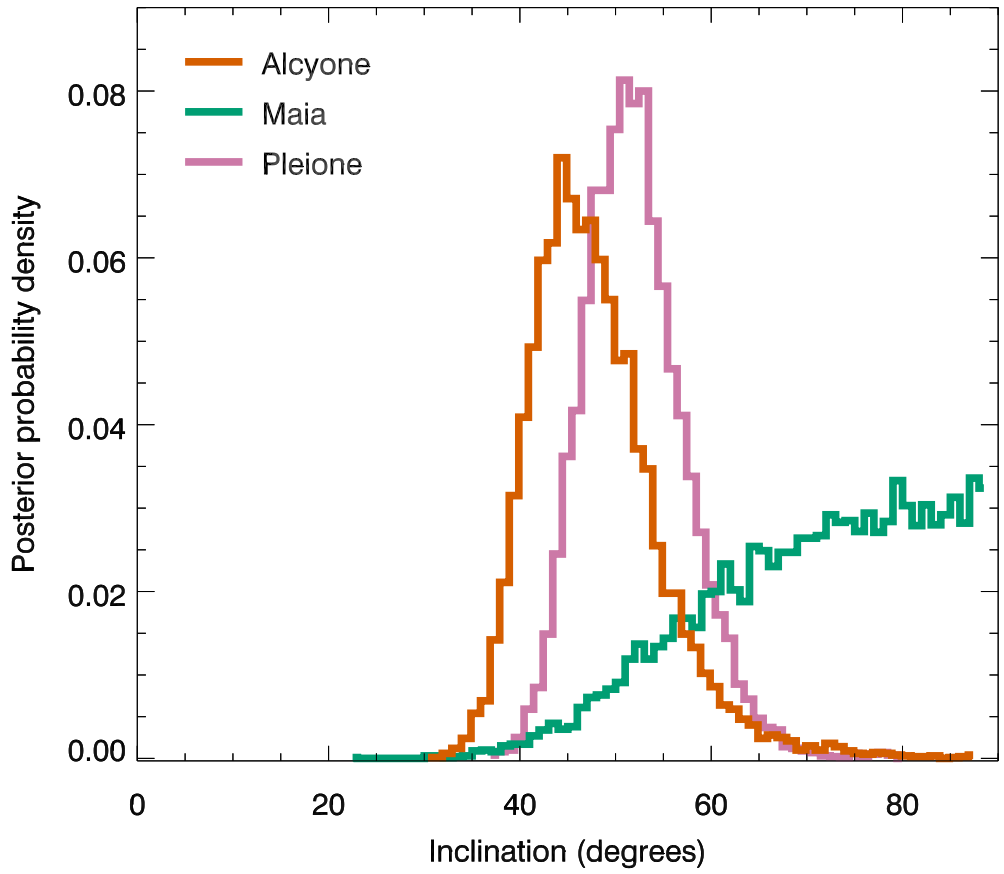

Figure 6.6: Posterior probability density functions for the possible inclinations of Alcyone, Maia, and Pleione calculated from their radii, projected rotational velocity, and possible rotation periods.

6.4.2 Atlas

Atlas (27 Tauri, HR 1178, HD 23850) is the second-brightest member of the Pleiades ($V = 3.63$ mag). Atlas is a binary system (McGraw et al., 1974; Bartholdi, 1975; de Vegt & Gehlich, 1976), whose primary component, identified as Atlas Aa1 in the Washington Double Star Catalog (Mason et al., 2001), is a B8III star, and has been used as the standard star for its spectral type (Morgan et al., 1943; Johnson & Morgan, 1953). It has a mass of $4.74 \pm 0.25\,M_\odot$ (Zwahlen et al., 2004). The secondary component, Atlas Aa2, orbits the primary in an eccentric (e=0.2384±0.0063), 290.984±0.079 d orbit with an inclination of $i = 107.87 \pm 0.49°$. It is a B8V star, with a mass of $3.42 \pm 0.25\,M_\odot$ (Zwahlen et al., 2004).

The K2 light curve and amplitude spectrum of Atlas are shown in the second row of Fig. 6.5; we clearly detect variability. The presence of the 13th mag star 2MASS J03491192+2403507, around 15 pixels from Atlas, dilutes the signal of Atlas in the halo light curve. We therefore use a 12 pixel radius mask to mitigate this effect.

Three prominent peaks are seen in the amplitude spectrum. The peak at $0.8236\,d^{-1}$ is the second harmonic of the lowest peak at $0.4121\,d^{-1}$. This lowest frequency coincides with the suspected period observed with STEREO (Wraight et al., 2012). A third prominent peak occurs at $1.341\,d^{-1}$. Several other low-amplitude peaks are also present in the amplitude spectra. Most of these frequencies are harmonics of the two principal frequencies, but there is also a third independent frequency at $0.7627\,d^{-1}$ and its harmonic, and a combination frequency of the two high-amplitude principal frequencies at 0.5092 and $0.8236\,d^{-1}$. The presence of this combination frequency reveals that this variability is caused by pulsations; such frequencies cannot be caused by rotation (e.g. Kurtz et al., 2015).

It is not immediately clear whether these pulsations are present in Atlas Aa1 or Aa2, although we note that the amplitudes are diluted by the presence of the other star. Atlas Aa1 is approximately five times brighter than Atlas Aa2, so the pulsations

will be diluted by a factor of 1.2 if they are present in the primary, and by a factor of 6 if they are present in the secondary. The large amplitude of two of the principal frequencies would seem to favour that they occur in the primary component, but further investigation including modelling the stars may provide greater clarity.

6.4.3 Electra

Electra (17 Tauri, HR 1142, HD 23302) is the third-brightest star in the Pleiades ($V = 3.70$ mag), and is a blue giant of spectral type B6IIIe. While some lunar occultation measurements of Electra have been found to be consistent with a single star (McGraw et al., 1974; Eitter & Beavers, 1974), others suggest it has a companion (Bartholdi, 1975; de Vegt & Gehlich, 1976; Richichi et al., 1996). Abt et al. (1965) found evidence that Electra was a spectroscopic binary with a period of ∼100 d. However, while finding Electra may have a variable radial velocity, Pearce & Hill (1971) were unable to confirm the period claimed by Abt et al. (1965). Jarad et al. (1989) also claim Electra may be a spectroscopic binary, although with a period of only ∼4 d.

Previous photometric observations of Electra have found it to be constant within the precision of the measurements. Subsequently, McNamara (1985, 1987) used Electra as the reference star for differential photometry with other members of the Pleiades.

The time series and amplitude spectrum of Electra are shown in the third row of Fig. 6.5. Electra has the lowest amplitude variability of any of the stars considered in this Chapter. Low-amplitude frequency groupings are present in the ranges 0.8–1 d^{-1} and 1.8–2 d^{-1}. These are SPB pulsations showing the same type of structure that was previously discussed for Alcyone, with several base frequencies and combination frequencies (Kurtz et al., 2015).

6.4.4 Maia

Maia (20 Tauri, HR 1149, HD 23408), a B7III star, is the fourth-brightest member of the Pleiades ($V = 3.87$ mag). The uniqueness of its relatively narrow-lined spectrum amongst the B stars in the Pleiades spurred early interest in detecting variability, although a clear detection proved elusive. After initial claims of variability (Adams, 1904; Henroteau, 1920), Struve (1955) hypothesised a class of variable stars with 1–4 h timescale pulsations, lying in the HR diagram between the β Cephei and δ Scuti pulsators, which he called the Maia variables.

Further searches for variability in Maia (Breger, 1972; Percy, 1978; McNamara, 1985, 1987; Percy & Wilson, 2000; Paunzen et al., 2013) and Maia variables (e.g. Lehmann et al., 1995; Scholz et al., 1998; Weiss et al., 1998; Kallinger et al., 2002, 2004; De Cat et al., 2007) have been negative, leading Aerts & Kolenberg (2005) to suggest that the Maia variable class was unnecessary.

Despite the ongoing debate over the existence of Maia variables, we can at least now settle the question of Maia's variability. The K2 time series and amplitude spectrum of Maia are shown in the fourth row of Fig. 6.5. For the first time, we have unambiguously detected variability in Maia. One clear frequency is found in the amplitude spectrum at $0.0967 \pm 0.0008\,\mathrm{d}^{-1}$; the variability has a 10 d period. Other low-amplitude peaks are present at similar periods, including at the harmonic of the primary frequency, but because these time-scales are similar to the instrumental long-term trends that were removed, we are cautious to not treat these low-amplitude modes as necessarily being intrinsic to the star. Nevertheless, this much is clear: Maia is variable, but Maia is *not* a Maia variable.

Maia is known to be chemically peculiar; Renson & Manfroid (2009) list Maia as a He-weak Mn star in their catalogue. Many HgMn stars show evidence of line-profile variations caused by the rotation of chemical surface spots (e.g. Ryabchikova et al., 1999; Adelman et al., 2002). Rotational modulation has also been observed in the

light curves of other HgMn stars (e.g. Balona et al., 2011). We suggest that the photometric variability of Maia is similarly caused by rotational modulation resulting from a large chemical spot. White et al. (submitted) using spectra from SONG (the Stellar Observations Network Group at Observatorio del Teide) show variability in an isolated Mn II line is consistent in phase and period with the broadband photometric variability determined by K2, supporting the chemical spot hypothesis.

White et al. (submitted) find using CHARA interferometry a limb-darkened angular diameter for Maia of $\theta_{LD} = 0.451 \pm 0.006$ mas. Adopting the distance to the Pleiades as determined from VLBI parallax measurements (136.2 ± 1.2 pc; Melis et al., 2014), we find a radius for Maia of $6.61 \pm 0.11 R_\odot$. Combining this angular diameter with the estimate of bolometric flux by van Belle et al. (2008), for which we adopt a 5 per cent uncertainty, we find an effective temperature of $T_{\rm eff} = 12550 \pm 150$ K.

Calculation of the inclination angle from the radius, projected rotational velocity, and rotation period reveals that Maia is seen close to equator-on. Using the same MCMC model that we previously used to determine the possible inclination of Alcyone in Section 6.4.1 to properly account for the prior distribution of i and propagate uncertainties correctly. The resulting posterior distribution is shown in Fig. 6.6. We find a range of possible inclinations, with a 99 per cent probability of it being above 42°.

6.4.5 Merope

Merope (23 Tauri, HR 1156, HD 23480) is the fifth-brightest member of the Pleiades ($V = 4.18$ mag) and is of spectral type B6IVe. Merope appears single in lunar occultation (McGraw et al., 1974; Eitter & Beavers, 1974; de Vegt & Gehlich, 1976) and speckle interferometry measurements (Mason et al., 1993).

Previous photometric observations of Merope have revealed high-amplitude variability. McNamara (1985, 1987) found a consistent frequency of $2.04\,{\rm d}^{-1}$ across several

years. This frequency is, coincidentally, half the thruster-firing frequency for the K2 mission. The K2 time series and amplitude spectrum of Merope are shown in the fifth row of Fig 6.5. The previously-known frequency at $2.04\,\mathrm{d}^{-1}$ is clearly recovered. The halo photometry method works remarkably well in this situation, preserving the stellar variability despite the unfortunate similarity to the thruster firing period, whereas other methods that attempt to detrend the telescope pointing drift signal would likely overfit and remove part of the stellar signal as well. While there are small peaks at 4.08 and $6.13\,\mathrm{d}^{-1}$ in the amplitude spectrum, it is unclear if these are harmonics of the primary frequency, or a residual of the pointing drift.

The width of the peak in the amplitude spectrum and the beating visible in the time series are indicative of there being several closely spaced periods or a non-coherent signal, resulting in the beating apparent in the time series. There are several possible explanations for the variability. Merope is a Be star so it has a circumstellar disc that may exhibit variability. Alternatively, the variability may have a stellar origin, either as rotation, with differential rotation accounting for incoherent variability, or from SPB pulsations, with several closely spaced g-mode frequencies.

Rotation may be ruled out as the cause of variability by considering the rotational velocity this would require. Using the radius we previously determined ($4.79\pm0.17\,\mathrm{R}_\odot$) with the mass determined by Zorec & Royer (2012) of $4.25\pm0.08\,\mathrm{M}_\odot$, we find that the critical rotation frequency of Merope is $1.39\pm0.07\,\mathrm{d}^{-1}$. The observed variability occurs well above this frequency, and therefore we can be confident that rotation is not the cause.

6.4.6 Taygeta

Taygeta (19 Tauri, HR 1145, HD 23338) is the sixth-brightest star in the Pleiades ($V = 4.30\,\mathrm{mag}$), and is of spectral type B6IV. A faint companion was unambiguously detected in lunar occultation measurements by Richichi et al. (1994). McNamara

(1985) found no evidence of photometric variability in Taygeta, and Adelman (2001) found it to be amongst the least variable stars observed by Hipparcos.

The K2 time series and amplitude spectrum of Taygeta are shown in the sixth row of Fig. 6.5. The light curve shows low-amplitude variability, consisting of several frequencies. The amplitude spectrum bears a striking resemblance to that of Electra, albeit scaled to a lower frequency, with a frequency grouping in the range 0.4–0.7 d^{-1}, and another group in the range 1.2–1.4 d^{-1}. We attribute this variability to SPB pulsations, with combination frequencies.

6.4.7 Pleione

Pleione (28 Tauri, HR 1180, HD 23862), the seventh-brightest member of the Pleiades ($V = 5.19$ mag), has spectral type B8Vne. Since first being identified as a Be star (A. C. Maury, reported by Pickering, 1889), Pleione has attracted a lot of attention due to its regular transitions between Be and shell star phases (e.g. Frost, 1906; Gulliver, 1977; Goraya et al., 1990). Pleione cycles between its Be and shell phases with a period of 34.5 yr. The most recent transitions have been from shell to Be in 1988 (Sharov & Lyutyj, 1988), and Be to shell in 2006 (Tanaka et al., 2007). Hummel (1998) suggested that such transitions are due to the precession of the disc, likely under the influence of a misaligned binary orbit. Polarimetric observations of Pleione by Hirata (2007) found the intrinsic polarization angle varied from 60° to 130° between 1974 and 2003, providing evidence of changes in the disc axis.

The transition between Be and shell phases is accompanied by photometric variability (Calder, 1937; Binnendijk, 1949; Sharov & Lyuty, 1976; Tanaka et al., 2007). Shorter time-scale variability was detected by McNamara (1987), who identified a primary frequency at either 1.21 or 2.21 d^{-1}, with a second frequency at 1.18 d^{-1}.

We consider it most likely that the cause of the variability is the same as what we have determined for Merope, namely SPB pulsations with several closely-spaced

modes. Beating between these modes may provide the additional angular momentum to eject material into the circumstellar decretion disc, as was proposed as the origin of the Be phenomenon by Rivinius et al. (1998).

We are, however, unable to entirely rule out rotation as the cause of Pleione's variability through consideration of the critical velocity. Using literature estimates of mass and radius (Frémat et al., 2005; Zorec et al., 2005), we find a critical rotational frequency of $1.62 \pm 0.10\,\mathrm{d}^{-1}$, which is commensurate with detected frequencies. If the variability is caused by rotation, then Pleione is rotating very close to its critical velocity. We have calculated the inclination angle this would imply, as we have done for Alcyone and Maia, finding $i = 53 \pm 5°$; the posterior probability distribution is shown in Fig. 6.6.

6.5 Source Code

We are committed to open science, and have made the software presented in this Chapter available open-source. The main halo algorithm, HALOPHOT, is available at `https://github.com/hvidy/halophot`. We invite interested users to apply this to other data and contribute to its ongoing development. The JUPYTER notebook used for estimating rotational inclinations with PYSTAN MCMC is available at `https://github.com/benjaminpope/inclinations`. Finally, the K2SC algorithm used for finer corrections (Aigrain et al., 2016), is also available at `https://github.com/OxES/k2sc`. All code is provided under a GPL v3 license.

All original light curves discussed in this Chapter will be made available on the Mikulski Archive for Space Telescopes (MAST) as High-Level Science Products, and through the *Kepler* Asteroseismic Science Operations Centre (KASOC) database [3].

[3] `http://kaosc.phys.au.dk`

6.6 Discussion and Conclusions

We have presented a new method for simultaneous photometry and systematics correction of saturated stars with K2, and used this method to obtain the first high-precision space-based light curves of the seven brightest stars in the Pleiades. Halo photometry extends the dynamic range of K2 to include naked-eye stars, allowing for the combined use of photometric time series with other astronomical tools, including high-resolution spectroscopy, interferometry and polarimetry, to form a more complete understanding of these stars and stellar systems.

The light curves of the bright Pleiades stars show a wide range of variability. Low amplitude SPB pulsations and combination frequencies have been detected in Alcyone, Electra and Taygeta. Pleione and Merope have high amplitude oscillations that may also be due to SPB pulsations, however longer time series are necessary to resolve individual modes; this may be achieved with the BRITE-Constellation of nanosatellites (Weiss et al., 2014). In contrast, the high amplitude oscillations of Atlas, which we believe are most likely to originate from the primary component, are well-resolved.

For Maia we have combined the photometric time series with high-resolution spectroscopy and interferometry to determine that Maia is viewed equator-on, with variability due to large chemical spots in the photosphere. With a 10 d period, we have conclusively determined that Maia is not a so-called Maia variable.

The halo photometry method is very general in its formulation and applicability, and will therefore be also of interest in planning for the Transiting Exoplanet Survey Satellite (TESS), which will cover nearly the whole sky in a succession of 27 d pointings to search for exoplanets transiting bright stars. TESS will provide full-frame images at a 30 min cadence, and postage stamps of individual targets at 2 min or 20 s cadence. As with *Kepler* and K2, competition for this pixel allocation will place pressure on bright targets with long bleed columns. In addition to this, detector

nonlinearity is expected to set in at ~ 30 times the single-well depth. With minimal saturation for $V \lesssim 6.2$–6.7 mag depending on how the PSF lands on the pixels, this would suggest that simple aperture photometry of stars much brighter than $V \sim 3$–4 mag will not be possible even with apertures that capture the entire bleed column (Jon Jenkins & Roland Vanderspek, priv. comm.). It will therefore be necessary to use halo photometry for any TESS targets brighter than this magnitude, or targets unfavourably close to the edge of the detector, and to economize on pixel allocation. A valuable future step will be to simulate the TESS PSF, saturation, and scattered light, to determine the required halo masks both for asteroseismology and for transiting exoplanet searches. The ability to observe very bright stars with TESS raises the prospect of searching for planets transiting some of the nearest main-sequence stars to the Solar System, which being so bright, are the most suitable systems for transit spectroscopy.

Because halo photometry needs many fewer pixels than the full bleed column would require, it is friendly for both TESS short-cadence proposals and future K2 proposals. Not only that, charge conservation for TESS is expected to fail at ~ 30 times the marginal saturation V magnitude of ~ 7, meaning halo is required for anything brighter than magnitudes of ~ 4. Applying halo photometry to TESS, it will be possible to recover from saturation light curves of a unique sample of stars unavailable with any other instrument or processing.

It may also be important to consider the halo method in the context of other upcoming ground-based and space-based photometry missions, such as PLATO (PLAnetary Transits and Oscillations of stars; Rauer et al., 2014), JWST (James Webb Space Telescope; Gardner et al., 2006; Beichman et al., 2014), NGTS (the Next Generation Transit Survey; Chazelas et al., 2012), or CHEOPS (CHaracterising ExOPlanets Satellite; Fortier et al., 2014). In each of these cases, it may be possible to enhance the photometry of a defocused PSF with or without saturation, for asteroseismology

or exoplanetary science. In this regime, TV minimization, or a similar algorithm, may improve the performance of any such instrument spreading astrophysical signal over many different pixel realizations. We note that we do not yet have a consistent explanation of why TV, as opposed to relatives such as QV, is so much more effective, and that there may be new insights to be gained from theoretical studies, that may expose limitations on the method or reveal improvements. We encourage other groups to refine the halo method and consider the applicability of Total Variation more generally in time-series analysis.

Chapter 7

Conclusions and Future Work

I am a part of all that I have met;
Yet all experience is an arch wherethro'
Gleams that untravell'd world, whose margin fades
For ever and forever when I move.

Tennyson, *Ulysses*, ll.18-21. (Tennyson, 1842)

7.1 Conclusions

In this thesis we have advanced several methods for self-calibration in optical astronomy, which permit newly-precise observations with ground-based and space telescopes. These methods rely on statistical and optical understanding of the instrument to remove systematics from astronomical data, revealing signals hidden in noise that would otherwise completely mask them. While the low-hanging fruit in exoplanet surveys such as *Kepler* have already been taken, I have shown here that with a detailed understanding of the telescope, image formation, and systematic noise, we can still pull out remarkable science – indeed, we can push the dynamic range of *Kepler* to entirely unprecedented levels, and do with ordinary adaptive optics and a little post-processing what was previously only possible with dedicated aperture masking instruments. Continued innovation in data analysis techniques will be vital for getting

the most out of upcoming missions.

While the kernel phase method permits calibration of phase errors in speckle interferometry with arbitrary telescopes as a generalization of the idea of closure phase (Martinache, 2010), the formalism did not previously include amplitude errors, such as from scintillation: in Chapter 2, I have introduced kernel amplitudes as a generalization of kernel phase to account for these errors as well, and conduct simulations to show that this is advantageous for imaging systems at high angular resolution under conditions of aberration in both phase and amplitude.

Likewise while I have already demonstrated the technique's applicability from space using the *Hubble Space Telescope* (Pope et al., 2013), kernel phase interferometry had not previously been used from the ground. In Chapter 3, I for the first time compare kernel phase and aperture masking side-by-side, achieving identical results on the close, bright binary α Ophiuchi. Similar results should be achievable with SPHERE, GPI, MagAO and future extreme AO instruments.

The failure of *Kepler*'s second reaction wheel could have been a disaster for exoplanetary science and stellar physics, if not for the ingenious *K2* configuration that gave the mission a second life. Although its 6 hr pattern of thruster firings introduces difficult pointing systematics, several groups have been able to correct these in post-processing, and during my DPhil I contributed to the K2SC pipeline (Aigrain, Parviainen & Pope, 2016). Using this, in Chapter 4, I have presented 145 new planet candidates, including 5 multiple systems, from Campaigns 5 and 6 of the *K2* Mission. Several of these have been confirmed with radial velocity observations, while others remain promising targets.

Kepler and *K2* were designed to look for planets around fainter stars (around the $\sim$ 12th magnitude), as indeed I have done in Chapter 4. Planets transiting brighter stars are, however, the most valuable - only these stars can be studied with the best adaptive optics, for instance, or transmission spectroscopy. These are also useful as

benchmarks for calibrating large surveys of faint stars, for example with machine learning methods. In Chapter 5, I have presented a pilot study for pushing *Kepler* and *K2* to much brighter targets, taking advantage of previously-unused archival calibration data to recover light curves of stars that were never even observed in the normal sense. I demonstrate the smear photometry technique for a small sample of stars, showing that we can attain sufficient precision with these collateral data to do useful science.

Although smear photometry is shown to be effective for bright stars that were never previously observed, it relies on the details of the readout process of the *Kepler* detector and is not necessarily generally-applicable, or indeed optimal for the brightest stars in *Kepler*, where even the smear pixels are saturated. In Chapter 6 I have investigated a much more general approach, in which the halo of diffracted and scattered light around bright stars can be used for photometry, with a weighted photometric aperture performing light curve extraction and detrending simultaneously. The halo algorithm attains the same precision as for other stars observed ordinarily by *K2*, even for stars as bright as the third magnitude. Using the seven brightest stars of the Pleiades as a test case, the brightest sources yet observed by *Kepler* or *K2*, we settle long-standing questions about their variability, detecting rotational modulation and slowly-pulsating B star-type pulsations.

7.2 Future Work

In this thesis, to borrow the words of Leonard Cohen, we have been "guided by the beauty of our weapons" — developing new techniques for astronomical data analysis, we have applied them to such instruments and datasets as have been available, aiming to establish their validity, with the refinement of technology the proximate goal. The next several years promise the launches of a succession of space missions which will

benefit from this new technology, in fact for which this technology will allow us to achieve significant scientific goals that would not otherwise be possible. I am very excited by these possibilities.

The most important of these is the *James Webb Space Telescope*, a mission whose budget and scale dwarf all previous astronomical instruments, including the *HST*. Provided launch and deployment go to plan, this will be the first space telescope for which we can plan kernel phase observations, given that the *HST*-NICMOS camera is no longer available and this was the only other high-performance, diffraction-limited optical instrument in orbit. An immediately valuable prospect will be developing an image deconvolution tool, using kernel phase and amplitude to attain super-resolution with *JWST*. The most compelling case for this is LkCa 15, the putative accreting protoplanet system resolved from the ground by aperture masking: kernel phase on *JWST* should significantly enhance the precision we can attain here and give us the best ever view of the process of planet formation. While *JWST* is the most promising prospect for kernel phase imaging, we should not neglect SPHERE, GPI, MagAO and other future extreme AO instruments, with which we will be able to observe circumstellar material with unprecedented detail.

Beyond imaging, unfolding and then correctly phasing *JWST* is an extremely difficult and time-consuming part of the commissioning process, and I believe kernel phase may help. The kernel phase wavefront sensing method (Martinache, 2013b; Pope et al., 2014a,b) can provide fine wavefront sensing without any additional hardware, and will potentially assist both in the commissioning process, and also in subsequent monitoring and maintenance of the mirror alignment and wavefront quality. The Gerchberg-Saxton (GS) phase retrieval algorithm (Gerchberg & Saxton, 1972) can be used to measure optical aberrations using only focal-plane images (famously used to characterize the *Hubble Space Telescope* mirror error; Fienup et al., 1993), but requires a diversity of images through focus in order to determine asymmetric modes.

For *JWST*, which will have a non-redundant aperture masking mode, Cheetham et al. (2014) have proposed a closure phase algorithm for phase retrieval, and Greenbaum & Sivaramakrishnan (2016) have proposed using such an algorithm to initialize a GS optimization and perform this measurement with only one exposure. I have discussed with Cheetham and Greenbaum the possibility of using kernel phase based wavefront sensing to replace the aperture masking stage in this hybrid GS approach, and hope that this may obviate the need for any dedicated hardware or special observing procedures to measure *JWST* mirror phases.

Finally, with kernel phase, I hope I can be permitted to speculate on the theory itself. Kernel phase and amplitude work by linearity: essentially, the fundamental theorem of linear algebra assures us that given that there are more baselines than pupil samples, we will generically have a subspace of observables which are resistant (to linear order) to error. An argument of this form should apply to arbitrary optical systems. If an analogous description of error propagation applies to coronagraphs, or nulling interferometers (Bracewell, 1978), it may be possible to apply this self-calibration method where it matters most, to directly image exoplanets where phase noise is currently the dominant source of noise both on the ground and in space. I therefore hope that a general theory of optical self-calibration can be found, just as already exists for radio-frequency interferometry.

JWST will be an enormous improvement in both precision and spectral range on existing instruments for exoplanet transmission spectroscopy, and the methods developed in this Thesis will help us make best use of the telescope's brief five-year lifetime. First, with the launch of TESS planned in 2018, Gaussian Process and Total Variation detrending will enhance the precision of light curves we can expect, and therefore the yield of planets suitable for *JWST* characterization. But we are interested in bright stars, and bright stars are the perfect targets for transmission spectroscopy. As well as this, one wild possibility with such bright stars is to directly

image the planet *as it transits the star* using long-baseline interferometry (van Belle, 2008).

Applying TV to TESS is especially exciting, because covering the whole sky, there are 906 FGK stars brighter than $V = 6.5$. Using the planet occurrence rates from Fressin et al. (2013), we can crudely calculate that of these, we expect to find one or so ($\sim 0.6 \pm 0.8$) short-period giant planet, $\sim 6.6 \pm 2.5$ Neptunes and $\sim 8 \pm 3$ super-Earths. Only two transiting systems brighter than magnitude 6.5 are known at the time of writing: HD 219134 and 55 Cancri. Even one addition to this list of planets transiting very bright stars will be significant for *JWST* and future instruments. With such a small number of planets predicted around these few bright stars, we might reasonably expect to discover *all* of the short period transiting planets down to super-Earth size and to this magnitude, making these by necessity the classic systems for future exoplanetary science. I very much hope that the TV method, or developments from it, can contribute towards finding these. The TV method may even help in processing *JWST* observations targets which might be bright enough to saturate its instruments. TV may likewise be useful for improving the precision and dynamic range of other space-based photometric missions such as CHEOPS, whose large defocused PSF is ideal for attaining the pixel diversity on which TV thrives.

More broadly, it will be valuable to extend the K2SC and K2PS planet search to all *K2* Campaigns, in order to better constrain overall exoplanet populations and to find particularly promising targets for follow-up. In doing this, it will be important to run rigorous and self-consistent injection tests to obtain a better statistical understanding of the sample and of the methods' effectiveness. We have already processed Campaigns 3 to 8, and intend to make our light curves and classifications public as a resource to the community. This code-base will also be useful for TESS photometry and planet-searches.

As with kernel phase, I also do not believe that the theory of halo photometry is

sufficiently worked-out, and I am not convinced that TV is the only objective function appropriate for high-precision photometry. We do not even know properly why it works! In the immediate future, establishing a sound mathematical basis for this algorithm will be important, as it may tell us whether (or not) it will generalize from photometry resistant to pointing errors to other scenarios. If we can beat the scintillation limit with ground-based photometry, we will open up realms of observational astronomy hitherto accessible only from space, and the ramifications for time-domain astronomy could be far-reaching. On the other hand, it may turn out that the method is not suited to such lofty goals! I hope that the halo method may have such valuable generalizations in astronomy, and I suspect it may have otherwise unforseen implications in other fields, or indeed that it may already be in use elsewhere under another guise.

Setting aside exoplanets – the combined smear and halo samples from *Kepler* and *K2* will cover nearly all sources in the respective fields which were too bright to observe conventionally, amounting to several hundred stars, including some yet to be released from Campaign 2 smear in the Upper Scorpius association. Even in the absence of planet discoveries, these will be a valuable resource for stellar physics, with this being the only opportunity in the near future to characterize so many bright stars with asteroseismology. With interferometry to obtain diameters, *Gaia* and *Hipparcos* parallaxes, and high-resolution spectroscopy, these will be ideal benchmark stars for large spectroscopic and asteroseismic surveys of fainter stars, which will need precisely-known calibrators to be most effective. This is doubly true in the context of extremely large surveys such as APOGEE, where machine learning software such as *The Cannon* (Ness et al., 2015; Casey et al., 2016) is dependent on the quality of training data available. Such surveys will tell us about the archaeology of our Galaxy, the history of its assembly, and the formation of its stellar populations.

The approach taken in this thesis has been of developing and testing new obser-

vational techniques and applying these to pathfinder observations. With the next generation of telescopes it will be important to match this new hardware investment with new approaches to data analysis that will deliver the best possible science. The ideas in this thesis will be, I hope, the seeds of ever-more-accurate ways of understanding observations in optical astronomy.

Appendix A

Tables

Table A.1: Full list of our 86 vetted single planet candidates in *K2* Campaign 5. RV semi-amplitude K (or limits) listed in Comments where applicable.

EPIC	RA	Dec	V (mag)	J-K (mag)	Period (days)	Epoch (BJD)	Depth (%)	$r_p/r_\star$ (%)	Duration (hours)	Impact Parameter	Density gcm-3	TRES (n)	Comments
211308899	08:53:18.006	+10:01:46.97	14.57	0.56	6.423	2457143.316	0.0395	1.9868	4.885	0.151	0.45		
211314705	08:36:31.182	+10:08:50.21	15.39	0.81	3.794	2457140.224	0.1007	3.1731	1.39	0	11.933	1	Hα emission
211319617	08:25:51.344	+10:14:49.08	12.6	0.47	8.866	2457143.397	0.1028	3.2056	2.679	0	3.893	1	OK
211328748	08:40:56.495	+10:25:20.56	9.96	0.3	17.178	2457139.95	0.0219	1.4808	2.452	0	9.833		
211331236	08:55:25.364	+10:28:08.87	14.65	0.86	1.292	2457140.193	0.1317	3.6291	1.153	0	7.162		
211333233	08:27:35.557	+10:30:23.62	9.95	1.04	5.409	2457142.885	0.0172	1.3096	2.344	0.028	3.544	1	Giant
211335816	08:26:29.764	+10:33:19.44	12.2	0.4	4.99	2457140.02	0.1907	4.3667	0.862	0.487	43.754	3	SB2
211336616	08:49:42.413	+10:34:13.95	13.1	0.62	44.13	2457149.28	0.0427	2.0655	4.635	0.037	3.731		
211342524	08:32:23.687	+10:40:38.06	12.42	0.35	14.449	2457149.367	9.1939	30.3214	0.595	0.991	1.38		
211351816	08:31:03.081	+10:50:51.31	12.61	0.66	8.406	2457142.05	0.0556	2.3577	5.668	0.205	0.367	1	Giant
211355342	08:30:12.968	+10:54:37.06	12.75	0.41	6.893	2457143.799	0.0585	2.4185	2.468	0	3.872	1	OK
211359660	08:40:43.278	+10:58:58.59	12	0.49	4.737	2457141.205	0.0977	3.1257	2.41	0.042	2.852	1	OK
211365543	08:29:48.825	+11:05:08.36	12.12	0.25	5.264	2457143.676	0.0096	0.9804	4.185	0.148	0.59		
211375488	08:43:20.828	+11:14:53.23		1.37	2.084	2457141.721	0.2385	4.8839	1.955	0.109	2.328		
211383821	08:44:09.925	+11:23:07.81	14.52	0.78	1.567	2457140.162	0.0326	1.8044	1.748	0.093	2.469		
211391664	08:25:57.189	+11:30:40.12	12.17	0.26	10.136	2457145.985	0.0869	2.9486	4.945	0.171	0.678	1	OK
211399359	08:32:16.114	+11:37:50.62	14.64	0.58	3.115	2457141.418	2.3415	15.3019	1.992	0.049	3.322		
211401787	08:27:35.269	+11:40:02.91	9.61	0.26	13.773	2457151.069	0.0245	1.5638	4.311	0.146	1.406	1	OK
211413752	08:54:50.291	+11:50:53.75	13.85	0.52	9.325	2457140.855	0.0923	3.0376	2.877	0	3.305		
211418729	08:31:31.911	+11:55:20.15	14.56	0.53	11.391	2457140.324	1.3265	11.5172	3.384	0.108	2.438		
211424769	08:35:24.644	+12:00:41.94	9.39	0.33	5.176	2457144.498	0.3485	5.9037	1.049	0.157	36.494	2	SB1
211428897	08:35:25.812	+12:04:33.04	14.09	0.79	1.611	2457140.661	0.0517	2.2748	1.059	0	11.471		
211439059	08:47:53.647	+12:13:54.85	13.29	0.51	18.641	2457146.51	0.0285	1.6896	5.22	0.173	1.057		
211442297	08:26:12.827	+12:16:54.97	13.36	0.38	20.272	2457157.159	1.4508	12.0449	3.141	0.101	5.435		
211490999	08:43:11.723	+13:00:34.53	13.6	0.43	9.844	2457146.33	0.0809	2.8435	3.425	0.118	2.026		
211491383	08:40:37.240	+13:00:52.83	11.78	0.33	4.144	2457141.601	0.0078	0.8845	2.717	0.101	1.722	1	OK

EPIC	RA	Dec	V (mag)	J-K (mag)	Period (days)	Epoch (BJD)	Depth (%)	$r_p/r_\star$ (%)	Duration (hours)	Impact Parameter	Density gcm-3	TRES (n)	Comments
211509553	09:00:04.744	+13:16:25.94	16.58	0.8	20.359	2457151.414	3.3123	18.1997	2.938	0.131	6.602		
211525389	08:21:40.866	+13:29:51.11	11.75	0.45	8.267	2457139.723	0.1053	3.2454	3.216	0.139	2.038	1	OK
211529065	08:45:03.983	+13:32:59.40	13.78	0.6	4.4	2457142.979	0.1297	3.6012	1.456	0	12.033		
211562654	08:20:01.718	+14:01:10.06	12.85	0.46	10.792	2457147.782	0.0523	2.2862	3.581	0.151	1.916	1	OK
211569704	08:28:01.122	+14:07:10.62	12.36	0.72	34.023	2457156.994	0.0308	1.7559	3	0	10.625		
211579112	09:03:32.001	+14:15:01.90		0.86	17.703	2457156.427	0.6508	8.0674	1.872	0	22.768	1	OK
211586387	09:07:12.268	+14:21:19.71	14.64	0.65	35.383	2457142.906	0.0945	3.0738	3.094	0	10.078		
211594205	08:36:33.626	+14:27:42.97	10.35	0.54	16.994	2457148.501	0.0315	1.7749	2.285	0	12.012	1	OK
211645912	08:19:59.301	+15:10:40.42	12.62	0.37	10.673	2457140.54	0.0274	1.6562	3.436	0.104	2.185	1	OK
211713099	08:20:53.731	+16:05:27.41	13.83	0.4	8.562	2457141.15	0.4581	6.768	2.975	0.109	2.696		
211733267	08:40:02.259	+16:22:20.66	12.4	0.55	8.658	2457144.931	0.5656	7.5206	1.098	0.261	49.683	2	OK, $K \lesssim 100$m/s[1]
211736671	08:13:31.650	+16:25:10.59	12.33	0.43	4.734	2457140.365	0.0778	2.7891	3.407	0.197	0.956	1	Giant
211743874	08:37:33.528	+16:31:19.57	12.57	0.3	12.281	2457148.217	0.0233	1.5248	3.876	0.151	1.72	1	OK
211763214	08:55:21.136	+16:47:39.05	12.73	0.5	21.199	2457146.569	0.0182	1.3507	4.283	0.123	2.224	1	OK
211770696	08:31:02.684	+16:54:02.04	12.41	0.38	16.271	2457145.973	0.0312	1.7668	7.534	0.223	0.298	1	OK
211770795	08:48:02.336	+16:54:06.67	14.88	0.67	7.728	2457141.099	0.0791	2.8133	2.83	0	2.88		
211770867	08:12:05.436	+16:54:10.82	12.28	0.3	27.693	2457147.872	1.8421	13.5722	6.343	0.465	0.636		
211779390	08:17:26.659	+17:01:27.68	13.45	0.72	3.85	2457141.528	0.0282	1.6802	1.627	0	7.553		
211783206	08:40:34.995	+17:04:40.57	14.6	0.65	7.134	2457146.467	0.045	2.1212	1.839	0	9.687		
211800191	08:51:32.348	+17:19:11.40	12.62	0.37	1.106	2457140.749	0.0975	3.1229	0.994	0	9.572	1	OK
211804579	08:36:16.266	+17:22:53.98	11.36	0.39	1.523	2457141.205	0.0605	2.4602	2.397	0.156	0.92		EB[2]
211808055	08:36:08.271	+17:25:48.30		0.4	3.383	2457142.603	0.1641	4.0506	3.721	0.353	0.46		
211814733	08:50:40.178	+17:31:29.61	11.21	0.57	14.71	2457145.892	0.4414	6.6437	2.382	0.079	9.096		
211816003	08:50:29.069	+17:32:32.80	13.84	0.49	14.452	2457144.86	0.1035	3.2178	3.32	0.228	3.077		
211818569	08:27:44.813	+17:34:45.83	13.32	0.69	5.186	2457143.561	1.0779	10.3821	1.778	0.133	7.584	2	OK, $K \lesssim 350$ m/s[3],
211834065	08:50:11.526	+17:47:57.57	11.81	0.29	10.545	2457142.426	0.0143	1.1974	3.259	0.164	2.469		EB[2]
211886472	09:08:31.807	+18:31:42.75	11.28	0.26	19.64	2457152.378	0.5501	7.4167	1.43	0.699	20.712		
211897691	08:40:19.814	+18:41:34.51	14.66	0.62	5.75	2457142.497	0.0945	3.0749	1.255	0	24.529		
211906259	08:45:14.646	+18:49:09.69	12.82	0.35	2.52	2457140.559	0.0105	1.0236	12.355	0.174	0.013		
211919004	08:39:06.491	+19:00:36.08	13.37	0.51	11.72	2457149.097	0.1051	3.2422	4.406	0	1.157		
211923431	08:31:44.965	+19:04:28.71	14.3	0.49	29.729	2457143.824	0.067	2.5878	4.998	0.196	1.895		
211924657	08:40:06.426	+19:05:34.36	16.25	0.81	2.645	2457141.999	0.2365	4.8634	1.404	0	8.086		
211929937	08:36:42.829	+19:10:25.72	14.43	0.52	3.477	2457142.412	1.7941	13.3945	2.205	0.016	2.743		
211941472	08:41:47.658	+19:20:50.99	11.95	0.39	5.78	2457143.635	0.0101	1.0064	3.138	0.154	1.525	1	OK
211945201	09:06:17.754	+19:24:08.11	10.15	0.31	19.491	2457158.827	0.1381	3.7166	3.369	0.035	4.29		
211965883	09:04:37.728	+19:42:52.51	14.63	0.82	10.555	2457146.496	0.1249	3.5337	1.307	0.3	34.611		
211969807	08:38:32.821	+19:46:25.78		0.86	1.974	2457140.376	0.1325	3.6401	1.407	0	6		
211990866	08:38:24.300	+20:06:21.83	10.65	0.28	1.674	2457140.72	0.0589	2.4261	1.398	0.218	4.832	1	OK
211993818	08:24:49.181	+20:09:10.78	7.34	0.47	8.986	2457140.043	4.8646	22.0558	0.002	1	0.24	3	SB2
211995398	08:14:37.512	+20:10:44.93			32.576	2457169.858	3.8336	19.5795	4.253	0	3.572		
212006318	08:42:00.319	+20:21:33.50	13.04	0.34	14.443	2457147.342	0.0245	1.5651	6.035	0.178	0.529	1	OK
212006344	08:25:54.315	+20:21:34.45	13.15	0.83	2.219	2457141.831	0.038	1.9484	1.118	0	13.438	1	Very Cool
212008766	08:37:07.785	+20:23:57.74	13.09	0.52	14.129	2457145.122	0.0854	2.9218	3.399	0	3.035	1	OK
212009427	08:31:29.870	+20:24:37.52		0.91	0.778	2457140.262	0.5428	7.3676	0.5	0.236	48.518		
212066407	08:39:21.244	+21:23:26.98	12.34	0.38	0.822	2457140.365	0.0437	2.0904	0.814	0.056	12.911	11	$K \sim 32.8 \pm 25$m/s
212069861	08:57:46.605	+21:27:12.72	14.78	0.85	30.953	2457147.496	0.1646	4.0566	3.236	0.152	7.442		
212088059	08:50:49.887	+21:47:20.84	15.61	0.88	10.366	2457141.715	0.124	3.5211	1.892	0	12.915		
212099230	08:32:17.657	+22:00:21.64	10.79	0.47	7.112	2457141.963	0.0585	2.418	2.651	0.009	3.222	1	OK
212110888	08:30:18.905	+22:14:09.27	11.45	0.34	2.996	2457141.351	0.6237	7.8978	1.971	0.068	3.292	5	HJ[4]
212130773	08:23:48.660	+22:38:02.48	14.63	0.61	18.711	2457151.886	0.1305	3.6132	5.972	0.162	0.713		
212132195	08:23:56.896	+22:39:46.96	12.03	0.63	26.198	2457164.39	0.0861	2.9347	3.173	0	6.919	1	OK
212136123	08:36:50.878	+22:44:28.04	15.09	0.5	2.226	2457140.262	0.0676	2.6003	1.679	0	3.986		
212138198	08:24:05.654	+22:46:59.84	13.21	0.58	3.209	2457142.373	0.2016	4.4905	0.725	0.131	69.121	1	OK
212141021	08:31:41.083	+22:50:30.01	13.55	0.57	2.918	2457140.099	0.0246	1.5674	1.914	0.066	3.499		
212150006	08:32:40.691	+23:01:55.20	14.77	0.51	0.898	2457139.982	0.1878	4.3334	0.958	0.122	8.524	5	[5]
212152341	08:51:00.966	+23:05:02.25			6.676	2457141.311	3.9424	19.8555	2.273	0.087	4.747		
212154564	08:54:33.884	+23:07:58.40		0.86	6.414	2457142.181	0.4643	6.8141	1.521	0.102	15.136		

[1]RV measurements were 22.554 and 22.551 km/s, without uncertainties so assuming standard error.
[2]Vanderburg, private communication.
[3]RV uncertainties added in quadrature
[4]Lillo-Box et al. (2016) and Hirano et al. (2016b)
[5]Adams et al. (2016)

EPIC	RA	Dec	V (mag)	J-K (mag)	Period (days)	Epoch (BJD)	Depth (%)	$r_p/r_\star$ (%)	Duration (hours)	Impact Parameter	Density gcm-3	TRES (n)	Comments
212157262	08:50:05.666	+23:11:33.36	13.08	0.49	7.15	2457146.322	0.1068	3.2683	2.803	0.03	2.739	1	OK
212161956	08:25:29.502	+23:17:50.56	15.21	0.75	7.187	2457140.698	0.1195	3.4576	2.391	0	4.437		
212164470	08:39:15.271	+23:21:26.93	12.65	0.35	7.809	2457144.86	0.042	2.0497	3.403	0.204	1.572	1	OK

Table A.2: Full list of our 71 vetted single planet candidates in *K2* C6. RV semi-amplitude K (or limits) listed in Comments where applicable.

EPIC	RA	Dec	V (mag)	J-K (mag)	Period (days)	Epoch (BJD)	Depth (%)	$r_p/r_\star$ (%)	Duration (hours)	Impact Parameter	Density gcm-3	TRES (n)	Comments
212270970	13:51:09.957	-18:27:42.22	13.48	0.42	1.717	2457218.134	0.0086	0.9286	6.192	0.185	0.065		
212278644	13:48:29.897	-18:11:47.77	14.15	0.37	12.426	2457227.549	0.0431	2.077	4.923	0.213	0.821		
212297394	13:48:49.493	-17:36:35.66	14.42	0.55	5.213	2457222.483	0.0709	2.6618	2.422	0.07	3.078		
212300977	13:35:01.945	-17:30:12.78	11.75	0.38	4.466	2457220.529	1.5619	12.4977	3.095	0.203	1.198		WASP-55
212301649	13:25:50.914	-17:28:59.27	14.33	0.56	1.225	2457217.565	0.0224	1.4962	9.016	0.554	0.019		
212310244	13:52:18.702	-17:13:31.61	14.27	0.55	6.669	2457220.874	0.0213	1.4607	4.984	0.166	0.438		
212321305	13:38:34.080	-16:54:36.35	14.08	0.41	34.144	2457228.926	0.2836	5.3257	7.923	0.196	0.546		
212330265	13:53:31.110	-16:39:34.92		0.9	4.174	2457220.427	0.1013	3.1828	1.863	0.019	5.453		
212351026	13:26:44.850	-16:06:18.54	15.51	0.81	2.548	2457218.171	0.2483	4.9828	4.903	0.423	0.143		
212351405	13:26:39.104	-16:05:42.00	14.32	0.57	2.549	2457218.158	0.1961	4.4285	3.833	0.407	0.3		
212357477	13:28:03.992	-15:56:16.15	10.36	0.39	6.327	2457221.228	0.0322	1.7952	1.675	0.083	11.238	1	OK
212370106	13:25:05.248	-15:37:30.26	14.71	0.83	22.446	2457225.441	0.1546	3.9319	3.48	0.011	4.491		
212380207	13:21:25.496	-15:22:37.99	13.37	0.44	26.147	2457241.871	0.0568	2.3842	4.341	0.094	2.66		
212394689	13:34:29.110	-15:02:10.89	12.4	0.45	6.679	2457223.42	0.0655	2.5593	2.427	0.123	3.854	1	OK
212398508	13:34:30.927	-14:56:49.78	13.87	0.47	46.423	2457237.276	0.0681	2.6102	6.591	0.211	1.277		
212418133	13:33:12.426	-14:30:14.60	13.41	0.4	3.333	2457219.846	0.0268	1.6372	3.792	0.118	0.511		
212420823	13:16:23.936	-14:26:40.67	14.4	0.54	9.029	2457219.139	0.0682	2.6107	3.009	0.078	2.772		
212424622	13:29:19.541	-14:21:34.07	13.35	0.33	12.012	2457219.497	0.0315	1.7745	5.162	0.153	0.712		
212425103	13:37:28.700	-14:20:56.00	14.73	0.52	0.946	2457218.175	0.0301	1.7346	1.324	0.077	3.467		
212432685	13:37:11.711	-14:10:50.12	13.28	0.33	1.063	2457217.992	0.0231	1.5188	1.316	0.072	3.958		
212435047	13:28:31.373	-14:07:34.65	12.5	0.33	1.115	2457218.451	0.0151	1.2269	1.562	0.099	2.475	1	OK
212440430	13:36:08.544	-14:00:33.18	13.46	0.42	19.991	2457228.16	0.0542	2.3276	4.266	0.122	2.125		
212443973	13:40:02.135	-13:55:55.34	16.03	0.79	0.779	2457217.748	0.0369	1.9207	0.66	0	23.004		
212451091	14:05:53.119	-13:46:45.80	14.46	0.52	12.666	2457226.371	0.1876	4.3318	3.51	0.053	2.462		
212454160	13:34:32.944	-13:42:45.42	12.88	0.42	0.876	2457218.236	0.0146	1.2103	7.372	0.526	0.032		
212454422	13:14:12.755	-13:42:24.76		0.91	3.269	2457220.227	1.2473	11.1682	0.966	0	30.571		
212460519	13:34:11.169	-13:34:36.94	12.92	0.8	7.387	2457223.798	0.0858	2.9294	2.422	0.064	4.362	1	OK
212480208	13:41:27.239	-13:09:39.23	11.14	0.42	10.099	2457224.771	0.0179	1.3385	3.71	0.141	1.62	1	OK
212495601	13:15:39.034	-12:49:37.35	13.96	0.41	21.677	2457229.646	0.0605	2.4596	4.534	0.13	1.913		
212496592	13:26:33.402	-12:48:23.65	13.26	0.53	2.858	2457219.561	0.0275	1.6582	2.043	0.188	2.69	1	OK
212499835	13:49:40.470	-12:44:17.29	16.45	0.58	6.883	2457221.015	0.4417	6.6463	5.531	0.232	0.318		
212499991	13:29:57.305	-12:44:05.00	13.55	0.51	15.381	2457225.459	0.0542	2.3288	2.187	0	12.41		
212521166	13:49:23.888	-12:17:04.17	11.91	0.58	13.864	2457219.875	0.1147	3.3865	3.007	0.043	4.292	1	OK[6]
212529560	13:28:31.542	-12:06:26.34	14.09	0.3	8.121	2457219.08	0.0406	2.014	3.398	0.164	1.678		
212534729	13:42:55.909	-11:59:39.30	13.29	0.49	13.479	2457223.541	0.0222	1.4904	2.84	0.01	4.966	1	OK
212543933	13:46:36.559	-11:48:17.80	14.15	0.37	7.806	2457223.497	0.0477	2.1838	2.75	0.042	3.159		
212554013	13:48:18.812	-11:35:20.32	15.04	0.58	3.588	2457220.338	1.2649	11.2466	1.868	0.073	4.618		
212555594	13:46:19.746	-11:33:22.51	12.7	0.46	4.163	2457220.44	0.0245	1.5661	1.441	0	11.741	1	OK
212562715	13:28:40.302	-11:23:57.59	13.28	0.42	13.524	2457220.467	0.0533	2.3085	2.314	0.191	8.706	1	OK
212563850	13:23:23.646	-11:22:29.11	13.71	0.77	14.311	2457222.751	0.0689	2.6248	1.96	0	16.029		
212570977	13:43:36.335	-11:13:24.85	14.08	0.42	8.853	2457223.894	2.4303	15.5895	3.534	0.536	1.022		
212572439	13:37:45.619	-11:11:33.26	13.18	0.53	2.581	2457217.866	0.3992	6.3185	1.51	0.052	6.319	1	HJ[2]
212572452	13:37:46.022	-11:11:32.00		0.81	2.581	2457217.865	3.029	17.404	1.509	0.153	6.14		Blend[7]
212575828	13:40:38.328	-11:07:01.53	15.79	0.57	2.06	2457217.849	0.1344	3.6658	1.378	0	6.668		
212577658	13:55:00.806	-11:04:47.35	11.8	0.45	14.069	2457221.323	0.0302	1.738	3.023	0.056	4.277	1	OK
212579424	13:11:25.778	-11:02:33.19			6.373	2457221.769	1.7919	13.3861	1.902	0	7.816		
212580872	13:40:56.895	-11:00:33.47	13.25	0.46	14.786	2457224.262	0.1334	3.6518	4.117	0	1.788	1	OK

[6]Mini-Neptune (Osborn et al., 2016b).
[7]Dressing et al. (2017)

EPIC	RA	Dec	V (mag)	J-K (mag)	Period (days)	Epoch (BJD)	Depth (%)	$r_p/r_\star$ (%)	Duration (hours)	Impact Parameter	Density gcm-3	TRES (n)	Comments
212586030	13:43:25.957	-10:53:48.92	12.02	0.65	7.785	2457220.882	0.0541	2.3269	1.568	0	17.048	1	OK
212587672	13:41:46.729	-10:51:44.75	12.49	0.32	23.226	2457237.044	0.0469	2.1656	3.038	0.399	5.382	1	OK
212592101	13:42:41.093	-10:46:06.70		0.86	4.545	2457217.55	0.6354	7.9711	1.047	0.221	30.975	1	Giant
212639319	13:18:18.754	-09:41:30.69	12.62	0.48	13.843	2457222.438	0.0781	2.7945	1.55	0.275	27.844	1	OK
212645891	14:01:05.526	-09:32:24.40	12.73	0.4	0.984	2457218.042	0.1628	4.0344	0.682	0.24	24.06		
212646483	14:06:39.170	-09:31:35.42	14.09	0.49	8.253	2457219.873	0.0845	2.9071	1.04	0.663	25.972	1	OK
212661144	13:56:56.001	-09:11:15.46	13.85	0.49	2.459	2457218.91	0.0739	2.7192	1.092	0.327	13.479		EB[2]
212672300	13:38:26.144	-08:55:37.74	12.91	0.31	39.699	2457243.008	0.0614	2.4786	7.367	0.273	0.746	1	OK
212679181	13:26:56.924	-08:45:46.85	12.99	0.86	1.055	2457217.551	0.0458	2.1401	0.517	0.243	58.735		
212688920	13:32:03.256	-08:31:53.33	14.18	0.5	62.841	2457220.233	5.3463	23.1222	2.023	0.818	12.203	1	Cool
212689874	13:19:19.563	-08:30:34.13	12.5	0.37	15.854	2457225.044	0.0902	3.0041	4.502	0.112	1.439		
212697709	13:26:37.247	-08:19:03.22	12.91	0.35	3.952	2457218.287	0.6205	7.8771	1.416	0.159	11.309	1	OK
212705192	13:30:25.305	-08:07:48.94	12.2	0.43	2.268	2457219.619	0.4633	6.8064	1.515	0.073	5.478	1	OK
212712473	13:56:04.647	-07:57:07.67		1.34	7.264	2457217.793	0.3232	5.6852	3.068	0.101	2.093		
212735333	13:29:34.479	-07:22:26.41	12.16	0.4	8.358	2457218.187	0.0515	2.2698	3.214	0.241	1.943	1	OK
212737443	13:36:53.207	-07:19:05.32		0.66	13.603	2457221.355	0.1212	3.481	2.76	0	5.457		
212756297	13:50:37.408	-06:48:14.42	13.42	0.73	1.337	2457218.11	3.1165	17.6536	1.507	0.641	1.538		Quatar-2b
212757601	13:52:37.115	-06:46:09.78		0.58	1.018	2457218.013	0.9794	9.8964	1.322	0	3.774		
212772113	13:32:53.284	-06:21:24.67	14.02	0.58	8.953	2457223.806	0.1178	3.4324	0.812	0.124	137.771		
212782836	13:39:07.134	-06:02:29.74	11.49	0.44	7.125	2457222.12	0.0153	1.2382	2.814	0.092	2.667		
212796016	13:41:10.488	-05:39:48.11	14.85	0.81	3.216	2457217.935	0.0308	1.754	1.343	0	11.218		
212803289	13:55:05.698	-05:26:32.88	11.15	0.3	18.25	2457233.823	0.1776	4.2143	10.868	0.343	0.1	3	$K \sim 50 \pm 28$m/s
212813907	13:47:19.838	-05:06:21.87	14.3	0.56	6.725	2457221.836	0.2425	4.9246	0.921	0.156	69.908		
212828909	13:29:00.385	-04:36:36.82	12.46	0.5	2.85	2457218.558	0.025	1.5815	1.33	0.132	9.965	1	OK

Table A.3: Full list of our vetted multiple system candidates. EPIC 212012119 is in C5, while the remaining objects are all from C6.

EPIC		RA	Dec	V (mag)	J-K (mag)	Period (days)	Epoch (BJD)	Depth (%)	$r_p/r_\star$ (%)	Duration (hours)	Impact Parameter	Density (gcm-3)	TRES (n)	Comments
212012119	b	08:48:40.775	+20:27:18.27	12.063	0.615	3.281	2457142.135	0.077	2.78	1.790	0	4.835	1	
	c					8.438	2457142.495	0.084	2.90	2.029	0.266	7.643		
212393193	b	14:02:11.279	-15:04:10.34	11.92	0.32	14.452	2457219.472	0.0331	1.82	2.958	0	4.711	1	
	c					36.152	2457236.741	0.0331	1.83	5.317	0.001	2.029		
212703473	b	13:24:56.770	-08:10:18.26	10.97	0.39	6.788	2457222.73	0.0204	1.4299	2.784	0.097	2.622	1	HJ Candidate
	c					18.516	2457221.169	0.03	1.73	2.62	0.323	7.362		
212768333	b	13:15:22.515	-06:27:53.59	10.97	0.51	3.359	2457218.397	0.018	1.33	1.420	0.054	9.866	1	Low SNR
	c					7.450	2457221.023	0.0681	2.61	2.610	0.003	3.539		Clear
	d					17.043	2457221.61	0.1737	4.1673	2.581	0.066	8.305		Clear
212779596	b	13:55:36.409	-06:08:10.12	12.29	0.65	3.225	2457218.739	0.058	2.41	1.827	0.020	4.469	1	
	c					7.374	2457222.93	0.1431	3.7832	2.316	0.13	4.887		

Bibliography

Abt, H. A., Barnes, R. C., Biggs, E. S. & Osmer, P. S., 1965. The Frequency of Spectroscopic Binaries in the Pleiades. *ApJ*, **142**, 1604.

Abt, H. A., Levato, H. & Grosso, M., 2002. Rotational Velocities of B Stars. *ApJ*, **573**, 359–365.

Adams, E. R., Jackson, B. & Endl, M., 2016. Ultra Short Period Planets in K2: SuPerPiG Results for Campaigns 0-5. *ArXiv e-prints*.

Adams, W. S., 1904. The radial velocities of the brighter stars in the Pleiades. *ApJ*, **19**.

Adelman, S. J., 2001. Research Note Hipparcos photometry: The least variable stars. *A&A*, **367**, 297–298.

Adelman, S. J., Gulliver, A. F., Kochukhov, O. P. & Ryabchikova, T. A., 2002. The Variability of the Hg II λ3984 Line of the Mercury-Manganese Star α Andromedae. *ApJ*, **575**, 449–460.

Aerts, C., 2006. The pulsations and potential for seismology of B stars. In *Proceedings of SOHO 18/GONG 2006/HELAS I, Beyond the spherical Sun*, vol. 624 of *ESA Special Publication*, 131.1.

Aerts, C., Christensen-Dalsgaard, J. & Kurtz, D. W., 2010. *Asteroseismology*.

Aerts, C., De Cat, P., Kuschnig, R., Matthews, J. M., Guenther, D. B., Moffat, A. F. J., Rucinski, S. M., Sasselov, D., Walker, G. A. H. & Weiss, W. W., 2006. Discovery of the New Slowly Pulsating B Star HD 163830 (B5 II/III) from MOST Space-based Photometry. *ApJ*, **642**, L165–L168.

Aerts, C. & Kolenberg, K., 2005. HD 121190: A cool multiperiodic slowly pulsating B star with moderate rotation. *A&A*, **431**, 615–622.

Aerts, C., Símon-Díaz, S., Bloemen, S., Debosscher, J., Pápics, P. I., Bryson, S., Still, M., Moravveji, E., Williamson, W. H., Grundahl, F., Fredslund Andersen, M., Antoci, V., Pallé, P. L., Christensen-Dalsgaard, J. & Rogers, T. M., 2017. Kepler sheds new and unprecedented light on the variability of a blue supergiant: gravity waves in the O9.5Iab star HD 188209. *A&A*, **in press**.

Agol, E., Steffen, J., Sari, R. & Clarkson, W., 2005. On detecting terrestrial planets with timing of giant planet transits. *MNRAS*, **359**, 567–579.

Aigrain, S., Hodgkin, S. T., Irwin, M. J., Lewis, J. R. & Roberts, S. J., 2015. Precise time series photometry for the Kepler-2.0 mission. *MNRAS*, **447**, 2880–2893.

Aigrain, S., Parviainen, H. & Pope, B., 2016. EPIC212521166: a transiting planet candidate discovered in Campaign 6 data from the K2 Mission. URL `http://dx.doi.org/10.5281/zenodo.45873`.

Aigrain, S., Parviainen, H. & Pope, B. J. S., 2016. K2SC: flexible systematics correction and

detrending of K2 light curves using Gaussian process regression. *MNRAS*, **459**, 2408–2419.

Aigrain, S., Pont, F., Fressin, F., Alapini, A., Alonso, R. et al., 2009. Noise properties of the CoRoT data. A planet-finding perspective. *A&A*, **506**, 425–429.

Airy, G. B., 1834. On the Diffraction of an Object-glass with Circular Aperture. *Transactions of the Cambridge Philosophical Society*, **5**(3).

Allison, R. & Dunkley, J., 2014. Comparison of sampling techniques for Bayesian parameter estimation. *MNRAS*, **437**, 3918–3928.

ALMA Partnership, Brogan, C. L., Pérez, L. M., Hunter, T. R., Dent, W. R. F. et al., 2015. The 2014 ALMA Long Baseline Campaign: First Results from High Angular Resolution Observations toward the HL Tau Region. *ApJ*, **808**, L3.

Alonso, A., Arribas, S. & Martínez-Roger, C., 1999. The effective temperature scale of giant stars (F0-K5). II. Empirical calibration of $T_{\rm eff}$ versus colours and [Fe/H]. *A&AS*, **140**, 261–277.

Ambartsumian, V. A., 1947. *Stellar Evolution and Astrophysics*. Armenian Academy of Sciences.

Anderson, J. A., 1920a. Application of Michelson's interferometer method to the measurement of close double stars. *ApJ*, **51**.

Anderson, J. A., 1920b. The Michelson Interferometer Method for Measuring Close Double Stars. *PASP*, **32**, 58–59.

Angel, J. R. P., 1994. Ground-based imaging of extrasolar planets using adaptive optics. *Nature*, **368**, 203–207.

Angus, R., Aigrain, S., Foreman-Mackey, D. & McQuillan, A., 2015. Calibrating gyrochronology using Kepler asteroseismic targets. *MNRAS*, **450**, 1787–1798.

Appourchaux, T., Belkacem, K., Broomhall, A.-M., Chaplin, W. J., Gough, D. O. et al., 2010. The quest for the solar g modes. *Astronomy and Astrophysics Review*, **18**, 197–277.

Appourchaux, T., Michel, E., Auvergne, M., Baglin, A., Toutain, T. et al., 2008. CoRoT sounds the stars: p-mode parameters of Sun-like oscillations on HD 49933. *A&A*, **488**, 705–714.

Armitage, P. J., 2011. Dynamics of Protoplanetary Disks. *ARA&A*, **49**, 195–236.

Armstrong, D. J., Kirk, J., Lam, K. W. F., McCormac, J., Walker, S. R., Brown, D. J. A., Osborn, H. P., Pollacco, D. L. & Spake, J., 2015. K2 Variable Catalogue: Variable stars and eclipsing binaries in K2 campaigns 1 and 0. *A&A*, **579**, A19.

Ayala, L., 2013. Worlds and Systems in Early Modern Europe. In M. J. Way & D. Hunter, eds., *Origins of the Expanding Universe: 1912-1932*, vol. 471 of *Astronomical Society of the Pacific Conference Series*, 193.

Baade, D., 1982. An unusually short stable period of absorption line asymmetries and V/R variations in the spectrum of the Be star 28 CMa. *A&A*, **105**, 65–75.

Baade, D., Rivinius, T., Pigulski, A., Carciofi, A. C., Martayan, C., Moffat, A. F. J., Wade, G. A., Weiss, W. W., Grunhut, J., Handler, G., Kuschnig, R., Mehner, A., Pablo, H., Popowicz, A., Rucinski, S. & Whittaker, G., 2016. Short-term variability and mass loss in Be stars. I. BRITE satellite photometry of η and μ Centauri. *A&A*, **588**, A56.

Babcock, H. W., 1953. The Possibility of Compensating Astronomical Seeing. *PASP*, **65**, 229.

Baglin, A., 2003. COROT: A minisat for pionnier science, asteroseismology and planets finding. *Advances in Space Research*, **31**, 345–349.

Bakos, G., Noyes, R. W., Kovács, G., Stanek, K. Z., Sasselov, D. D. & Domsa, I., 2004. Wide-Field Millimagnitude Photometry with the HAT: A Tool for Extrasolar Planet Detection. *PASP*, **116**, 266–277.

Balbus, S. A. & Hawley, J. F., 1991. A powerful local shear instability in weakly magnetized disks. I - Linear analysis. II - Nonlinear evolution. *ApJ*, **376**, 214–233.

Baldwin, J. E., Beckett, M. G., Boysen, R. C., Burns, D., Buscher, D. F., Cox, G. C., Haniff, C. A., Mackay, C. D., Nightingale, N. S., Rogers, J., Scheuer, P. A. G., Scott, T. R., Tuthill, P. G., Warner, P. J., Wilson, D. M. A. & Wilson, R. W., 1996. The first images from an optical aperture synthesis array: mapping of Capella with COAST at two epochs. *A&A*, **306**, L13+.

Baldwin, J. E., Boysen, R. C., Cox, G. C., Haniff, C. A., Rogers, J., Warner, P. J., Wilson, D. M. & Mackay, C. D., 1994. Design and performance of COAST. In J. B. Breckinridge, ed., *Amplitude and Intensity Spatial Interferometry II*, vol. 2200 of *Proc. SPIE*, 118–128.

Baldwin, J. E., Haniff, C. A., Mackay, C. D. & Warner, P. J., 1986. Closure phase in high-resolution optical imaging. *Nature*, **320**, 595–597.

Balona, L. A., Pigulski, A., Cat, P. D., Handler, G., Gutiérrez-Soto, J. et al., 2011. Kepler observations of the variability in B-type stars. *MNRAS*, **413**, 2403–2420.

Baranne, A., Queloz, D., Mayor, M., Adrianzyk, G., Knispel, G., Kohler, D., Lacroix, D., Meunier, J.-P., Rimbaud, G. & Vin, A., 1996. ELODIE: A spectrograph for accurate radial velocity measurements. *A&AS*, **119**, 373–390.

Barclay, T., Barentsen, G. & Colon, K., 2016. KeplerScienceWebsite: 20160106. URL `http://dx.doi.org/10.5281/zenodo.44393`.

Barclay, T., Rowe, J. F., Lissauer, J. J., Huber, D., Fressin, F. et al., 2013. A sub-Mercury-sized exoplanet. *Nature*, **494**, 452–454.

Barnard, E. E., 1916. A small star with large proper-motion. *AJ*, **29**, 181–183.

Barros, S. C. C., Almenara, J. M., Deleuil, M., Diaz, R. F., Csizmadia, S. et al., 2014. Revisiting the transits of CoRoT-7b at a lower activity level. *A&A*, **569**, A74.

Barstow, J. K., Aigrain, S., Irwin, P. G. J. & Sing, D. K., 2017. A Consistent Retrieval Analysis of 10 Hot Jupiters Observed in Transmission. *ApJ*, **834**, 50.

Barstow, J. K. & Irwin, P. G. J., 2016. Habitable worlds with JWST: transit spectroscopy of the TRAPPIST-1 system? *MNRAS*, **461**, L92–L96.

Barstow, M. A., Barstow, J. K., Casewell, S. L., Holberg, J. B. & Hubeny, I., 2014. Evidence for an external origin of heavy elements in hot DA white dwarfs. *MNRAS*, **440**, 1607–1625.

Bartholdi, P., 1975. Photoelectric observations of occultations of the Pleiades and the incidence of duplicity in the cluster. *AJ*, **80**, 445–448.

Bartlett, J. L., 2007. *Knowing our neighbors: Fundamental properties of nearby stars*. Ph.D. thesis, University of Virginia.

Basri, G. & Brown, M. E., 2006. Planetesimals to Brown Dwarfs: What is a Planet? *Annual Review of Earth and Planetary Sciences*, **34**, 193–216.

Basu, S., Grundahl, F., Stello, D., Kallinger, T., Hekker, S. et al., 2011. Sounding Open Clusters: Asteroseismic Constraints from Kepler on the Properties of NGC 6791 and NGC

6819. *ApJ*, **729**, L10.

Batalha, N. M., 2014. Exploring exoplanet populations with NASA's Kepler Mission. *Proceedings of the National Academy of Science*, **111**, 12647–12654.

Batalha, N. M., Borucki, W. J., Bryson, S. T., Buchhave, L. A., Caldwell, D. A. et al., 2011. Kepler's First Rocky Planet: Kepler-10b. *ApJ*, **729**, 27.

Batalha, N. M., Rowe, J. F., Gilliland, R. L., Jenkins, J. J., Caldwell, D., Borucki, W. J., Koch, D. G., Lissauer, J. J., Dunham, E. W., Gautier, T. N., Howell, S. B., Latham, D. W., Marcy, G. W. & Prsa, A., 2010. Pre-spectroscopic False-positive Elimination of Kepler Planet Candidates. *ApJ*, **713**, L103–L108.

Baudin, F., Barban, C., Belkacem, K., Hekker, S., Morel, T., Samadi, R., Benomar, O., Goupil, M.-J., Carrier, F., Ballot, J., Deheuvels, S., De Ridder, J., Hatzes, A. P., Kallinger, T. & Weiss, W. W., 2011. Amplitudes and lifetimes of solar-like oscillations observed by CoRoT. Red-giant versus main-sequence stars. *A&A*, **529**, A84.

Bean, J. L., Miller-Ricci Kempton, E. & Homeier, D., 2010. A ground-based transmission spectrum of the super-Earth exoplanet GJ 1214b. *Nature*, **468**, 669–672.

Beck, P. G., Bedding, T. R., Mosser, B., Stello, D., Garcia, R. A. et al., 2011. Kepler Detected Gravity-Mode Period Spacings in a Red Giant Star. *Science*, **332**, 205.

Beck, P. G., Montalban, J., Kallinger, T., De Ridder, J., Aerts, C. et al., 2012a. Fast core rotation in red-giant stars as revealed by gravity-dominated mixed modes. *Nature*, **481**, 55–57.

Beck, P. G., Montalban, J., Kallinger, T., De Ridder, J., Aerts, C. et al., 2012b. Fast core rotation in red-giant stars as revealed by gravity-dominated mixed modes. *Nature*, **481**, 55–57.

Becker, J. C., Vanderburg, A., Adams, F. C., Rappaport, S. A. & Schwengeler, H. M., 2015. WASP-47: A Hot Jupiter System with Two Additional Planets Discovered by K2. *ApJ*, **812**, L18.

Bedding, T. R., Mosser, B., Huber, D., Montalbán, J., Beck, P. et al., 2011. Gravity modes as a way to distinguish between hydrogen- and helium-burning red giant stars. *Nature*, **471**, 608–611.

Beichman, C., Benneke, B., Knutson, H., Smith, R., Lagage, P.-O. et al., 2014. Observations of Transiting Exoplanets with the James Webb Space Telescope (JWST). *PASP*, **126**, 1134.

Belkacem, K., Goupil, M. J., Dupret, M. A., Samadi, R., Baudin, F., Noels, A. & Mosser, B., 2011. The underlying physical meaning of the ν_{max} - ν_c relation. *A&A*, **530**, A142.

Benedict, G. F., McArthur, B., Chappell, D. W., Nelan, E., Jefferys, W. H., van Altena, W., Lee, J., Cornell, D., Shelus, P. J., Hemenway, P. D., Franz, O. G., Wasserman, L. H., Duncombe, R. L., Story, D., Whipple, A. L. & Fredrick, L. W., 1999. Interferometric Astrometry of Proxima Centauri and Barnard's Star Using HUBBLE SPACE TELESCOPE Fine Guidance Sensor 3: Detection Limits for Substellar Companions. *AJ*, **118**, 1086–1100.

Berta, Z. K., Irwin, J., Charbonneau, D., Burke, C. J. & Falco, E. E., 2012. Transit Detection in the MEarth Survey of Nearby M Dwarfs: Bridging the Clean-first, Search-later Divide. *AJ*, **144**, 145.

Beuzit, J.-L., Feldt, M., Dohlen, K., Mouillet, D., Puget, P. et al., 2008. SPHERE: a 'Planet Finder' instrument for the VLT. In *Ground-based and Airborne Instrumentation for Astronomy II*, vol. 7014 of *Proc. SPIE*, 701418.

Binnendijk, L., 1949. The light variation of Pleione. *AJ*, **54**, 117.

Blum, P. R., 2012. *Giordano Bruno: An Introduction*. Editions Rodopi.

Bodenheimer, P. & Pollack, J. B., 1986. Calculations of the accretion and evolution of giant planets The effects of solid cores. *Icarus*, **67**, 391–408.

Bolton, C. T., 1982. A preliminary report on simultaneous ultraviolet and optical observations of Lambda Eridani. In M. Jaschek & H.-G. Groth, eds., *Be Stars*, vol. 98 of *IAU Symposium*, 181–183.

Borucki, W., Caldwell, D., Koch, D., Jenkins, J. & Ninkov, Z., 1999. Photometric Observations of 6000 Stars in the Cygnus Field. *NASA STI/Recon Technical Report N*.

Borucki, W. & Koch, D., 1994. Multiplex approach to the photometric detection of planets. *Ap&SS*, **212**, 293–298.

Borucki, W., Koch, D., Batalha, N., Caldwell, D., Christensen-Dalsgaard, J., Cochran, W. D., Dunham, E., Gautier, T. N., Geary, J., Gilliland, R., Jenkins, J., Kjeldsen, H., Lissauer, J. J. & Rowe, J., 2009. KEPLER: Search for Earth-Size Planets in the Habitable Zone. In F. Pont, D. Sasselov & M. J. Holman, eds., *Transiting Planets*, vol. 253 of *IAU Symposium*, 289–299.

Borucki, W., Koch, D., Dunham, E., Cullers, D., Webster, L., Granados, A., Ford, C., Reitsema, H., Cochran, W. & Bell, J., 1994. Fresip: a Discovery Mission Concept to Find Earth-Sized Planets around Solar like Stars. In *AAS/Division for Planetary Sciences Meeting Abstracts #26*, vol. 26 of *Bulletin of the American Astronomical Society*, 1091.

Borucki, W. J., Allen, L. E., Taylor, S. W., Torbet, E. B., Schaefer, A. R. & Fowler, J., 1989. Test of a multichannel photometer to detect earth-sized planets. In H. A. Weaver & L. Danly, eds., *The Formation and Evolution of Planetary Systems*, 340.

Borucki, W. J., Caldwell, D., Koch, D. G., Webster, L. D., Jenkins, J. M., Ninkov, Z. & Showen, R., 2001. The Vulcan Photometer: A Dedicated Photometer for Extrasolar Planet Searches. *PASP*, **113**, 439–451.

Borucki, W. J., Koch, D., Basri, G., Batalha, N., Brown, T. et al., 2010. Kepler Planet-Detection Mission: Introduction and First Results. *Science*, **327**, 977.

Borucki, W. J., Koch, D. G., Dunham, E. W. & Jenkins, J. M., 1997. The Kepler Mission: A Mission To Determine The Frequency Of Inner Planets Near The Habitable Zone For A Wide Range Of Stars. In D. Soderblom, ed., *Planets Beyond the Solar System and the Next Generation of Space Missions*, vol. 119 of *Astronomical Society of the Pacific Conference Series*, 153.

Borucki, W. J., Scargle, J. D. & Hudson, H. S., 1985. Detectability of extrasolar planetary transits. *ApJ*, **291**, 852–854.

Borucki, W. J. & Summers, A. L., 1984. The photometric method of detecting other planetary systems. *Icarus*, **58**, 121–134.

Borucki, W. J., Torbet, E. B. & Pham, P. C., 1988. High precision photometry with fiber optics. In S. C. Barden, ed., *Fiber Optics in Astronomy*, vol. 3 of *Astronomical Society of the Pacific Conference Series*, 247–260.

Boss, A. P., 2011. Formation of Giant Planets by Disk Instability on Wide Orbits Around Proto-

stars with Varied Masses. *ApJ*, **731**, 74.

Bouy, H., Bertin, E., Sarro, L. M., Barrado, D., Moraux, E., Bouvier, J., Cuillandre, J.-C., Berihuete, A., Olivares, J. & Beletsky, Y., 2015. The Seven Sisters DANCe. I. Empirical isochrones, luminosity, and mass functions of the Pleiades cluster. *A&A*, **577**, A148.

Bowler, B. P., 2016. Imaging Extrasolar Giant Planets. *PASP*, **128**(10), 102001.

Bowman, D. M. & Kurtz, D. W., 2014. Pulsational frequency and amplitude modulation in the δ Sct star KIC 7106205. *MNRAS*, **444**, 1909–1918.

Boyajian, T. S., LaCourse, D. M., Rappaport, S. A., Fabrycky, D., Fischer, D. A. et al., 2016. Planet Hunters IX. KIC 8462852 - where's the flux? *MNRAS*, **457**, 3988–4004.

Bracewell, R. N., 1974. *The Galactic Club: Intelligent Life in Outer Space*.

Bracewell, R. N., 1978. Detecting nonsolar planets by spinning infrared interferometer. *Nature*, **274**, 780.

Breger, M., 1972. Pulsating Variables in the Pleiades Cluster. *ApJ*, **176**, 367.

Brogaard, K., Jessen-Hansen, J., Handberg, R., Arentoft, T., Frandsen, S., Grundahl, F., Bruntt, H., Sandquist, E. L., Miglio, A., Beck, P. G., Thygesen, A. O., Kjærgaard, K. L. & Haugaard, N. A., 2016. Testing asteroseismic scaling relations using eclipsing binaries in star clusters and the field. *Astronomische Nachrichten*, **337**, 793.

Brown, T. M., Gilliland, R. L., Noyes, R. W. & Ramsey, L. W., 1991. Detection of possible p-mode oscillations on Procyon. *ApJ*, **368**, 599–609.

Bruno, G., 1584a. *Cena de le ceneri*.

Bruno, G., 1584b. *De l'infinito, universo e mondi*.

Bryson, S., Tennenbaum, P., Jenkins, J. M., Chandrasekaran, H., Caldwell, D. A., Gilliland, R. L., Haas, M. R., Dotson, J. L., Koch, D. G., Borucki, W. J. & Kepler Team, 2010. Characterization and Application of the Kepler Pixel Response Function. In *American Astronomical Society Meeting Abstracts #215*, vol. 42 of *Bulletin of the American Astronomical Society*, 285.

Burrows, A. S., 2014a. Highlights in the study of exoplanet atmospheres. *Nature*, **513**, 345–352.

Burrows, A. S., 2014b. Spectra as windows into exoplanet atmospheres. *Proceedings of the National Academy of Science*, **111**, 12601–12609.

Butler, R. P. & Marcy, G. W., 1996. A Planet Orbiting 47 Ursae Majoris. *ApJ*, **464**, L153.

Butler, R. P., Marcy, G. W., Fischer, D. A., Brown, T. M., Contos, A. R., Korzennik, S. G., Nisenson, P. & Noyes, R. W., 1999. Evidence for Multiple Companions to upsilon Andromedae. *ApJ*, **526**, 916–927.

Butler, R. P., Marcy, G. W., Williams, E., Hauser, H. & Shirts, P., 1997. Three New "51 Pegasi-Type" Planets. *ApJ*, **474**, L115–L118.

Butler, R. P., Wright, J. T., Marcy, G. W., Fischer, D. A., Vogt, S. S., Tinney, C. G., Jones, H. R. A., Carter, B. D., Johnson, J. A., McCarthy, C. & Penny, A. J., 2006. Catalog of Nearby Exoplanets. *ApJ*, **646**, 505–522.

Calder, W. A., 1937. A photoelectric magnitude sequence in the Pleiades. *Annals of Harvard College Observatory*, **105**, 453–458.

Caldwell, D. A., Kolodziejczak, J. J., Van Cleve, J. E., Jenkins, J. M., Gazis, P. R. et al., 2010. Instrument Performance in Kepler's First Months. *ApJ*, **713**, L92–L96.

Callingham, J., 2017. Time evolution of the number of sources observed by widefield radio

continuum surveys. URL https://figshare.com/articles/number_srcs_v_year_concl_eps/4780411.

Cameron, A. G. W., 1978. Physics of the primitive solar accretion disk. *Moon and Planets*, **18**, 5–40.

Cameron, C., Saio, H., Kuschnig, R., Walker, G. A. H., Matthews, J. M., Guenther, D. B., Moffat, A. F. J., Rucinski, S. M., Sasselov, D. & Weiss, W. W., 2008. MOST Detects SPBe Pulsations in HD 127756 and HD 217543: Asteroseismic Rotation Rates Independent of v sin i. *ApJ*, **685**, 489–507.

Campante, T. L., Barclay, T., Swift, J. J., Huber, D., Adibekyan, V. Z. et al., 2015. An Ancient Extrasolar System with Five Sub-Earth-size Planets. *ApJ*, **799**, 170.

Campbell, B., Walker, G. A. H. & Yang, S., 1988. A search for substellar companions to solar-type stars. *ApJ*, **331**, 902–921.

Candes, E., Romberg, J. & Tao, T., 2006. Robust uncertainty principles: Exact signal reconstruction from highly incomplete frequency information. *IEEE Transactions on Information Theory*, **52**(2), 489–509.

Carpano, S., Aigrain, S. & Favata, F., 2003. Detecting planetary transits in the presence of stellar variability. Optimal filtering and the use of colour information. *A&A*, **401**, 743–753.

Casagrande, L., Portinari, L., Glass, I. S., Laney, D., Silva Aguirre, V., Datson, J., Andersen, J., Nordström, B., Holmberg, J., Flynn, C. & Asplund, M., 2014. Towards stellar effective temperatures and diameters at 1 per cent accuracy for future surveys. *MNRAS*, **439**, 2060–2073.

Casey, A. R., Hogg, D. W., Ness, M., Rix, H.-W., Ho, A. Q. & Gilmore, G., 2016. The Cannon 2: A data-driven model of stellar spectra for detailed chemical abundance analyses. *ArXiv e-prints*.

Catanzarite, J. & Shao, M., 2011. The Occurrence Rate of Earth Analog Planets Orbiting Sun-like Stars. *ApJ*, **738**, 151.

Chamberlin, T. C., 1901. On a Possible Function of Disruptive Approach in the Formation of Meteorites, Comets, and nebulae. *ApJ*, **14**, 17.

Chambers, J., 2006. A semi-analytic model for oligarchic growth. *Icarus*, **180**, 496–513.

Chaplin, W. J., Basu, S., Huber, D., Serenelli, A., Casagrande, L. et al., 2014. Asteroseismic Fundamental Properties of Solar-type Stars Observed by the NASA Kepler Mission. *ApJS*, **210**, 1.

Chaplin, W. J. & Miglio, A., 2013. Asteroseismology of Solar-Type and Red-Giant Stars. *ARA&A*, **51**, 353–392.

Charbonneau, D., Brown, T. M., Dunham, E. W., Latham, D. W., Looper, D. L. & Mandushev, G., 2004. Astrophysical False Positives Encountered in Wide-Field Transit Searches. In S. S. Holt & D. Deming, eds., *The Search for Other Worlds*, vol. 713 of *American Institute of Physics Conference Series*, 151–160.

Charbonneau, D., Brown, T. M., Latham, D. W. & Mayor, M., 2000. Detection of Planetary Transits Across a Sun-like Star. *ApJ*, **529**, L45–L48.

Charbonneau, D., Brown, T. M., Noyes, R. W. & Gilliland, R. L., 2002. Detection of an Extrasolar Planet Atmosphere. *ApJ*, **568**, 377–384.

Charpinet, S., Fontaine, G., Brassard, P., Green, E. M., Van Grootel, V., Randall,

S. K., Silvotti, R., Baran, A. S., Østensen, R. H., Kawaler, S. D. & Telting, J. H., 2011. A compact system of small planets around a former red-giant star. *Nature*, **480**, 496–499.

Chazelas, B., Pollacco, D., Queloz, D., Rauer, H., Wheatley, P. J., West, R., Da Silva Bento, J., Burleigh, M., McCormac, J., Eigmüller, P., Erikson, A., Genolet, L., Goad, M., Jordán, A., Neveu, M. & Walker, S., 2012. NGTS: a robotic transit survey to detect Neptune and super-Earth mass planets. In *Ground-based and Airborne Telescopes IV*, vol. 8444 of *Proc. SPIE*, 84440E.

Cheetham, A. C., Cvetojevic, N., Sivaramakrishnan, A., Norris, B. & Tuthill, P. G., 2014. Fizeau interferometric cophasing of segmented mirrors. In *Space Telescopes and Instrumentation 2014: Optical, Infrared, and Millimeter Wave*, vol. 9143 of *Proc. SPIE*, 914352.

Choi, J., McCarthy, C., Marcy, G. W., Howard, A. W., Fischer, D. A., Johnson, J. A., Isaacson, H. & Wright, J. T., 2013. Precise Doppler Monitoring of Barnard's Star. *ApJ*, **764**, 131.

Christiansen, J. L., Jenkins, J. M., Caldwell, D. A., Burke, C. J., Tenenbaum, P., Seader, S., Thompson, S. E., Barclay, T. S., Clarke, B. D., Li, J., Smith, J. C., Stumpe, M. C., Twicken, J. D. & Van Cleve, J., 2012. The Derivation, Properties, and Value of Kepler's Combined Differential Photometric Precision. *PASP*, **124**, 1279–1287.

Chwolson, O., 1924. Über eine mögliche Form fiktiver Doppelsterne. *Astronomische Nachrichten*, **221**, 329.

Clanton, C. & Gaudi, B. S., 2017. Constraining the Frequency of Free-floating Planets from a Synthesis of Microlensing, Radial Velocity, and Direct Imaging Survey Results. *ApJ*, **834**, 46.

Close, L. M., Males, J. R., Kopon, D. A., Gasho, V., Follette, K. B. et al., 2012. First closed-loop visible AO test results for the advanced adaptive secondary AO system for the Magellan Telescope: MagAO's performance and status. In *Adaptive Optics Systems III*, vol. 8447 of *Proc. SPIE*, 84470X.

Cocconi, G. & Morrison, P., 1959. Searching for Interstellar Communications. *Nature*, **184**, 844–846.

Cochran, W. D., Hatzes, A. P. & Hancock, T. J., 1991. Constraints on the companion object to HD 114762. *ApJ*, **380**, L35–L38.

Corsaro, E., Lee, Y.-N., García, R. A., Hennebelle, P., Mathur, S., Beck, P. G., Mathis, S., Stello, D. & Bouvier, J., 2017. Spin alignment of stars in old open clusters. *Nature Astronomy*, **1**, 0064 EP –. URL `http://dx.doi.org/10.1038/s41550-017-0064`. Letter.

Cowling, T. G., 1941. The non-radial oscillations of polytropic stars. *MNRAS*, **101**, 367.

Cowling, T. G. & Newing, R. A., 1949. The Oscillations of a Rotating Star. *ApJ*, **109**, 149.

Creevey, O. L., Thévenin, F., Basu, S., Chaplin, W. J., Bigot, L., Elsworth, Y., Huber, D., Monteiro, M. J. P. F. G. & Serenelli, A., 2013. A large sample of calibration stars for Gaia: log g from Kepler and CoRoT fields. *MNRAS*, **431**, 2419–2432.

Creevey, O. L., Thévenin, F., Berio, P., Heiter, U., von Braun, K. et al., 2015. Benchmark stars for Gaia Fundamental properties of the Population II star HD 140283 from interferometric, spectroscopic, and photometric data. *A&A*, **575**, A26.

Cressie, N., 1990. The origins of kriging. *Mathematical Geology*, **22**(3), 239–252. ISSN 1573-8868. URL `http://dx.doi.org/10.1007/BF00889887`.

Crossfield, I. J. M., Ciardi, D. R., Petigura, E. A., Sinukoff, E., Schlieder, J. E.

et al., 2016. Two Hundred Planets and Candidates Discovered in K2's First Five Fields. *ApJ*.

Crossfield, I. J. M., Petigura, E., Schlieder, J. E., Howard, A. W., Fulton, B. J. et al., 2015. A Nearby M Star with Three Transiting Super-Earths Discovered by K2. *ApJ*, **804**, 10.

Cunha, M. S., Aerts, C., Christensen-Dalsgaard, J., Baglin, A., Bigot, L. et al., 2007. Asteroseismology and interferometry. *Astronomy and Astrophysics Review*, **14**, 217–360.

Currie, T., Guyon, O., Martinache, F., Clergeon, C., McElwain, M., Thalmann, C., Jovanovic, N., Singh, G. & Kudo, T., 2013. The Subaru Coronagraphic Extreme Adaptive Optics Imager: First Results and On-Sky Performance. *ArXiv e-prints*.

D'Angelo, G. & Lubow, S. H., 2008. Evolution of Migrating Planets Undergoing Gas Accretion. *ApJ*, **685**, 560–583.

Davies, R. & Kasper, M., 2012. Adaptive Optics for Astronomy. *ARA&A*, **50**, 305–351.

De Cat, P. & Aerts, C., 2002. A study of bright southern slowly pulsating B stars. II. The intrinsic frequencies. *A&A*, **393**, 965–981.

De Cat, P., Briquet, M., Aerts, C., Goossens, K., Saesen, S. et al., 2007. Long term photometric monitoring with the Mercator telescope. Frequencies and mode identification of variable O-B stars. *A&A*, **463**, 243–249.

De Ridder, J., Barban, C., Baudin, F., Carrier, F., Hatzes, A. P., Hekker, S., Kallinger, T., Weiss, W. W., Baglin, A., Auvergne, M., Samadi, R., Barge, P. & Deleuil, M., 2009. Non-radial oscillation modes with long lifetimes in giant stars. *Nature*, **459**, 398–400.

de Vegt, C. & Gehlich, U. K., 1976. Results of photoelectric lunar occultation observations obtained at the Hamburg Observatory during 1969-1973. *A&A*, **48**, 245–252.

Debosscher, J., Blomme, J., Aerts, C. & De Ridder, J., 2011. Global stellar variability study in the field-of-view of the Kepler satellite. *A&A*, **529**, A89.

Degroote, P., Aerts, C., Baglin, A., Miglio, A., Briquet, M., Noels, A., Niemczura, E., Montalban, J., Bloemen, S., Oreiro, R., Vučković, M., Smolders, K., Auvergne, M., Baudin, F., Catala, C. & Michel, E., 2010. Deviations from a uniform period spacing of gravity modes in a massive star. *Nature*, **464**, 259–261.

Degroote, P., Aerts, C., Ollivier, M., Miglio, A., Debosscher, J. et al., 2009. CoRoT's view of newly discovered B-star pulsators: results for 358 candidate B pulsators from the initial run's exoplanet field data. *A&A*, **506**, 471–489.

Deleuil, M., Deeg, H. J., Alonso, R., Bouchy, F., Rouan, D. et al., 2008. Transiting exoplanets from the CoRoT space mission . VI. CoRoT-Exo-3b: the first secure inhabitant of the brown-dwarf desert. *A&A*, **491**, 889–897.

Deming, D., Knutson, H., Kammer, J., Fulton, B. J., Ingalls, J., Carey, S., Burrows, A., Fortney, J. J., Todorov, K., Agol, E., Cowan, N., Desert, J.-M., Fraine, J., Langton, J., Morley, C. & Showman, A. P., 2015. Spitzer Secondary Eclipses of the Dense, Modestly-irradiated, Giant Exoplanet HAT-P-20b Using Pixel-level Decorrelation. *ApJ*, **805**, 132.

Demory, B.-O., Gillon, M., de Wit, J., Madhusudhan, N., Bolmont, E., Heng, K., Kataria, T., Lewis, N., Hu, R., Krick, J., Stamenković, V., Benneke, B., Kane, S. & Queloz, D., 2016a. A map of the large day-night temperature gradient of a super-Earth

exoplanet. *Nature*, **532**, 207–209.

Demory, B.-O., Gillon, M., Deming, D., Valencia, D., Seager, S., Benneke, B., Lovis, C., Cubillos, P., Harrington, J., Stevenson, K. B., Mayor, M., Pepe, F., Queloz, D., Ségransan, D. & Udry, S., 2011. Detection of a transit of the super-Earth 55 Cancri e with warm Spitzer. *A&A*, **533**, A114.

Demory, B.-O., Gillon, M., Madhusudhan, N. & Queloz, D., 2016b. Variability in the super-Earth 55 Cnc e. *MNRAS*, **455**, 2018–2027.

Diago, P. D., Gutiérrez-Soto, J., Auvergne, M., Fabregat, J., Hubert, A.-M. et al., 2009. Pulsations in the late-type Be star HD 50 209 detected by CoRoT. *A&A*, **506**, 125–131.

Dick, S. J., 1996. *The biological universe: the twentieth-century extraterrestrial life debate and the limits of science*.

Dodson-Robinson, S. E., Veras, D., Ford, E. B. & Beichman, C. A., 2009. The Formation Mechanism of Gas Giants on Wide Orbits. *ApJ*, **707**, 79–88.

Dong, S. & Zhu, Z., 2013. Fast Rise of "Neptune-size" Planets (4-8 R $_{\oplus}$) from P ˜ 10 to ˜250 Days - Statistics of Kepler Planet Candidates up to ˜0.75 AU. *ApJ*, **778**, 53.

Doppler, C., 1842. Ueber das farbige Licht der Doppelsterne und einiger anderer gestirne des Himmels. Versuch einer das Bradley'sche Aberrationstheorem als integrirenden Theil in sich schliessenden allgemeineren Theorie. Zur Feier seines hundertsten Geburtstages als erste Veröffentlichung des nach ihm benannten physikalischen Princips. *Proceedings of the Bohemian Society of Sciences*.

Dormand, J. R. & Woolfson, M. M., 1989. *The origin of the solar system: The capture theory*.

Doyle, L. R., Carter, J. A., Fabrycky, D. C., Slawson, R. W., Howell, S. B. et al., 2011. Kepler-16: A Transiting Circumbinary Planet. *Science*, **333**, 1602.

Dreizler, S., Hauschildt, P. H., Kley, W., Rauch, T., Schuh, S. L., Werner, K. & Wolff, B., 2003. OGLE-TR-3: A possible new transiting planet. *A&A*, **402**, 791–799.

Dressing, C. D. & Charbonneau, D., 2015. The Occurrence of Potentially Habitable Planets Orbiting M Dwarfs Estimated from the Full Kepler Dataset and an Empirical Measurement of the Detection Sensitivity. *ApJ*, **807**, 45.

Dressing, C. D., Vanderburg, A., Schlieder, J. E., Crossfield, I. J. M., Knutson, H. A., Newton, E. R., Ciardi, D. R., Fulton, B. J., Gonzales, E. J., Howard, A. W., Isaacson, H., Livingston, J., Petigura, E. A., Sinukoff, E., Everett, M., Horch, E. & Howell, S. B., 2017. Characterizing K2 Candidate Planetary Systems Orbiting Low-Mass Stars II: Planetary Systems Observed During Campaigns 1-7. *ArXiv e-prints*.

Dyson, F. J., 1960. Search for Artificial Stellar Sources of Infrared Radiation. *Science*, **131**, 1667–1668.

Dyson, F. W., Eddington, A. S. & Davidson, C., 1920. A Determination of the Deflection of Light by the Sun's Gravitational Field, from Observations Made at the Total Eclipse of May 29, 1919. *Philosophical Transactions of the Royal Society of London Series A*, **220**, 291–333.

Dziembowski, W. A., Moskalik, P. & Pamyatnykh, A. A., 1993. The Opacity Mechanism in B-Type Stars - Part Two - Excitation of High-Order G-Modes in Main Sequence Stars. *MNRAS*, **265**, 588.

Eddington, A. S., 1917. The pulsation theory of Cepheid variables. *The Observatory*, **40**, 290–293.

Eddington, A. S., 1919. The total eclipse of 1919 May 29 and the influence of gravitation on light.

The Observatory, **42**, 119–122.

Einstein, A., 1905. Zur Elektrodynamik bewegter Körper. *Annalen der Physik*, **322**, 891–921.

Einstein, A., 1936. Lens-Like Action of a Star by the Deviation of Light in the Gravitational Field. *Science*, **84**, 506–507.

Eitter, J. J. & Beavers, W. I., 1974. Lunar Occultation Summary. I. *ApJS*, **28**, 405.

Evans, T. M., Aigrain, S., Gibson, N., Barstow, J. K., Amundsen, D. S., Tremblin, P. & Mourier, P., 2015. A uniform analysis of HD 209458b Spitzer/IRAC light curves with Gaussian process models. *MNRAS*, **451**, 680–694.

Evans, T. M., Pont, F., Sing, D. K., Aigrain, S., Barstow, J. K., Désert, J.-M., Gibson, N., Heng, K., Knutson, H. A. & Lecavelier des Etangs, A., 2013. The Deep Blue Color of HD 189733b: Albedo Measurements with Hubble Space Telescope/Space Telescope Imaging Spectrograph at Visible Wavelengths. *ApJ*, **772**, L16.

Fabrycky, D. C., Ford, E. B., Steffen, J. H., Rowe, J. F., Carter, J. A. et al., 2012. Transit Timing Observations from Kepler. IV. Confirmation of Four Multiple-planet Systems by Simple Physical Models. *ApJ*, **750**, 114.

Fanelli, M. N., Jenkins, J. M., Bryson, S. T., Quintana, E. V., Twicken, J. D. et al., 2011. Kepler Data Processing Handbook (KSCI-19081-001).

Faria, J. P., Haywood, R. D., Brewer, B. J., Figueira, P., Oshagh, M., Santerne, A. & Santos, N. C., 2016. Uncovering the planets and stellar activity of CoRoT-7 using only radial velocities. *A&A*, **588**, A31.

Feroz, F., Hobson, M. P. & Bridges, M., 2009. MULTINEST: an efficient and robust Bayesian inference tool for cosmology and particle physics. *MNRAS*, **398**, 1601–1614.

Feroz, F., Hobson, M. P., Cameron, E. & Pettitt, A. N., 2013. Importance Nested Sampling and the MultiNest Algorithm. *ArXiv e-prints*.

Fienup, J. R., Marron, J. C., Schulz, T. J. & Seldin, J. H., 1993. Hubble Space Telescope characterized by using phase-retrieval algorithms. *Appl. Opt.*, **32**(10), 1747–1767. URL `http://ao.osa.org/abstract.cfm?URI=ao-32-10-1747`.

Fischer, D. A., Marcy, G. W. & Spronck, J. F. P., 2014. The Twenty-five Year Lick Planet Search. *ApJS*, **210**, 5.

Fizeau, H., 1868. Prix Bordin: Rapport sur le concours de l'année 1867. *Comptes Rendus de l'Académie des Sciences*, **66**, 932.

Flammarion, C., 1862. *La Pluralité des Mondes Habités*.

Fontenelle, B. d., 1686. *Entretiens sur la pluralité des mondes*.

Ford, E. B., Fabrycky, D. C., Steffen, J. H., Carter, J. A., Fressin, F. et al., 2012a. Transit Timing Observations from Kepler. II. Confirmation of Two Multiplanet Systems via a Non-parametric Correlation Analysis. *ApJ*, **750**, 113.

Ford, E. B., Ragozzine, D., Rowe, J. F., Steffen, J. H., Barclay, T. et al., 2012b. Transit Timing Observations from Kepler. V. Transit Timing Variation Candidates in the First Sixteen Months from Polynomial Models. *ApJ*, **756**, 185.

Ford, E. B., Rowe, J. F., Fabrycky, D. C., Carter, J. A., Holman, M. J. et al., 2011. Transit Timing Observations from Kepler. I. Statistical Analysis of the First Four Months. *ApJS*, **197**, 2.

Foreman-Mackey, D., Hogg, D. W., Lang, D. & Goodman, J., 2013. emcee: The MCMC

Hammer. *PASP*, **125**, 306–312.

Foreman-Mackey, D., Hogg, D. W. & Morton, T. D., 2014. Exoplanet Population Inference and the Abundance of Earth Analogs from Noisy, Incomplete Catalogs. *ApJ*, **795**, 64.

Foreman-Mackey, D., Hogg, D. W. & Schölkopf, B., 2015a. The search for single exoplanet transits in the Kepler light curves. *IAU General Assembly*, **22**, 2258352.

Foreman-Mackey, D., Montet, B. T., Hogg, D. W., Morton, T. D., Wang, D. & Schölkopf, B., 2015b. A Systematic Search for Transiting Planets in the K2 Data. *ApJ*, **806**, 215.

Fortier, A., Beck, T., Benz, W., Broeg, C., Cessa, V., Ehrenreich, D. & Thomas, N., 2014. CHEOPS: a space telescope for ultra-high precision photometry of exoplanet transits. In *Space Telescopes and Instrumentation 2014: Optical, Infrared, and Millimeter Wave*, vol. 9143 of *Proc. SPIE*, 91432J.

Frater, R. H., Robertson, J. G., O'Sullivan, J. D. & Norris, R. P., 1987. High Resolution Interferometric Imaging Using a Large Optical Telescope. In *Image Detection and Quality*, vol. 702 of *Proc. SPIE*, 255.

Freeman, K. & Bland-Hawthorn, J., 2002. The New Galaxy: Signatures of Its Formation. *ARA&A*, **40**, 487–537.

Frémat, Y., Zorec, J., Hubert, A.-M. & Floquet, M., 2005. Effects of gravitational darkening on the determination of fundamental parameters in fast-rotating B-type stars. *A&A*, **440**, 305–320.

Fressin, F., Torres, G., Charbonneau, D., Bryson, S. T., Christiansen, J., Dressing, C. D., Jenkins, J. M., Walkowicz, L. M. & Batalha, N. M., 2013. The False Positive Rate of Kepler and the Occurrence of Planets. *ApJ*, **766**, 81.

Fressin, F., Torres, G., Rowe, J. F., Charbonneau, D., Rogers, L. A. et al., 2012. Two Earth-sized planets orbiting Kepler-20. *Nature*, **482**, 195–198.

Frost, E. B., 1906. Spectrographic observations. *ApJ*, **23**, 264–269.

Fu, L.-S., 1965. Teng Mu: A Forgotten Chinese Philosopher. *T'oung Pao*, **52**(1/3), 35–96. ISSN 00825433. URL `http://www.jstor.org/stable/4527624`.

García, R. A., Turck-Chièze, S., Jiménez-Reyes, S. J., Ballot, J., Pallé, P. L., Eff-Darwich, A., Mathur, S. & Provost, J., 2007. Tracking Solar Gravity Modes: The Dynamics of the Solar Core. *Science*, **316**, 1591.

Gardner, J. P., Mather, J. C., Clampin, M., Doyon, R., Greenhouse, M. A. et al., 2006. The James Webb Space Telescope. *Space Sci. Rev.*, **123**, 485–606.

Gatewood, G. & Eichhorn, H., 1973. An unsuccessful search for a planetary companion of Barnard's star BD +4 3561. *AJ*, **78**, 769–776.

Gautier, III, T. N., Charbonneau, D., Rowe, J. F., Marcy, G. W., Isaacson, H. et al., 2012. Kepler-20: A Sun-like Star with Three Sub-Neptune Exoplanets and Two Earth-size Candidates. *ApJ*, **749**, 15.

Gautschy, A. & Saio, H., 1993. On non-radial oscillations of B-type stars. *MNRAS*, **262**, 213–219.

Gerchberg, R. W. & Saxton, W. O., 1972. A practical algorithm for the determination of the phase from image and diffraction plane pictures. *Optik (Jena)*, **35**, 237+.

Gibson, N. P., 2014. Reliable inference of exoplanet light-curve parameters using deterministic

and stochastic systematics models. *MNRAS*, **445**, 3401–3414.

Gibson, N. P., Aigrain, S., Barstow, J. K., Evans, T. M., Fletcher, L. N. & Irwin, P. G. J., 2013. A Gemini ground-based transmission spectrum of WASP-29b: a featureless spectrum from 515 to 720 nm. *MNRAS*, **428**, 3680–3692.

Gibson, N. P., Aigrain, S., Roberts, S., Evans, T. M., Osborne, M. & Pont, F., 2012. A Gaussian process framework for modelling instrumental systematics: application to transmission spectroscopy. *MNRAS*, **419**, 2683–2694.

Gibson, N. P., Pont, F. & Aigrain, S., 2011. A new look at NICMOS transmission spectroscopy of HD 189733, GJ-436 and XO-1: no conclusive evidence for molecular features. *MNRAS*, **411**, 2199–2213.

Gies, D. R., Williams, S. J., Matson, R. A., Guo, Z., Thomas, S. M., Orosz, J. A. & Peters, G. J., 2012. A Search for Hierarchical Triples using Kepler Eclipse Timing. *AJ*, **143**, 137.

Gilliland, R. L., Brown, T. M., Christensen-Dalsgaard, J., Kjeldsen, H., Aerts, C. et al., 2010. Kepler Asteroseismology Program: Introduction and First Results. *PASP*, **122**, 131–143.

Gillon, M., Courbin, F., Magain, P. & Borguet, B., 2005. On the potential of extrasolar planet transit surveys. *A&A*, **442**, 731–744.

Gillon, M., Demory, B.-O., Van Grootel, V., Motalebi, F., Lovis, C., Cameron, A. C., Charbonneau, D., Latham, D., Molinari, E., Pepe, F. A., Ségransan, D., Sasselov, D., Udry, S., Mayor, M., Micela, G., Piotto, G. & Sozzetti, A., 2017. Two massive rocky planets transiting a K-dwarf 6.5 parsecs away. *Nature Astronomy*, **1**, 0056.

Gillon, M., Jehin, E., Lederer, S. M., Delrez, L., de Wit, J., Burdanov, A., Van Grootel, V., Burgasser, A. J., Triaud, A. H. M. J., Opitom, C., Demory, B.-O., Sahu, D. K., Bardalez Gagliuffi, D., Magain, P. & Queloz, D., 2016. Temperate Earth-sized planets transiting a nearby ultracool dwarf star. *Nature*, **533**, 221–224.

Gillon, M., Triaud, A. H. M. J., Demory, B.-O., Jehin, E., Agol, E. et al., 2017. Seven temperate terrestrial planets around the nearby ultracool dwarf star TRAPPIST-1. *Nature*, **542**(7642), 456–460. ISSN 0028-0836. URL `http://dx.doi.org/10.1038/nature21360`. Letter.

Giménez, A., 2006. Equations for the analysis of the light curves of extra-solar planetary transits. *A&A*, **450**, 1231–1237.

Glindemann, A., Abuter, R., Carbognani, F., Delplancke, F., Derie, F. et al., 2001. The VLT Interferometer. *Academie des Sciences Paris Comptes Rendus Serie Physique Astrophysique*, **2**, 57–65.

Goldreich, P. & Keeley, D. A., 1977. Solar seismology. II - The stochastic excitation of the solar p-modes by turbulent convection. *ApJ*, **212**, 243–251.

Goldreich, P. & Tremaine, S., 1980. Disk-satellite interactions. *ApJ*, **241**, 425–441.

Goodricke, J., 1786. A Series of Observations on, and a Discovery of, the Period of the Variation of the Light of the Star Marked δ by Bayer, Near the Head of Cepheus. In a Letter from John Goodricke, Esq. to Nevil Maskelyne, D. D. F. R. S. and Astronomer Royal. *Philosophical Transactions of the Royal Society of London*, **76**, 48–61. URL `http://rstl.royalsocietypublishing.org/content/76/48.short`.

Goraya, P. S., Sharma, S. D., Malhi, J. S. & Tur, N. S., 1990. Variable nature of Pleione.

Ap&SS, **174**, 1–11.

Goss, M., 2012. First Interferometry in Radio Astronomy- Ruby Payne-Scott - Type I Solar Bursts Observed on Australia Day, 26 January 1946. In *Resolving The Sky - Radio Interferometry: Past, Present and Future*, 1.

Goss, M., 2013. *Making Waves: The Story of Ruby Payne-Scott: Australian Pioneer Radio Astronomer*.

Gough, D. O., 1986. Solar and solar-like oscillations - Theory. *Highlights of Astronomy*, **7**, 283–293.

Green, J., Schechter, P., Baltay, C., Bean, R., Bennett, D. et al., 2012. Wide-Field InfraRed Survey Telescope (WFIRST) Final Report. *ArXiv e-prints*.

Green, J. J., Beichman, C., Basinger, S. A., Horner, S., Meyer, M., Redding, D. C., Rieke, M. & Trauger, J. T., 2005. High contrast imaging with the JWST NIRCAM coronagraph. In D. R. Coulter, ed., *Techniques and Instrumentation for Detection of Exoplanets II*, vol. 5905 of *Proc. SPIE*, 185–195.

Greenbaum, A. Z. & Sivaramakrishnan, A., 2016. In-focus wavefront sensing using non-redundant mask-induced pupil diversity. *Optics Express*, **24**, 15506.

Greenough, J. B., 1900. *Bucolics, Aeneid, and Georgics Of Vergil*. Ginn & Co. Boston.

Gulliver, A. F., 1977. The spectrum variations of Pleione from 1938 to 1975. *ApJS*, **35**, 441–459.

Guzik, J. A., Houdek, G., Chaplin, W. J., Smalley, B., Kurtz, D. W. et al., 2016. Detection of Solar-like Oscillations, Observational Constraints, and Stellar Models for theta Cyg, the Brightest Star Observed By the Kepler Mission. *ApJ*, **831**, 17.

Hadden, S. & Lithwick, Y., 2014. Densities and Eccentricities of 139 Kepler Planets from Transit Time Variations. *ApJ*, **787**, 80.

Hale, G. E., 1919. Preliminary Results of a Comparative Test of the 60-inch and 100-inch Telescopes of the Mount Wilson Observatory. *PASP*, **31**, 257.

Hamy, M., 1899. Mémoires et observations. Sur la mesure interférentielle des petits diamètres application aux satellites de Jupiter et à Vesta. *Bulletin Astronomique, Serie I*, **16**, 257–274.

Han, I., Lee, B.-C., Kim, K.-M. & Mkrtichian, D. E., 2008. Confirmation of the Exoplanet around β GEM from the RV Observations Using Boes. *Journal of Korean Astronomical Society*, **41**, 59–64.

Hanbury Brown, R., Davis, J. & Allen, L. R., 1967. The stellar interferometer at Narrabri Observatory I. A. description of the instrument and the observational procedure. *MNRAS*, **137**, 375.

Hands, T. O. & Alexander, R. D., 2016. There might be giants: unseen Jupiter-mass planets as sculptors of tightly packed planetary systems. *MNRAS*, **456**, 4121–4127.

Hands, T. O., Alexander, R. D. & Dehnen, W., 2014. Understanding the assembly of Kepler's compact planetary systems. *MNRAS*, **445**, 749–760.

Haniff, C. A. & Buscher, D. F., 1992. Diffraction-limited imaging with partially redundant masks. I. Infrared imaging of bright objects. *Journal of the Optical Society of America A*, **9**, 203–218.

Haniff, C. A. & Wilson, R. W., 1994. Closure-phase imaging with partial adaptive correction. *PASP*, **106**, 1003–1014.

Hartmann, L., Herczeg, G. & Calvet, N., 2016. Accretion onto Pre-Main-Sequence Stars. *ARA&A*, **54**, 135–180.

Hatzes, A. P., 2014. The role of space telescopes in the characterization of transiting exoplanets. *Nature*, **513**, 353–357.

Hatzes, A. P. & Cochran, W. D., 1993. Long-period radial velocity variations in three K giants. *ApJ*, **413**, 339–348.

Hatzes, A. P., Cochran, W. D., Endl, M., Guenther, E. W., Saar, S. H., Walker, G. A. H., Yang, S., Hartmann, M., Esposito, M., Paulson, D. B. & Döllinger, M. P., 2006. Confirmation of the planet hypothesis for the long-period radial velocity variations of β Geminorum. *A&A*, **457**, 335–341.

Hawkins, K., Jofré, P., Heiter, U., Soubiran, C., Blanco-Cuaresma, S., Casagrande, L., Gilmore, G., Lind, K., Magrini, L., Masseron, T., Pancino, E., Randich, S. & Worley, C. C., 2016a. Gaia FGK benchmark stars: new candidates at low metallicities. *A&A*, **592**, A70.

Hawkins, K., Masseron, T., Jofré, P., Gilmore, G., Elsworth, Y. & Hekker, S., 2016b. An accurate and self-consistent chemical abundance catalogue for the APOGEE/Kepler sample. *A&A*, **594**, A43.

Hayward, T. L., Brandl, B., Pirger, B., Blacken, C., Gull, G. E., Schoenwald, J. & Houck, J. R., 2001. PHARO: A Near-Infrared Camera for the Palomar Adaptive Optics System. *PASP*, **113**, 105–118.

Haywood, R. D., Collier Cameron, A., Queloz, D., Barros, S. C. C., Deleuil, M., Fares, R., Gillon, M., Lanza, A. F., Lovis, C., Moutou, C., Pepe, F., Pollacco, D., Santerne, A., Ségransan, D. & Unruh, Y. C., 2014. Planets and stellar activity: hide and seek in the CoRoT-7 system. *MNRAS*, **443**, 2517–2531.

Heintz, W. D., 1978. Reexamination of suspected unresolved binaries. *ApJ*, **220**, 931–934.

Hekker, S., Kallinger, T., Baudin, F., De Ridder, J., Barban, C., Carrier, F., Hatzes, A. P., Weiss, W. W. & Baglin, A., 2009. Characteristics of solar-like oscillations in red giants observed in the CoRoT exoplanet field. *A&A*, **506**, 465–469.

Henroteau, F., 1920. A spectrographic study of early class B stars, II. *Publications of the Dominion Observatory Ottawa*, **5**, 45–88.

Henry, G. W., Marcy, G., Butler, R. P. & Vogt, S. S., 1999. HD 209458. *IAU Circ.*, **7307**.

Henry, G. W., Marcy, G. W., Butler, R. P. & Vogt, S. S., 2000. A Transiting "51 Peg-like" Planet. *ApJ*, **529**, L41–L44.

Herbig, G. H., 1962. The properties and problems of T Tauri stars and related objects. *Advances in Astronomy and Astrophysics*, **1**, 47–103.

Hevelius, J. & Horrocks, J., 1662. *Iohannis Hevelii Mercurius in Sole visus Gedani, anno christiano observationibus, rarisque phaenomenis : Cui annexa est, Venus in Sole MDCLXI, d. III Maii, St. n. cum aliis quibusdam rerum coelestium pariter visa, anno 1639, d. 24 Nov. St. V. ... a Ieremia Horroxio ... : quibus accedit succincta historiola, novae illius, ac mirae stellae in collo Ceti, certis anni temporibus clare admodum affulgentis, rursus omnino evanescentis ....*

Hidas, M. G., Ashley, M. C. B., Webb, J. K., Irwin, M., Phillips, A., Toyozumi, H., Derekas, A., Christiansen, J. L., Nutto, C. & Crothers, S., 2005. The University of New South Wales Extrasolar Planet Search: methods and first results from a field centred on NGC 6633. *MNRAS*, **360**, 703–717.

Hildebrandt, G., 1992. Rapid oscillations of five stars in the spectral range A and F. I. *As-*

tronomische Nachrichten, **313**, 233–241.

Hinkley, S., Monnier, J. D., Oppenheimer, B. R., Roberts, Jr., L. C., Ireland, M. et al., 2011a. Establishing α Oph as a Prototype Rotator: Improved Astrometric Orbit. *ApJ*, **726**, 104.

Hinkley, S., Oppenheimer, B. R., Brenner, D., Parry, I. R., Sivaramakrishnan, A., Soummer, R. & King, D., 2008. A new integral field spectrograph for exoplanetary science at Palomar. In *Adaptive Optics Systems*, vol. 7015 of *Proc. SPIE*, 701519.

Hinkley, S., Oppenheimer, B. R., Zimmerman, N., Brenner, D., Parry, I. R. et al., 2011b. A New High Contrast Imaging Program at Palomar Observatory. *PASP*, **123**, 74.

Hinkley, S., Pope, B., Martinache, F., Hillenbrand, L., Kraus, A. L., Ireland, M., Oppenheimer, B. R., Rice, E. L., Monnier, J. D., Tuthill, P. & Latyshev, A., 2015. The Surprising Outburst Behavior of Z Canis Majoris, and Resolving the Alpha Oph Companion Near the Diffraction limit. In *American Astronomical Society Meeting Abstracts*, vol. 225 of *American Astronomical Society Meeting Abstracts*, 313.02.

Hirano, T., Fukui, A., Mann, A. W., Sanchis-Ojeda, R., Gaidos, E. et al., 2016a. The K2-ESPRINT Project III: A Close-in Super-Earth around a Metal-rich Mid-M Dwarf. *ApJ*, **820**, 41.

Hirano, T., Nowak, G., Kuzuhara, M., Palle, E., Dai, F. et al., 2016b. The K2-ESPRINT Project IV: A Hot Jupiter in a Prograde Orbit with a Possible Stellar Companion. *ArXiv e-prints*.

Hirata, R., 2007. Disk Precession in Pleione. In A. T. Okazaki, S. P. Owocki & S. Stefl, eds., *Active OB-Stars: Laboratories for Stellare and Circumstellar Physics*, vol. 361 of *Astronomical Society of the Pacific Conference Series*, 267.

Hjørringgaard, J. G., Silva Aguirre, V., White, T. R., Huber, D., Pope, B. J. S., Casagrande, L., Justesen, A. B. & Christensen-Dalsgaard, J., 2017. Testing stellar evolution models with the retired A star HD 185351. *MNRAS*, **464**, 3713–3719.

Hogg, D. W., Angus, R., Barclay, T., Dawson, R., Fergus, R., Foreman-Mackey, D., Harmeling, S., Hirsch, M., Lang, D., Montet, B. T., Schiminovich, D. & Schölkopf, B., 2013. Maximizing Kepler science return per telemetered pixel: Detailed models of the focal plane in the two-wheel era. *ArXiv e-prints*.

Holman, M. J., Fabrycky, D. C., Ragozzine, D., Ford, E. B., Steffen, J. H. et al., 2010. Kepler-9: A System of Multiple Planets Transiting a Sun-Like Star, Confirmed by Timing Variations. *Science*, **330**, 51.

Holman, M. J. & Murray, N. W., 2005. The Use of Transit Timing to Detect Terrestrial-Mass Extrasolar Planets. *Science*, **307**, 1288–1291.

Houdek, G. & Gough, D. O., 2011. On the seismic age and heavy-element abundance of the Sun. *MNRAS*, **418**, 1217–1230.

Howell, S. B., 1989. Two-dimensional aperture photometry - Signal-to-noise ratio of point-source observations and optimal data-extraction techniques. *PASP*, **101**, 616–622.

Howell, S. B., Sobeck, C., Haas, M., Still, M., Barclay, T. et al., 2014. The K2 Mission: Characterization and Early Results. *PASP*, **126**, 398–408.

Hoyle, F., 1960. The Origin of the Solar Nebula. *QQJRAS*, **1**, 28.

Huang, S.-S., 1959. The Problem of Life in the Universe and the Mode of Star Formation. *PASP*, **71**, 421.

Huat, A.-L., Hubert, A.-M., Baudin, F., Floquet, M., Neiner, C. et al., 2009. The B0.5IVe CoRoT target HD 49330. I. Photometric analysis from CoRoT data. *A&A*, **506**, 95–101.

Hubble, E., 1929. A Relation between Distance and Radial Velocity among Extra-Galactic Nebulae. *Proceedings of the National Academy of Science*, **15**, 168–173.

Huber, D., Bedding, T. R., Stello, D., Hekker, S., Mathur, S. et al., 2011. Testing Scaling Relations for Solar-like Oscillations from the Main Sequence to Red Giants Using Kepler Data. *ApJ*, **743**, 143.

Huber, D. & Bryson, S. T., 2015. K2: Extending Kepler's Power to the Ecliptic. Ecliptic Plane Input Catalog.

Huber, D., Chaplin, W. J., Christensen-Dalsgaard, J., Gilliland, R. L., Kjeldsen, H. et al., 2013a. Fundamental Properties of Kepler Planet-candidate Host Stars using Asteroseismology. *ApJ*, **767**, 127.

Huber, D., Chaplin, W. J., Christensen-Dalsgaard, J., Gilliland, R. L., Kjeldsen, H. et al., 2013b. Fundamental Properties of Kepler Planet-candidate Host Stars using Asteroseismology. *ApJ*, **767**, 127.

Huber, D., Ireland, M. J., Bedding, T. R., Brandão, I. M., Piau, L. et al., 2012. Fundamental Properties of Stars Using Asteroseismology from Kepler and CoRoT and Interferometry from the CHARA Array. *ApJ*, **760**, 32.

Huber, D., Stello, D., Bedding, T. R., Chaplin, W. J., Arentoft, T., Quirion, P.-O. & Kjeldsen, H., 2009. Automated extraction of oscillation parameters for Kepler observations of solar-type stars. *Communications in Asteroseismology*, **160**, 74–91.

Huggins, W. & Miller, W. A., 1864. On the Spectra of Some of the Fixed Stars. *Philosophical Transactions of the Royal Society of London Series I*, **154**, 413–435.

Hummel, W., 1998. On the spectacular variations of Be stars. Evidence for a temporarily tilted circumstellar disk. *A&A*, **330**, 243–252.

Huygens, C., 1678. Traité de la Lumière.

Ida, S. & Lin, D. N. C., 2004. Toward a Deterministic Model of Planetary Formation. II. The Formation and Retention of Gas Giant Planets around Stars with a Range of Metallicities. *ApJ*, **616**, 567–572.

Ida, S. & Lin, D. N. C., 2008. Toward a Deterministic Model of Planetary Formation. V. Accumulation Near the Ice Line and Super-Earths. *ApJ*, **685**, 584–595.

Ireland, M. J., 2013. Phase errors in diffraction-limited imaging: contrast limits for sparse aperture masking. *MNRAS*, **433**, 1718–1728.

Ireland, M. J. & Kraus, A. L., 2014. Orbital Motion and Multi-Wavelength Monitoring of LkCa15 b. In M. Booth, B. C. Matthews & J. R. Graham, eds., *IAU Symposium*, vol. 299 of *IAU Symposium*, 199–203.

Izidoro, A., Ogihara, M., Raymond, S. N., Morbidelli, A., Pierens, A., Bitsch, B., Cossou, C. & Hersant, F., 2017. Breaking the Chains: Hot Super-Earth systems from migration and disruption of compact resonant chains. *ArXiv e-prints*.

Jacob, W. S., 1855. On certain Anomalies presented by the Binary Star 70 Ophiuchi. *MNRAS*, **15**, 228.

Jansky, K. G., 1933. Radio Waves from Outside the Solar System. *Nature*, **132**, 66.

Jarad, M. M., Hilditch, R. W. & Skillen, I., 1989. A radial-velocity study of 18 emission-line

B stars. *MNRAS*, **238**, 1085–1106.

Jeans, J. H., 1942. Origin of the Solar System. *Nature*, **149**, 695.

Jeffreys, H., 1929. Collision and the origin of rotation in the solar system. *MNRAS*, **89**, 636.

Jehin, E., Gillon, M., Queloz, D., Magain, P., Manfroid, J., Chantry, V., Lendl, M., Hutsemékers, D. & Udry, S., 2011. TRAPPIST: TRAnsiting Planets and PlanetesImals Small Telescope. *The Messenger*, **145**, 2–6.

Jenkins, J. M., Twicken, J. D., Batalha, N. M., Caldwell, D. A., Cochran, W. D. et al., 2015. Discovery and Validation of Kepler-452b: A 1.6 $R_\oplus$ Super Earth Exoplanet in the Habitable Zone of a G2 Star. *AJ*, **150**, 56.

Jenkins, J. M., Witteborn, F., Koch, D. G., Dunham, E. W., Borucki, W. J., Updike, T. F., Skinner, M. A. & Jordan, S. P., 2000. Processing CCD images to detect transits of Earth-sized planets: maximizing sensitivity while achieving reasonable downlink requirements. In J. B. Breckinridge & P. Jakobsen, eds., *UV, Optical, and IR Space Telescopes and Instruments*, vol. 4013 of *Proc. SPIE*, 520–531.

Jennison, R. C., 1958. A phase sensitive interferometer technique for the measurement of the Fourier transforms of spatial brightness distributions of small angular extent. *MNRAS*, **118**, 276–+.

Johnson, H. L. & Morgan, W. W., 1953. Fundamental stellar photometry for standards of spectral type on the revised system of the Yerkes spectral atlas. *ApJ*, **117**, 313.

Johnson, J. A., Huber, D., Boyajian, T., Brewer, J. M., White, T. R., von Braun, K., Maestro, V., Stello, D. & Barclay, T., 2014. The Physical Parameters of the Retired a Star HD 185351. *ApJ*, **794**, 15.

Jones, E., Oliphant, T., Peterson, P. & Others, 2001. SciPy: Open source scientific tools for Python. URL `http://www.scipy.org/`.

Joy, A. H., 1942. Spectral Criteria in the Classification of Variable Stars. *PASP*, **54**, 15.

Joy, A. H., 1945. T Tauri Variable Stars. *ApJ*, **102**, 168.

Kallinger, T., Iliev, I., Lehmann, H. & Weiss, W. W., 2004. The puzzling Maia candidate star α Draconis. In J. Zverko, J. Ziznovsky, S. J. Adelman & W. W. Weiss, eds., *The A-Star Puzzle*, vol. 224 of *IAU Symposium*, 848–852.

Kallinger, T., Reegen, P. & Weiss, W. W., 2002. The MAIA candidate star HD 208727. *A&A*, **388**, L37–L39.

Kane, S. R., Henry, G. W., Dragomir, D., Fischer, D. A., Howard, A. W., Wang, X. & Wright, J. T., 2011. Revised Orbit and Transit Exclusion for HD 114762b. *ApJ*, **735**, L41.

Kant, I., 1755. *Allgemeine Naturgeschichte und Theorie des Himmels*. Works. Fischer. URL `https://books.google.co.uk/books?id=nCcaAQAAMAAJ`.

Kardashev, N. S., 1964. Transmission of Information by Extraterrestrial Civilizations. *Soviet Astronomy*, **8**, 217.

Kasting, J., 2010. *How to Find a Habitable Planet*. Science Essentials. Princeton University Press. ISBN 9780691138053. URL `https://books.google.co.uk/books?id=xPqEeB-SRvUC`.

Kawahara, H., Matsuo, T., Takami, M., Fujii, Y., Kotani, T., Murakami, N., Tamura, M. & Guyon, O., 2012. Can Ground-based Telescopes Detect the Oxygen 1.27 μm Absorption Feature as a Biomarker in Exoplanets? *ApJ*, **758**, 13.

Kaye, A. B., Handler, G., Krisciunas, K., Poretti, E. & Zerbi, F. M., 1999. Gamma

Doradus Stars: Defining a New Class of Pulsating Variables. *PASP*, **111**, 840–844.

Kee, N., Owocki, S., Townsend, R. & Müller, H.-R., 2014. Pulsational Mass Ejection in Be Star Disks. *ArXiv e-prints*.

Khinchin, A., 1934. Korrelationstheorie der stationären stochastischen Prozesse. *Mathematische Annalen*, **109**(1), 604–615. ISSN 1432-1807. URL http://dx.doi.org/10.1007/BF01449156.

Kipping, D. M., 2008. Transiting planets - light-curve analysis for eccentric orbits. *MNRAS*, **389**, 1383–1390.

Kirchhoff, G., 1882. Zur Theorie der Lichtstrahlen. *Annalen der Physik*, **254**, 663–695.

Kjeldsen, H. & Bedding, T. R., 1995. Amplitudes of stellar oscillations: the implications for asteroseismology. *A&A*, **293**, 87–106.

Kley, W. & Nelson, R. P., 2012. Planet-Disk Interaction and Orbital Evolution. *ARA&A*, **50**, 211–249.

Koch, D., Witteborn, F., Dunham, E., Jenkins, J., Borucki, W. & Webster, W., 1999. The AMES Photometric Testbed for the Kepler Mission. In *AAS/Division for Planetary Sciences Meeting Abstracts #31*, vol. 31 of *AAS/Division for Planetary Sciences Meeting Abstracts*, 09.03.

Koch, D. G., Borucki, W. J., Basri, G., Batalha, N. M., Brown, T. M. et al., 2010. Kepler Mission Design, Realized Photometric Performance, and Early Science. *ApJ*, **713**, L79–L86.

Kokubo, E. & Ida, S., 1998. Oligarchic Growth of Protoplanets. *Icarus*, **131**, 171–178.

Kokubo, E. & Ida, S., 2000. Formation of Protoplanets from Planetesimals in the Solar Nebula. *Icarus*, **143**, 15–27.

Kolenberg, K., Bryson, S., Szabó, R., Kurtz, D. W., Smolec, R. et al., 2011. Kepler photometry of the prototypical Blazhko star RR Lyr: an old friend seen in a new light. *MNRAS*, **411**, 878–890.

Kolodziejczak, J. & Caldwell, D., 2011. Science from Kepler Collateral Data: 150 ksec/year from 13 Million Stars? Tech. Rep. 20120003045, NASA Marshall Space Flight Centre. URL http://ntrs.nasa.gov/archive/nasa/casi.ntrs.nasa.gov/20120003045.pdf.

Kovács, G., Zucker, S. & Mazeh, T., 2002. A box-fitting algorithm in the search for periodic transits. *A&A*, **391**, 369–377.

Koyre, A., 1957. *From the Closed World to the Infinite Universe*. From the closed world to the infinite universe. Johns Hopkins University Press. ISBN 9780801803475. URL https://books.google.co.uk/books?id=5e3ECWvkJOwC.

Kratter, K. & Lodato, G., 2016. Gravitational Instabilities in Circumstellar Disks. *ARA&A*, **54**, 271–311.

Kratter, K. M., Murray-Clay, R. A. & Youdin, A. N., 2010. The Runts of the Litter: Why Planets Formed Through Gravitational Instability Can Only Be Failed Binary Stars. *ApJ*, **710**, 1375–1386.

Kraus, A. L. & Ireland, M. J., 2012. LkCa 15: A Young Exoplanet Caught at Formation? *ApJ*, **745**, 5.

Krige, D. G., 1951. A Statistical Approach to Some Basic Mine Valuation Problems on the Witwatersrand. *Journal of the Chemical, Metallurgical and Mining Society of South Africa*, **52**(6), 119–139. URL http://dx.doi.org/10.2307/3006914.

Krist, J. E., Balasubramanian, K., Beichman, C. A., Echternach, P. M., Green, J. J.,

Liewer, K. M., Muller, R. E., Serabyn, E., Shaklan, S. B., Trauger, J. T., Wilson, D. W., Horner, S. D., Mao, Y., Somerstein, S. F., Vasudevan, G., Kelly, D. M. & Rieke, M. J., 2009. The JWST/NIRCam coronagraph: mask design and fabrication. In *Techniques and Instrumentation for Detection of Exoplanets IV*, vol. 7440 of *Proc. SPIE*, 74400W.

Krist, J. E., Beichman, C. A., Trauger, J. T., Rieke, M. J., Somerstein, S., Green, J. J., Horner, S. D., Stansberry, J. A., Shi, F., Meyer, M. R., Stapelfeldt, K. R. & Roellig, T. L., 2007. Hunting planets and observing disks with the JWST NIRCam coronagraph. In *Techniques and Instrumentation for Detection of Exoplanets III*, vol. 6693 of *Proc. SPIE*, 66930H.

Kurtz, D. W., Shibahashi, H., Murphy, S. J., Bedding, T. R. & Bowman, D. M., 2015. A unifying explanation of complex frequency spectra of γ Dor, SPB and Be stars: combination frequencies and highly non-sinusoidal light curves. *MNRAS*, **450**, 3015–3029.

Labeyrie, A., 1970. Attainment of Diffraction Limited Resolution in Large Telescopes by Fourier Analysing Speckle Patterns in Star Images. *A&A*, **6**, 85.

Labeyrie, A., 1975. Interference fringes obtained on VEGA with two optical telescopes. *ApJ*, **196**, L71–L75.

Labeyrie, A., Lipson, S. & Nisenson, P., 2006. *An Introduction to Optical Stellar Interferometry*. Cambridge University Press, Cambridge, Cambridgeshire, UK. ISBN 978090521082872-7.

Lafrenière, D., Marois, C., Doyon, R., Nadeau, D. & Artigau, É., 2007. A New Algorithm for Point-Spread Function Subtraction in High-Contrast Imaging: A Demonstration with Angular Differential Imaging. *ApJ*, **660**, 770–780.

Langlois, M., Dohlen, K., Vigan, A., Zurlo, A., Moutou, C. et al., 2014. High contrast polarimetry in the infrared with SPHERE on the VLT. In *Society of Photo-Optical Instrumentation Engineers (SPIE) Conference Series*, vol. 9147 of *Society of Photo-Optical Instrumentation Engineers (SPIE) Conference Series*, 1.

Lannes, A., 1991. Phase and amplitude calibration in aperture synthesis. Algebraic structures. *Inverse Problems*, **7**, 261–298.

Laplace, P.-S., 1796. *Exposition du système du monde*. Works. Fischer. URL `http://books.google.com/books?id=f7Kv2iFUNJoC&hl`.

Lardner, D., 1875. *Handbook of Astronomy, 4th edition*.

Latham, D. W., 2012. The unseen companion of HD 114762. *New Astron. Rev.*, **56**, 16–18.

Latham, D. W., Stefanik, R. P., Mazeh, T., Mayor, M. & Burki, G., 1989. The unseen companion of HD114762 - A probable brown dwarf. *Nature*, **339**, 38–40.

Laughlin, G. & Adams, F. C., 2000. The Frozen Earth: Binary Scattering Events and the Fate of the Solar System. *Icarus*, **145**, 614–627.

Lawson, P. R., Cotton, W. D., Hummel, C. A., Monnier, J. D., Zhao, M., Young, J. S., Thorsteinsson, H., Meimon, S. C., Mugnier, L. M., Le Besnerais, G., Thiebaut, E. M. & Tuthill, P. G., 2004. An interferometry imaging beauty contest. In W. A. Traub, ed., *New Frontiers in Stellar Interferometry*, vol. 5491 of *Proc. SPIE*, 886.

Leavitt, H. S., 1908. 1777 variables in the Magellanic Clouds. *Annals of Harvard College Observatory*, **60**, 87–108.3.

Leavitt, H. S. & Pickering, E. C., 1912. Periods of 25 Variable Stars in the Small Magellanic Cloud. *Harvard College Observatory Circular*, **173**, 1–3.

LeCun, Y., Bengio, Y. & Hinton, G., 2015. Deep learning. *Nature*, **521**, 436–444.

Lee, L. H., Baker, G. J. & Benson, R. S., 2006. Correctability limitations imposed by plane-wave scintillation in multiconjugate adaptive optics. *Journal of the Optical Society of America A*, **23**, 2602–2612.

Léger, A., Defrère, D., Malbet, F., Labadie, L. & Absil, O., 2015. Impact of η_{Earth} on the Capabilities of Affordable Space Missions to Detect Biosignatures on Extrasolar Planets. *ApJ*, **808**, 194.

Léger, A., Rouan, D., Schneider, J., Barge, P., Fridlund, M. et al., 2009. Transiting exoplanets from the CoRoT space mission. VIII. CoRoT-7b: the first super-Earth with measured radius. *A&A*, **506**, 287–302.

Lehmann, H., Scholz, G., Hildebrandt, G., Klose, S., Panov, K. P., Reimann, H.-G., Woche, M. & Ziener, R., 1995. Variability investigations of possible Maia stars. *A&A*, **300**, 783.

Lenz, P. & Breger, M., 2005. Period04 User Guide. *Communications in Asteroseismology*, **146**, 53–136.

Lewis, J. S., 1974. The temperature gradient in the solar nebula. *Science*, **186**, 440–443.

Libralato, M., Bedin, L. R., Nardiello, D. & Piotto, G., 2016. A PSF-based approach to Kepler/K2 data - I. Variability within the K2 Campaign 0 star clusters M 35 and NGC 2158. *MNRAS*, **456**, 1137–1162.

Liebes, S., 1964. Gravitational Lenses. *Physical Review*, **133**, 835–844.

Lillo-Box, J., Demangeon, O., Santerne, A., Barros, S. C. C., Barrado, D. et al., 2016. EPIC210957318b and EPIC212110888b: two inflated hot-Jupiters around Solar-type stars. *ArXiv e-prints*.

Lin, D. N. C., Bodenheimer, P. & Richardson, D. C., 1996. Orbital migration of the planetary companion of 51 Pegasi to its present location. *Nature*, **380**, 606–607.

Lin, D. N. C. & Papaloizou, J., 1985. On the dynamical origin of the solar system. In D. C. Black & M. S. Matthews, eds., *Protostars and Planets II*, 981–1072.

Lineweaver, C. H. & Chopra, A., 2012. The Habitability of Our Earth and Other Earths: Astrophysical, Geochemical, Geophysical, and Biological Limits on Planet Habitability. *Annual Review of Earth and Planetary Sciences*, **40**, 597–623.

Lissauer, J. J., 1987. Timescales for planetary accretion and the structure of the protoplanetary disk. *Icarus*, **69**, 249–265.

Lissauer, J. J., Dawson, R. I. & Tremaine, S., 2014a. Advances in exoplanet science from Kepler. *Nature*, **513**, 336–344.

Lissauer, J. J., Fabrycky, D. C., Ford, E. B., Borucki, W. J., Fressin, F. et al., 2011. A closely packed system of low-mass, low-density planets transiting Kepler-11. *Nature*, **470**, 53–58.

Lissauer, J. J., Marcy, G. W., Bryson, S. T., Rowe, J. F., Jontof-Hutter, D., Agol, E., Borucki, W. J., Carter, J. A., Ford, E. B., Gilliland, R. L., Kolbl, R., Star, K. M., Steffen, J. H. & Torres, G., 2014b. Validation of Kepler's Multiple Planet Candidates. II. Refined Statistical Framework and Descriptions of Systems of Special Interest. *ApJ*, **784**, 44.

Lissauer, J. J., Marcy, G. W., Rowe, J. F., Bryson, S. T., Adams, E. et al., 2012. Almost All of Kepler's Multiple-planet Candidates Are Planets. *ApJ*, **750**, 112.

Lloyd, H., 1834. Unknown title: Lloyd's Mirror. *Transactions of the Royal Irish Academy*, **17**.

Lomb, N. R., 1976. Least-squares frequency analysis of unequally spaced data. *Ap&SS*, **39**, 447–462.

Lovelock, J. E., 1965. A Physical Basis for Life Detection Experiments. *Nature*, **207**, 568–570.

Luger, R., Agol, E., Kruse, E., Barnes, R., Becker, A., Foreman-Mackey, D. & Deming, D., 2016. EVEREST: Pixel Level Decorrelation of K2 Light Curves. *AJ*, **152**, 100.

Luger, R., Kruse, E., Foreman-Mackey, D., Agol, E. & Saunders, N., 2017. An update to the EVEREST K2 pipeline: Short cadence, saturated stars, and Kepler-like photometry down to Kp = 15. *ArXiv e-prints*.

Lund, M. N., Handberg, R., Davies, G. R., Chaplin, W. J. & Jones, C. D., 2015. K2P^2– A Photometry Pipeline for the K2 Mission. *ApJ*, **806**, 30.

Lund, M. N., Silva Aguirre, V., Davies, G. R., Chaplin, W. J., Christensen-Dalsgaard, J. et al., 2016. Standing on the shoulders of Dwarfs: the *Kepler* asteroseismic LEGACY sample I - oscillation mode parameters. *ArXiv e-prints*.

Lynden-Bell, D. & Pringle, J. E., 1974. The evolution of viscous discs and the origin of the nebular variables. *MNRAS*, **168**, 603–637.

Lyot, B., 1930. La couronne solaire étudiée en dehors des éclipses. *Bulletin Astronomique*, **6**, 305–316.

Lyot, B., 1939. The study of the solar corona and prominences without eclipses (George Darwin Lecture, 1939). *MNRAS*, **99**, 580.

Lyttleton, R. A., 1961. An accretion hypothesis for the origin of the solar system. *MNRAS*, **122**, 399.

Macintosh, B., Graham, J. R., Ingraham, P., Konopacky, Q., Marois, C. et al., 2014. First light of the Gemini Planet Imager. *Proceedings of the National Academy of Science*, **111**, 12661–12666.

Macintosh, B. A., Graham, J. R., Palmer, D. W., Doyon, R., Dunn, J., Gavel, D. T., Larkin, J., Oppenheimer, B., Saddlemyer, L., Sivaramakrishnan, A., Wallace, J. K., Bauman, B., Erickson, D. A., Marois, C., Poyneer, L. A. & Soummer, R., 2008. The Gemini Planet Imager: from science to design to construction. In *Adaptive Optics Systems*, vol. 7015 of *Proc. SPIE*, 701518.

Mackay, C. D. & Baldwin, J. E., 1988. The COAST interferometer project. In F. Merkle, ed., *European Southern Observatory Conference and Workshop Proceedings*, vol. 29 of *European Southern Observatory Conference and Workshop Proceedings*, 935–938.

Mackay, D. J. C., 2003. *Information Theory, Inference and Learning Algorithms*.

Mallén-Ornelas, G., Seager, S., Yee, H. K. C., Minniti, D., Gladders, M. D., Mallén-Fullerton, G. M. & Brown, T. M., 2003. The EXPLORE Project. I. A Deep Search for Transiting Extrasolar Planets. *ApJ*, **582**, 1123–1140.

Mamajek, E., 2016. Cumulative Number of Exoplanets Discoveries Versus Time. URL `https://figshare.com/articles/Cumulative_Number_of_Exoplanets_Discoveries_Versus_Time/4057704`.

Mandel, K. & Agol, E., 2002. Analytic Light Curves for Planetary Transit Searches. *ApJ*, **580**, L171–L175.

Mann, A. W., Gaidos, E., Mace, G. N., Johnson, M. C., Bowler, B. P., LaCourse, D., Jacobs, T. L., Vanderburg, A., Kraus, A. L., Kaplan, K. F. & Jaffe, D. T., 2016a.

Zodiacal Exoplanets in Time (ZEIT). I. A Neptune-sized Planet Orbiting an M4.5 Dwarf in the Hyades Star Cluster. *ApJ*, **818**, 46.

Mann, A. W., Newton, E. R., Rizzuto, A. C., Irwin, J., Feiden, G. A., Gaidos, E., Mace, G. N., Kraus, A. L., James, D. J., Ansdell, M., Charbonneau, D., Covey, K. R., Ireland, M. J., Jaffe, D. T., Johnson, M. C., Kidder, B. & Vanderburg, A., 2016b. Zodiacal Exoplanets in Time (ZEIT) III: A Neptune-sized planet orbiting a pre-main-sequence star in the Upper Scorpius OB Association. *ArXiv e-prints*.

Marcy, G. W. & Butler, R. P., 1996. A Planetary Companion to 70 Virginis. *ApJ*, **464**, L147.

Marcy, G. W. & Butler, R. P., 2000. Planets Orbiting Other Suns. *PASP*, **112**, 137–140.

Martinache, F., 2010. Kernel Phase in Fizeau Interferometry. *ApJ*, **724**, 464–469.

Martinache, F., 2011. Kernel-phases for high-contrast detection beyond the resolution limit. In *Society of Photo-Optical Instrumentation Engineers (SPIE) Conference Series*, vol. 8151 of *Society of Photo-Optical Instrumentation Engineers (SPIE) Conference Series*.

Martinache, F., 2013a. Super resolution imaging with an ELT: Kernel-phase interferometry. In S. Esposito & L. Fini, eds., *Proceedings of the Third AO4ELT Conference*, 6.

Martinache, F., 2013b. The Asymmetric Pupil Fourier Wavefront Sensor. *PASP*, **125**, 422–430.

Martinache, F. & Guyon, O., 2009. The Subaru Coronagraphic Extreme-AO Project. In *Techniques and Instrumentation for Detection of Exoplanets IV*, vol. 7440 of *Proc. SPIE*, 74400O.

Mason, B. D., Hartkopf, W. I., McAlister, H. A. & Sowell, J. R., 1993. ICCD speckle observations of binary stars. IX - A duplicity survey of the Pleiades, Praesepe, and IC 4665 clusters. *AJ*, **106**, 637–641.

Mason, B. D., Wycoff, G. L., Hartkopf, W. I., Douglass, G. G. & Worley, C. E., 2001. The 2001 US Naval Observatory Double Star CD-ROM. I. The Washington Double Star Catalog. *AJ*, **122**, 3466–3471.

Matheron, G., 1963. *Traité de Géostatistique Appliquée*. Works. Editions Technip. Paris.

Mawet, D., Milli, J., Wahhaj, Z., Pelat, D., Absil, O., Delacroix, C., Boccaletti, A., Kasper, M., Kenworthy, M., Marois, C., Mennesson, B. & Pueyo, L., 2014. Fundamental Limitations of High Contrast Imaging Set by Small Sample Statistics. *ApJ*, **792**, 97.

Mayor, M., Lovis, C. & Santos, N. C., 2014. Doppler spectroscopy as a path to the detection of Earth-like planets. *Nature*, **513**, 328–335.

Mayor, M. & Queloz, D., 1995. A Jupiter-mass companion to a solar-type star. *Nature*, **378**, 355–359.

Mazeh, T., Nachmani, G., Holczer, T., Fabrycky, D. C., Ford, E. B., Sanchis-Ojeda, R., Sokol, G., Rowe, J. F., Zucker, S., Agol, E., Carter, J. A., Lissauer, J. J., Quintana, E. V., Ragozzine, D., Steffen, J. H. & Welsh, W., 2013. Transit Timing Observations from Kepler. VIII. Catalog of Transit Timing Measurements of the First Twelve Quarters. *ApJS*, **208**, 16.

McAlister, H. A., ten Brummelaar, T. A., Gies, D. R., Huang, W., Bagnuolo, Jr., W. G., Shure, M. A., Sturmann, J., Sturmann, L., Turner, N. H., Taylor, S. F., Berger, D. H., Baines, E. K., Grundstrom, E., Ogden, C., Ridgway, S. T. & van Belle, G., 2005. First Results from the CHARA Array. I. An Interferometric and Spectroscopic Study of the Fast Rotator α Leonis (Regulus). *ApJ*, **628**, 439–452.

McCauliff, S. D., Jenkins, J. M., Catanzarite, J., Burke, C. J., Coughlin, J. L.,

Twicken, J. D., Tenenbaum, P., Seader, S., Li, J. & Cote, M., 2015. Automatic Classification of Kepler Planetary Transit Candidates. *ApJ*, **806**, 6.

McCready, L. L., Pawsey, J. L. & Payne-Scott, R., 1947. Solar Radiation at Radio Frequencies and Its Relation to Sunspots. *Proceedings of the Royal Society of London Series A*, **190**, 357–375.

McGraw, J. T., Dunham, D. W., Evans, D. S. & Moffett, T. J., 1974. Occultations of the Pleiades: photoelectric observations at Tonantzintla with a discussion of the duplicity of Atlas. *AJ*, **79**, 1299–1303.

McNamara, B. J., 1985. Maia variables and upper-main-sequence phenomena. *ApJ*, **289**, 213–219.

McNamara, B. J., 1987. Light variability among the late type B Pleiades stars. *ApJ*, **312**, 778–783.

McNamara, B. J., Jackiewicz, J. & McKeever, J., 2012. The Classification of Kepler B-star Variables. *AJ*, **143**, 101.

McNulty, R., 1960. Bruno at Oxford. *Renaissance News*, **13**(4), 300–305. ISSN 0277903X. URL `http://www.jstor.org/stable/2857769`.

Melis, C., Reid, M. J., Mioduszewski, A. J., Stauffer, J. R. & Bower, G. C., 2014. A VLBI resolution of the Pleiades distance controversy. *Science*, **345**, 1029–1032.

Menger, K. & Sutton, R. M., 1952. You Will Like Geometry. *American Journal of Physics*, **20**, 521–521.

Merrill, P. W., 1922. Interferometer observations of double stars. *ApJ*, **56**.

Metcalfe, T. S., Chaplin, W. J., Appourchaux, T., García, R. A., Basu, S. et al., 2012. Asteroseismology of the Solar Analogs 16 Cyg A and B from Kepler Observations. *ApJ*, **748**, L10.

Michell, J., 1767. An Inquiry into the Probable Parallax, and Magnitude of the Fixed Stars, from the Quantity of Light Which They Afford us, and the Particular Circumstances of Their Situation, by the Rev. John Michell, B. D. F. R. S. *Philosophical Transactions*, **57**, 234–264. URL `http://rstl.royalsocietypublishing.org/content/57/234.short`.

Michelson, A. A., 1891a. Measurement of Jupiter's Satellites by Interference. *Nature*, **45**, 160–161.

Michelson, A. A., 1891b. Visibility of Interference-Fringes in the Focus of a Telescope. *PASP*, **3**, 217–220.

Michelson, A. A. & Morley, E. W., 1887. On the Relative Motion of the Earth and of the Luminiferous Ether. *Sidereal Messenger, vol. 6, pp.306-310*, **6**, 306–310.

Michelson, A. A. & Pease, F. G., 1921. Measurement of the diameter of alpha Orionis with the interferometer. *ApJ*, **53**.

Michelson, A. A. & Pease, F. G., 1922. Interferometer Measures of Star Diameters. In *Publications of the American Astronomical Society*, vol. 4 of *Publications of the American Astronomical Society*, 375.

Miglio, A., Chiappini, C., Morel, T., Barbieri, M., Chaplin, W. J., Girardi, L., Montalbán, J., Valentini, M., Mosser, B., Baudin, F., Casagrande, L., Fossati, L., Aguirre, V. S. & Baglin, A., 2013. Galactic archaeology: mapping and dating stellar populations with asteroseismology of red-giant stars. *MNRAS*, **429**, 423–428.

Miglio, A., Montalbán, J., Noels, A. & Eggenberger, P., 2008. Probing the properties of convective cores through g modes: high-order g modes in SPB and γ Doradus stars. *MNRAS*,

386, 1487–1502.

Monnier, J. D., 2007. Phases in interferometry. *New Astron. Rev.*, **51**, 604–616.

Monnier, J. D., Townsend, R. H. D., Che, X., Zhao, M., Kallinger, T., Matthews, J. & Moffat, A. F. J., 2010. Rotationally Modulated g-modes in the Rapidly Rotating δ Scuti Star Rasalhague (α Ophiuchi). *ApJ*, **725**, 1192–1201.

Monnier, J. D., Tuthill, P. G. & Danchi, W. C., 1999. Pinwheel Nebula around WR 98A. *ApJ*, **525**, L97–L100.

Moore, E. H., 1920. The fourteenth western meeting of the American Mathematical Society. *Bull. Amer. Math. Soc.*, **26**(9), 385–396. URL `http://projecteuclid.org/euclid.bams/1183425340`.

Moore, W. B., Lenardic, A., Jellinek, A. M., Johnson, C. L., Goldblatt, C. & Lorenz, R. D., 2017. How habitable zones and super-Earths lead us astray. *Nature Astronomy*, **1**, 0043 EP –. URL `http://dx.doi.org/10.1038/s41550-017-0043`. Comment.

Moravveji, E., Aerts, C., Pápics, P. I., Triana, S. A. & Vandoren, B., 2015. Tight asteroseismic constraints on core overshooting and diffusive mixing in the slowly rotating pulsating B8.3V star KIC 10526294. *A&A*, **580**, A27.

Moravveji, E., Townsend, R. H. D., Aerts, C. & Mathis, S., 2016. Sub-inertial Gravity Modes in the B8V Star KIC 7760680 Reveal Moderate Core Overshooting and Low Vertical Diffusive Mixing. *ApJ*, **823**, 130.

Morbidelli, A., Lunine, J. I., O'Brien, D. P., Raymond, S. N. & Walsh, K. J., 2012. Building Terrestrial Planets. *Annual Review of Earth and Planetary Sciences*, **40**, 251–275.

Morgan, W. W., Keenan, P. C. & Kellman, E., 1943. *An atlas of stellar spectra, with an outline of spectral classification*. The University of Chicago press, Chicago, Ill.

Morton, T. D., Bryson, S. T., Coughlin, J. L., Rowe, J. F., Ravichandran, G., Petigura, E. A., Haas, M. R. & Batalha, N. M., 2016. False Positive Probabilities for all Kepler Objects of Interest: 1284 Newly Validated Planets and 428 Likely False Positives. *ApJ*, **822**, 86.

Morton, T. D. & Johnson, J. A., 2011. On the Low False Positive Probabilities of Kepler Planet Candidates. *ApJ*, **738**, 170.

Mosser, B., Belkacem, K., Goupil, M.-J., Miglio, A., Morel, T., Barban, C., Baudin, F., Hekker, S., Samadi, R., De Ridder, J., Weiss, W., Auvergne, M. & Baglin, A., 2010. Red-giant seismic properties analyzed with CoRoT. *A&A*, **517**, A22.

Motalebi, F., Udry, S., Gillon, M., Lovis, C., Ségransan, D. et al., 2015. The HARPS-N Rocky Planet Search. I. HD 219134 b: A transiting rocky planet in a multi-planet system at 6.5 pc from the Sun. *A&A*, **584**, A72.

Moulton, F. R., 1905. On the Evolution of the Solar System. *ApJ*, **22**, 165.

Moutou, C., Deleuil, M., Guillot, T., Baglin, A., Bordé, P., Bouchy, F., Cabrera, J., Csizmadia, S. & Deeg, H. J., 2013. CoRoT: Harvest of the exoplanet program. *Icarus*, **226**, 1625–1634.

Murphy, S. J., 2014. *Investigating the A-Type Stars Using Kepler Data*. Ph.D. thesis, Univ. of Central Lancashire.

Murphy, S. J., Bedding, T. R. & Shibahashi, H., 2016. A Planet in an 840 Day Orbit around a Kepler Main-sequence A Star Found from Phase Modulation of Its Pulsations. *The Astrophysical*

Journal Letters, **827**(1), L17. URL http://stacks.iop.org/2041-8205/827/i=1/a=L17.

Murphy, S. J., Grigahcène, A., Niemczura, E., Kurtz, D. W. & Uytterhoeven, K., 2012. Pulsational amplitude growth of the star KIC 3429637 (HD 178875) in the context of Am and ρ Pup stars. *MNRAS*, **427**, 1418–1428.

Muterspaugh, M. W., Lane, B. F., Kulkarni, S. R., Konacki, M., Burke, B. F., Colavita, M. M., Shao, M., Hartkopf, W. I., Boss, A. P. & Williamson, M., 2010. The Phases Differential Astrometry Data Archive. V. Candidate Substellar Companions to Binary Systems. *AJ*, **140**, 1657–1671.

Neiner, C., de Batz, B., Cochard, F., Floquet, M., Mekkas, A. & Desnoux, V., 2011. The Be Star Spectra (BeSS) Database. *AJ*, **142**, 149.

Neiner, C., Gutiérrez-Soto, J., Baudin, F., de Batz, B., Frémat, Y. et al., 2009. The pulsations of the B5IVe star HD 181231 observed with CoRoT and ground-based spectroscopy. *A&A*, **506**, 143–151.

Ness, M., Hogg, D. W., Rix, H.-W., Ho, A. Y. Q. & Zasowski, G., 2015. The Cannon: A data-driven approach to Stellar Label Determination. *ApJ*, **808**, 16.

Nesvorný, D., Kipping, D. M., Buchhave, L. A., Bakos, G. Á., Hartman, J. & Schmitt, A. R., 2012. The Detection and Characterization of a Nontransiting Planet by Transit Timing Variations. *Science*, **336**, 1133.

Newton, I., 1730. *Opticks:: Or, A Treatise of the Reflections, Refractions, Inflections and Colours of Light*. Opticks:: Or, A Treatise of the Reflections, Refractions, Inflections and Colours of Light. William Innys at the West-End of St. Paul's. URL https://books.google.co.uk/books?id=GnAFAAAAQAAJ.

Newton, I. & Cotes, R., 1713. *Philosophiae Naturalis Principia Mathematica. Auctore Isaaco Newtono*.

Nittler, L. R. & Ciesla, F., 2016. Astrophysics with Extraterrestrial Materials. *ARA&A*, **54**, 53–93.

Noecker, M. C., Zhao, F., Demers, R., Trauger, J., Guyon, O. & Jeremy Kasdin, N., 2016. Coronagraph instrument for WFIRST-AFTA. *Journal of Astronomical Telescopes, Instruments, and Systems*, **2**(1), 011001.

Norris, B., Schworer, G., Tuthill, P., Jovanovic, N., Guyon, O., Stewart, P. & Martinache, F., 2015. The VAMPIRES instrument: imaging the innermost regions of protoplanetary discs with polarimetric interferometry. *MNRAS*, **447**, 2894–2906.

Norris, B. R. M., Tuthill, P. G., Ireland, M. J., Lacour, S., Zijlstra, A. A., Lykou, F., Evans, T. M., Stewart, P. & Bedding, T. R., 2012. A close halo of large transparent grains around extreme red giant stars. *Nature*, **484**, 220–222.

Oppenheimer, B. R. & Hinkley, S., 2009. High-Contrast Observations in Optical and Infrared Astronomy. *ARA&A*, **47**, 253–289.

Orchiston, W., 2005. Dr Elizabeth Alexander: First Female Radio Astronomer. In W. Orchiston, ed., *The New Astronomy: Opening the Electromagnetic Window and Expanding Our View of Planet Earth*, vol. 334 of *Astrophysics and Space Science Library*, 71.

Osborn, H. P., Armstrong, D. J., Brown, D. J. A., McCormac, J., Doyle, A. P., Louden, T. M., Kirk, J., Spake, J. J., Lam, K. W. F., Walker, S. R., Faedi, F. & Pollacco, D. L., 2016a. Single transit candidates from K2: detection and period estimation. *MNRAS*, **457**,

2273–2286.

Osborn, H. P., Santerne, A., Barros, S. C. C., Armstrong, D. J., Santos, N. C. et al., 2016b. EPIC212521166 b: a Neptune-mass planet with Earth-like density. *ArXiv e-prints*.

Paczynski, B., 1986. Gravitational microlensing by the galactic halo. *ApJ*, **304**, 1–5.

Paine, T., 1794. *The Age of Reason*.

Pál, A., 2008. Properties of analytic transit light-curve models. *MNRAS*, **390**, 281–288.

Pápics, P. I., Moravveji, E., Aerts, C., Tkachenko, A., Triana, S. A., Bloemen, S. & Southworth, J., 2014. KIC 10526294: a slowly rotating B star with rotationally split, quasi-equally spaced gravity modes. *A&A*, **570**, A8.

Pápics, P. I., Tkachenko, A., Aerts, C., Van Reeth, T., De Smedt, K., Hillen, M., Østensen, R. & Moravveji, E., 2015. Asteroseismic Fingerprints of Rotation and Mixing in the Slowly Pulsating B8 V Star KIC 7760680. *ApJ*, **803**, L25.

Pápics, P. I., Tkachenko, A., Van Reeth, T., Aerts, C., Moravveji, E., Van de Sande, M., De Smedt, K., Bloemen, S., Southworth, J., Debosscher, J., Niemczura, E. & Gameiro, J. F., 2017. Signatures of internal rotation discovered in the Kepler data of five slowly pulsating B stars. *A&A*, **598**, A74.

Parviainen, H., 2015. PYTRANSIT: fast and easy exoplanet transit modelling in PYTHON. *MNRAS*, **450**, 3233–3238. URL `http://mnras.oxfordjournals.org/cgi/doi/10.1093/mnras/stv894`.

Parviainen, H., 2016. PyBLS: v0.9. URL `http://dx.doi.org/10.5281/zenodo.45604`.

Parviainen, H., Pope, B. & Aigrain, S., 2016. K2PS: K2 Planet search. Astrophysics Source Code Library.

Patterson, C., 1956. Age of meteorites and the earth. *Geochimica et Cosmochimica Acta*, **10**, 230–237.

Paunzen, E., Handler, G., Weiss, W. W., Nesvacil, N., Hempel, A., Romero-Colmenero, E., Vuthela, F. F., Reegen, P., Shobbrook, R. R. & Kilkenny, D., 2002. On the Period-Luminosity-Colour-Metallicity relation and the pulsational characteristics of lambda Bootis type stars. *A&A*, **392**, 515–528.

Paunzen, E., Wraight, K. T., Fossati, L., Netopil, M., White, G. J. & Bewsher, D., 2013. A photometric study of chemically peculiar stars with the STEREO satellites - II. Non-magnetic chemically peculiar stars. *MNRAS*, **429**, 119–125.

Pawsey, J. L., Payne-Scott, R. & McCready, L. L., 1946. Radio-Frequency Energy from the Sun. *Nature*, **157**, 158–159.

Pearce, J. A. & Hill, G., 1971. Four Suspected Spectroscopic Binaries in the Pleiades. *PASP*, **83**, 493.

Pearson, T. J. & Readhead, A. C. S., 1984. Image Formation by Self-Calibration in Radio Astronomy. *ARA&A*, **22**, 97–130.

Penrose, R., 1955. A generalized inverse for matrices. **51**(3), 406–413. ISSN 0305-0041. URL `https://www.cambridge.org/core/article/generalized-inverse-for-matrices/5F4516D6B9989BB6563A4B267CC7D615`.

Pepper, J., Gillen, E., Parviainen, H., Hillenbrand, L. A., Cody, A. M., Aigrain, S., Stauffer, J., Vrba, F. J., David, T., Lillo-Box, J., Stassun, K. G., Conroy, K. E., Pope, B. J. S. & Barrado, D., 2017. A Low-mass Exoplanet Candidate Detected

by K2 Transiting the Praesepe M Dwarf JS 183. *The Astronomical Journal*, **153**(4), 177. URL http://stacks.iop.org/1538-3881/153/i=4/a=177.

Percy, J. R., 1978. The photometric constancy of Maia (20 Tauri) and related stars. *PASP*, **90**, 703–705.

Percy, J. R. & Wilson, J. B., 2000. Another Search for Maia Variable Stars. *PASP*, **112**, 846–851.

Perrin, G., Lacour, S., Woillez, J. & Thiébaut, É., 2006. High dynamic range imaging by pupil single-mode filtering and remapping. *MNRAS*, **373**, 747–751.

Perryman, M., 2011. *The Exoplanet Handbook*.

Perryman, M., 2012. The History of Exoplanet Detection. *Astrobiology*, **12**, 928–939.

Perryman, M., Hartman, J., Bakos, G. Á. & Lindegren, L., 2014. Astrometric Exoplanet Detection with Gaia. *ApJ*, **797**, 14.

Petigura, E. A., Howard, A. W. & Marcy, G. W., 2013. Prevalence of Earth-size planets orbiting Sun-like stars. *Proceedings of the National Academy of Science*, **110**, 19273–19278.

Pickering, E. C., 1889. Spectrum of Pleione. *Astronomische Nachrichten*, **123**, 95.

Pollacco, D. L., Skillen, I., Collier Cameron, A., Christian, D. J., Hellier, C. et al., 2006. The WASP Project and the SuperWASP Cameras. *PASP*, **118**, 1407–1418.

Pont, F., Aigrain, S. & Zucker, S., 2011. Reassessing the radial-velocity evidence for planets around CoRoT-7. *MNRAS*, **411**, 1953–1962.

Pope, A., 1734. *Essay on Man*.

Pope, B., Cvetojevic, N., Cheetham, A., Martinache, F., Norris, B. & Tuthill, P., 2014a. A demonstration of wavefront sensing and mirror phasing from the image domain. *MNRAS*, **440**, 125–133.

Pope, B., Martinache, F. & Tuthill, P., 2013. Dancing in the Dark: New Brown Dwarf Binaries from Kernel Phase Interferometry. *ApJ*, **767**, 110.

Pope, B., Thatte, N., Burruss, R., Tecza, M., Clarke, F. & Cotter, G., 2014b. Wavefront sensing from the image domain with the Oxford-SWIFT integral field spectrograph. In *Adaptive Optics Systems IV*, vol. 9148 of *Proc. SPIE*, 914859.

Pope, B., Tuthill, P., Hinkley, S., Ireland, M. J., Greenbaum, A., Latyshev, A., Monnier, J. D. & Martinache, F., 2016a. The Palomar kernel-phase experiment: testing kernel phase interferometry for ground-based astronomical observations. *MNRAS*, **455**, 1647–1653.

Pope, B. J. S., 2016. Kernel phase and kernel amplitude in Fizeau imaging. *MNRAS*, **463**, 3573–3581.

Pope, B. J. S., Parviainen, H. & Aigrain, S., 2016b. Transiting exoplanet candidates from K2 Campaigns 5 and 6. *MNRAS*, **461**, 3399–3409.

Pope, B. J. S., White, T. R., Huber, D., Murphy, S. J., Bedding, T. R., Caldwell, D. A., Sarai, A., Aigrain, S. & Barclay, T., 2016c. Photometry of very bright stars with Kepler and K2 smear data. *MNRAS*, **455**, L36–L40.

Proctor, R. A., 1870. *Other world than ours : The plurality of Worlds studied under the light of recent scientific researches*.

Puig, L., Pilbratt, G. L., Heske, A., Escudero Sanz, I. & Crouzet, P.-E., 2016. ARIEL: an ESA M4 mission candidate. vol. 9904, 99041W–99041W–9. URL http://dx.doi.org/10.1117/12.2230964.

Queloz, D., Bouchy, F., Moutou, C., Hatzes, A., Hébrard, G. et al., 2009. The CoRoT-7 planetary system: two orbiting super-Earths. *A&A*, **506**, 303–319.

Quintana, E. V., Jenkins, J. M., Clarke, B. D., Chandrasekaran, H., Twicken, J. D., McCauliff, S. D., Cote, M. T., Klaus, T. C., Allen, C., Caldwell, D. A. & Bryson, S. T., 2010. Pixel-level calibration in the Kepler Science Operations Center pipeline. vol. 7740, 77401X–77401X–12. URL http://dx.doi.org/10.1117/12.857678.

Quirrenbach, A., Bjorkman, K. S., Bjorkman, J. E., Hummel, C. A., Buscher, D. F., Armstrong, J. T., Mozurkewich, D., Elias, II, N. M. & Babler, B. L., 1997. Constraints on the Geometry of Circumstellar Envelopes: Optical Interferometric and Spectropolarimetric Observations of Seven Be Stars. *ApJ*, **479**, 477–496.

Rajagopal, J. K., Barry, R., Lopez, B., Danchi, W. C., Monnier, J. D., Tuthill, P. G. & Townes, C. H., 2004. Adaptive optics and aperture masking: a comparison. In W. A. Traub, ed., *Society of Photo-Optical Instrumentation Engineers (SPIE) Conference Series*, vol. 5491 of *Presented at the Society of Photo-Optical Instrumentation Engineers (SPIE) Conference*, 1120–+.

Ramírez, I. & Meléndez, J., 2005. The Effective Temperature Scale of FGK Stars. II. T_{eff}:Color:[Fe/H] Calibrations. *ApJ*, **626**, 465–485.

Rappaport, S., Barclay, T., DeVore, J., Rowe, J., Sanchis-Ojeda, R. & Still, M., 2014. KOI-2700b - A Planet Candidate with Dusty Effluents on a 22 hr Orbit. *ApJ*, **784**, 40.

Rappaport, S., Levine, A., Chiang, E., El Mellah, I., Jenkins, J., Kalomeni, B., Kite, E. S., Kotson, M., Nelson, L., Rousseau-Nepton, L. & Tran, K., 2012. Possible Disintegrating Short-period Super-Mercury Orbiting KIC 12557548. *ApJ*, **752**, 1.

Rasmussen, C. E. & Williams, C. K. I., 2005. *Gaussian Processes for Machine Learning (Adaptive Computation and Machine Learning)*. The MIT Press. ISBN 026218253X.

Rauer, H., Catala, C., Aerts, C., Appourchaux, T., Benz, W. et al., 2014. The PLATO 2.0 mission. *Experimental Astronomy*, **38**, 249–330.

Rayleigh, J. W. S., 1879. XXXI. Investigations in optics, with special reference to the spectroscope. *Philosophical Magazine Series 5*, **8**(49), 261–274. URL http://dx.doi.org/10.1080/14786447908639684.

Readhead, A. C. S., Nakajima, T. S., Pearson, T. J., Neugebauer, G., Oke, J. B. & Sargent, W. L. W., 1988. Diffraction-limited imaging with ground-based optical telescopes. *AJ*, **95**, 1278–1296.

Readhead, A. C. S., Walker, R. C., Pearson, T. J. & Cohen, M. H., 1980. Mapping radio sources with uncalibrated visibility data. *Nature*, **285**, 137–140.

Rebull, L. M., Stauffer, J. R., Bouvier, J., Cody, A. M., Hillenbrand, L. A. et al., 2016a. Rotation in the Pleiades with K2. I. Data and First Results. *AJ*, **152**, 113.

Rebull, L. M., Stauffer, J. R., Bouvier, J., Cody, A. M., Hillenbrand, L. A. et al., 2016b. Rotation in the Pleiades with K2. II. Multiperiod Stars. *AJ*, **152**, 114.

Reid, I. N., Cruz, K. L., Burgasser, A. J. & Liu, M. C., 2008. L-Dwarf Binaries in the 20-Parsec Sample. *AJ*, **135**, 580–587.

Reid, I. N., Lewitus, E., Allen, P. R., Cruz, K. L. & Burgasser, A. J., 2006. A Search for Binary Systems among the Nearest L Dwarfs. *AJ*, **132**, 891–901.

Reiter, J., Rhodes, Jr., E. J., Kosovichev, A. G., Schou, J., Scherrer, P. H. & Larson, T. P., 2015. A Method for the Estimation of p-Mode Parameters from Averaged Solar Oscillation

Power Spectra. *ApJ*, **803**, 92.

Ren, D., Dong, B., Zhu, Y. & Christian, D. J., 2012. Correction of Non-Common-Path Error for Extreme Adaptive Optics. *PASP*, **124**, 247–253.

Renson, P. & Manfroid, J., 2009. Catalogue of Ap, HgMn and Am stars. *A&A*, **498**, 961–966.

Rhodes, W. T. & Goodman, J. W., 1973. Interferometric technique for recording and restoring images degraded by unknown aberrations. *Journal of the Optical Society of America (1917-1983)*, **63**, 647–657.

Richichi, A., Calamai, G. & Leinert, C., 1994. New binary stars discovered by lunar occultations. *A&A*, **286**, 829–837.

Richichi, A., Calamai, G., Leinert, C., Stecklum, B. & Trunkovsky, E. M., 1996. New binary stars discovered by lunar occultations. II. *A&A*, **309**, 163–170.

Ricker, G. R., Winn, J. N., Vanderspek, R., Latham, D. W., Bakos, G. Á. et al., 2015. Transiting Exoplanet Survey Satellite (TESS). *Journal of Astronomical Telescopes, Instruments, and Systems*, **1**(1), 014003.

Rivinius, T., Baade, D., Stefl, S. & et al., 1998. Predicting the Outbursts of the Be Star mu Cen. In L. Kaper & A. W. Fullerton, eds., *Cyclical Variability in Stellar Winds*, 207.

Rivinius, T., Baade, D. & Štefl, S., 2003. Non-radially pulsating Be stars. *A&A*, **411**, 229–247.

Rivinius, T., Carciofi, A. C. & Martayan, C., 2013. Classical Be stars. Rapidly rotating B stars with viscous Keplerian decretion disks. *Astronomy and Astrophysics Review*, **21**, 69.

Roberts, S., Osborne, M., Ebden, M., Reece, S., Gibson, N. & Aigrain, S., 2012. Gaussian processes for time-series modelling. *Philosophical Transactions of the Royal Society of London Series A*, **371**, 20110550–20110550.

Robinson, E. L., Cochran, A. L., Cochran, W. D., Shafter, A. W. & Zhang, E.-H., 1990. A search for eclipses of HD 114762 by a low-mass companion. *AJ*, **99**, 672–674.

Roddier, F., 1986. Triple correlation as a phase closure technique. *Optics Communications*, **60**, 145–148.

Rodríguez, E., López-González, M. J. & López de Coca, P., 2000. A revised catalogue of delta Sct stars. *A&AS*, **144**, 469–474.

Rogstad, D. H., 1968. A technique for measuring visibility phase with an optical interferometer in the presence of atmospheric seeing. *Appl. Opt.*, **7**, 585.

Rosenblatt, F., 1958. The Perceptron: A Probabilistic Model for Information Storage and Organization in The Brain. *Psychological Review*, 65–386.

Rosenblatt, F., 1971. A Two-Color Photometric Method for Detection of Extra solar Planetary Systems. *Icarus*, **14**, 71–93.

Royer, F., Zorec, J. & Gómez, A. E., 2007. Rotational velocities of A-type stars. III. Velocity distributions. *A&A*, **463**, 671–682.

Rudin, L. I., Osher, S. & Fatemi, E., 1992. Nonlinear total variation based noise removal algorithms. *Physica D Nonlinear Phenomena*, **60**, 259–268.

Rufenach, C. L., 1975. Ionospheric scintillation by a random phase screen Spectral approach. *Radio Science*, **10**, 155–165.

Ruggles, C. L. N., 2015. *Handbook of Archaeoastronomy and Ethnoastronomy*.

Ryabchikova, T. A., Malanushenko, V. P. & Adelman, S. J., 1999. Orbital elements and abundance analyses of the double-lined spectroscopic binary alpha Andromedae. *A&A*, **351**,

963–972.

Ryle, M. & Vonberg, D. D., 1948. An Investigation of Radio-Frequency Radiation from the Sun. *Proceedings of the Royal Society of London Series A*, **193**, 98–120.

Safronov, V. S., 1972. *Evolution of the protoplanetary cloud and formation of the earth and planets.*.

Sagan, C. & Salpeter, E. E., 1976. Particles, environments, and possible ecologies in the Jovian atmosphere. *ApJS*, **32**, 737–755.

Sagan, C., Thompson, W. R., Carlson, R., Gurnett, D. & Hord, C., 1993. A search for life on Earth from the Galileo spacecraft. *Nature*, **365**, 715–721.

Sahlmann, J., Lazorenko, P. F., Ségransan, D., Martín, E. L., Mayor, M., Queloz, D. & Udry, S., 2014. Astrometric planet search around southern ultracool dwarfs. I. First results, including parallaxes of 20 M8-L2 dwarfs. *A&A*, **565**, A20.

Saio, H., Cameron, C., Kuschnig, R., Walker, G. A. H., Matthews, J. M., Rowe, J. F., Lee, U., Huber, D., Weiss, W. W., Guenther, D. B., Moffat, A. F. J., Rucinski, S. M. & Sasselov, D., 2007. MOST Detects g-Modes in the Late-Type Be Star β Canis Minoris (B8 Ve). *ApJ*, **654**, 544–550.

Saio, H., Kuschnig, R., Gautschy, A., Cameron, C., Walker, G. A. H., Matthews, J. M., Guenther, D. B., Moffat, A. F. J., Rucinski, S. M., Sasselov, D. & Weiss, W. W., 2006. MOST Detects g- and p-Modes in the B Supergiant HD 163899 (B2 Ib/II). *ApJ*, **650**, 1111–1118.

Sallum, S., Eisner, J. A., Close, L. M., Hinz, P. M., Skemer, A. J., Bailey, V., Briguglio, R., Follette, K. B., Males, J. R., Morzinski, K. M., Puglisi, A., Rodigas, T. J., Weinberger, A. J. & Xompero, M., 2015a. New Spatially Resolved Observations of the T Cha Transition Disk and Constraints on the Previously Claimed Substellar Companion. *ApJ*, **801**, 85.

Sallum, S., Follette, K. B., Eisner, J. A., Close, L. M., Hinz, P., Kratter, K., Males, J., Skemer, A., Macintosh, B., Tuthill, P., Bailey, V., Defrère, D., Morzinski, K., Rodigas, T., Spalding, E., Vaz, A. & Weinberger, A. J., 2015b. Accreting protoplanets in the LkCa 15 transition disk. *Nature*, **527**, 342–344.

Samadi, R. & Goupil, M.-J., 2001. Excitation of stellar p-modes by turbulent convection. I. Theoretical formulation. *A&A*, **370**, 136–146.

Sanchis-Ojeda, R., Rappaport, S., Pallè, E., Delrez, L., DeVore, J. et al., 2015. The K2-ESPRINT Project I: Discovery of the Disintegrating Rocky Planet K2-22b with a Cometary Head and Leading Tail. *ApJ*, **812**, 112.

Schechter, P. L., Mateo, M. & Saha, A., 1993. DOPHOT, a CCD photometry program: Description and tests. *PASP*, **105**, 1342–1353.

Schlieder, J. E., Crossfield, I. J. M., Petigura, E. A., Howard, A. W., Aller, K. M. et al., 2016. Two Small Temperate Planets Transiting Nearby M Dwarfs in K2 Campaigns 0 and 1. *ApJ*, **818**, 87.

Schneider, J., Chevreton, M. & Martin, E. L., 1990. New efforts in the search for extrasolar planets. In B. Battrick, ed., *ESA Special Publication*, vol. 315 of *ESA Special Publication*.

Scholz, G., Lehmann, H., Hildebrandt, G., Panov, K. & Iliev, L., 1998. Spectroscopic and photometric investigations of MAIA candidate stars. *A&A*, **337**, 447–459.

Schwarzschild, K., 1896. Über Messung von Doppelsternen durch Interferenzen. *Astronomische Nachrichten*, **139**, 353.

Schwarzschild, K., 1916. Über das Gravitationsfeld einer Kugel aus inkompressibler Flüssigkeit nach der Einsteinschen Theorie. In *Sitzungsberichte der Königlich Preussischen Akademie der Wissenschaften zu Berlin, Phys.-Math. Klasse, 424-434 (1916)*.

Scott, E. R. D., 2007. Chondrites and the Protoplanetary Disk. *Annual Review of Earth and Planetary Sciences*, **35**, 577–620.

Seager, S., Bains, W. & Petkowski, J. J., 2016. Toward a List of Molecules as Potential Biosignature Gases for the Search for Life on Exoplanets and Applications to Terrestrial Biochemistry. *Astrobiology*, **16**, 465–485.

Seager, S. & Deming, D., 2010. Exoplanet Atmospheres. *ARA&A*, **48**, 631–672.

Seager, S. & Mallén-Ornelas, G., 2003. A Unique Solution of Planet and Star Parameters from an Extrasolar Planet Transit Light Curve. *ApJ*, **585**, 1038–1055.

Seager, S. & Sasselov, D. D., 2000. Theoretical Transmission Spectra during Extrasolar Giant Planet Transits. *ApJ*, **537**, 916–921.

Seager, S., Turner, E. L., Schafer, J. & Ford, E. B., 2005. Vegetation's Red Edge: A Possible Spectroscopic Biosignature of Extraterrestrial Plants. *Astrobiology*, **5**, 372–390.

See, T. J. J., 1895. Perturbations in the motion of the double star 70 Ophiuchi = T, 2272. *AJ*, **15**, 180–180.

Shaklan, S., Levine, M., Foote, M., Rodgers, M., Underhill, M., Marchen, L. & Klein, D., 2013. The AFTA coronagraph instrument. In *Techniques and Instrumentation for Detection of Exoplanets VI*, vol. 8864 of *Proc. SPIE*, 886415.

Shao, M. & Staelin, D. H., 1980. First fringe measurements with a phase-tracking stellar interferometer. *Appl. Opt.*, **19**, 1519–1522.

Sharov, A. S. & Lyuty, V. M., 1976. Pleione as a Variable Star. In A. Slettebak, ed., *Be and Shell Stars*, vol. 70 of *IAU Symposium*, 105.

Sharov, A. S. & Lyutyj, V. M., 1988. Three-color photoelectric photometry of Pleione during shell ejection in 1971-1986. *Astronomicheskii Zhurnal*, **65**, 593–600.

Shields, A. L., Ballard, S. & Johnson, J. A., 2016. The Habitability of Planets Orbiting M-dwarf Stars. *ArXiv e-prints*.

Shklovskii, I. S. & Sagan, C., 1966. *Intelligent life in the universe*.

Shmidt, O. I., 1958. *A theory of earth's origin; four lectures.*.

Silburt, A., Gaidos, E. & Wu, Y., 2015. A Statistical Reconstruction of the Planet Population around Kepler Solar-type Stars. *ApJ*, **799**, 180.

Silva Aguirre, V., Basu, S., Brandão, I. M., Christensen-Dalsgaard, J., Deheuvels, S. et al., 2013. Stellar Ages and Convective Cores in Field Main-sequence Stars: First Asteroseismic Application to Two Kepler Targets. *ApJ*, **769**, 141.

Silva Aguirre, V., Davies, G. R., Basu, S., Christensen-Dalsgaard, J., Creevey, O. et al., 2015. Ages and fundamental properties of Kepler exoplanet host stars from asteroseismology. *MNRAS*, **452**, 2127–2148.

Silva Aguirre, V., Lund, M. N., Antia, H. M., Ball, W. H., Basu, S. et al., 2016. Standing on the shoulders of Dwarfs: the Kepler asteroseismic LEGACY sample II - radii, masses, and ages. *ArXiv e-prints*.

Silvotti, R., Schuh, S., Janulis, R., Solheim, J.-E., Bernabei, S. et al., 2007. A giant planet orbiting the 'extreme horizontal branch' star V391 Pegasi. *Nature*, **449**, 189–191.

Sing, D. K., Fortney, J. J., Nikolov, N., Wakeford, H. R., Kataria, T. et al., 2016. A continuum from clear to cloudy hot-Jupiter exoplanets without primordial water depletion. *Nature*, **529**, 59–62.

Sing, D. K., Lecavelier des Etangs, A., Fortney, J. J., Burrows, A. S., Pont, F. et al., 2013. HST hot-Jupiter transmission spectral survey: evidence for aerosols and lack of TiO in the atmosphere of WASP-12b. *MNRAS*, **436**, 2956–2973.

Sing, D. K., Wakeford, H. R., Showman, A. P., Nikolov, N., Fortney, J. J. et al., 2015. HST hot-Jupiter transmission spectral survey: detection of potassium in WASP-31b along with a cloud deck and Rayleigh scattering. *MNRAS*, **446**, 2428–2443.

Skilling, J. & Bryan, R. K., 1984. Maximum Entropy Image Reconstruction - General Algorithm. *MNRAS*, **211**, 111.

Smirnov, O. M., 2011. Revisiting the radio interferometer measurement equation. I. A full-sky Jones formalism. *A&A*, **527**, A106.

Smith, J. C., Stumpe, M. C., Van Cleve, J. E., Jenkins, J. M., Barclay, T. S., Fanelli, M. N., Girouard, F. R., Kolodziejczak, J. J., McCauliff, S. D., Morris, R. L. & Twicken, J. D., 2012. Kepler Presearch Data Conditioning II - A Bayesian Approach to Systematic Error Correction. *PASP*, **124**, 1000–1014.

Soter, S., 2006. What Is a Planet? *AJ*, **132**, 2513–2519.

Soummer, R., Pueyo, L. & Larkin, J., 2012. Detection and Characterization of Exoplanets and Disks Using Projections on Karhunen-Loève Eigenimages. *ApJ*, **755**, L28.

Stamatellos, D., Hubber, D. A. & Whitworth, A. P., 2007. Brown dwarf formation by gravitational fragmentation of massive, extended protostellar discs. *MNRAS*, **382**, L30–L34.

Stauffer, J., Rebull, L., Bouvier, J., Hillenbrand, L. A., Collier-Cameron, A. et al., 2016. Rotation in the Pleiades with K2. III. Speculations on Origins and Evolution. *AJ*, **152**, 115.

Stauffer, J. R., Schultz, G. & Kirkpatrick, J. D., 1998. Keck Spectra of Pleiades Brown Dwarf Candidates and a Precise Determination of the Lithium Depletion Edge in the Pleiades. *ApJ*, **499**, L199–L203.

Steffen, J. H., Fabrycky, D. C., Agol, E., Ford, E. B., Morehead, R. C. et al., 2013. Transit timing observations from Kepler - VII. Confirmation of 27 planets in 13 multiplanet systems via transit timing variations and orbital stability. *MNRAS*, **428**, 1077–1087.

Steffen, J. H., Fabrycky, D. C., Ford, E. B., Carter, J. A., Désert, J.-M. et al., 2012a. Transit timing observations from Kepler - III. Confirmation of four multiple planet systems by a Fourier-domain study of anticorrelated transit timing variations. *MNRAS*, **421**, 2342–2354.

Steffen, J. H., Ford, E. B., Rowe, J. F., Fabrycky, D. C., Holman, M. J. et al., 2012b. Transit Timing Observations from Kepler. VI. Potentially Interesting Candidate Systems from Fourier-based Statistical Tests. *ApJ*, **756**, 186.

Stello, D., Huber, D., Bedding, T. R., Benomar, O., Bildsten, L., Elsworth, Y. P., Gilliland, R. L., Mosser, B., Paxton, B. & White, T. R., 2013. Asteroseismic Classification of Stellar Populations among 13,000 Red Giants Observed by Kepler. *ApJ*, **765**, L41.

Stello, D., Huber, D., Kallinger, T., Basu, S., Mosser, B. et al., 2011a. Amplitudes of

Solar-like Oscillations: Constraints from Red Giants in Open Clusters Observed by Kepler. *ApJ*, **737**, L10.

Stello, D., Meibom, S., Gilliland, R. L., Grundahl, F., Hekker, S. et al., 2011b. An Asteroseismic Membership Study of the Red Giants in Three Open Clusters Observed by Kepler: NGC 6791, NGC 6819, and NGC 6811. *ApJ*, **739**, 13.

Stello, D., Vanderburg, A., Casagrande, L., Gilliland, R., Silva Aguirre, V., Sandquist, E., Leiner, E., Mathieu, R. & Soderblom, D. R., 2016. The K2 M67 Study: Revisiting Old Friends with K2 Reveals Oscillating Red Giants in the Open Cluster M67. *ApJ*, **832**, 133.

Stéphan, E., 1874. Sur l'extrême petitesse du diamètre apparent des étoiles fixes. *Comptes Rendus de l'Académie des Sciences*, **78**, 1008–1012.

Stevenson, D. J. & Lunine, J. I., 1988. Rapid formation of Jupiter by diffuse redistribution of water vapor in the solar nebula. *Icarus*, **75**, 146–155.

Strand, K. A., 1943. 61 Cygni as a Triple System. *PASP*, **55**, 29–32.

Strong, D. & Chan, T., 2003. Edge-preserving and scale-dependent properties of total variation regularization. *Inverse Problems*, **19**(6), S165. URL `http://stacks.iop.org/0266-5611/19/i=6/a=059`.

Struve, O., 1931. On the Origin of Bright Lines in Spectra of Stars of Class B. *ApJ*, **73**, 94.

Struve, O., 1952. Proposal for a project of high-precision stellar radial velocity work. *The Observatory*, **72**, 199–200.

Struve, O., 1955. Some Unusual Short-period Variables. *Sky and Telescope*, **14**.

Stumpe, M. C., Smith, J. C., Catanzarite, J. H., Van Cleve, J. E., Jenkins, J. M., Twicken, J. D. & Girouard, F. R., 2014. Multiscale Systematic Error Correction via Wavelet-Based Bandsplitting in Kepler Data. *PASP*, **126**, 100–114.

Stumpe, M. C., Smith, J. C., Van Cleve, J. E., Twicken, J. D., Barclay, T. S., Fanelli, M. N., Girouard, F. R., Jenkins, J. M., Kolodziejczak, J. J., McCauliff, S. D. & Morris, R. L., 2012. Kepler Presearch Data Conditioning I - Architecture and Algorithms for Error Correction in Kepler Light Curves. *PASP*, **124**, 985–999.

Sumi, T., Kamiya, K., Bennett, D. P., Bond, I. A., Abe, F. et al., 2011. Unbound or distant planetary mass population detected by gravitational microlensing. *Nature*, **473**, 349–352.

Swain, M. R., Deroo, P., Griffith, C. A., Tinetti, G., Thatte, A., Vasisht, G., Chen, P., Bouwman, J., Crossfield, I. J., Angerhausen, D., Afonso, C. & Henning, T., 2010. A ground-based near-infrared emission spectrum of the exoplanet HD189733b. *Nature*, **463**, 637–639.

Swain, M. R., Tinetti, G., Vasisht, G., Deroo, P., Griffith, C., Bouwman, J., Chen, P., Yung, Y., Burrows, A., Brown, L. R., Matthews, J., Rowe, J. F., Kuschnig, R. & Angerhausen, D., 2009a. Water, Methane, and Carbon Dioxide Present in the Dayside Spectrum of the Exoplanet HD 209458b. *ApJ*, **704**, 1616–1621.

Swain, M. R., Vasisht, G. & Tinetti, G., 2008. The presence of methane in the atmosphere of an extrasolar planet. *Nature*, **452**, 329–331.

Swain, M. R., Vasisht, G., Tinetti, G., Bouwman, J., Chen, P., Yung, Y., Deming, D. & Deroo, P., 2009b. Molecular Signatures in the Near-Infrared Dayside Spectrum of HD 189733b. *ApJ*, **690**, L114–L117.

Swedenborg, E., 1743. *The principia or The first principles of natural things: to which are added the minor principia*. London: The Swedenborg Society.

Tanaka, K., Sadakane, K., Narusawa, S.-Y., Naito, H., Kambe, E., Katahira, J.-I. & Hirata, R., 2007. Dramatic Spectral and Photometric Changes of Pleione (28 Tau) between 2005 November and 2007 April. *Publications of the Astronomical Society of Japan*, **59**, L35–L39.

Tarter, J. C., 1975. *The interaction of gas and galaxies within galaxy clusters*. Ph.D. thesis, California Univ., Berkeley.

Tarter, J. C., 2001. The Search for Extraterrestrial Intelligence (SETI). *ARA&A*, **39**, 511–548.

Tarter, J. C., 2014. Brown Is Not a Color: Introduction of the Term 'Brown Dwarf'. In V. Joergens, ed., *50 Years of Brown Dwarfs*, vol. 401 of *Astrophysics and Space Science Library*, 19.

Tasker, E., Tan, J., Heng, K., Kane, S. & Spiegel, D., 2017. The language of exoplanet ranking metrics needs to change. *Nature Astronomy*, **1**, 0042 EP –. URL `http://dx.doi.org/10.1038/s41550-017-0042`. Comment.

Tassoul, M., 1980. Asymptotic approximations for stellar nonradial pulsations. *ApJS*, **43**, 469–490.

Tennyson, A., 1842. *Poems*. Edward Moxon.

Tessenyi, M., Savini, G., Tinetti, G., Tennyson, J., Dhesi, M. & Joshua, M., 2016. TWINKLE - A Low Earth Orbit Visible and Infrared Exoplanet Spectroscopy Observatory. In *AAS/Division for Planetary Sciences Meeting Abstracts*, vol. 48 of *AAS/Division for Planetary Sciences Meeting Abstracts*, 123.33.

Texereau, J., 1962. Turbulence et structure d'images photographiques dans un grand télescope. *L'Astronomie*, **76**, 159.

Tinetti, G., Drossart, P., Eccleston, P., Hartogh, P., Heske, A. et al., 2016. The science of ARIEL (Atmospheric Remote-sensing Infrared Exoplanet Large-survey). vol. 9904, 99041X–99041X–10. URL `http://dx.doi.org/10.1117/12.2232370`.

Tinetti, G., Encrenaz, T. & Coustenis, A., 2013. Spectroscopy of planetary atmospheres in our Galaxy. *The Astronomy and Astrophysics Review*, **21**(1), 63. ISSN 1432-0754. URL `http://dx.doi.org/10.1007/s00159-013-0063-6`.

Tinetti, G., Vidal-Madjar, A., Liang, M.-C., Beaulieu, J.-P., Yung, Y., Carey, S., Barber, R. J., Tennyson, J., Ribas, I., Allard, N., Ballester, G. E., Sing, D. K. & Selsis, F., 2007. Water vapour in the atmosphere of a transiting extrasolar planet. *Nature*, **448**, 169–171.

Titchmarsh, P. F., 1941. Lloyd's single-mirror interference fringes. *Proceedings of the Physical Society*, **53**(4), 391. URL `http://stacks.iop.org/0959-5309/53/i=4/a=304`.

Tkachenko, A., Aerts, C., Pavlovski, K., Southworth, J., Degroote, P. et al., 2012. Detection of gravity modes in the massive binary V380 Cyg from Kepler space-based photometry and high-resolution spectroscopy. *MNRAS*, **424**, L21–L25.

Torres, G., Fressin, F., Batalha, N. M., Borucki, W. J., Brown, T. M. et al., 2011. Modeling Kepler Transit Light Curves as False Positives: Rejection of Blend Scenarios for Kepler-9, and Validation of Kepler-9 d, A Super-earth-size Planet in a Multiple System. *ApJ*, **727**, 24.

Traub, W. A., 2012. Terrestrial, Habitable-zone Exoplanet Frequency from Kepler. *ApJ*, **745**, 20.

Triana, S. A., Moravveji, E., Pápics, P. I., Aerts, C., Kawaler, S. D. & Christensen-Dalsgaard, J., 2015. The Internal Rotation Profile of the B-type Star KIC 10526294 from Frequency Inversion of its Dipole Gravity Modes. *ApJ*, **810**, 16.

Triaud, A., 2016. Exoplanets: Migration of giants. *Nature*, **537**, 496–497.

Tuthill, P., Lloyd, J., Ireland, M., Martinache, F., Monnier, J., Woodruff, H., ten Brummelaar, T., Turner, N. & Townes, C., 2006. Sparse-aperture adaptive optics. In *Society of Photo-Optical Instrumentation Engineers (SPIE) Conference Series*, vol. 6272 of *Society of Photo-Optical Instrumentation Engineers (SPIE) Conference Series*.

Tuthill, P. G., 2012. The unlikely rise of masking interferometry: leading the way with 19th century technology. In *Optical and Infrared Interferometry III*, vol. 8445 of *Proc. SPIE*, 844502.

Tuthill, P. G., Monnier, J. D. & Danchi, W. C., 1999. A dusty pinwheel nebula around the massive star WR104. *Nature*, **398**, 487–489.

Tuthill, P. G., Monnier, J. D., Danchi, W. C., Hale, D. D. S. & Townes, C. H., 2002. Imaging the Disk around the Luminous Young Star LkHα 101 with Infrared Interferometry. *ApJ*, **577**, 826–838.

Tuthill, P. G., Monnier, J. D., Danchi, W. C. & Lopez, B., 2000a. Smoke Signals from IRC +10216. I. Milliarcsecond Proper Motions of the Dust. *ApJ*, **543**, 284–290.

Tuthill, P. G., Monnier, J. D., Danchi, W. C., Wishnow, E. H. & Haniff, C. A., 2000b. Michelson Interferometry with the Keck I Telescope. *PASP*, **112**, 555–565.

Twicken, J. D., Chandrasekaran, H., Jenkins, J. M., Gunter, J. P., Girouard, F. & Klaus, T. C., 2010. Presearch data conditioning in the Kepler Science Operations Center pipeline. In *Software and Cyberinfrastructure for Astronomy*, vol. 7740 of *Proc. SPIE*, 77401U.

Twiss, R. Q., Carter, A. W. L. & Little, A. G., 1960. Brightness distribution over some strong radio sources at 1427 Mc/s. *The Observatory*, **80**, 153–159.

Tycner, C., Lester, J. B., Hajian, A. R., Armstrong, J. T., Benson, J. A., Gilbreath, G. C., Hutter, D. J., Pauls, T. A. & White, N. M., 2005. Properties of the Hα-emitting Circumstellar Regions of Be Stars. *ApJ*, **624**, 359–371.

Udalski, A., Zebrun, K., Szymanski, M., Kubiak, M., Soszynski, I., Szewczyk, O., Wyrzykowski, L. & Pietrzynski, G., 2002. The Optical Gravitational Lensing Experiment. Search for Planetary and Low- Luminosity Object Transits in the Galactic Disk. Results of 2001 Campaign – Supplement. *Acta Astronomica*, **52**, 115–128.

Ulrich, R. K., 1986. Determination of stellar ages from asteroseismology. *ApJ*, **306**, L37–L40.

van Belle, G. T., 2008. Closure Phase Signatures of Planet Transit Events. *PASP*, **120**, 617.

van Belle, G. T., van Belle, G., Creech-Eakman, M. J., Coyne, J., Boden, A. F., Akeson, R. L., Ciardi, D. R., Rykoski, K. M., Thompson, R. R., Lane, B. F. & PTI Collaboration, 2008. The Palomar Testbed Interferometer Calibrator Catalog. *ApJS*, **176**, 276–292.

van Cittert, P. H., 1934. Die Wahrscheinliche Schwingungsverteilung in Einer von Einer Lichtquelle Direkt Oder Mittels Einer Linse Beleuchteten Ebene. *Physica*, **1**, 201–210.

Van Cleve, J. E. & Caldwell, D. A., 2009. Kepler Instrument Handbook (KSCI-19033).

van de Kamp, P., 1963. Astrometric study of Barnard's star from plates taken with the 24-inch Sproul refractor. *AJ*, **68**, 515–521.

van de Kamp, P., 1969a. Alternate dynamical analysis of Barnard's star. *AJ*, **74**, 757–759.

van de Kamp, P., 1969b. Parallax, Proper Motion, Acceleration, and Orbital Motion of Barnard's Star. *AJ*, **74**, 238.

van de Kamp, P., 1975. Astrometric study of Barnard's star from plates taken with the Sproul

61-cm refractor. *AJ*, **80**, 658.

van de Kamp, P., 1982. The planetary system of Barnard's star. *Vistas in Astronomy*, **26**, 141–157.

van Leeuwen, F., 2007. Validation of the new Hipparcos reduction. *A&A*, **474**, 653–664.

van Maanen, A., 1917. Two Faint Stars with Large Proper Motion. *PASP*, **29**, 258.

van Maanen, A., 1919. A Very Faint Star of Spectral Type F. *PASP*, **31**, 42.

van Saders, J. L., Ceillier, T., Metcalfe, T. S., Silva Aguirre, V., Pinsonneault, M. H., García, R. A., Mathur, S. & Davies, G. R., 2016. Weakened magnetic braking as the origin of anomalously rapid rotation in old field stars. *Nature*, **529**, 181–184.

Vandakurov, Y. V., 1967. The Frequency Distribution of Stellar Oscillations. *Astronomicheskii Zhurnal*, **44**, 786.

Vanderburg, A. & Johnson, J. A., 2014a. A Technique for Extracting Highly Precise Photometry for the Two-Wheeled Kepler Mission. *PASP*, **126**, 948–958.

Vanderburg, A. & Johnson, J. A., 2014b. A Technique for Extracting Highly Precise Photometry for the Two-Wheeled Kepler Mission. *PASP*, **126**, 948–958.

Vanderburg, A., Johnson, J. A., Rappaport, S., Bieryla, A., Irwin, J. et al., 2015. A disintegrating minor planet transiting a white dwarf. *Nature*, **526**, 546–549.

Vanderburg, A., Latham, D. W., Buchhave, L. A., Bieryla, A., Berlind, P., Calkins, M. L., Esquerdo, G. A., Welsh, S. & Johnson, J. A., 2016. Planetary Candidates from the First Year of the K2 Mission. *ApJS*, **222**, 14.

Vidal-Madjar, A., Lecavelier des Etangs, A., Désert, J.-M., Ballester, G. E., Ferlet, R., Hébrard, G. & Mayor, M., 2003. An extended upper atmosphere around the extrasolar planet HD209458b. *Nature*, **422**, 143–146.

Vigan, A., Bonavita, M., Biller, B., Forgan, D., Rice, K. et al., 2017. The VLT/NaCo large program to probe the occurrence of exoplanets and brown dwarfs at wide orbits. IV. Gravitational instability rarely forms wide, giant planets. *ArXiv e-prints*.

Vigan, A., Bonnefoy, M., Ginski, C., Beust, H., Galicher, R. et al., 2016. First light of the VLT planet finder SPHERE. I. Detection and characterization of the substellar companion GJ 758 B. *A&A*, **587**, A55.

Waelkens, C., 1991. Slowly pulsating B stars. *A&A*, **246**, 453–468.

Wakeford, H. R., Sing, D. K., Evans, T., Deming, D. & Mandell, A., 2016. Marginalizing Instrument Systematics in HST WFC3 Transit Light Curves. *ApJ*, **819**, 10.

Walker, G. A. H., 2012. The first high-precision radial velocity search for extra-solar planets. *New Astron. Rev.*, **56**, 9–15.

Walker, G. A. H., Kuschnig, R., Matthews, J. M., Cameron, C., Saio, H., Lee, U., Kambe, E., Masuda, S., Guenther, D. B., Moffat, A. F. J., Rucinski, S. M., Sasselov, D. & Weiss, W. W., 2005. MOST Detects g-Modes in the Be Star HD 163868. *ApJ*, **635**, L77–L80.

Wallace, A. R., 1903. *Man's place in the universe; a study of the results of scientific research in relation to the unity or plurality of worlds*.

Ward, W. R., 1986. Density waves in the solar nebula - Differential Lindblad torque. *Icarus*, **67**, 164–180.

Weigelt, G. P., 1977. Modified astronomical speckle interferometry 'speckle masking'. *Optics Communications*, **21**, 55–59.

Weintraub, D. A., 2014. *Religions and Extraterrestrial Life: How Will We Deal With It?*. Springer.

Weiss, W. W., 1977. HR 239 and HR 8676: Two delta Scuti-Type Variables. *Information Bulletin on Variable Stars*, **1364**, 1.

Weiss, W. W., Kuschnig, R., Mkrtichian, D. E., Kusakin, A. V., Kreidl, T. J. et al., 1998. Photometry of ET Andromedae and pulsation of HD 219891. *A&A*, **338**, 919–922.

Weiss, W. W., Rucinski, S. M., Moffat, A. F. J., Schwarzenberg-Czerny, A., Koudelka, O. F. et al., 2014. BRITE-Constellation: Nanosatellites for Precision Photometry of Bright Stars. *PASP*, **126**, 573.

Wetherill, G. W., 1980. Formation of the terrestrial planets. *ARA&A*, **18**, 77–113.

Whewell, W., 1853. *Of the Plurality of Worlds*. ISBN 9780226894355.

White, T. R., Huber, D., Maestro, V., Bedding, T. R., Ireland, M. J. et al., 2013. Interferometric radii of bright Kepler stars with the CHARA Array: θ Cygni and 16 Cygni A and B. *MNRAS*, **433**, 1262–1270.

White, T. R., Pope, B. J. S., Antoci, V., Pápics, P. I., Aerts, C. et al., submitted. Beyond the *Kepler*/K2 bright limit: variability in the seven brightest members of the Pleiades. *MNRAS*.

White, T. R., Silva Aguirre, V., Boyajian, T., Creevey, O., Huber, D., von Braun, K., Bedding, T. R., Elsworth, Y., Hekker, S., Stello, D. & Weiss, A., 2015. Testing Asteroseismic Scaling Relations with Interferometry. In *European Physical Journal Web of Conferences*, vol. 101 of *European Physical Journal Web of Conferences*, 06068.

Wiener, N., 1930. Generalized harmonic analysis. *Acta Math.*, **55**, 117–258. URL `http://dx.doi.org/10.1007/BF02546511`.

Williams, J. P. & Cieza, L. A., 2011. Protoplanetary Disks and Their Evolution. *ARA&A*, **49**, 67–117.

Williams, T. C., 1910. *The Aeneid of Virgil Translated into English Verse*. Houghton Mifflin Co. Boston.

Winn, J. N. & Fabrycky, D. C., 2015. The Occurrence and Architecture of Exoplanetary Systems. *Annual Review of Astronomy and Astrophysics*, **53**(1), 409–447. URL `http://dx.doi.org/10.1146/annurev-astro-082214-122246`.

Winn, J. N., Matthews, J. M., Dawson, R. I., Fabrycky, D., Holman, M. J., Kallinger, T., Kuschnig, R., Sasselov, D., Dragomir, D., Guenther, D. B., Moffat, A. F. J., Rowe, J. F., Rucinski, S. & Weiss, W. W., 2011. A Super-Earth Transiting a Naked-eye Star. *ApJ*, **737**, L18.

Wolstencroft, R. D. & Raven, J. A., 2002. Photosynthesis: Likelihood of Occurrence and Possibility of Detection on Earth-like Planets. *Icarus*, **157**, 535–548.

Wolszczan, A., 1994. Confirmation of Earth-Mass Planets Orbiting the Millisecond Pulsar PSR B1257+12. *Science*, **264**, 538–542.

Wolszczan, A., 2012. Discovery of pulsar planets. *New Astron. Rev.*, **56**, 2–8.

Wolszczan, A. & Frail, D. A., 1992. A planetary system around the millisecond pulsar PSR1257 + 12. *Nature*, **355**, 145–147.

Woolfson, M. M., 1964. A Capture Theory of the Origin of the Solar System. *Proceedings of the Royal Society of London Series A*, **282**, 485–507.

Woolfson, M. M., 1979. Cosmogony today. *QQJRAS*, **20**, 97–114.

Woolfson, M. M., 1993. The Solar - Origin and Evolution. *QQJRAS*, **34**.

Wraight, K. T., Fossati, L., Netopil, M., Paunzen, E., Rode-Paunzen, M., Bewsher, D., Norton, A. J. & White, G. J., 2012. A photometric study of chemically peculiar stars with the STEREO satellites - I. Magnetic chemically peculiar stars. *MNRAS*, **420**, 757–772.

Wright, J. T., Marcy, G. W., Howard, A. W., Johnson, J. A., Morton, T. D. & Fischer, D. A., 2012. The Frequency of Hot Jupiters Orbiting nearby Solar-type Stars. *ApJ*, **753**, 160.

Wright, J. T., Mullan, B., Sigurdsson, S. & Povich, M. S., 2014. The $\hat{\mathrm{G}}$ Infrared Search for Extraterrestrial Civilizations with Large Energy Supplies. I. Background and Justification. *ApJ*, **792**, 26.

Wright, T., 1734. *An Original Theory Or New Hypothesis of the Universe, 1750: A Facsimile Reprint Together with the First Publication of A Theory of the Universe, 1734*.

Young, T., 1804. The Bakerian Lecture: Experiments and Calculations Relative to Physical Optics. *Philosophical Transactions of the Royal Society of London*, **94**, 1–16. URL `http://rstl.royalsocietypublishing.org/content/94/1.1.short`.

Zastrow, M., 2014. Sun's stroke keeps Kepler online. *Nature*, **514**, 414–415.

Zernike, F., 1938. The concept of degree of coherence and its application to optical problems. *Physica*, **5**, 785–795.

Zhao, F., 2014. WFIRST-AFTA coronagraph instrument overview. In *Space Telescopes and Instrumentation 2014: Optical, Infrared, and Millimeter Wave*, vol. 9143 of *Proc. SPIE*, 91430O.

Zhao, M., Monnier, J. D., Pedretti, E., Thureau, N., Mérand, A., ten Brummelaar, T., McAlister, H., Ridgway, S. T., Turner, N., Sturmann, J., Sturmann, L., Goldfinger, P. J. & Farrington, C., 2009. Imaging and Modeling Rapidly Rotating Stars: α Cephei and α Ophiuchi. *ApJ*, **701**, 209–224.

Zorec, J., Frémat, Y. & Cidale, L., 2005. On the evolutionary status of Be stars. I. Field Be stars near the Sun. *A&A*, **441**, 235–248.

Zorec, J. & Royer, F., 2012. Rotational velocities of A-type stars. IV. Evolution of rotational velocities. *A&A*, **537**, A120.

Zuckerman, B., 2015. Recognition of the First Observational Evidence of an Extrasolar Planetary System. In P. Dufour, P. Bergeron & G. Fontaine, eds., *19th European Workshop on White Dwarfs*, vol. 493 of *Astronomical Society of the Pacific Conference Series*, 291.

Zwahlen, N., North, P., Debernardi, Y., Eyer, L., Galland, F., Groenewegen, M. A. T. & Hummel, C. A., 2004. A purely geometric distance to the binary star Atlas, a member of the Pleiades. *A&A*, **425**, L45–L48.